Multinuclear magnetic resonance and X-ray crystallographic scrutinization of crystal-engineered chalcogen-bonded cocrystals

Tamali Nag

A thesis submitted in partial fulfillment of the requirements for the Doctorate in Philosophy degree in Chemistry

Department of Chemistry and Biomolecular Sciences

Faculty of Science

University of Ottawa

uOttawa

Abstract

Chalcogen bonds, a growing class of noncovalent interactions, have been extensively studied in recent years due to their rising utility and applications in the fields of catalysis, crystal engineering, pharmaceuticals, active anion recognition, and materials chemistry. A chalcogen bond's physical properties, reactivity, and electronic structure are very much under study and development by chemists of today.

A chalcogen bond consists of a chalcogen bond donor which features an electron-depleted region on the chalcogen atom (σ-hole) and a chalcogen bond acceptor, which features a region of rich electron density in an atom or functional group of another molecule or the same molecule that contains the chalcogen bond donor. The σ-hole of the chalcogen bond donor imparts high directionality and tuneability as compared to a simple covalent bond, resulting in a versatile class of noncovalent interactions.

This thesis presents work where chalcogen-bonded cocrystals were synthesized and analyzed using techniques such as single-crystal X-ray diffraction, powder X-ray diffraction, multinuclear solid-state magnetic resonance spectroscopy and nuclear quadrupole resonance spectroscopy. The beginning of the research work involved working with Te and Se based chalcogen bond donors, namely 3,4-dicyano-1,2,5-selenodiazole (selenodiazole) and 3,4-dicyano-1,2,5-telluradiazole (telluradiazole) with a variety of chalcogen bond acceptors such as hydroquinone, tetraphenylphosphonium chloride, and tetraethylphosphonium chloride. Their electronic structure and geometry were explored using solid-state NMR and X-ray diffraction techniques. The chemical shift (CS) tensors obtained from solid-state NMR experiments on the

chalcogen bonded cocrystals featuring selenodiazole-hydroquinone, telluradiazole-tetraphenylphosphonium chloride and telluradiazole-tetraethylphosphonium chloride were used to probe the chalcogen bond donors, selenodiazole and telluradiazole. The principal components of the chalcogen atom chemical shift tensors, as well as their spans and skews, were compared to previous results from our group and a trend in these SSNMR parameters was established. The ^{125}Te chemical shift tensor span was found to be sensitive to the ChB formation. The small changes observed in the chemical shift tensor of ^{77}Se SSNMR for the selenodiazole-hydroquinone cocrystal are consistent with the retention of self-complementary chalcogen bonds between two selenodiazole molecules.

The next project revealed how chemical shift tensors served as simultaneous and complementary probes of both the ChB donor and the acceptor of chalcogen-bonded salt cocrystals. ChB salt cocrystals featuring [K(18-crown-6)]$^+$ 3,4-dicyano-1,2,5-telluradiazole-XCN$^-$ (X = O, S, Se) were synthesized and compared to pure ChB donor 3,4-dicyano-1,2,5-telluradiazole. The cocrystal of 18-crown-6, KOCN (ChB acceptor part) and telluradiazole (ChB donor), highlighted a ChB between Te and the N atom of the cyanate anion. The further enrichment of KOC^{15}N helped in inspecting the trend of chemical shift tensor components of the ChB acceptor, in this case, the nitrogen of cyanate ion with the help of ^{15}N SSNMR. The reduced spans of the ^{125}Te and ^{15}N chemical shift tensors upon ChB formation with respect to pure ChB donor, telluradiazole, are complemented by DFT computation studies on cluster models and corroborates the experimental finding that upon formation of [K(18-crown-6)]$^+$[**1**-OC^{15}N]$^-$, the ^{15}N isotropic CS and CS tensor span both decrease relative to the values for pure KOC^{15}N, and the axial symmetry of this tensor is lost.

The works in Chapter 7 and Chapter 8 deal with experimental NMR measurements carried out on ChB cocrystals featuring interactions between spin-½ chalcogen nuclei and a quadrupolar nucleus (I>1/2). Chapter 7 provides experimental evidence of non-Fermi contact (FC) spin-spin coupling across the ChB between Te and Br in two ionic polymorphic cocrystals of telluradiazole and tetraphenylphosphonium bromide due to large anisotropic $J(^{125}\text{Te}, ^{79/81}\text{Br})$ coupling tensors extracted with the aid of SSNMR. The crystal structures and phase purity of the two polymorphs were characterized by X-ray diffraction (XRD) techniques prior to SSNMR experiments.

Chapter 8 revealed higher-order quadrupolar effects of a spin-5/2 ^{127}I nucleus when coupled to spin-1/2 ^{125}Te in a ChB cocrystal of telluradiazole (ChB donor) and tetraphenylphosphonium iodide (ChB acceptor) featuring a ChB between tellurium and iodine. The increase in the value of the ^{127}I quadrupolar coupling constant in the cocrystal of telluradiazole and tetraphenylphosphonium iodide as compared with that for the pure ChB acceptor, tetraphenylphosphonium iodide, implied a reduction of local symmetry. ^{127}I nuclear quadrupole resonance (NQR) experiments were carried out to confirm the findings from ^{127}I SSNMR spectroscopy.

Acknowledgements

I would like to dedicate this thesis to my *Maa* (mom, Mrs. Ruma Nag), *Baba* (dad, Mr. Tapan Kumar Nag), *Dadu* (grandfather, Late Dr. Naresh Chandra Nag), *Dada* (grandpa, Late Mr. Manoranjan Majumder) and *Shejo* (grandma, Late Mrs. Parul Nag).

- Thank you for believing in me, leading me to pursue my passion and dream.

I would like to express my heartfelt gratitude to the University of Ottawa for giving me an opportunity to pursue my doctoral research and for being my home for the past 4 years and 4 months of my joining the university as an international student. The facilities, higher-class research programmes, diverse ambience, excellent teachers, amiable co-workers made it easy for a struggling international student in her first year to get past her times of blues and difficulties. The best part was the 24*7 access to the NMR facility which I had and spent nights of acquiring spectra, especially during my NQR experiments and ^{127}I solid-state NMR experiments, which I will cherish forever.

The person, without whom this thesis would not have been possible, is my supervisor, Dr. David L. Bryce, who took me as a Ph.D. student in his lab in fall, 2019. Dave, I am much obliged to you beyond words for getting me interested in solid-state NMR starting from your grad course and your constant motivation to keep us interested in this field of research to the very end of my research days where you believed in me to do “crazy bromine-multiplet line shape deduction at the high field NMR facility in NRC” which I still saw written on your whiteboard in your office and I can gladly say, we were able to get the result as a team. This experience has been the most

unique of all. Dave, your guidance, discussions and explaining me the workings and possibilities of NMR, I am thankful to you for everything.

Dr. Glenn A. Facey, our NMR hero and I can bet on the fact that you are one of the finest NMR spectroscopists the NMR community will ever see, NMR facility at UOttawa was sad on your retirement and I can definitively say the basics of NMR could not have been better taught if it was not for you. All the learnings that I acquired under your guidance made a huge change and even inspired me to look through and dig deeper into the fundamentals of solid-state NMR. I would also like to mention my gratitude to Dr. Peter J. Pallister for holding my hand as a novice to solid-state NMR and training us in all the NMR instruments and help me optimize the acquisition parameters on my first "zg" experiment. Thank you for being a great mentor and being available all the time for all my questions/doubts. Now that you are in Carleton, I would say, they are lucky to have you there.

The final Chapters would not have been complete without the ginormous help, teaching, and guidance of Dr. Victor V. Terskikh. To be able to work with you in person was a real experience, the way you have walked me through the importance and understanding of the experimental aspects in the 900 MHz NMR facility is beyond imagination. I thoroughly enjoyed running experiments and the useful discussions we had regarding the resolution of the research regarding the quadrupoles, more importantly the discipline I got to imbibe from you was incomparable. I would also express my regards to Dr. Andreas Brinkmann for his input in computational ideas on my final research projects.

Dr. Patrick M. J. Szell, I owe you a huge thank you, our current NMR manager at UOttawa, you have been an amazing senior right from the very beginning when I came to Canada in 2019 fall and you helped me hunt down an apartment in this foreign land. Since then, you have always

showed me pathways to pursue exotic NMR experiments and supported me to perform them on the spectrometers. Your insight on NQR to which I was very intrigued about and your help with all those days of me trying to set up a NQR probe, or fixing the Hahn-echo experiments, I really appreciate that. Thank you for bearing all kinds of my crazy to try Iodine NMR at the 500 MHz! you have been a great senior and now a great NMR manager. As per your words "Tamali, listen to a light that never comes by Linkin Park while you spend nights in finding the NQR frequencies", and that led me to light, thank you Pat.

The X-ray facility at the University of Ottawa has been one of the best learning experiences for me. Dr. Jeffrey S. Ovens, I would like to thank you for your unmatched energy to train me on single-crystal X-ray diffraction, right from choosing a good quality single-crystal to solving a crystal structure beside helping us master the powder X-ray diffraction experiments on the diffractometers. The help I received from you in refining my cocrystal structures to discuss possibilities with me as to whenever there was an ambiguity in powder X-ray results, kudos. Sarah Osterholm, I thank you for being a great colleague and a great technician at the X-ray facility.

Shubha, we started this journey of Ph.D. candidates together, from being roommates for 4.4 years to graduating together, it has been quite the journey, I express all my love for you for being a great lab mate, a friend, and an elder sister to me. I will cherish all our precious moments running experiments together and trying to overcome the difficulties as an international student. I would mostly remember our conference days in Calgary and Copper Mountain where we got to experience lots of NMR and fun. I wish you all the very best for your future and all my respect to you for being patient and teaching me all the nooks and crannies of operating glove box and giving ideas on synthesis to this theoretical chemist when she started in the lab. You are a great researcher. Vincent (Vince), thank you for all your help around the lab when I started in and you helped me

understand the experimental and wet lab techniques and Dr. Vijith Kumar for leading me to chalcogen bonds and crystallography. Dr. Kirill Levin, Dr. Tristan Georges, both our postdocs during our time in the group, I owe you people a lot for your numerous help and suggestion in the lab and with the experiments. Tristan, your dedication and work ethic is unfathomable, and I appreciate you for that. Dr. Volodymyr Semeniuchenko (Vova), I thank you for all your help with the technical aspects in the NMR lab. Ali, I would also like to thank you, and now, you must take care of the lab!

I am thankful to all my undergrad students and my colleagues who I had an opportunity to collaborate with. Carina, you have been my best student, our work together on the Chapter 6 of my dissertation, I would like to dedicate that piece of work to you. Your inquisitiveness, hard-working nature and kindness have always made me admire you and I wish you all the very best now that you are treading the path to be a dentist. Ella, Matthew, I wish all the best to both of you; your dedication and interest in the research in our group were amazing. Christelle, I am also thankful to you for having been there during the tough covid times and I am proud of you to complete your Master's while being an young mom.

I want to address all the members of Bryce lab, past and current for their countless help and motivation. Dr. Scott Southern, you were always there an email away whenever I had any computational questions and I appreciate you for that and Dr. Yijue Xu, I thank you a ton for showing me how to simulate spectra right from the very beginning till the day you left for MagLab the moments we spent in lab under your guidance were surreal, we miss you, you were an amazing senior to us. Ezana, Sachin, Dan, Audrey, Teo, Janice and Mahee, thank you.

I would further express all my gratitude to the professors of my thesis advisory committee, Dr. Tom Woo, Dr. Darrin Richeson and Dr. Muralee Murugesu for giving me useful suggestions and advise me throughout my research journey and help me with their ideas for which I will always be obliged. Dr. Woo, I owe you an immense recognition for having given me access to Wooki where I was able to perform numerous computations on CASTEP and Gaussian. I thank Compute Canada for letting me have access to Graham and run my DFT calculations on AMS suite. I am also indebted to Dr. M. M. Balakrishnarajan, my Master's degree supervisor at Pondicherry University, for getting me enlightened to computational chemistry and pursue its different aspects and also Dr. Amlan K. Roy, my summer internship supervisor at IISER Kolkata, I highly appreciate you for deflecting my interests to solid-state chemistry and helping me choose UOttawa during my initial stages of Ph.D. applications.

I am also indebted to all my friends without whom I would not have been able to come this far. Diganta, I am glad I met you at CCCE 2022. You have been a source of motivation and good vibes for me, our NMR related discussions and "life-talks" are beyond par. I appreciate all your help and useful suggestions on research-related topics/SSNMR and the humble and kind man that you are, I admire you genuinely. I wish you all the best for your future and I know you will be an amazing spectroscopist without a doubt. Chiranjit, Sharif, both of your support throughout this journey must be mentioned, all my love and respect to both of you. Samantha, Braeden, Lauren, Amy, James, Farhiya, Neal, Sukham, Matt, Kayla, Laura, Neha, Chanjot, Kumardip, Ekin, you people are a family I made here in Canada. Thank you for making me feel at home and help me survive all this while. Sampreeti, Sushmita, Vishnu, Pk, Abhi, Kavya, and to my best friend Daisy, you all were a part of this journey and owe all of you this gratefulness, so, thank you. Marcin, I thank you for being such a kind and great guardian to me here in Ottawa. Suman, I owe you a

heartfelt thank you for strengthening me at my lowest and making me realize the importance of not giving up on oneself. Last, but not the least I thank all my family and other friends for their continued support and patience.

Quotes that kept me inspired throughout my research journey from two of my most favourite scientists:

- "**Of all its many values, the greatest must be the freedom to doubt**"----- The Value of Science, **Richard P. Feynman**, *Engineering and Science*, XIX, **1955**, 13-15.
- "**Idealism, however impractical, gives a meaning to our existence**" **–** from Bose-Einstein stat to God particle, **Satyendra Nath Bose**.

Statement of Authenticity

This is to certify that the research presented in this thesis is my work and all other works mentioned are explicitly referenced and acknowledged. Permissions to reuse published manuscripts in Chapter 5 and Chapter 6 were obtained as well from the co-authors and are stated before each Chapter. Chapter 7 and 8 contains finished research work and manuscripts under submission and progress. My supervisor, Dr. David L. Bryce is acknowledged here for having contributed to all the edits, revisions and corrections of the manuscripts presented here beside his guidance, support, and motivation.

Table of Contents

List of Figures

List of Tables

List of abbreviations and recurring symbols

AMS	Amsterdam Modelling Suite
ADF	Amsterdam Density Functional
B3LYP	Becke 3-parameter Lee Yang Parr
CASTEP	Cambridge Serial Total Energy Package
CCDC	Cambridge Crystallographic Data centre
ChB	Chalcogen Bond
CP	Cross-Polarization
CPMG	Carr-Purcell Meiboom-Gill
CSA	Chemical Shift Anisotropy
CT	Central Transition
DCB	Dirac-Coulomb-Breit Hamiltonian
DFT	Density Functional Theory
DK	Douglas-Kroll Hamiltonian
DSO	Diamagnetic Spin Orbital
DZP	Double Zeta Basis Set with 1 Polarization Function
DGDZVP	Density Gauss Double Zeta Basis Set with Polarization Functions
EFG	Electric Field Gradient
FC	Fermi Contact
FID	Free Induction Decay
FT	Fourier Transform
GGA	Generalized Gradient Approximation
GIPAW	Gauge-Included Projector-Augmented Wave

HB	Hydrogen Bond
HF	Hartree-Fock method
HOMO	Highest Occupied Molecular Orbital
HPDEC	High Power Decoupling
IUPAC	International union of Pure and Applied Chemistry
LCAO	Linear Combination of Atomic Orbitals
LDA	Local Density Approximation
LUMO	Lowest Unoccupied Molecular Orbital
MAS	Magic Angle Spinning
MO	Molecular Orbital
NMR	Nuclear Magnetic Resonance Spectroscopy
NQR	Nuclear Quadrupole Resonance Spectroscopy
NLMO	Natural Localized Molecular Orbital
PAS	Principal Axis System
PBE	Perdew Burke Ernzerhof
ppm	Parts per million
PSO	Paramagnetic Spin Orbital
PXRD	Powder X-ray diffraction
QCPMG	Quadrupolar Carr-Purcell Meiboom-Gill
rf	Radiofrequency
revPBE	revised Perdew Burke Ernzerhof
SAPT	Symmetry-Adapted Perturbation Theory
SAOP	Statistically Averaged Orbital Potential

SCXRD	Single-crystal X-ray Diffraction
SD	Spin dipolar coupling
SO	Spin Orbital
ST	Satellite Transition
TZP	Triple-Zeta Basis with 1 Polarization Function
VOCS	Variable Offset Cumulative Frequency
WURST	Wideband Uniform-Rate Smooth Truncation
XB	Halogen Bond
ZORA	Zeroth Order Regular Approximation
a, b, c	Unit Cell Dimensions
B_0	Magnetic Field
$\mathbf{B_0}$	Magnetic Field Vector
B_1	Radiofrequency Magnetic Field
B_{eff}	Effective Magnetic Field
c	Speed of Light
C_Q	Quadrupolar Coupling Constant
D or R_{DD}	Dipolar Coupling Constant
$d_{Ch\text{---}B}$	Distance Between Chalcogen Bond Donor and Acceptor Atoms
$\sum d_{vdW}$	Sum of van der Waals Radii of ChB Donor and Acceptor
e	Fundamental Charge
h	Planck's Constant
$\hbar$	Reduced Planck's Constant ($\frac{h}{2\pi}$)

$\widehat{H}$	General Hamiltonian Operator
$\widehat{H}_Q$	Quadrupolar Hamiltonian
υ_0/ω_0	Larmor Frequency
η	Asymmetry Parameter
J	J-Coupling
δ_{iso}	Isotropic Chemical Shift
Ω	Span
κ	Skew
J_{iso}	Isotropic J-Coupling
ΔJ	Anisotropic J-Coupling
K	Reduced J-Coupling

Part 1: Objectives and Introduction

Objectives and Overview

The main objective of this dissertation is to comprehend the nature, structure, and usefulness of chalcogen bonds in crystal-engineered chalcogen bonded systems using solid-state nuclear magnetic resonance spectroscopy (SSNMR). SSNMR is used as probe of chalcogen bonded cocrystals. NMR observables, such as chemical shift tensors, *J*-coupling tensors, and electric field gradient tensors are measured and interpreted to contribute to our understanding of the local environments and geometry of chalcogen bonds in various cocrystals.

Chalcogen bonds (ChB) are a special class of non-covalent (or 'noncovalent') interactions that have a wide range of importance in the fields of crystal engineering, energy materials, biopharmaceuticals and organocatalysis. Chapter 1 comprises information on the origin, development, and classification of noncovalent interactions and chemical bonds in general. Chalcogen bonds, much like their analogues, tetrel bonds, pnictogen bonds, halogen bonds, and matere bonds, tend to exhibit great tunability and directionality that makes them an important class of non-covalent interactions. ChB, however, exhibit characteristics that differ from those of other non-covalent interactions in the context of crystal-engineered systems, which will be discussed extensively in Part 2.

NMR, also well known as nuclear magnetic resonance spectroscopy, is a non-invasive and nucleus-specific spectroscopic technique that provides us with information down to the atomic

level. Solution and solid-state NMR are powerful tools to extract information on different nuclei, providing insight into local geometry and electronic environment that could lead to ground-breaking discoveries and information. SSNMR, however, considers the major nuclear spin interactions that are orientation-dependent, which are overlooked or averaged to zero in the solution state, thereby making the former technique a better probe to study crystalline and polycrystalline systems as discussed in Chapter 2.

NMR can be paired with several X-ray diffraction techniques to obtain a more accurate structure description. NMR observables such as chemical shift tensors, dipolar tensors, and quadrupolar tensors can also be modeled to refine the positions of atoms. Basic diffraction techniques require a single set of data unlike NMR, which often benefits from multiple experiments. In Chapter 3, single-crystal X-ray diffraction techniques, powder X-ray diffraction techniques, and their measurement strategies are described. This Chapter also covers the basics of crystals and crystallographic conventions. Chapter 4 of this dissertation covers the basics of computational chemistry and computing NMR observables.

Part 2 of this dissertation presents the results and discussion. The works cover the study of crystal-engineered chalcogen-bonded systems, commonly termed as cocrystals. The synthesis, crystallization, and characterization techniques of ChB cocrystals are emphasized. Cocrystallization techniques such as slow evaporation, vapour diffusion, and mechanochemistry were used to prepare samples prior to their characterization. Various aspects of the ChB (local environment, chalcogen bond donors, chalcogen bond acceptors, geometry) are analyzed with various solid-state NMR experiments followed by quantum chemical calculations to understand the relationship between NMR data and structural features, as described in Chapters 5 and 6.

More than half of the nuclei in the periodic table are quadrupolar in nature (spin $I > ½$). Novel cocrystals described in part 3 feature Te···Br and Te···I chalcogen bonds, and these are studied using a variety of NMR approaches. Dipolar coupling, quadrupolar coupling, and *J*-coupling will be discussed in Chapters 7 and 8, and how these important interactions can affect the NMR spectra in each case. Quantum chemical computations on various model systems to support the study of the experiments will add depth of knowledge to assess the efficiency and importance of ^{127}I and $^{79/81}$Br high-field NMR experiments. NQR, or nuclear quadrupole resonance spectroscopy, is used as a complement to NMR in cases where the quadrupolar interaction is very large.

Chapter 1. Introduction to non-covalent bonding

1.1 Chemical Bonds

The lasting attraction (the forces) that holds atoms/ions together is defined as a chemical bond. It is the foundation of any molecule or crystal structure formation that determines the structure of matter. They can be classified into various types such as covalent, metallic, or ionic.[1] A covalent bond involves sharing of electrons between two non-metals, or two nuclei that are surrounded by an electron cloud and their orbitals overlap to form such bonds (like H_2, CO_2, N_2). Ionic bonds on the other hand result from the transfer of valence electrons from the electropositive metals to the electronegative non-metals, e.g., NaCl, KF, $MgSO_4$. Across the periodic table, the general trend is, ionization potential increases left to right across a period and so does electronegativity. The metallic bond is an outcome of the electrostatic interaction where positively charged metals interact among themselves in a delocalized electron cloud. The above classifications of chemical bonds are defined as the set of "strong chemical bonds". The other classes of chemical bonds depicting weaker bonds but important to be considered are intermolecular bonding which are bound together by intermolecular forces, which is formed between two or more molecules. Dipole-dipole interactions, London-dispersion forces and hydrogen bonding belong to such classes of bonding. Description of these bonds are vital here to understand the concept of noncovalent interactions better. An atom which is highly electronegative in a molecule have a highly polarizable nature having a partial negative charge and thus creates an attraction with an atom which is highly electropositive or polarizing having a partial positive

charge of another molecule that results in the dipole-dipole interaction. The International Union of Pure and Applied Chemistry defines the hydrogen bond as "an attractive interaction between a hydrogen atom from a molecule or a molecular fragment X-H in which X is more electronegative than H, and an atom or a group of atoms in the same or different molecule."[2] It is a type of interaction that can be classified into weak or strong chemical bond, i.e. 16 kJ/mol up to 170 kJ/mol as seen in HF_2^+.[3]

Noncovalent interactions are ubiquitous in crystalline solids and are discussed in this dissertation. The presence of noncovalent interactions is sometimes described by close contact or normalized contact parameter (R_{ChB} or N_c)[4] and they are generally weaker than covalent interaction. Chalcogen bond (ChB) which is a sub-category of noncovalent interactions, are focused on in this entire research journey because this is a budding arena of research for structural chemists to learn more about these kinds of bonding interactions in order to expand the application horizons of ChB interactions.

1.2 Chalcogen Bonding Interaction

1.2.1 σ-Hole Interaction and History of Chalcogen Bonding Interactions

The concept of noncovalent interactions dates to the time of 18th century when Van der Waal first generalized them as intermolecular interactions.[5] The concept at that time, however, did not include ion-pairs or hydrogen bonds. The forms of noncovalent interactions highlighting dispersion forces or even electrostatic interactions have always been a topic of debate. It is generally seen that the lighter elements tend to form a noncovalent interaction based mostly on

electrostatic interactions, but as we move to the heavier congeners in the group, the dispersion forces form the basis of the noncovalent interactions.[6] An early example of chalcogen bond from Kubiniok et al,[7] between Se and I in a diphenyldiselane iodine complex. It was very interesting back then to see the interaction/bond-distance between Se···I rather than just the Se-Se interaction on the diphenyldiselane entity. Ever since, there has been a progress with the studying and understanding these types of interactions which are like halogen bonds and have a wide range of importance in areas such as biomolecular systems, crystals, catalysis. The σ-hole term was introduced by Clark and coworkers in 2007.[8] It was used to better understand the electronic structure when a halogen bond forms.The σ-hole (electron-deficient/low electron density on the halogen atom) is formed owing to the presence of electron-withdrawing functional groups attached to the halogen atom. The σ-hole of the halogen bond donor (electrophilic centre) interacts intramolecularly or intermolecularly with another molecule having an electron rich centre atom/ion (the halogen bond acceptor, nucleophilic centre). The concept is alike in case of chalcogen bonds where the chalcogen bond donor possess a σ-hole and interacts with the chalcogen bond acceptor, which might be intramolecular or intermolecular.

1.2.2 Definition of the Chalcogen Bond

The International Union of Pure and Applied Chemistry defines chalcogen bond as “net attractive interaction between an electrophilic region associated with a chalcogen atom in a molecular entity and a nucleophilic region in another, or the same, molecular entity.” [9]

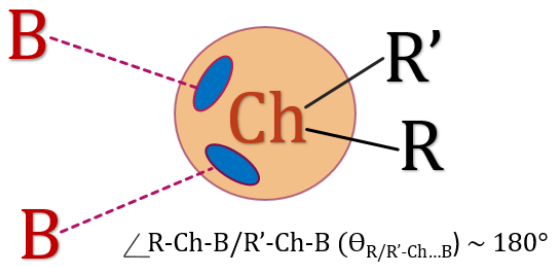

Figure 1.2.1: Schematic of ChB formation, blue is the region of sigma holes of the chalcogen atom, where the ChB acceptor, B, interacts with the chalcogen atom.

A chalcogen bond is usually depicted by R/R'-Ch···B, where R/R' is the group/atom/ion attached to the chalcogen atom, Ch is the chalcogen atom (O, S, Se or Te), also known as the chalcogen bond donor and B is the chalcogen bond acceptor/the Lewis base or the nucleophile that interacts with the σ-hole of the chalcogen atom and earlier its essential function was not discussed in most of the original papers.[10] There are several constraints taken into account while a ChB formation is monitored. One such example is presence of the substituent groups in the ChB donor and the nucleophilicity of the ChB acceptors. The directionality of a ChB bond is an important characteristic to be considered as it is proven that that the more it deviates from linearity, the strength of ChB weakens.[11] In group 16, the chalcogen bond strength is given as follows:

Te>Se>O>S

The justification of the chalcogen bond strength is due to the following few aspects:

i) The polarizing nature, size of the chalcogen atoms

ii) The chalcogen bond acceptor's Lewis basicity and higher electron density

iii) The groups/atoms/ions attached to the chalcogen atom in consideration. For instance, aromatic, heteroarene or polyfluorinated backbones tend to increase the polarization of the chalcogen atoms (with comparable electronegativities)

iv) The R-Ch···B angle approaches linear geometric shape, i.e., 180°

The above factors are crucial in determining the strength, tunability and usefulness of the chalcogen bond. When considering a cocrystal that comprises of a chalcogen bond donor and a chalcogen bond acceptor, the choice of the substituents attached to the chalcogen atom becomes important in determining the propensity of the σ- hole formation in the chalcogen bond donor and the ease of formation of a chalcogen bond with the respective chalcogen bond acceptor. A wide array of chalcogen bond donors and chalcogen bond acceptors have been studied in the recent few decades to highlight chalcogen bond's application. Few well known examples of chalcogen bond donors include a five-membered ring or a chalcogen containing heterocycle, polycyclic derivatives of thio-,[12] seleno-,[13] and tellurophene, chalcogen containing azoles[14] (thiazoles, dithiazoles selenazoles, selenodiazoles, tellurazoles, telluradiazoles), benzo-fused derivatives of the respective azoles, N-oxides[15] of a chalcogen containing azole and many more. Various electron-withdrawing groups could be present as substituents in the chalcogen bond donors to drive away the electron density from the chalcogen atom. Some examples of such substituents could be nitro, sulfonyl, carbonyl, carboxylic acids, halides, etc. The chalcogen bond acceptors can be an atom of N present in molecules such as pyridine, amine, or O in hydroxyls, ethers, a π-bond, an anion such as halide, to generalize, some system that can withheld a higher electron density and is electron rich in nature and its essential function was not discussed in most of the original papers in early years.

The formula to describe the electrostatic potential of a molecule is given as follows:[16]

$$\boldsymbol{V}(\boldsymbol{r}) = \sum \frac{\boldsymbol{Z_A}}{|\boldsymbol{R_A} - \boldsymbol{r}|} - \int \frac{\boldsymbol{\rho}(\boldsymbol{r\prime})\boldsymbol{dr}''}{|\boldsymbol{r\prime} - \boldsymbol{r}|} \qquad \text{Eq. 1.2.2.1}$$

Where V is the potential at any point in the molecule due to the influence of the point $\boldsymbol{r}$ by the nuclei and the electrons present in the molecule. $\boldsymbol{Z_A}$ is the charge of the nucleus A, where it is located at the distance of $\boldsymbol{R_A}$ and $\rho(\boldsymbol{r'})$ is the electron density in the molecule. An electrostatic potential of a molecule is a real physical property which can be experimentally and computationally characterized.[17] The sign of this potential depends on the effects of electrons (negative density) or the nuclei (positive density). $\boldsymbol{V}(\boldsymbol{r})$, the potential when is plotted on a molecular surface is also depicted as $\boldsymbol{V_s\,(r)}$, depending on the maximum electron density region ($\boldsymbol{V_s\,max(r)}$)or the minimum electron density ($\boldsymbol{V_s\,min\,(r)}$), the σ-hole region could be defined and studied with clarity as it denotes the ($\boldsymbol{V_s\,max(r)}$) whereas the other atoms/groups in the molecule possesses the ($\boldsymbol{V_s\,min\,(r)}$) .

The example below highlights the literature study of σ-holes using electrostatic potential map of various chalcogen-bonded systems featuring different chalcogens taken from Esrafili and Sabet in 2022.[18] The blue region highlights the σ-hole, where the electron density is low in the chalcogen bond donors (XCY, X=O, S, Se, Te) and the red region highlights the region of maximum electron density. The chalcogen bond acceptors used are 1,2-dimethoxybenzene (DMB) and 1,2-dihydroxybenzene (DHB). The justification of Te being the most polarizing ChB donor atom among the chalcogen atoms in terms of a stronger and ease of ChB formation.

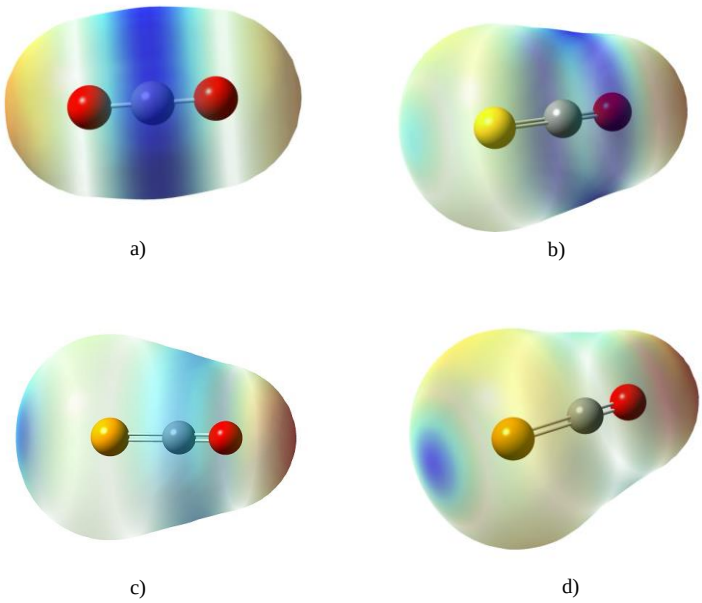

Figure 1.2.2: Electrostatic potential map of XCY extracted using Gaussian '09 and viewed with gauss view 4.1, where X= a) O (red atom), b) S (yellow atom), c) Se (golden) d) Te (dark golden) and Y= O (red atom), C (grey atom), the isovalue used was 0.001, the blue region depicts the electron deficient region (σ-hole) and red is the high.[34]

Depending on the substituents on the chalcogen bond donor, the electron-withdrawing nature intensifies the σ-hole[19] in the chalcogen atom. The higher electron density is depicted with the blue and the red depicts the region of higher electron density.[20] In the above Figure 1.2.2, it shows the sigma hole on the chalcogen atoms and the σ-hole on each chalcogen atom that is responsible for the higher probability and ease of chalcogen bond formation. The $\boldsymbol{V_s\,max}$ is the potential energy that is related to the interaction energies with respect to the different chalcogen atoms responsible for the chalcogen-bonded interactions with the chalcogen bond acceptors.[21-26]

These non-covalent interactions are directional in nature and tends towards being almost linear. Their tunable property is well-studied where we get evidence of the trend of Te being most susceptible to “strong chalcogen bonds”.[27]

Since σ-holes are formed due to the polarization of an atom's electronic charge toward the covalent bonds that it forms, any factor that enhances this polarization will strengthen the σ-hole. Accordingly, a σ-hole (***V_s max (r)***) tends to be more positive the greater is the atom's polarizability and the less is its electronegativity relative to the remainder of the molecule.

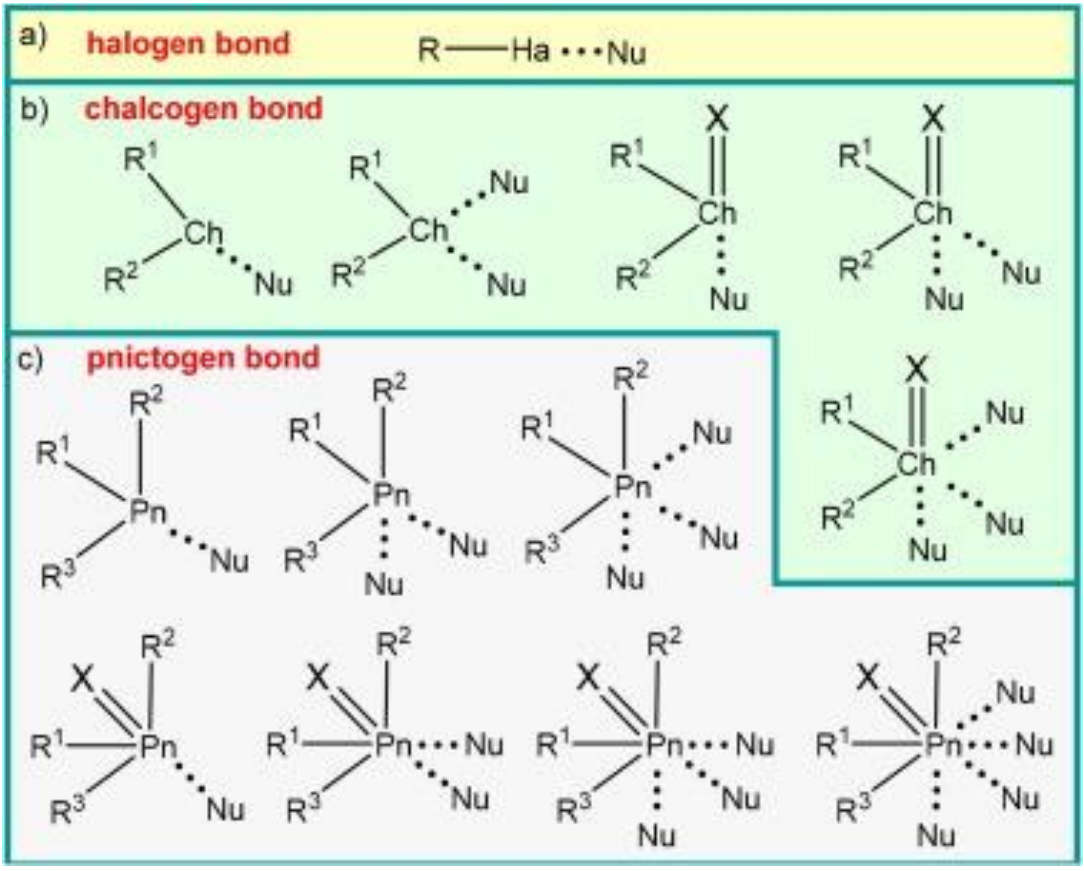

Figure 1.2.3: Schematic illustration of halogen (a), *chalcogen* (b) and *pnictogen* (c) bonds (electron-withdrawing ability of substituents: R1 > R2 > R3). Ha = F, Cl, Br or I. Ch = O, S, Se or

Te. Pn = N, P, As, Sb or Bi. X = O, S, Se, etc. Taken from Mahmudov et al.[10] (permission was obtained to reuse this Figure).

It has been evident from the literature that the study of chalcogen-bonded systems become important to understand the strength, stability and orientation of the substituents present in the chalcogen bond donor. One such example has been greatly developed by Haberhauer and Gleiter[27] where they explain why Te containing heterocycles, the potential chalcogen bond donors contribute highly to the field of crystal engineering, catalysis, and ion recognition.[40] The conventional reasons attributing to any noncovalent interaction pertaining to σ-holes like electrostatic potential or orbital delocalization effects were not completely acknowledged when the heterocycles with Te such as tellurazoles or isotellurazoles were considered. The SAPT calculations added an extra weight of study to understand these chalcogen-bond donors which exhibited steric properties (Pauli repulsions). The Symmetry Adapted intermolecular Perturbation Theory (SAPT) calculations[36] shed a light on how weak or strong the intermolecular interaction is and how the ChB donor and acceptor affect the interaction energy by taking up energy terms up to the second-order perturbation theory.

The equation for SAPT can be written as:

$$E^{SAPT} = E^{(1)}_{ELST} = E^{(1)}_{EXCH} + E^{(2)}_{IND} + E^{(2)}_{DISP} + \delta(HF) \quad \text{Eq 1.2.2.2}$$

Where the electrostatic, exchange, induction and dispersion terms are abbreviated as ELST, EXCH, IND and DISP. The partitioning of interaction energies into the electrostatic, exchange, induction and dispersion and contribution from the Hartree-Fock energy term ($\delta(HF)$)

gives us the total SAPT energy. The "ELST", "DISP", "IND" and $\delta(HF)$ term are attributed to the attraction interaction energies. The breakdown of the induction and dispersion contribution to the interaction energy is given as:

$$E^{(2)}_{IND} = E^{(2)}_{ind} + E^{(2)}_{exch\text{-}ind} \quad \text{Eq 1.2.2.3}$$

$$E^{(2)}_{DISP} = E^{(2)}_{disp} + E^{(2)}_{exch\text{-}disp} \quad \text{Eq 1.2.2.4}$$

The "exch" term here denotes the Pauli repulsion term between two overlapping orbital densities of the interacting atoms/systems. The $\delta(HF)$ adds an essence of higher order perturbation term in the total SAPT calculation of the intermolecular interaction.[36-39] It can be described by the following equation:

$$\delta(HF) = E^{HF}_{int} - E^{(1)}_{el}(HF) + E^{(1)}_{exch}(HF) - E^{(2)}_{ind}(HF) - E^{(2)}_{exch\text{-}ind}(HF) \quad \text{Eq 1.2.2.5}$$

Where, $E^{HF}_{int,\ is}$ the counterpoise corrected supramolecular level Hartree-Fock (HF) level interaction energy. The detailed contribution from the restricted HF and the HF-SAPT contributions are considered together to evaluate the intermolecular interaction energies.

Chalcogen bonds, due to their highly directional property[42] can be classified as stronger or weaker ChB interaction by a parameter called the reduced distance parameter or the normalized contact R_{ChB} or N_c,

$$R_{ChB} = \frac{d_{Ch\cdots B}}{\sum d_{vdW}} \quad \text{Eq 1.2.2.6}$$

Where, $\sum d_{vdW}$ represents the sum of van der Waal radii of the Ch atom interacation with the nucleophile/electron rich atom/ion of the ChB acceptor and $d_{Ch\cdots B}$ is the ChB distance formed due to ChB interaction.

1.2.3 Applications of Chalcogen Bonding interactions

In recent years, the study of chalcogen bonds have become of utmost importance. It highlighted utilities in areas of chemistry, biochemistry, medicinal chemistry, and material sciences that brought light to the research of these bonds. Coordination chemistry, which is an important branch of chemistry, has been thoroughly understood by the effects of noncovalent interactions, chalcogen bonds being one of them.[10] Metalloenzymes,[33] the versatile molecules that have shown great performance in wide variety of chemical transformations in bio systems possess high selectivity and efficiency. A secondary coordination sphere,[28] which sometimes is referred to as the outer sphere in metal coordination complexes are shown to be well cooperated in holding the complexes together with the help of these important noncovalent interactions, here, namely, chalcogen bonds. Besides holding the complexes together, arrangement, positioning of inert moieties closer to the metal centres to stabilize the reactive intermediates in the process of selective transformation or activation of various organic substrates[29] is one of the other utilities that has been well researched and studied. The directionality and tunable strength of certain noncovalent interactions, particularly chalcogen bonds lead to modification of kinetic and thermodynamic stability of the molecules/complexes developed.[30] The yield can also be altered owing to change in the synthetic route to get a desired chalcogen bonded system which can be comparable to study regioselectivity, stereoselectivity and chemoselectivity of catalytic reactions.[34] The study of chalcogen-bonded noncovalent interactions become essential in this time as they are not explicitly and vastly explored as that of its sister bonds such as halogen bonds, hydrogen bonds or pi-interactions. The chalcogen bond has been recently defined by the IUPAC committee and still has

lots to be explored and understood as the conventional literature dating to a decade back, doesn't show much acknowledgement of its importance and fundamental properties that are inevitable in understanding the contribution of chalcogen bonds. Crystal engineering is other fundamental application[31] and the basis of this dissertation, which will be discussed in detail in Chapter 5. Organic synthetic and catalytic application[35] of chalcogen bonds is found in several fields of interdisciplinary branches of chemistry. One such work where the importance of chalcogen bonds in organic synthesis is highlighted encapsulates the usage of functionalized cyclophenes with chalcogen atoms. The heterocycles show the mechanism of ring-closure addition-elimination reaction[41] as in Diels-Alder reaction mechanism where in 3,4-methoxytellurophene that is being produced, the Te---Te intermolecular interaction showed a new pathway for metallic importance in new electronic material synthesis owing to chalcogen bonding interaction.

Chalcogen bonds, as compared to its sister noncovalent interaction bonds such as the hydrogen bond, halogen bond or even π-stacking can be tweaked in various ways to achieve a higher selectivity of a reaction due to their much higher directionality. The former mentioned property of the chalcogen bonding interactions play a key role in catalytic reactions aside from noticing enticing characteristic of such catalytic reactions when performed in a nonpolar media that brings out the hydrophobic nature of the chalcogen bonds. Catalytic applications[32] of chalcogen-bonded interactions in literature are low as compared to their sister bonds as it is fairly a recent area of research, unconventional and challenging to study, however, expected scientific progress in this area is yet to be explored in the coming years. Some examples highlight the catalytic applications of ChBs in the literature discusses the acceleration of hydrogenation of quinolones and imines when diithieno[3,2-b;2',3'-d] thiophenes or their diimides, the potential

ChB donor catalyst candidates cooperate to bind together the chalcogen bonds in a specific binding motif (as "tongs") that promote the expected substrate-catalyst interactions. The intermediate formation that precedes the product formation is also stabilized by ChB interactions. Similar to the catalytic application of ChB described in the above few lines, an example where a chiral isothiourea[35] catalyst of R- configuration or 2-phenyl-2,3-dihydrobenzo[d]imidazo[2/1-b]thiazole of S- configuration is seen to be effectively transformed into intermediates such as α,β-unsaturated acylammonmium ion on its reaction with a α,β-unsaturated anhydride resulting in chemoselective products such as 1,5-benzothiaphenes in majority and other by-products. S---O ChB contributes to the stabilization and facilitate this discussed catalytic cycle as verified in the schematic in scheme 19 in Mahmudov and coworkers.[10] The above examples are a proof to the blooming catalytic prospects of ChBs and their importance in rendering a desired product in majority and mould a reaction in a way to get the most out of ChB interactions.

Drug design and pharmaceutical importance of ChB interactions are explored in a very well-known drug called riluzole[43] that features the S---O ChB bonding interaction including the less polarizable Sulphur atom as compared to Se or Te. Riluzole is known to cure skin diseases and the non-classical S---O synthon that is seen in the riluzole drug coformer is a unit that is used vastly in the field of supramolecular chemistry and crystal engineering. Multi-component crystals or MCCs also known as pharmaceutical cocrystals play an essential role which makes use of the supramolecular synthons/recognition units and the coformer which are interlinked using noncovalent interactions, in here via ChB interaction. Various functional and energy storage materials have been extensively researched in the recent years which acknowledges the benefits

and applications of ChB interactions. MOFs are one such example. Material science has various facets where ChB are found to have wide range of applications, one such example is the coordinate complex of Mn, $[MnCl_2(C_6H_4N_2Se)_2]$[44] which consists of Mn μ-bonds with Cl on each side of the benzoselenodiazole moiety, where the Se-N unit provides an unique spin-spin coupling mechanism to induce paramagnetic behaviour in the Mn atom.

References

[1] Atkins, P. W.; Overton, T. L.; Rourke, J. P.; Weller, M. T.; and Armstrong, F. A. *Shriver & Atkins*' *Inorganic Chemistry fifth edition.* W. H. Freeman and Company, New York, **2010**.

[2] Desiraju, G. R.; and Steiner, T. *The Weak Hydrogen Bond: In Structural Chemistry and Biology,* International Union of Crystallography, Oxford Science Publications, Oxford, **1999**.

[3] Varshey, D. B.; Sander, J. R. G.; Friščić, T.; MacGillivray, L. R. Supramolecular Interactions. In *Supramolecular Chemistry: From Molecules to Nanomaterials*. Gale, P. A.; Steed, J. W. Eds. Wiley & Sons: New York, **2012**.

[4] Murray, J. S.; Resnati, G.; Politzer, P. *Faraday Discuss.* **2017**, 203, 113-130.

[5] Kuzmina, L. G.; BokII, N. G.; Struchkov, Y. T.; Ravtsov, D. N.; Rohklina, E. M. *J. Struct. Chem.* **1974**, 15, 419.

[6] Sein, R. S.; Sutherland, G. B. B. M. *J. Chem. Phys.* **1954**, 22, 1993-1999.

[7] Kubiniok, S.; du Mont, W. W.; Pohl, S.; Saak. W. *Angew. Chem. In. Ed.* **1988**, 27, 431-433.

[8] Clark, T.; Hennemann. M.; Murray, J. S.; Politzer, P. *J. Mol. Model*. **2007**, 13, 291–296.

[9] Aakeroy, C. B.; Bryce, D. L.; Desiraju, G. R.; Frontera, A.; Legon, A. C.; Nicotra, F.; Rissanen, K.; Scheiner, S.; Terraneo, G.; Metrangolo, P.; Resnati, G. *Pure Appl. Chem*. **2019**, 91, 1889-1892.

[10] Mahmudov, K. T.; Gurbanov, A. V.; Aliveva, V. A., da Silva, M. F. C. G.; Resnati, G.; Pombeiro, A. J. L. *Coord. Chem. Rev.* **2022**, 464, 1-20.

[11] Vogel, L.; Wonner, P.; Huber, S. M. *Angew.Chem.Int.Ed*. **2019**, 58, 1880-1891.

[12] Akiba, K.; Tsuchiya, T.; Inamoto, N.; Onuma, N.; Nagashima. N.; Nakamura, A. *Chem. Lett.* **1976**, 5, 723-726.

[13] Zhu, C.; Yoshimura, A.; Ji, L.; Wei, Y.; Nemykin,V. N.; Zhdankin, V. V. *Org. Lett*. **2012,** 14, 3170-3173.

[14] Sharma, C.; Singh, A. K.; Joy, J.; Jemmis E. D.; Awas, S. K. *RSC Adv*. **2016**, 6, 91689-91693.

[15] Ho, P. C.; Szydlowski, P.; Sinclair, J.; Elder, P. J. W.; Kübel, J.; Gendy, C.; Lee, L. M.; Jenkins, H. A.; Britten, J. F.; Morim, D. R.; Vargas Baca, I. *Nat. Commun*. **2016**, 7, 1-10.

[16] Weinstein, H.; Politzer, P.; Srebrenik, S. *Theor. Chim. Acta.* **1975**, 38, 159–163.

[17] Mikherdov, A. S.; Kinzhalov, M. A.; Novikov, A. S.; Boyarskiy, V. P.; Boyarskaya, I. A.; Dar'in, D. V.; Starova G.L.; Yu. Kukushkin, V. *J. Am. Chem. Soc*. **2016**, 138, 14129-14137.

[18] Esrafili, M. D.; Sabet, F. M. *Chem. Phys. Lett*. **2015**, 634, 210-215.

[19] Brinck, T.; Murray, J. S.; Politzer, P. *Int. J. Quantum Chem*. **1992**, 44, 57-64.

[20] Murray, J. S.; Lane, P; Clark, T.; Politzer, P. J. *Mol. Model*. **2007**, 13, 1033-1038.

[21] Politzer, P.; Riley, K. E.; Bulat, F. A.; Murray, J. S. *Comput. Theor. Chem*. **2012**, 998, 2-8.

[22] Bauzá, A.; Mooibroek, T. J.; Frontera, A. *ChemPhysChem*. **2015**, 16, 2496-2517.

[23] Wang, H.; Wang, W.; Jin, W. J. *Chem. Rev*. **2016**, 116, 5072-5104.

[24] Alkorta, I.; Elguero, J.; Frontera, A. *Crystals*. **2020**, 10, 1-29.

[25] Scheiner, S. *Acc. Chem. Res*. **2013**, 46, 280-288.

[26] Gurbanov, A. V.; Kuznetsov, M. L.; Mahmudov, K. T.; Pombeiro, A. J. L.; Resnati, G. *Chem. Eur. J*. **2020**, 26, 14833-14837.

[27] Haberhauer G.; Gleiter, R. *Angew. Chem. Int. Ed*. **2020**, 59, 21236– 21243.

[28] Borovik, A. S. *Acc. Chem. Res*. **2005**, 38, 54-61.

[29] van Leeuwen, P.W.N.M. *Supramolecular Catalysis*. Wiley, 2008.

[30] Raynal, M.; Ballester, P.; Vidal-Ferran, A.; van Leeuwen, P.W.N.M. *Chem. Soc. Rev*. **2014**, 43, 1660-1733.

[31] Desiraju, D. R. *Angew. Chem. Int. Ed*. 1995, 34, 2311-2327.

[32] Mahmudov, K. T.; Kopylovich, M. N.; Guedes da Silva, M. F. C.; Pombeiro, A. J. L. *Noncovalent Interactions in Catalysis*. Royal Society of Chemistry, UK, **2019**.

[33] M. Diéguez, J.-E. Bäckvall, O. Pàmies. *Artificial Metalloenzymes and Metalloenzymes in Catalysis: From Design to Applications*. Wiley-VCH, **2018.**

[34] Frisch, M. J.; et al. Gaussian 09, Revision A.02; Gaussian Inc.: Wallingford, CT, 2009.

[35] Kolb, S.; Oliver, G. A.; Werz, D. B. *Angew. Chem. Int. Ed*. **2020**, 59, 22306–2231.

[36] Jansen, G.; *WIREs Comput. Mol. Sci*. **2014**, 4, 127–144.

[37] Hesselmann, A.; Jansen, G.; Schütz, M. *J. Chem. Phys.* **2005**, 122, 014103.

[38]. Szalewicz, K.; Patkowski, K.; Jeziorski, B. *Struct. Bond*. **2005**, 116, 43–117.

[39] Jeziorski, J. B.; Moszynski, R.; Szalewicz, K. *Chem. Rev*. **1994**, 94, 1887–1930

[40] Benz, S.; López-Andarias, J.; Mareda, J.; Sakai, N.; Matile, S. *Angew. Chem. Int. Ed*. **2017**, 56, 812 –815.

[41] Steinke, T.; Wonner, P.; Gauld, R. M.; Heinrich, S.; Huber, S. M. *Chem. Eur. J*. **2022**, 28, 1-7.

[42] Iwaoka, M.; Tomoda, S. *J. Am. Chem. Soc*. **1996**, 118, 8077–8084.

[43] Thomas, S. P.; Kumar, V.; Alhameedi, K.; Guru Row, T.N. *Chem. Eur. J*. **2019**, 25, 3591 –359

[44] Ho, P. C.; Wang, J. Z.; Meloni, F.; Vargas-Baca, I. *Coord. Chem. Rev.* **2020**, 422, 213464.

Chapter 2. Introduction to Nuclear Magnetic Resonance Spectroscopy

2.1 Theory of Nuclear Magnetic Resonance Spectroscopy

Quantum numbers, namely, principal(*n*), azimuthal(*l),* magnetic(*m*) and spin(*I)* quantum numbers are used to describe the position and energy of an electron in an atom.[1] Spin is an intrinsic property of a nucleus just like an electron. For a nucleus, the spin magnetic quantum number is denoted by *I.* Spin exhibits physical properties similar to that of angular momentum.[2] The number of allowed spin states for a spin magnetic quantum (*m*) number is given as $2I+1$ from $-I$ to $+I$ and the states are degenerate unless an external magnetic field is applied. For nuclei with even number of proton and neutrons, $I = 0$, which do not respond to NMR or are known as NMR inactive nuclides whereas $I \neq 0$, are NMR active nuclides.

Owing to the nuclear shell model,[3] the nuclides that have both an odd number of neutrons and protons have an integer spin quantum number and the nuclides that either have an odd number of neutrons or protons give a half-integer spin quantum number. Unlike electrons with spin quantum number 1/2, nuclear spin can take up integral multiples of ½ such as $I = 1/2, 3/2, 1$, etc. The nuclear spin quantum number considers the total angular momentum because of the intrinsic property of spin that is related to every nucleus and has an inherent magnetic moment associated with the angular momentum of the nucleus. The magnetic moment of a nuclear spin is treated like an electron's spin and orbital angular momentum. The nuclear and electronic spin and magnetic moments are expressed analogously, including a term known as the Bohr magneton[4] in case of electron spin and orbital quantum numbers whereas that term is replaced by a term analogous to

Bohr magneton ((μ_B), called the Nuclear magneton (μ_N). The term g is a dimensionless quantity which characterizes the angular momentum and magnetic moment of the nucleus. The subscript "*S*" and "*L*" are the spin orbital quantum number and the orbital angular momentum quantum numbers respectively.The expressions for both the nuclear and electron magnetic moments are given as the following:

$$\mu_L = -g_L \frac{e}{2\,m_e} L\,, \qquad \mu_S = -g_S \frac{e}{2\,m_e} S \quad \text{Eq 2.1.1}$$

$$\mu_B = \frac{e\,\hbar}{2\,m_e} = 9.274 \times 10^{-24}\,J/T \quad \text{Eq 2.1.2}$$

$$\mu_{Lz} = -g_L \frac{e}{2\,m_e} m_l \;=\; -m_l\,\mu_B \;\; \mu_{Sz} = -g_L \frac{e}{2\,m_e} m_s = -2 m_s \mu_B; \text{ Eq 2.1.3 and 2.1.4}$$

$$g_L = 1 \; and \; g_S = 2.0023 \approx 2$$

$$\mu = g\;\frac{e}{2\,m_p} I \quad \text{Eq 2.1.5}$$

$$\mu_Z = g \frac{e\,\hbar}{2\,m_p}\; m_I = g\;\mu_N m_I;\; \mu_N = 5.051 \times 10^{-27}\,J/T \text{ Eq 2.1.6}$$

2.1.1 Zeeman interaction

A nucleus with $I \neq 0$, under the application of an external magnetic field B_0, splits into different energy states of ($2I$+1) sublevels. This is known as the Zeeman effect, named after the Dutch physicist, Pieter Zeeman, who in 1896 discovered this effect caused due to the presence of a static magnetic field that caused the splitting of spectral lines into several components.[5] This effect is analogous to the Stark effect[21] that is observed upon the application of an electric field. The magnetic moment of a nucleus can be written as:

$$\mu = \gamma I \qquad \text{Eq 2.1.1.1}$$

Where γ is the gyromagnetic ratio of the nucleus that can either be negative (antiparallel orientation of magnetic moment and spin angular momentum) or positive (parallel orientation of magnetic moment and spin angular momentum), the energy separation between the energy levels arising due to the Zeeman effect is denoted by ΔE. This Zeeman splitting is dependent on the magnetic moment and the strength of the magnetic field. The following equations verify the dependency of the physical variables of the Zeeman splitting phenomenon:

$$E_m = -\frac{m\gamma h B_0}{2\pi} \qquad \text{Eq 2.1.1.2}$$

$$\Delta E = \frac{\gamma h B_0}{2\pi} \qquad \text{Eq 2.1.1.3}$$

Figure 2.1.1: Zeeman splitting energy level diagrams for spin 1/2 and spin 3/2.

$$\Delta E = h\upsilon \qquad \text{Eq 2.1.1.4}$$

$$\upsilon_0 = \left(\frac{\gamma}{2\pi}\right) B_0 \text{ or } \omega_0 = \gamma B_0 \quad \text{Eq 2.1.1.5}$$

The Larmor equation[6] (eq. 2.1.1.5) is an expression that relates the frequency (υ_0 *in Hz or* ω_0 *in rad/s*), the gyromagnetic ratio, and the applied external magnetic field, B_0. The Boltzmann distribution,[7] which helps us understand the population density of spins at different energy levels, tells us that at thermal equilibrium, the lower energy level is slightly more populated than the higher energy level for spin-½ nuclei which leads to bulk magnetization (*M*). The Boltzmann distribution is described below (eq. 2.1.1.6) to show the difference in occupancy of the different energy levels by the spins.

$$\frac{N_\alpha}{N_\beta} = e^{-\frac{\Delta E}{k_B T}} \quad \text{Eq 2.1.1.6}$$

Here, k_B is the Boltzmann constant and has the value of 1.3806×10^{-23} J K^{-1} and T is the absolute temperature in Kelvin. The bulk magnetization vector is denoted as **M**. It is stationary and usually aligned with the applied external magnetic field as seen in Figure 2.1.2. The size of the bulk magnetization can be well understood by the Boltzmann distribution as mentioned in equation 2.1.1.7. Under the high temperature approximation, the Boltzmann distribution leads to the following equation that tells us about the polarization of the spins α (lower spin state) and β (higher spin state):

$$\frac{\Delta n_{eq}}{n_{total}} = \frac{n_\alpha - n_\beta}{n_\alpha + n_\beta} \approx \frac{\Delta E}{2k_B T} \quad \text{Eq 2.1.1.7}$$

In the presence of magnetic field, the net distribution of magnetic moment vector gradually builds-up in the direction of applied magnetic field, z-axis in here that generates the bulk

magnetization vector **M**. The build-up of magnetization along the z-axis (M_z) follows an exponential trend:

$$M_Z(t) = M_0\left(1 - e^{-\frac{1}{T_1}}\right) \quad \text{Eq 2.1.1.8}$$

Where the time taken to reach the thermal equilibrium (M_0) is also known as the longitudinal relaxation (also explained in section 2.2.4).

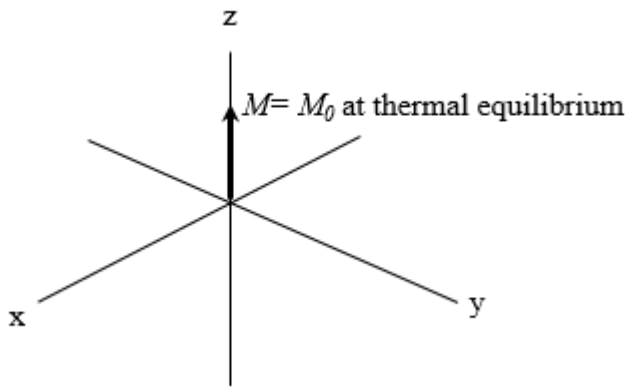

Figure 2.1.2: The bulk magnetization vector at thermal equilibrium

As discussed in the previous section, the bulk magnetization (M) is seen to emerge in the case of thermal equilibrium and the size of M can be predicted by the Boltzmann distribution. However, it can be well understood from Figure 2.1.4 that the net bulk magnetization builds up only when the sample is placed in the presence of a magnetic field. In the absence of a magnetic field, the spins do not align in the direction of the applied external magnetic field B_0 and hence there is no net magnetization.

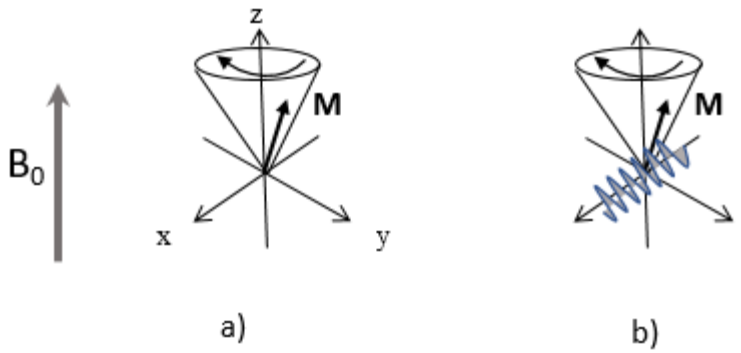

Figure 2.1.3: a) Precessing magnetization vector on the application of magnetic field B_0 along z-axis. b) precessing magnetization will "cut" a coil wound around the x-axis leading to an induced current in the coil which is then amplified to give FID signal.

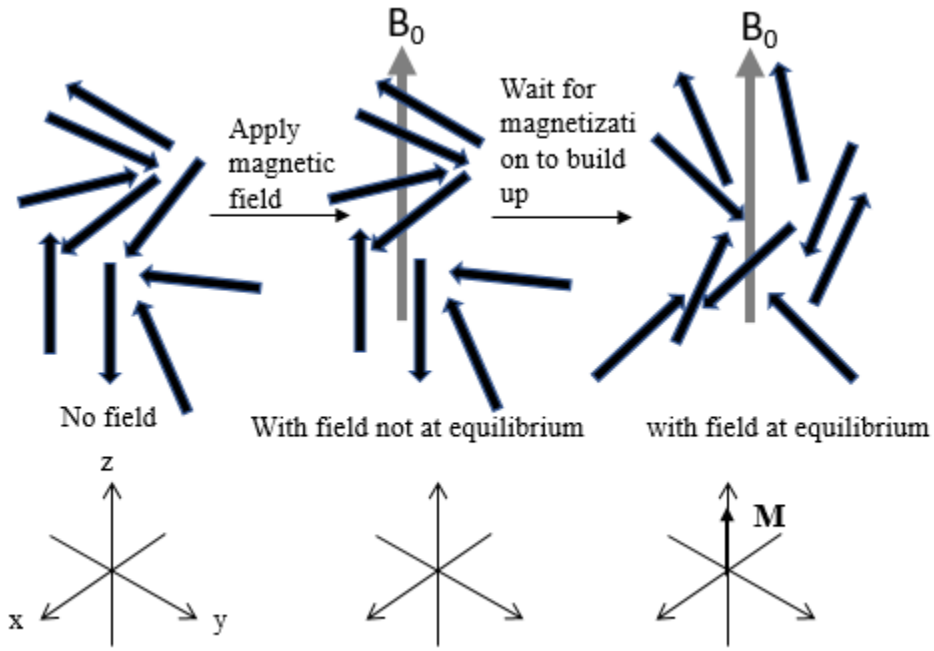

Figure 2.1.4: Mechanism of magnetization build-up in the presence of an applied magnetic field along the z-direction.

2.2 Pulses and signal detection in NMR

The Larmor precession that was discussed in Section 2.1, is related to the magnetization vector, **M**, and is detected in an NMR experiment. Imagine mounting a small coil of wire round with the axis of the coil. The coil is aligned along the xy-plane and it is inferred that the precessing magnetization vector negates (cuts) the current induced by the coil, which is then amplified and detected by the detector as FID or free induction signal or free induction decay (Fig 2.1.3 b). The magnetization vector precesses around the z-axis or the axis of the cone (Figure 2.1.3 a). The x- and y-components are resolved by obtaining the projection of the magnetization vector.[8] The visualization of what happens to the x component for instance is given below in Figure 2.2.1:

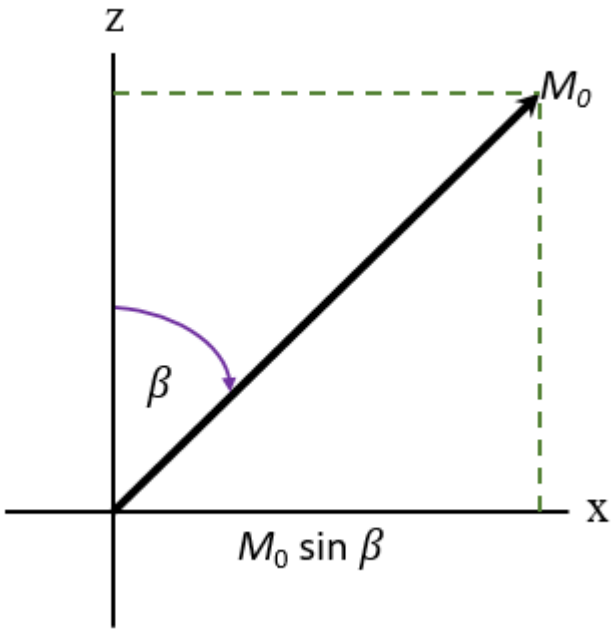

Figure 2.2.1: Tilting of *M* through an angle β towards the x-axis to obtain the x-component of size $\boldsymbol{M_0 \sin \beta}$

The length of the vector is given as:

$$r = M_0 \sin\beta \quad \text{Eq 2.2.1}$$

When the vector rotates with Larmor angular frequency ω_0 at time *t*, the x and y components can be simplified as $r \sin\omega_0 t$ and $r \cos\omega_0 t$ which leads us to resolving the magnetization vector components as:[9]

$$M_x = M_0 \sin\beta \cos\omega_0 t \quad \text{Eq 2.2.2}$$

$$M_y = -M_0 \sin\beta \sin\omega_0 t \quad \text{Eq 2.2.3}$$

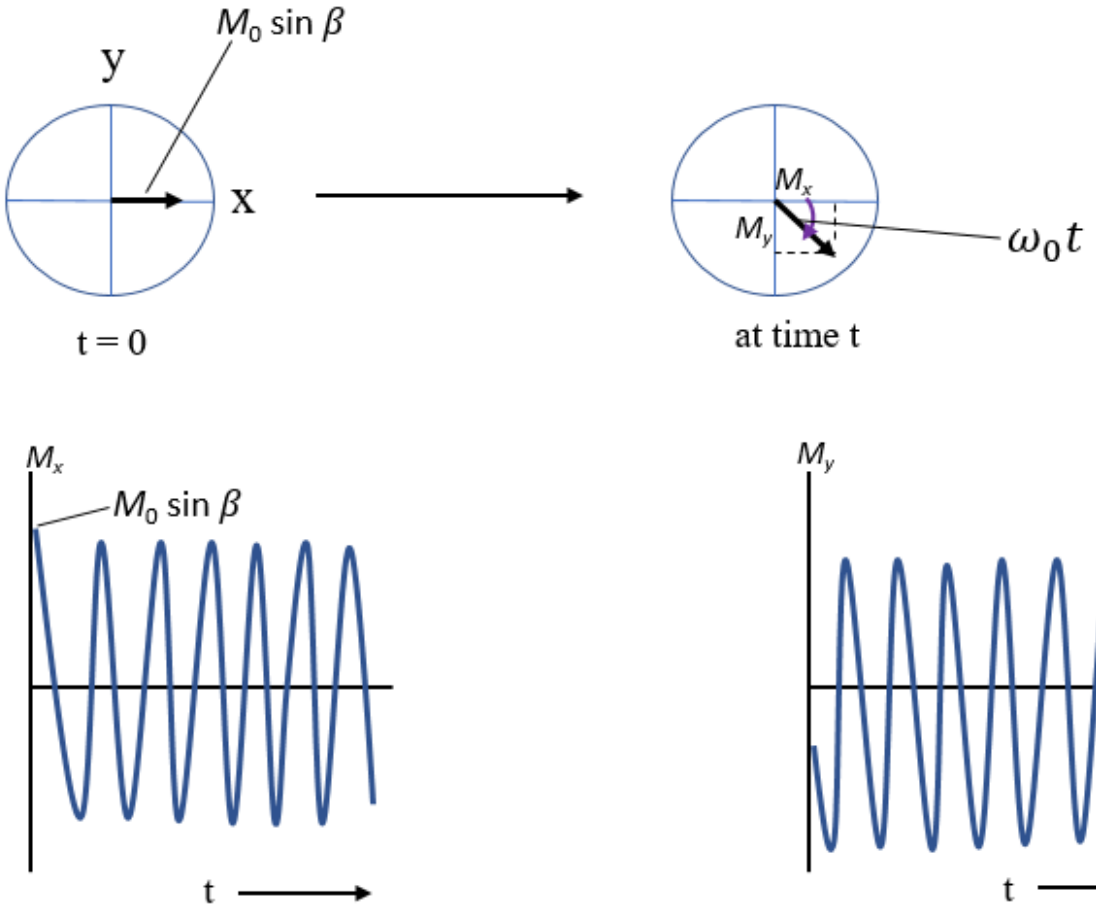

Figure 2.2.2: Diagram of magnetization vector along x and y direction as a result of their resolved components when magnetization is tilted to the x-axis and y-axis is set to zero.

The magnetization vector along the z-axis is the equilibrium position in the direction of applied magnetic field, B_0. When the magnetization is rotated away from the equilibrium position that is the z-axis, it will be no longer aligned with the z-axis but will turn towards the xy-plane on doing so. The precession of the magnetization vector switches to yz-plane, which will bring the

magnetization to the transverse plane, which is ideally our point of interest, however, the superconducting magnet, in which the pulses are detected and then Fourier transformed[11] to obtain a signal is not a place to switch off the magnetic field and turn the magnetization vector to the other plane deviating away from its main magnetic field, it is an impossible approach. To address to this impossible approach, one might use a resonant oscillating field near the Larmor frequency (say a small magnetic field is applied along the x-axis), which can move away the magnetic field from the z-axis even under the influence of B_0 when the resonance frequency condition prevails. The RF power is introduced in to the coil that detects precession of the magnetization vector so that an oscillating magnetic field is generated (say in the x-direction), which is often termed as the "radiofrequency field" or "RF field" which needs a rotating frame of reference to be understood better relative to a laboratory frame of reference The laboratory frame, in which the pulses and net bulk magnetization is depicted in the vector model is usually said to be as "static" which rotates just about the z-axis.

The Figure 2.2.3 demonstrates the production of an oscillating field along x-direction and the oscillating field along the x-axis is decomposed into two fields rotating at ω_{tx} in opposite directions resulting in $2\mathbf{B}_x = 2\mathbf{B}_x \cos(\omega_{tx}t)$.

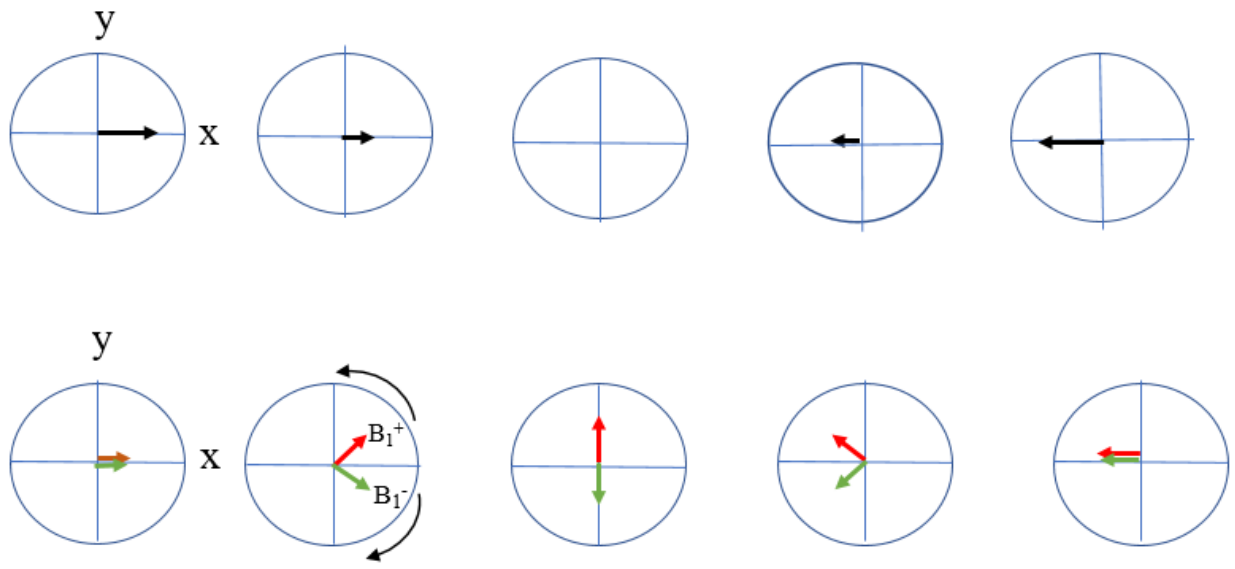

Figure 2.2.3: Schematic of two counter-rotating magnetic fields B_1^+ and B_1^- add up together to give an oscillating field along the x-axis.

The usefulness of introducing a rotating frame of reference is useful in understanding how the weak RF field can rotate the magnetization vector **M** from the precessing magnetic field at B_0. The main difference between laboratory and rotating frame of reference can be seen in the following equations:

$$\omega_0 = \gamma\beta_0 \qquad \text{Eq 2.2.4}$$

$$\Omega = (\omega_0 - \omega_{tx}) \quad \text{Eq 2.2.5}$$

The rotating frame of reference involves an offset term Ω, which is related to the apparent precession along **M**, the term ω_{tx} relates to the rotating frame of the magnetization vector by the

xy-plane to retain a static magnetic field, $\mathbf{B_x}$ and a field rotating at $2\omega_{tx}$. The magnetic field therefore in the rotating frame of reference can be represented as:

$$B_{rot} = \frac{\Omega}{\gamma} \qquad \text{Eq 2.2.6}$$

The condition where the transmitter frequency, $\omega_{tx}$is equal to the Larmor frequency, the static field becomes negligible as, Ω=0, then on substitution of the Ω term in equation 2.2.6, B_{rot}=0. Which shows that the applied external magnetic field was switched off and the nucleus in consideration will only experience the transverse magnetization along the xy-plane as **Bx.**

2.2.1 Nutation

The rotating frame of reference conveys that under the effect of RF pulse, the bulk magnetization vector, **M**, "sees" an apparent static magnetic field B_x and precesses/nutates about it until it is turned off. The phase of the pulse about which M rotates is same as the axis to which the pulse is applied (to the same phase) and the angle of rotation M is given by

$$\beta = \omega_1 t_p \quad \text{Eq 2.2.7}$$

where β is the flip angle or the angle of rotation along the axis of M during the pulse duration of t_p. The on-resonance pulses, which can be simplified as the pulse generated when the transmitter frequency equals to the Larmor frequency can be described using the equation of flip angle.

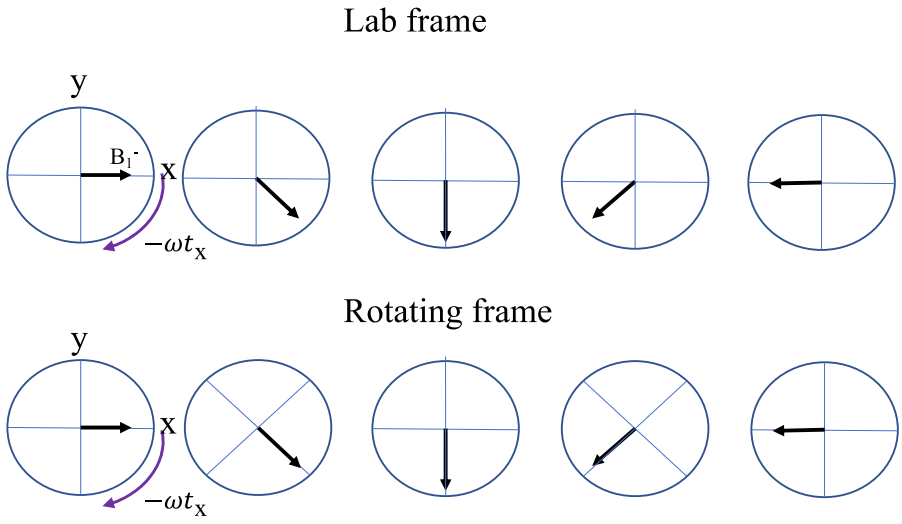

Figure 2.2.4: Representation of the magnetic field B_1^+ r in a laboratory frame or fixed axis system rotating at $-\boldsymbol{\omega_{tx}}$ (clockwise) in the top row and the bottom row represents the motion of same field but at the rotating frame of reference, where B_1^+ appears static.

2.2.3 Pulse detection in rotating frame of reference

The rotating frame of reference implements a standard perspective to detect the magnetization vector when a pulse is applied to a certain axis in terms of the way the spectrometer works. The offset frequency, Ω is the one at which the detected magnetization vector oscillates at and because of the applied pulse the magnetization vector results in the following components analogous to equation 2.2.2 and 2.2.3 replaced with the offset term that produces the following magnetization components:

$$M_x = M_0 \sin\beta \cos\Omega t \quad \text{Eq 2.2.8}$$

$$M_y = M_0 \sin\beta \sin\Omega t \quad \text{Eq 2.2.9}$$

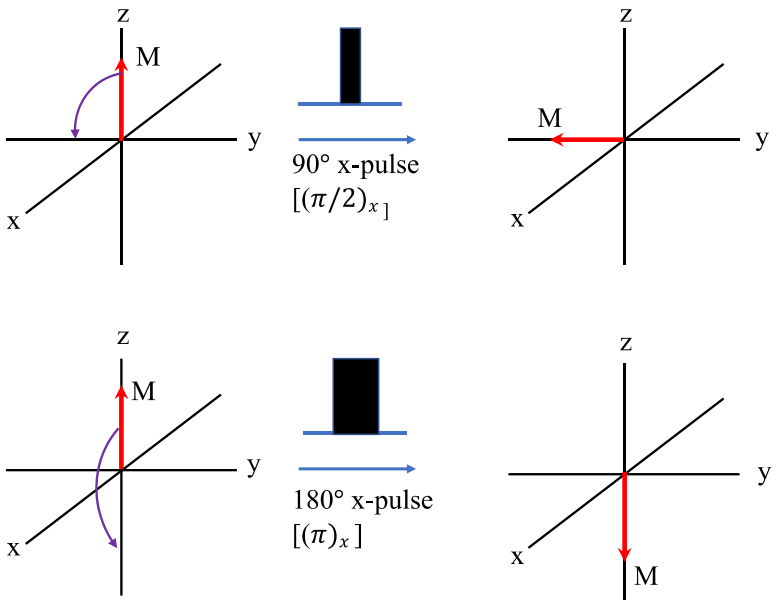

Figure 2.2.5: Effect on magnetization vector when a 90°and 180° pulse is applied to the x-axis.

2.2.4 Calibration of pulses and relaxation

It is important for an NMR experiment to have a well-calibrated pulse leading to amplified signal intensity with a higher signal to noise ratio. It is essential for the pulses used to set up an NMR experiment ought to have a correct flip angle as discussed in equation 2.2.7. To obtain a maximum signal intensity, a 90° pulse is to be used, whereas if we wanted to flip the entire magnetization vector, we must use a 180° pulse instead. A sinusoidal function leads to a maximum

signal intensity when the pulse is 90° as, sin 90°=1, the different flip angle of how the **M** value is varied over a period is shown below to decipher the pulses in work better.

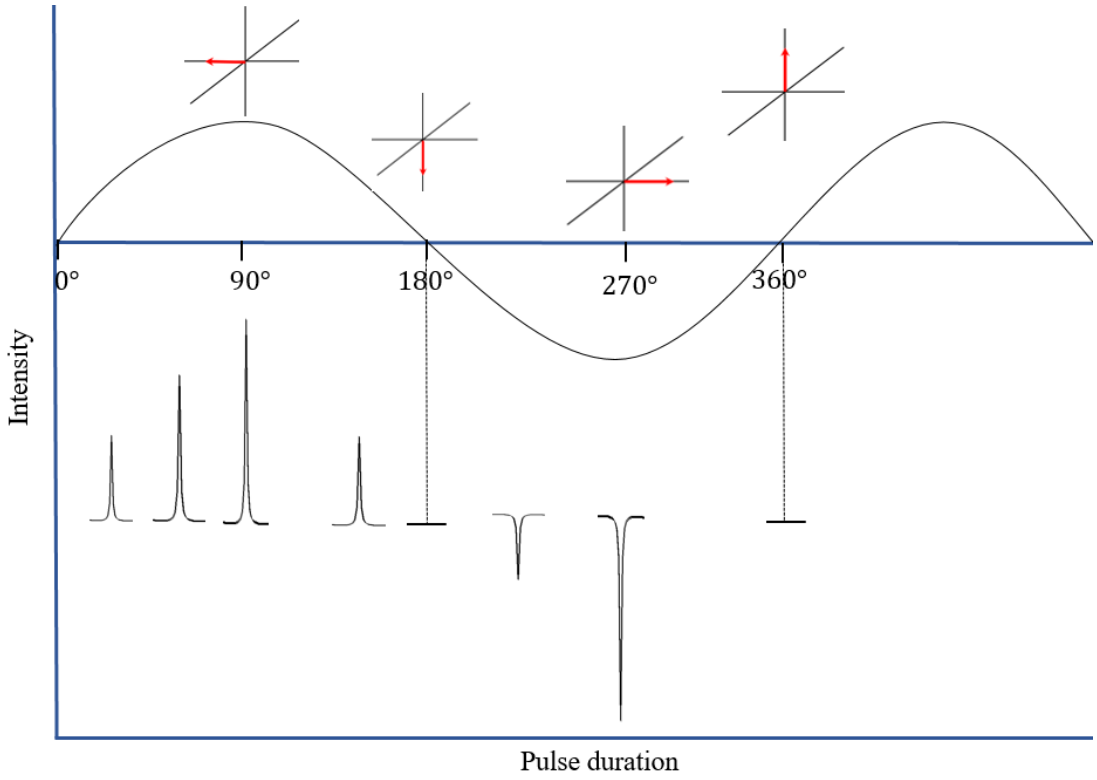

Figure 2.2.6: Schematic showing the working of a pulse as a function of sine curve where the maximum is attained at a 90°.

The precession of **M** is not an indefinite phenomenon along the xy-plane after the effect of a 90° pulse. The spins comprising the population level of the different energy levels reach thermal equilibrium after the application of the pulse. In the beginning when the magnetization vector is rotated away from the z-axis after a pulse is applied, the spins in the energy levels experience increase in energy and they tend to reach equilibrium by reducing the energy of the spins in

compliance with the Boltzmann distribution as seen in section 2.1.1. The process of how the *M* spins along z-axis return to the equilibrium is known as spin-lattice relaxation or longitudinal relaxation[8,9] and is denoted with T_1. On the other hand, the *M* in the xy-plane (called transverse magnetization) also decays with time, the process of which the transverse magnetization vector approaches to its equilibrium position of zero, is known as spin-spin or transverse relaxation and is denoted as T_2 relaxation. The T_2 relaxation has a difficult understanding approach, but in simpler terms it may be attributed to what is known as loss of phase coherence between the individual spins. A simple demonstration of how *M* is approached as during the T_1 and T_2 relaxation is given below in the Figure 2.2.8 and 2.2.7.

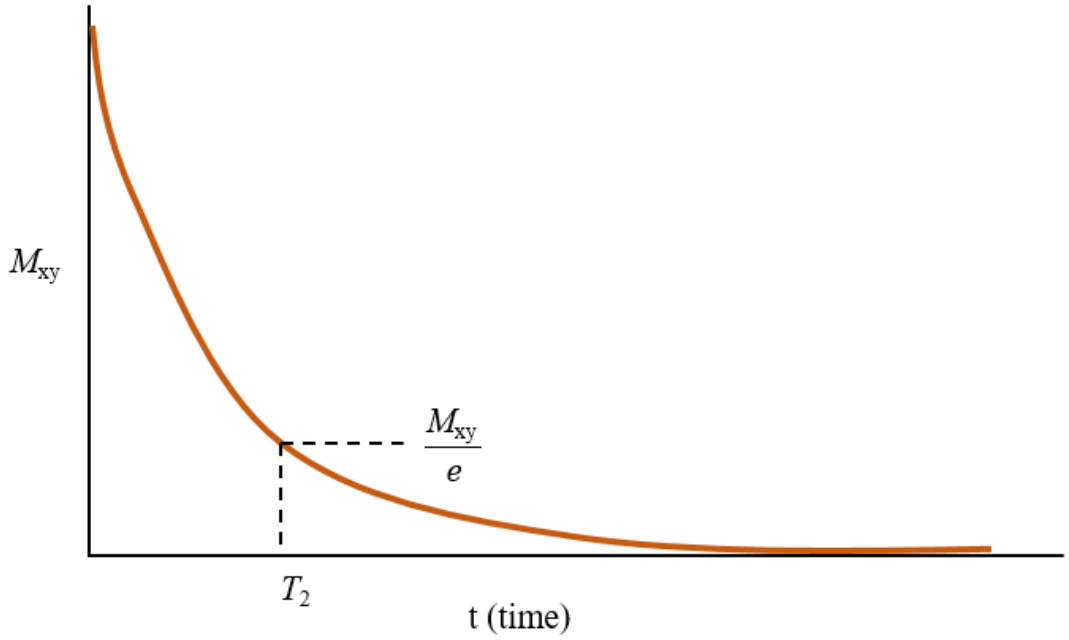

Figure 2.2.7: Schematic of a T_2 relaxation, decay of transverse magnetization (xy) against time t.

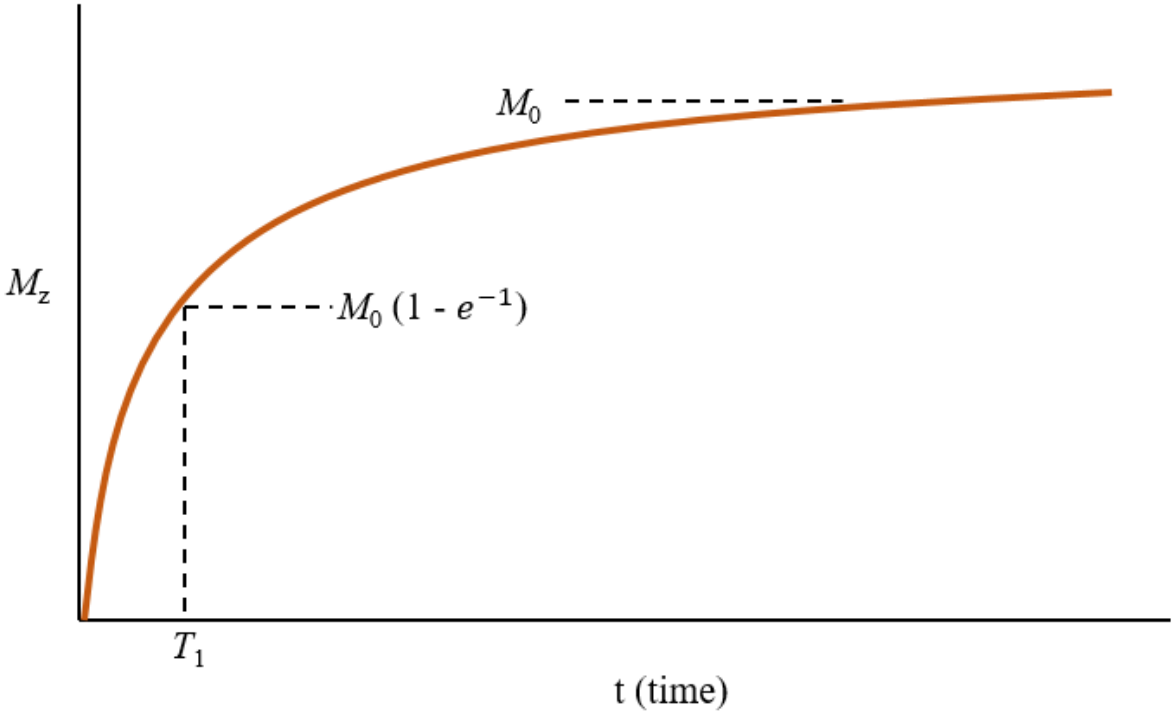

Figure 2.2.8: Schematic of T_1 relaxation mechanism, growth of magnetization (along z) against time t.

2.3 NMR interactions

Under the effect of a homogeneous magnetic field, a nucleus experiences several interactions that is governed by the Hamiltonian operator[22] that results in the spectrum. The Hamiltonian operator, a fundamental operator of quantum mechanics in terms of nuclear magnetic interactions can be divided into four key parts beside the basic Zeeman interaction (Z): the nuclear magnetic shielding interaction (σ), the indirect spin-spin coupling (J), the direct dipolar coupling

interaction (*D*) and the nuclear quadrupolar coupling interaction (*Q*). The four interactions beside the Zeeman interaction are caused due to perturbation theory and are treated as perturbations to the Zeeman interaction.

The total Hamiltonian including all the nuclear magnetic interactions that contribute to an NMR spectrum can be written as:

$$\widehat{H} = \widehat{H_Z} + \widehat{H_\sigma} + \widehat{H_J} + \widehat{H_D} + \widehat{H_Q} \quad \text{Eq 2.3.1}$$

The fundamental four interaction that are added to the Zeeman interaction Hamiltonian term can be generalized as:

$$\widehat{H_A} = \hat{I}.\boldsymbol{A}.\hat{S} \quad \text{Eq 2.3.2}$$

Where, $\hat{I}$ and $\hat{S}$ are the nuclear spin operators where S is a second spin operator and they can be depicted as three components along the three axes ($\hat{I} = (\hat{I}_x,\ \hat{I}_y, \hat{I}_z)$) and $\boldsymbol{A}$ is a second-rank Cartesian tensor matrix which can be simplified as:

$$\boldsymbol{A} = \begin{pmatrix} A_{xx} & A_{xy} & A_{xz} \\ A_{yx} & A_{yy} & A_{yz} \\ A_{zx} & A_{zy} & A_{zz} \end{pmatrix}$$

2.3.1 Nuclear magnetic shielding interaction

In terms of molecules, big or small, it is an assembly of nuclei connected by bonds in a molecule and electrons which influences the spectrum of a specific nucleus. The presence of other nuclei can interact in several ways to affect the resonances of the observed nucleus. The electrons

that surround the nucleus are sensitive to the present magnetic field and thus generate a weak magnetic field thus the nucleus in study senses a different effective field apart from the applied magnetic field due to the electron effects thereby causing them to be shielded and giving rise to a nuclear magnetic shielding term (σ). The importance of this effective field can be demonstrated by the equation below that shows the effect on the applied magnetic field due to the incorporation of the nuclear magnetic shielding term.

$$\boldsymbol{B_{eff}} = \boldsymbol{B_0}\,(1-\sigma) \quad \text{Eq 2.3.1.1}$$

The nuclear magnetic shielding term has two parts that effect the shielding effect, the diamagnetic and paramagnetic part, as described by Ramsey's equation:[10]

$$\sigma = \sigma^d + \sigma^p \quad \text{Eq 2.3.1.2}$$

This equation is a simplistic nonrelativistic approach where Ramsey based his equation on the Hamiltonian where the second-order perturbation theory is included however, neglecting the spin-orbit and relativistic correction terms. Diamagnetic shielding and paramagnetic deshielding terms that go together when it comes to describing the shielding constant will be discussed explicitly in the next part.

2.3.1.1 Chemical shift anisotropy

The way that electrons are distributed surrounding a nucleus are not a uniform sphere, it thus creates a concept of anisotropy in the nuclear shielding tensor term which is often averaged out in solution NMR spectrum in comparison to solid-state NMR, thus taking this interaction into consideration is essential. The nuclear magnetic shielding constant when studied for a specific molecule to obtain an NMR spectrum can be called as the chemical shielding and thus also

considers of how the electrons surrounding the observed nucleus affect the NMR shielding constant whether the molecule is under the effect of diamagnetic shielding interaction or paramagnetic deshielding interaction. To simplify things, we will describe here something known as the “chemical shift” or the standard scale in which a Fourier transformed[11] NMR spectrum is always recorded in. Chemical shift scale is the reverse of chemical shielding scale and is denoted with "δ", from Ramsey’s equation the diamagnetic shielding term is positive ($\boldsymbol{B}_{\mathbf{eff}}$ is less than $\boldsymbol{B}_0$) whereas the paramagnetic shielding term is negative (often known as paramagnetic deshielding), these two fundamental contributions to the shielding constant has effects on an NMR spectrum for a nucleus under examination in a molecule. For instance, diamagnetic shielding is directly proportional to the electron density surrounding the molecule of the concerned nucleus as these diamagnetic currents arise from the motion of electrons within the atomic orbitals. Diamagnetic shielding term is applicable to only closed shell atoms or spherical atoms. The magnitude of this term is extracted from the ground-state configuration of the electronic configuration of the atom/molecule in picture. To be precise, if the diamagnetic shielding term experiences higher electron density, the shielding is higher and the reverse scale that is the chemical shift, is less or opposite in magnitude. The paramagnetic shielding term is caused due to paramagnetic currents that are generated from the ground-state electron wavefunction on mixing with that of the excited state. The s-orbital electron density does not contribute to the paramagnetic shielding term and the paramagnetic deshielding term is inversely proportional to the energy difference between the ground and excited state and the cube of internuclear distance r.

$$\sigma_p \propto \frac{1}{\Delta E . r^3} \quad \text{Eq 2.3.1.1.1}$$

The paramagnetic current that is generated causes a small local magnetic field that deshields the nucleus from the surrounding electron density. Other shielding effects like neighbouring group anisotropy, ring currents or hydrogen bonding also affects the magnitude of the shielding constant and the chemical shift of the observed nucleus in a molecule that is reciprocated in the NMR spectrum. The expression of the resonance frequency to define the effective field generated by the shielding terms is given as

$$\nu = \frac{-\gamma B_0 (1-\sigma)}{2\pi} \quad \text{Eq 2.3.1.1.2}$$

Since the shielding constants are inconvenient to measure, the chemical shift scale that is relative to every nucleus in terms of a reference compound is written as:

$$\delta = 10^6 \frac{(\nu-\nu_{ref})}{\nu_{ref}} \quad \text{Eq 2.3.1.1.3}$$

Thus, the shielding term and the shift term of nuclear magnetic interaction are related as:

$$\delta = 10^6 \frac{(\sigma_{ref}-\sigma)}{(1-\sigma_{ref})} \approx 10^6 (\sigma_{ref} - \sigma) \quad \text{Eq 2.3.1.1.4}$$

Owing to the non-spherical electron distribution in a molecule that gives rise to anisotropic effect are one of the important interactions to consider for powdered solids where the interactions prevail and are the prime factors to consider and study as to how it affects the local environment, structure, chemical information, and mechanism from the NMR spectrum. The frequency of NMR line shapes depends on the orientation of the nucleus under observation with respect to the applied magnetic field:

The equation governing the resonance frequency when the three different components along three different axes are considered in the anisotropic effect is given as:

$$\nu = \frac{-\gamma B_0}{2\pi}\left[1 - (\sigma_{11}cos^2\theta_{11} + \sigma_{22}cos^2\theta_{22} + \sigma_{33}cos^2\theta_{33})\right] \text{ Eq 2.3.1.1.5}$$

Where, σ_{ii} represent the principal shielding components of the chemical shielding tensor, where the second-rank tensor matrix here is the shielding tensor and $\theta_{ii}$are the angles between the applied magnetic field and the principal components.

For a powdered sample, the orientation for the crystallites can be summed up into what is called a "powder pattern" and to do so, the chemical shift tensor can be written as the second-rank tensor analogous to the shielding tensor[13]:

$$\delta = \begin{bmatrix} \delta_{11} & 0 & 0 \\ 0 & \delta_{22} & 0 \\ 0 & 0 & \delta_{33} \end{bmatrix}$$

$$\delta_{11} \geq \delta_{22} \geq \delta_{33} \text{ Whereas } \sigma_{33} \geq \sigma_{22} \geq \sigma_{11}$$

$$\delta_{iso}(\text{isotropic chemical shift}) = \frac{1}{3}(\delta_{11} + \delta_{22} + \delta_{33}) \text{ Eq 2.3.1.1.6}$$

$$\Omega \text{ (span)} = (\delta_{11} - \delta_{33}), \Omega > 0 \quad \text{Eq 2.3.1.1.7}$$

$$\kappa \text{ (skew)} = \frac{3(\delta_{22} - \delta_{iso})}{\Omega}, (-1 \leq \kappa \leq 1) \text{ Eq 2.3.1.1.8}$$

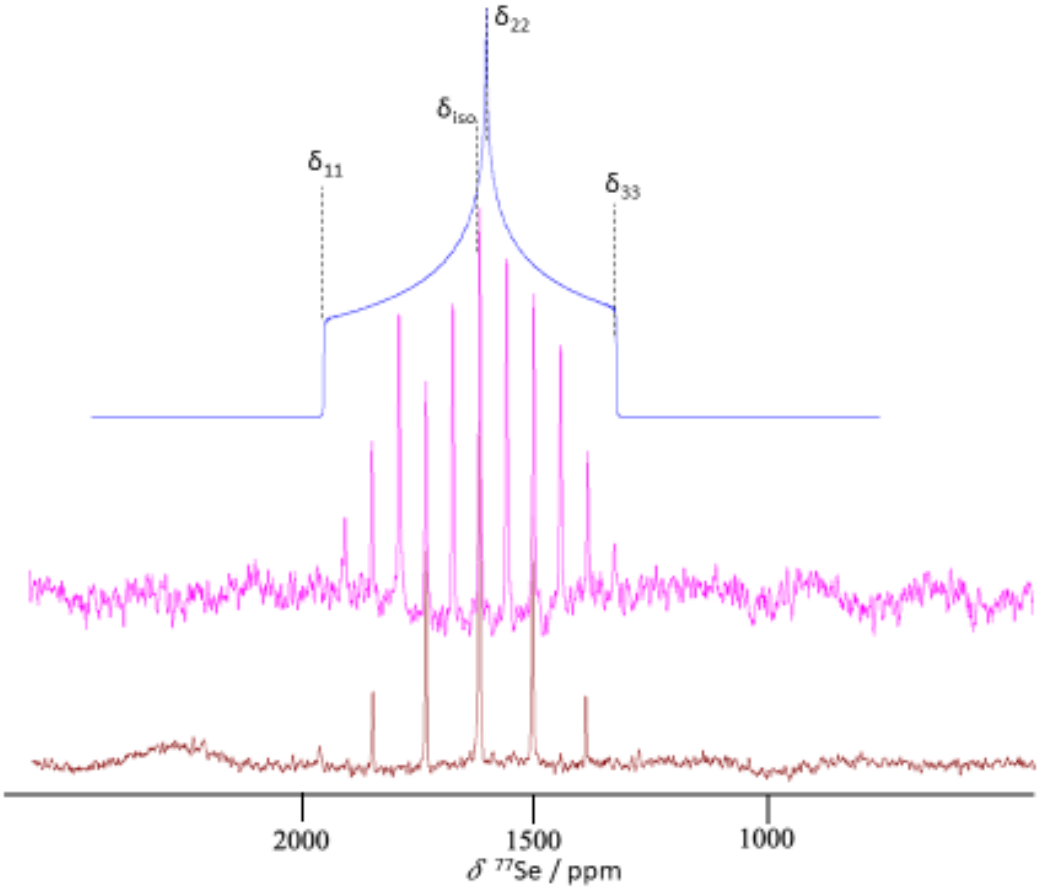

Figure 2.3.1: ^{77}Se spectrum of selenodiazole and hydroquinone cocrystal where the static powder pattern (top, blue) highlights the distribution of the principal nuclear magnetic shielding components and the isotropic chemical shift obtained by spinning the sample at 9 kHz (bottom, brown) and 4 kHz (middle, pink).

2.3.2 Indirect spin-spin coupling interaction

The indirect spin-spin coupling, or *J*-coupling is the interaction that involves "through bond coupling" caused by electrons with a nucleus in observation. Electrons are spin ½ or fermions with gyromagnetic ratio of 660 times than that of a proton thus it becomes important to consider the

Fermi contact term at very short distances for an electron and the nucleus as it is then almost isotropic in nature. The Fermi contact term (FC) is the initiation that leads to spin-spin coupling pairs of the nuclei via the bonding electrons. *J* value can either be positive or negative depending on the stabilization of the spins, when low energy antiparallel spins are stabilized between the two neighbouring nuclei to the adjacent electrons, it is positive else negative. The signs are as important as the magnitude of the *J* values in Hz. A typical one-bond J-coupling is represented as: $^{1}J_{\text{M-N}}$, where M and N are the nuclei in study, it can either be different or same, M-M or N-N .

Analogous to the shielding interaction, the *J*-coupling is also affected by four other terms apart from FC term discussed earlier. These five mechanisms[12] contribute to the magnitude of *J*-coupling to determine how strong a bond is and how the coupling of the electron-nuclei spin pairs behave. From Ramsey's formulations, paramagnetic spin-orbital coupling (PSO), diamagnetic spin-orbital coupling (DSO), spin-dipolar coupling (SD) and Fermi contact spin-dipolar cross-coupling (FC×SD) are the terms that along with the Fermi contact (FC) mediate the basis of *J*-coupling. The FC term as described before is the most dominant and prevail only for s-orbitals owing to one of the nuclei's magnetic moment and electron's orbital current that induces a magnetic field to the other nuclei which is same as the concept of magnetic shielding. The PSO and DSO terms are the interactions that takes into account the orbital angular momentum and spin orbital momentum of the nucleus involved in the spin-spin coupling. The direct dipolar coupling between the magnetic moment of the nucleus and the electronic spin is the idea of SD interaction. The final interaction is a bit complicated as it is usually overlooked when we talk about scalar coupling as this term contributes to anisotropy of the indirect spin-spin coupling, but it is as important and essential as this term is inseparable from the other coupling effect known as the

dipolar coupling which will be talked about in the next part, this FC×SD interaction plays a massive role in determining the effect of a quadrupolar nucleus coupled to a spin-1/2 nucleus and how the local environment changes when such a bond/type of a bond is formed. The FC, PSO, DSO and SD contributes to isotropic part of *J*-coupling. The **J**-Hamiltonian can be represented as follows:

$$\widehat{H_J} = h\,\hat{I}_1 \mathbf{J}\,\hat{I}_2 = \mathrm{h}\,(\hat{\mathrm{I}}_{1x}, \hat{\mathrm{I}}_{1y}, \hat{\mathrm{I}}_{1z}) \begin{pmatrix} J_{xx} & J_{xy} & J_{xz} \\ J_{yx} & J_{yy} & J_{yz} \\ J_{zx} & J_{zy} & J_{zz} \end{pmatrix} \begin{pmatrix} \hat{\mathrm{I}}_{2x} \\ \hat{\mathrm{I}}_{2y} \\ \hat{\mathrm{I}}_{2z} \end{pmatrix} \quad \text{Eq 2.3.2.1}$$

From the Hamiltonian, the *J* tensor give rise to the principal components on diagonalization namely, J_{11}, J_{22} and J_{33} with respect to the molecular frame that is analogous to the shielding principal components. The isotropic, anisotropic and the asymmetry parameter can be defined as:

$$J_{iso} = (J_{11} + J_{22} + J_{33})/3 \quad \text{Eq 2.3.2.1}$$

$$\Delta J = J_{33} - (J_{11} - J_{22})/2 \quad \text{Eq 2.3.2.2}$$

$$\eta_J = (J_{22} - J_{11})/(J_{33} - J_{iso}) \quad \text{Eq 2.3.2.3}$$

The order of the principal components for *J*-coupling interaction is given as:

$$(|J_{33} - J_{iso}| \geq |J_{11} - J_{iso}| \geq |J_{22} - J_{iso}) \quad \text{Eq 2.3.2.4}$$

2.3.3 Dipolar coupling interaction

When the spin of a nucleus with *I*=1/2 affects the resonance frequency of surrounding nuclei in a molecule due to its behaviour as a tiny bar magnet, it is said to be directly dipolar

coupled. Dipolar coupling, or "through space coupling" is the interaction that predominantly is dependent on the internuclear distance between the spin pairs. It is a useful tool to trace the internuclear distances between the nuclei in picture. The dipolar coupling can be seen between two similar nuclei (homonuclear) or different ones (heteronuclear) and are perceived differently due to influence of the gyromagnetic term involved in determining the resonances that show up in the NMR spectrum. To understand better, the following Hamiltonian for D for a heteronuclear spin system is written as:

$$\widehat{H}_D = (\gamma_1\gamma_2\hbar^2)\frac{\mu_0}{4\pi}\left[\frac{\hat{I}_{2x}.\hat{I}_{2x}}{r^3} - 3\left\{\frac{(\hat{I}_{2x}.\vec{r})\,(\hat{I}_{2x}.\vec{r})}{r^5}\right\}\right] \quad \text{Eq 2.3.3.1}$$

And the difference in the resonance frequency term for a heteronuclear spin system can be written as:

$$\Delta\nu_{hetero} = \left(\frac{\hbar}{2\pi}\right)\left(\frac{\mu_0}{4\pi}\right)\gamma_1\gamma_2\left(\frac{1}{r^3}\right)(3cos^2\theta - 1) = R\,(3cos^2\theta - 1) \quad \text{Eq 2.3.3.2}$$

Whereas, for a homonuclear spin system the only difference would be in the gyromagnetic ratio term and the coefficient of Planck's constant as it involves two same nuclei:

$$\Delta\nu_{homo} = \left(\frac{3\hbar}{4\pi}\right)\left(\frac{\mu_0}{4\pi}\right)\gamma^2\left(\frac{1}{r^3}\right)(3cos^2\theta - 1) = \frac{3}{2}R\,(3cos^2\theta - 1) \quad \text{Eq 2.3.3.3}$$

Where, the term r = internuclear distance, θ = angle between the applied magnetic field $\mathbf{B}_0$ and the internuclear vector ($\vec{r}$) seen from equation 2.3.3.3, R is the dipolar coupling constant and $\left(\frac{\mu_0}{4\pi}\right)$ is the permeability of free space which equals to the value of 1×10^{-7} kg m s^{-2} A^{-2}.

2.3.4 Quadrupolar coupling interaction

More than 50% of the nuclei in the periodic table are quadrupolar in nature; the nuclei possessing $I>1/2$ are known as quadrupolar for example, ^{14}N (I)= 1; $^{35/37}Cl$ (I)=3/2; ^{127}I (I)=5/2 and many more. In the context of Zeeman interaction equation seen earlier from equation 2.1.1.3, the energy levels for a quadrupolar nucleus can be visualized as follows:

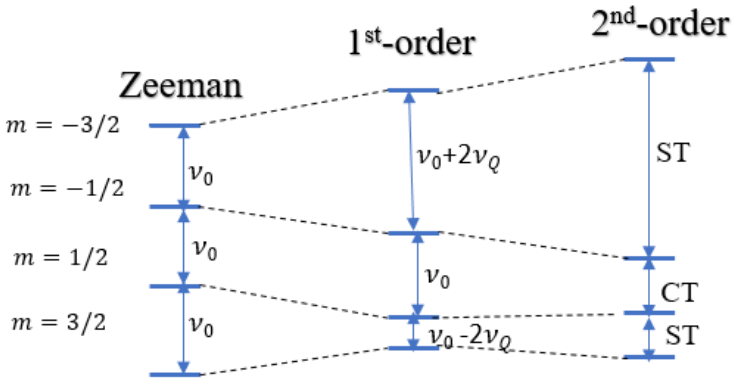

Figure 2.3.2: Energy level diagrams from Zeeman perturbed mechanism to first and second order quadrupolar effects.

However, for a quadrupolar nucleus, they have asymmetric distribution of charges that leads to quadrupole moment Q, often expressed as eQ where e is referred as proton's charge and they range from 10^{-28} to 10^{-31} m^{-2} typically. The asymmetric charge of the $I>1/2$ nucleus can be classified into two different kinds a) prolate (eQ>0) and b) oblate (eQ<0) showing the non-spherical charge distribution that differs from a spin ½ nucleus which do not possess the asymmetric charge or non-spherical charge distribution. The Q which is specific to each nucleus

interacts with the electric field gradients eq that is the distribution and symmetry of the electrons creates the quadrupolar interaction and have different order of interaction (first-order, second order, will be talked in the following pages). The electric field gradient tensor is also analogous to the other interaction tensors and is a second-rank tensor as well given as:

$$\boldsymbol{V} = \begin{pmatrix} V_{xx} & V_{xy} & V_{xz} \\ V_{yx} & V_{yy} & V_{yz} \\ V_{zx} & V_{zy} & V_{zz} \end{pmatrix} = \begin{pmatrix} V_{11} & O & 0 \\ 0 & V_{22} & 0 \\ 0 & 0 & V_{33} \end{pmatrix}$$ (on diagonalization in the principal axis system) Eq 2.3.4.1

The EFG (electric field gradient) tensor is traceless and on diagonalization yields three principal components in the principal axis system as V_{11}, V_{22} and V_{33}. The order of the principal components can be represented as: $|V_{33}| \geq |V_{22}| \geq |V_{11}|$.

On the contrary, to other NMR interactions, quadrupolar interaction extensively focuses on the electric field gradient tensor interaction with the asymmetric charge distribution of the quadrupolar nucleus, the Hamiltonian that best describes the quadrupolar interaction is:[14]

$$\widehat{H}_Q = \frac{eQ}{2I(2I-1)\hbar} (\hat{\mathrm{I}}_{1\mathrm{x}}, \hat{\mathrm{I}}_{1\mathrm{y}}, \hat{\mathrm{I}}_{1\mathrm{z}}) \begin{pmatrix} V_{xx} & V_{xy} & V_{xz} \\ V_{yx} & V_{yy} & V_{yz} \\ V_{zx} & V_{zy} & V_{zz} \end{pmatrix} \begin{pmatrix} \hat{\mathrm{I}}_{\mathrm{x}} \\ \hat{\mathrm{I}}_{\mathrm{y}} \\ \hat{\mathrm{I}}_{\mathrm{z}} \end{pmatrix}$$ Eq 2.3.4.2

Where V is the EFG tensor, $\hbar$ is the Planck's constant = h/2π

The quadrupolar Hamiltonian can be modified in the PAS as below:

$$\widehat{H}_Q = \frac{eQ}{6I(2I-1)\hbar} [V_{11} \left(3\hat{\mathrm{I}}_{\mathrm{x}}{}^2 - \hat{I}\right) + V_{22} \left(3\hat{\mathrm{I}}_{\mathrm{y}}{}^2 - \hat{I}\right) + V_{33} \left(3\hat{\mathrm{I}}_{\mathrm{z}}{}^2 - \hat{I}\right)$$ Eq 2.3.4.3

Eq 2.3.4.3 can be further simplified as:

$$\widehat{H}_Q = \frac{eQ}{4I(2I-1)\hbar}\left[V_{11}\left(3\hat{\mathrm{I}}_{\mathrm{x}}{}^2 - \hat{I}\right) + \eta_Q\left(3\hat{\mathrm{I}}_x{}^2 - \hat{\mathrm{I}}_y{}^2\right)\right.$$ Eq 2.3.4.4

Where η_Q is the asymmetry parameter and is given by:

$$\eta_Q = \frac{(V_{11}-V_{22})}{V_{33}}, 0 \leq \eta_Q \leq 1$$ Eq 2.3.4.5

The value of asymmetry parameter decodes the breakdown of symmetry of a molecule when quadrupolar interaction plays a key role in determining the NMR spectrum. The asymmetry parameter ranges from 0 to 1 and the η_Q value of zero signifies that the EFG tensor is axially symmetric about V_{33}, the largest EFG principal component ($\eta_Q = 0, (V_{11} = V_{22} = \frac{1}{2}V_{33})$).

The quadrupolar interaction can be divided into various order of perturbation when treated as a high-field approximation. The Hamiltonian that resembles the perturbation applied to the quadrupolar term which is much smaller than Zeeman interaction in high field is:

$$\widehat{H}_Q = \widehat{H}_Q{}^1 + \widehat{H}_Q{}^2 + \widehat{H}_Q{}^3 + \cdots$$ Eq 2.3.4.6

Where $\widehat{H}_Q{}^1$ is the first-order perturbation term and is given by the equation below:

$$\widehat{H}_Q{}^1 = \frac{C_Q}{8I(2I-1)\hbar}(3cos^2\theta' - 1 + \eta_Q sin^2\theta' cos2\phi')(3m^2 - I(I+1))$$ Eq 2.3.4.7

Where C_Q is the quadrupolar coupling constant and is represented as:

$$C_Q = \frac{eQV_{33}}{h}$$ Eq 2.3.4.8

Quadrupolar coupling constant term determines the magnitude of quadrupolar interaction and is one of the most important parameters to characterize the EFG tensor, the other one is η_Q, the asymmetry parameter. C_Q is generally measured in MHz.

Referring to equation 2.3.4.7, the polar angles, θ' and ϕ' defines the direction of the magnetic field in the principal axis system of the EFG tensors.

The significance of Figure 2.3.2 is inspired by the fact that the central transition remains unaffected by the first order quadrupolar perturbation term but the satellite transitions respond to the perturbation term.

The second-order perturbation term is also given as follows:

$$\widehat{H}_Q{}^2 = -\left(\frac{C_Q}{8I(2I-1)\hbar}\right)^2\left(\frac{m}{\upsilon_0}\right)\left[-\frac{1}{5}(I(I+1)-3m^2)\left(3+\eta_Q{}^2\right)+\frac{1}{28}(8I(I+1)-12m^2-3)\left\{\left(\eta_Q{}^2-3\right)(3cos^2\theta'-1)+6\eta_Q sin^2\theta' cos2\phi'\right\}+\frac{1}{8}(18I(I+1)-34m^2-5\left\{\frac{1}{140}\left(18+\eta_Q{}^2\right)(35cos^4\theta'-30cos^2\theta'+3)+\frac{3}{7}\eta_Q sin^2\theta'(7cos^2\theta'-1)cos2\phi'+\frac{1}{4}\eta_Q{}^2 sin^4\theta' cos4\phi'\right\}\right] \quad \text{Eq 2.3.4.9}$$

The quadrupolar term related to the second-order perturbation is mathematically detailed but is also important to describe the effect on the CT (central transition) and ST (satellite transition) as it affects both the transitions in the NMR spectrum observed and deflects them away from the resonance frequency, this effect becomes even crucial for nuclei having larger quadrupolar coupling interaction (larger C_Q value).

It is observed that nuclei with larger quadrupolar coupling constant values result in broader lines in the NMR spectrum, for example, ^{79}Br, ^{127}I, ^{185}Re. On the other hand, nuclei such as ^{2}H, ^{133}Cs or ^{7}Li yield in narrower lines in the NMR spectrum due to lower quadrupolar coupling constants. For molecules with higher symmetry, such as a cubic system, the EFG tensor at the site of the observed nucleus in the system is very small or equal to zero, making it easier to observe the line shapes in the NMR spectrum. The breakdown of symmetry sees a rise in quadrupolar coupling constant value, thereby making it challenging to extract the quadrupolar coupling constant of the nucleus in consideration and gets even more challenging when higher-order perturbation effects become prominent in the nucleus under study in the molecule/system.

The coupling between $I = ½$ nuclei and $I > ½$ nuclei is observed in various molecules and is an important factor to be considered to explain the structure, bonding interactions, and chemistry of systems where quadrupolar nucleus interacts with spin ½ nucleus and is projected in the NMR spectrum of the observed nucleus. The spin ½ nucleus (for example, ^{13}C, ^{77}Se) when coupled to a quadripolar nucleus (such as $^{35/37}$Cl, $^{79/81}$Br) give ($2nI+1$) lines in the NMR spectrum where n is the number of equivalent nuclei, and I is the spin quantum number of the quadrupolar nucleus.
If the T_1 relaxation between the energy levels of a quadrupolar nucleus is very slow than indirect spin-spin coupling, *J*, the spin ½ nucleus then exhibits coupling and is prominent in the NMR spectrum of the spin ½ nucleus, whereas if the relaxation is fast compared to *J*, the spin ½ nucleus "sees" an average of the energy levels and only one peak is observed in the NMR spectrum.

The relation which is a proof for observing multiple peaks in the NMR spectrum due to the coupling between spin ½ nucleus and a quadrupolar nucleus is given as:

$$\frac{1}{T_1} \ll J \quad \text{Eq 2.3.4.10}$$

2.4 NMR Experiments

This section of the dissertation explains the basic solid-state NMR experiments performed to acquire the spectra of the target nuclei throughout the research journey. This section vastly deals with the principle and working of the experiments described later based on static and magic angle spinning (MAS) condition. The static condition is where the samples were finely ground into a powder and packed in a rotor without spinning up to a certain frequency to obtain broader line shapes of a quadrupolar nucleus or the quadrupolar nucleus attached to a spin-1/2 nucleus and to extract the asymmetry parameter and quadrupolar coupling constant values, whereas the MAS conditions were used to extract the spinning sidebands, simulate each of the peaks and obtain the isotropic peaks and the principal NMR parameters of chemical shielding. The MAS condition is described below.

Magic angle spinning (MAS): MAS condition is conventionally applied to the finely ground powdered samples consisting of polycrystalline powder. The polycrystallites in the sample are orientation dependant and the NMR interactions in solids due to lack of averaging out of molecular tumbling often lead to broad line shapes, to adhere to this and intensify the spectral resolution, MAS condition is implied. The “magic-angle” in this case is referred to the sample that is packed in a rotor is aligned to an angle of 54.74° with respect to the applied magnetic field, B_0, and in turn it averages out the first-order NMR interactions like magnetic shielding, dipolar coupling, *J*-coupling, to obtain “solution-like” sharp peaks. The first-order quadrupolar interaction

is also averaged out under presence of MAS conditions but the second-order effects still persist but reduced. The equations 2.4.1 and 2.4.2 below justify the working of the MAS condition for a solid-state NMR spectra acquisition.

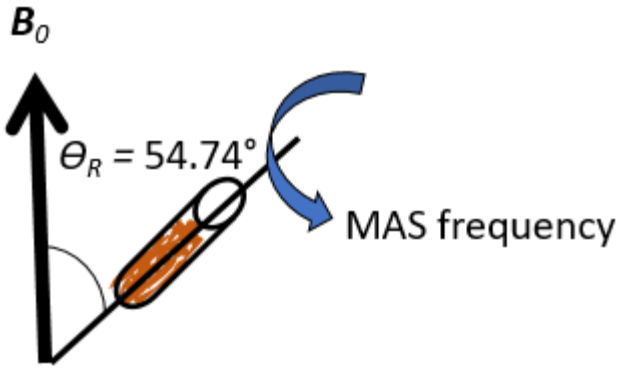

Figure 2.4.1: Schematic representation of a rotor's orientation ($\boldsymbol{\theta_R}$) with respect to the applied magnetic field during MAS experiment.

The term involving the orientation dependence of the NMR interactions is $(3cos^2\theta - 1)$, which should equal to zero in order to average out the first-order interaction terms under MAS, owing to the angle $\theta's$ dependency in the principal axis system (PAS), it cannot be changed however in terms of the spinning rate the MAS condition is applied at the equation could be modified as:

$$\langle 3cos^2\theta - 1\rangle = \frac{1}{2}\,(3cos^2\theta_R - 1)(3cos^2\rho - 1) \quad \text{Eq 2.4.1}$$

Where, θ_R is the angle with which the spinning frequency, ν_{MAS} is chosen around the axis with respect to the magnetic field and ρ is the difference between θ_R and θ, thus the average of the MAS term's average can be equated to zero to yield averaged out first-order NMR interactions as discussed above.

$$\langle 3cos^2\theta - 1\rangle = 0 \quad \text{Eq 2.4.2}$$

2.4.1 CP (Cross-Polarization)

Cross-polarization experiment[15] in solid-state NMR is used as a signal enhancement tool for low abundant spins. The way it is achieved is by transferring the higher abundance of magnetization vectors (spins) from a larger spin-abundant nuclei (like ^{1}H or ^{19}F) to low abundant spin systems (^{13}C, ^{77}Se, ^{125}Te). The following diagram enunciates the working of this pulse sequence where the two spin systems are brought in contact under the application of RF pulse irradiating both spin's resonant frequencies, attained at "Hartmann-Hahn" matching condition. It is important that this Hartmann-Hahn condition is optimized at the power level the nutation pulses are optimized for maximum signal to noise ratio and sensitivity boost to the low abundant spin system. In the CP pulse sequence diagram, the ^{1}H (or high-abundant spin system) magnetization spins are transferred to the low abundant spin system (X) after the initial 90 degree pulse obeying the Hartmann-Hahn condition during the contact time, succeeded by the recycle delay, D1 on the proton channel, having a rather a rather shorter recycle delay due to relatively shorter T_1 relaxation times followed by a period of decoupling time during which the FID is acquired in the X channel (low spin) to an increased signal intensity as a ratio of $\frac{\gamma_{abundant\ spin}}{\gamma_{low\ spin}}$, where the gyromagnetic ratio is γ. The Hartmann-Hahn condition is depicted as:

$$|\gamma_{abundant\ spin}|B_{\text{abundant spin}} = |\gamma_{low\ spin}|\ B_{\text{low spin.}} \quad \text{Eq 2.4.1.1}$$

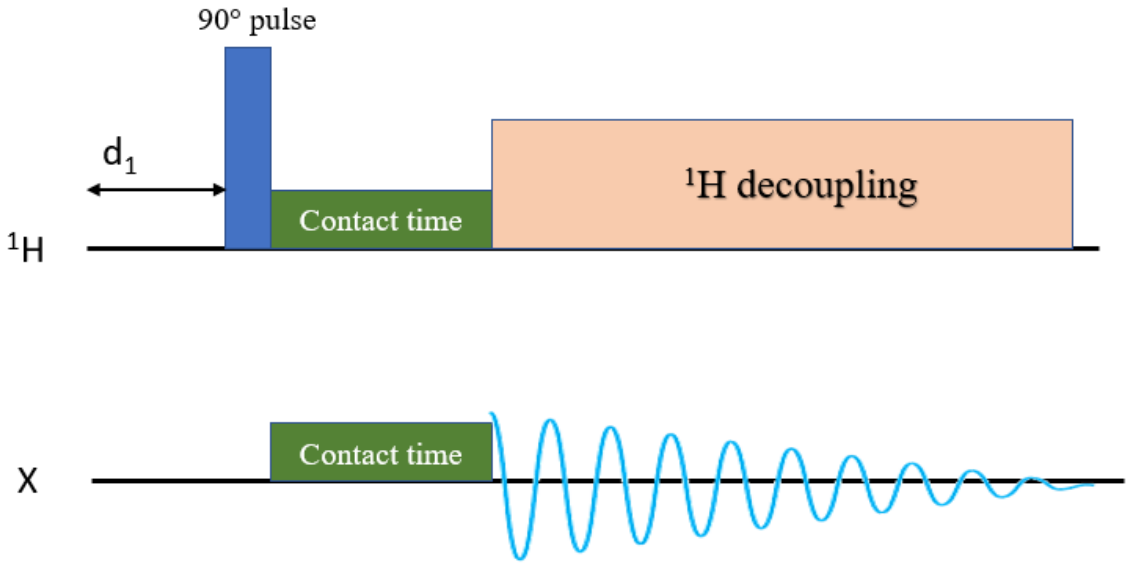

Figure 2.4.2: CP/MAS pulse sequence.

2.4.2 HPDEC (High-Power DECoupling)

A much-used pulse sequence to detect and intensify the signal of low spin system is to directly excite the low spin system (X) nuclei when the protons/ more abundant spins are relatively further and have prolonged relaxation times. The pulse sequence below gives the working of a direct excitation pulse sequence where such cases are dealt keeping in mind the 90° direct excitation pulse is obtained on optimization with respect to the reference used on the X-channel after a recycle delay period and then left for the acquisition during the period of abundant-spin decoupling (in some cases decoupling sequence could be chosen to be used or not depending on the demand of the sample and the ease of signal visibility).

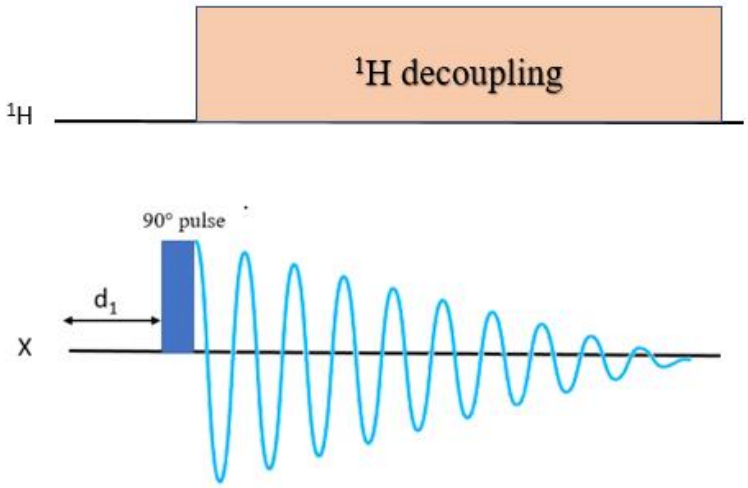

Figure 2.4.3: HPDEC/MAS pulse sequence.

2.4.3 Spin-echo

A spin-echo sequence, the most fundamental approach to understanding a simple NMR pulse-sequence illustrates the working of a static experimental setup in solids where often broad line shapes are observed due to NMR interactions and are tackled by pulse sequences such as Hahn-echo and solid-echo experiments. The basic difference between both the sequence is that the Hahn-echo the pulse sequence works as (90°-τ-180°) instead of (90°-τ-90°) which is observed in solid-echo. The basic purpose of running a solid or a quadrupolar echo instead of a Hahn echo sequence lies in the fact that a quadrupolar coupling is rather pronounced in the compound and the nucleus of interest to obtain the NMR spectrum of. The simplicity of an echo sequence lies in the fact of pulse focusing and refocusing back (be it chemical shift or *J*-coupling) depending on the

type of pulse applied. During the application of the first 90° pulse, the spins are aligned in the transverse plane and after waiting for a period of τ as the delay period, the spins precess and dephase, on the application of a further 180 degree or a 90 degree pulse the spins are brought back to their original states (phased in solid-echo and not phased in Hahn-echo) after waiting for a period of τ again to finally acquire the FID.

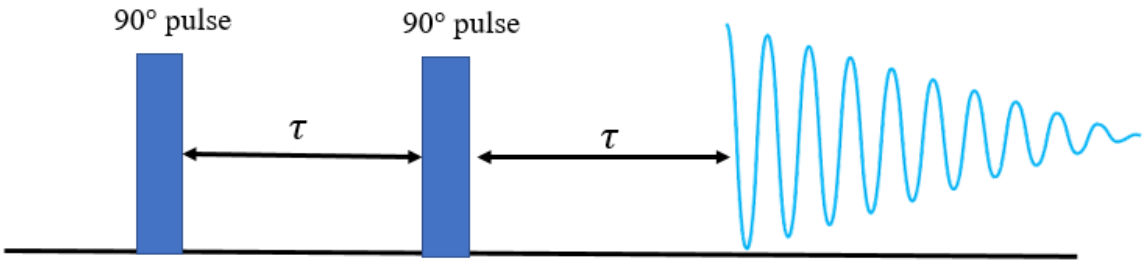

Figure 2.4.4: Solid-echo pulse sequence.

2.4.4 WURST-QCPMG (Wideband Uniform-Rate Smooth Truncation Quadrupolar Carr-Purcell Meiboom-Gill)

The QCPMG (Quadrupolar Carr-Purcell Meiboom-Gill) pulse sequence[16,17] is used to intensify the signal to noise ratio for a broad NMR spectrum mostly seen in quadrupolar nuclei with longer T_2 relaxation times. The echo train extensively studied in the WURST-QCPMG pulse sequence shown below involves two different WURST pulses mainly used to focus a wide

excitation profile range and refocusing. These specialized WURST pulses are amplitude modulated and are specific to each nucleus (quadrupolar) under observation.

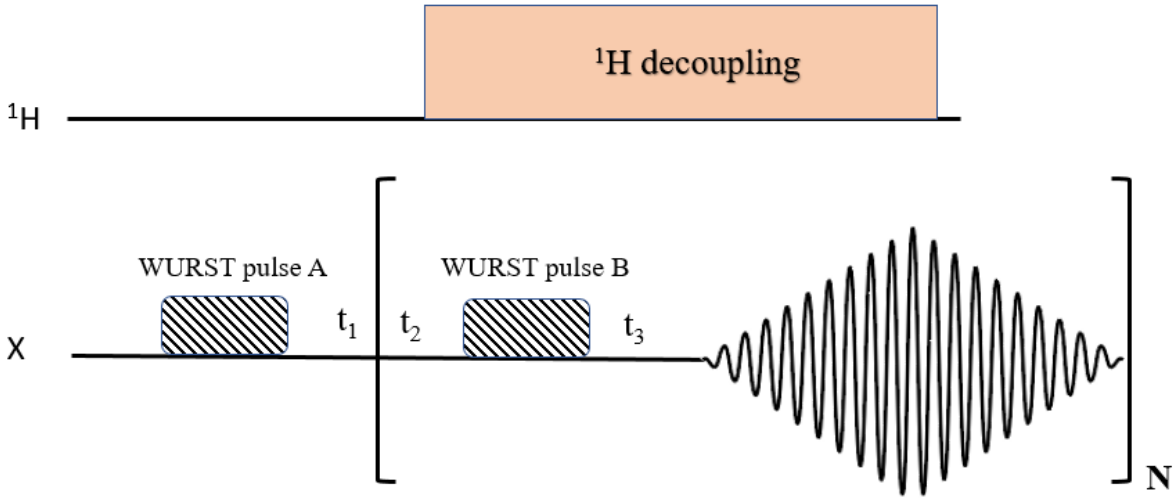

Figure 2.4.5: WURST-QCPMG pulse sequence**.**

2.5 Nuclear Quadrupole Resonance Spectroscopy (NQR)

2.5.1 Introduction and theory of NQR

NQR spectroscopy is a relevant technique and finds its practical importance in cases where a nucleus is highly quadrupolar in nature. There have been developments and techniques over the past years in finding better alternatives to NQR with the help of SSNMR, however, there are

certain prospects where the advantages and disadvantages of NQR spectroscopy can be listed to prove the effectiveness of the technique.[19]

The quadrupolar Hamiltonian that is discussed in section 2.3.4 is the Zeeman interaction Hamiltonian in addition to the quadrupolar higher order perturbation terms. Second-order perturbation effects in a quadrupolar interaction is a crucial to be able to quantify the solid-state NMR spectrum of the observed quadrupolar nucleus, however, there are certain limitations to its application in cases where the quadrupolar interaction becomes dominant. According to literature, for the perturbation theory to be fully functional and reliable, it could be applied where the ratio of Larmor frequency to the quadrupolar frequency is above 10.

The equation of a quadrupolar frequency of a $I > ½$ nucleus is given as follows:

$$\nu_Q = \frac{3C_Q\sqrt{1+\frac{\eta^2}{3}}}{2I\,(2I-1)} \quad \text{Eq 2.5.1.1}$$

The CT frequency usually gives broader line shapes in the NMR spectrum of a quadrupolar nucleus due to the width of the CT frequency being inversely proportional to the Larmor frequency, to tackle the broader lines of the NMR spectrum, usually a higher field is required to perform the experiments. Higher-magnetic fields are not always practical or available at ease, to switch to a rather practical and economical alternative, NQR can be applied as it requires no magnetic field, and the Zeeman interaction term of the Hamiltonian can be left out to just obtain the quadrupolar interaction terms (along with first and second order perturbation terms applied) in addition to the dipolar, indirect spin-spin and dipolar coupling Hamiltonians.[20]

$$\Delta\nu_{CT} = \left(\frac{25+22\eta+\eta^2}{144}\right)\left[\frac{(3C_Q)^2}{(2I\,(2I-1))^2}\right]\left[\frac{I(I+1)-\frac{3}{4}}{\nu_0}\right] \quad \text{Eq 2.5.1.2}$$

$$\hat{H}_{NQR} = \hat{H}_Q + \hat{H}_J + \hat{H}_D + \hat{H}_{RF} \quad \text{Eq 2.5.1.3}$$

The coupling interactions in equation 2.5.1.3 is dominated by the presence of the quadrupolar interaction Hamiltonian and the line broadening observed in the NQR peaks are from the dipolar ($\hat{H}_D$) and J-coupling ($\hat{H}_J$)Hamiltonian terms as they are not dropped from the equation.

The energy level diagram below depicts how the NQR energy levels, in absence of a magnetic field leads to two degenerate energy levels for a spin 3/2 quadrupolar nucleus.

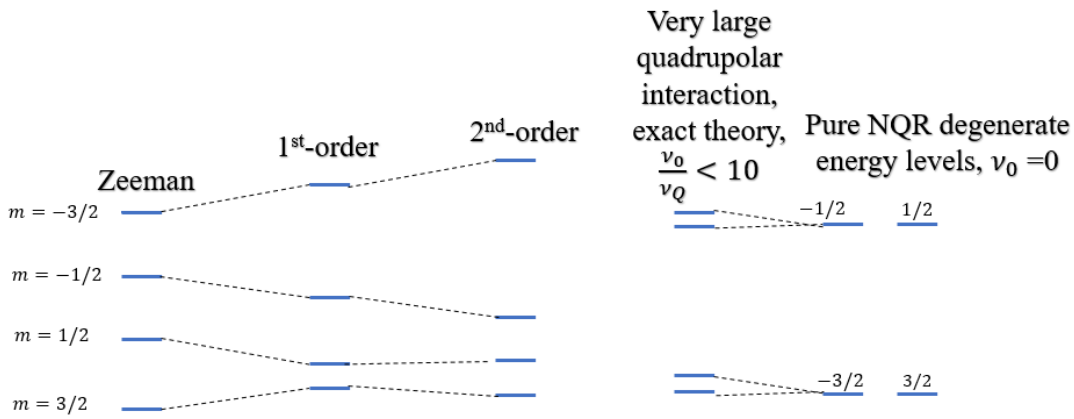

Figure 2.5.1: Energy level diagram of a spin 1/2 nucleus showing the Zeeman splitting with no quadrupolar interaction followed by the first order perturbation($\frac{\boldsymbol{\nu_0}}{\boldsymbol{\nu_Q}} > \mathbf{10}$), second order perturbation ($\frac{\boldsymbol{\nu_0}}{\boldsymbol{\nu_Q}} > \mathbf{10}$), very large quadrupolar interaction ($\frac{\boldsymbol{\nu_0}}{\boldsymbol{\nu_Q}} < \mathbf{10}$) and finally pure NQR where the two degenerate energy states for a spin 3/2 nucleus is depicted in absence of magnetic field, $\boldsymbol{\nu_0}$=0 (not drawn to scale).

For weaker quadrupolar interactions where the ratio of Larmor frequency to quadrupolar frequency is greater than 10 ($\frac{\nu_0}{\nu_Q} > 10$), the first order and second order perturbation terms are applied and are visible in the energy level diagrams for a spin 3/2 nucleus,[20] however, a larger quadrupolar interaction where the Larmor frequency to quadrupolar frequency is less than 10 ($\frac{\nu_0}{\nu_Q} < 10$), the perturbation theory becomes less reliable and a thus demands a higher magnetic field due to broader line shapes. For a spin 3/2 nucleus, the NQR transition observed is from $\pm$1/2 to $\pm$ 3/2 and gives one frequency owing to the 3/2 quadrupole, that is, the transition is a function of the spin quantum number (*I*) of the quadrupole.

For a spin 5/2 nucleus, there would thus be two observed NQR transitions $\pm$1/2 to $\pm$3/2 and $\pm$3/2 to $\pm$5/2. We might also observe overtone transition sometimes that is responsible for transitions from $\pm$1/2 to $\pm$5/2. To enhance the sensitivity of a NQR experiment, higher quadrupolar interaction is a constraint as the difference between the energy levels is proportional to the Boltzmann distribution of the spin population.

The perturbation theory which cannot be reliably applied to cases where quadrupolar interactions are larger, an exact theory is applied to simulate the spectrum, QUEST software developed by our group can treat quadrupolar interactions exactly and help extract NMR and NQR parameters accurately.

2.5.2 Instrumentation to perform NQR experiments

NQR spectrometers are the best options to perform NQR experiments, however, a SSNMR spectrometer could also be used a substitute to perform NQR experiments. The NMR probe could be used to serve as a mediator for the NQR experiments in absence of magnetic field. In most

cases, the NMR probe is placed far away from the magnet and is manipulated in such a way that the RF coil in the probe is optimized to the range of frequency the quadrupolar nucleus would show transitions at. The probe is then connected to a preamplifier via a RF cable of the NMR spectrometer and to the console. The experiments could then be performed depending upon the magnitude of quadrupolar interaction of the observed nucleus.

References

[1] Dirac, Paul A. M. *Principles of quantum mechanics*. Oxford University Press, Oxford, **1982**.

[2] Atkins, P. W. *Molecular Quantum Mechanics Parts I and II: An Introduction to Quantum Chemistry*. Vol. 1. Oxford University Press, Oxford, **1977**.

[3] Heyde, K. L. G. *The Nuclear Shell Model*; Springer Berlin, Heidelberg, **2013**.

[4] Mahajan, A. S.; Rangwala, A. A. *Electricity and Magnetism*. Tata McGraw-Hill, New Delhi, **2012**.

[5] Zeeman, P. *Phil. Mag*. **1897**, 44, 55-60.

[6] Levitt, M. H. *Spin Dynamics, second edition*. John Wiley & Sons. Chichester, **2009**.

[7] Hore, P. J.; Jones, J. A.; Wimperis, S. *NMR: The Toolkit How Pulse Sequences Work, second edition.* Oxford university Press, Oxford, **2014**.

[8] Keeler, J. *Understanding NMR Spectroscopy*. John Wiley & Sons, Chichester, **200**5.

[9] Bloch, F. *Phys. Rev*. **1946**, 70, 460-474.

[10] Ramsey, N. F. *Phys. Rev*. **1950**, 78, 699-703.

[11] Ernst, R. R.; Anderson, W. A. *Rev. Sci. Instrum*. **1966**, 69, 37-38.

[12] Ramsey, N. F. *Phys. Rev*. **1953**, 91, 303-307.

[13] Herzfeld, J.; Berger, A. E. *J. Chem. Phys*. **1980**, 73, 6021-6030.

[14] Man, P. P.; Harris, R. K.; Wasylishen, R. E. *Quadrupolar Interactions In Encyclopedia of Nuclear Magnetic Resonance*. John Wiley & Sons, Chichester, **201**1.

[15] Pines, A.; Gibby, M. G.; Waugh, J. S. *J. Chem. Phys*. **1972**, 56, 1776-1777.

[16] Hartmann, S. R.; Hahn, E. L. *Phys. Rev*. **1962**, 128, 2042-2053.

[17] O'Dell, L. A.; Schurko, R. W. *Chem. Phys. Lett*. **2008**, 464, 97-102.

[18] O'Dell, L. A. *Solid State Nucl. Magn. Reson*. **2013**, 55-56, 28-41.

[19] Szell, P. M. J.; Bryce, D. L. *Annu. Rep. Nucl. Magn. Reson. Spectrosc*. **2020**, 100, 97-152.

[20] Seliger, J. *"Nuclear Quadrupole Resonance, theory" in Encyclopedia of Spectroscopy and Spectrometry, Third Edition*. Elsevier, **2017**, 447-455.

[21] Stark, J. *Ann. Phys*. **1914**, 43, 965-983.

[22] Hamilton, W. R. *On a general method of expressing the paths of light, & of the planets, by the coefficients of a characteristic function.* Hardy, P. D. Dublin, **1833**.

Chapter 3. X-ray diffraction methods

3.1 Theory of X-ray diffraction technique

X-rays, the electromagnetic waves that originate in the frequency region 3×10^{16} to 3×10^{19} Hz of the electromagnetic spectrum, are widely used in fields of medical science and material sciences. Identification of chemical elements, structures of compounds find real importance under the application of X-rays. X-ray diffraction technique is a powerful analytical tool to study composition and structure of a chemical element or a crystalline structure. It depends on the size of the crystal structure (too small or macromolecules) to determine the phase purity,[1] atomic connectivity, and crystallinity in the crystal structure.[2] The process is regulated by passing X-ray beams of comparable wavelength between the spacing of the atoms. The intensities of the peaks are directly proportional to the number of crystals or molecules present within the spacing of the atoms. The size of a crystal is inversely related to the peak widths. Amorphous nature or crystalline nature can be depicted with broadness of a peak, higher broadness of peaks refers to an amorphous nature of the compound or simply a smaller crystal structure and/or presence of crystalline defects in the compound.

X-rays are produced using CRT (cathode ray tubes) that generates the series of electrons in a strong electric field hitting the metallic surface, generally copper or molybdenum. The electrons hitting the metallic surface emits Bremsstrahlung X-rays, a series of broad wavelengths. The diffraction of the X-rays when incident from a metal atom electron, typically from the inner shells lead to K_α and K_β radiation.[3]

William H. Bragg and William L. Bragg were the scientists to win a Nobel in 1915[13] for the early advancements in X-ray diffraction. The Bragg's law of diffraction[4] describes the phenomenon of diffraction of a plane wave by a family of lattice planes:[5]

$$n\lambda = 2d \sin\theta$$

Where d is the lattice spacing, θ, the angle between the diffracted X-ray and scattering lattice plane, n is the integer of scattering lattice planes and λ is the wavelength of the incident X-ray. The Figure below describes the working principle of X-ray diffraction as per Bragg's law of diffraction.

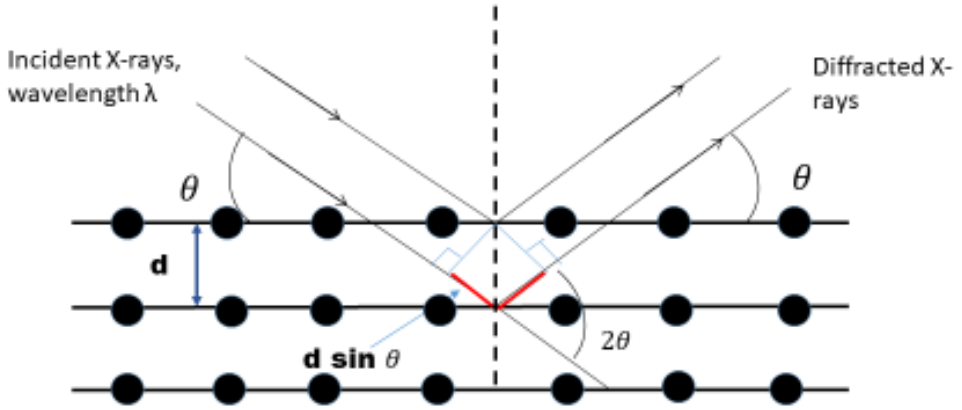

Figure 3.1.1: X-ray diffraction principle as described by Bragg's law of diffraction.

3.2 Crystals and crystallographic conventions

In X-ray crystallography, we can define the symmetry and class in which various crystals are classified into. A crystal is an ordered solid and a repeating subunit of the ordered lattice is

defined as the unit cell. A crystal is usually classified into a crystal system based on their point group geometry, the Bravais lattice system and crystal families. Space groups are used to study the symmetry of a crystal system according to their point groups and as lattice systems in Bravais lattice systems.[6] There are 7 crystal systems known so far, namely, triclinic, monoclinic, orthorhombic, tetragonal, trigonal, hexagonal, and cubic. Bravais lattices are 14 in number with a group of lattices consisting same set of lattice point groups.

A crystal family comprises of lattices and point groups which are related to space groups of a crystal system combined with a common lattice system, for example, the trigonal and hexagonal crystal systems are a part of same crystal family. Conventional coordinate systems and cells are usually described using space groups following the crystal coordinate system that includes crystallographic basis. The uniqueness of the crystal coordinate system basis or basis vector is ambiguous; however, right-handed set of basis vectors is considered for best understanding of space groups. Cell parameters a, b and c are edge-lengths of the unit cell of the lattice, whereas the angular denotation is given by α, β and γ.

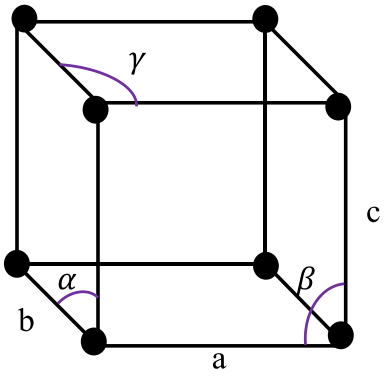

a=b=c, $\alpha = \beta = \gamma = 90°$

Figure 3.2.1: Schematic of a cubic unit cell showing the cell edges and cell angles.

The unit cell convention of cell-length follows a<b<c in Angstrom unit. The angles determine the shape of the unit cell. α, β and γ in (°) are angles between cell-lengths b and c, a and c, a and b respectively. For a cell, the volume, the effective formula unit Z are important parameters in describing a unit cell relative to each crystal system.

Table 3.2.1 denotes the breakdown of connection between crystal systems, lattice systems and crystal families:

Table 3.2.1: Relation between crystal families, lattice systems and crystal system

Crystal family	symbol	Point groups	Number of space groups	Bravais lattices	Conventional coordinate system		Crystal system
					Restriction on cell parameters	Parameters to be determined	
One dimension -	-	1, *m*	2	/’	none	*a*	-

Two dimensions Oblique (monoclinic)	*m*	1, 2	2	*mp*	none	*a, b,* γ^*	oblique
Rectangular (orthorhombic)	*o*	*m*, 2*mm*	7	*op* *oc*	$\gamma = 90°$	*a, b*	rectangular
Square (tetragonal)	*t*	4, 4*mm*	3	*tp*	a=b $\gamma = 90°$	*a*	square
Hexagonal	*h*	3, 6 3*m*, 6*mm*	5	*hp*	a=b $\gamma = 120°$	*a*	hexagonal
Three dimensions Triclinic (anorthic)	*a*	1, $\bar{1}$	2	*aP*	none	*a, b, c* α, β, γ	triclinic
Monoclinic	*m*	2, *m*, 2/*m*	13	*mP* *mS (mA, mB, mI)* *mP* *mS (mA, mB, mI)*	b-unique, $\alpha = \gamma = 90°$ c-unique, $\alpha = \beta = 90°$	*a, b ,c* β^* *a, b, c* γ^*	monoclinic
Orthorhombic	*o*	222, *mm*2, *mmm*	59	*oP* *oS (oC, oA, oB)* *oI* *oF*	$\alpha = \beta = \gamma = 90°$	*a, b, c*	orthorhombic
Tetragonal	*t*	4, $\bar{4}$, 4/*m* 422, 4*mm*, $\bar{4}$2*m*, 4/*mmm*	68	*tP* *tI*	a=b $\alpha = \beta = \gamma = 90°$	*a, c*	tetragonal

Hexagonal	*h*	3, $\bar{3}$ 32, 3*m*, $\bar{3}m$	18	*hP*	a=b $\alpha = \beta = 90°$ $\gamma = 120°$ (hexagonal axis)	*a, c*	trigonal
			7	*hR*	a=b $\alpha = \beta = \gamma$	*a, α*	
		6, $\bar{6}$, *6/m* *622, 6mm, 62m, 6/mmm*	27	*hP*	a=b $\alpha = \beta = 90°$ $\gamma = 120°$	*a, c*	
Cubic	*c*	23, $m\bar{3}$ 432, $\bar{4}3m$, $m\bar{3}m$	36	*cP* *cI* *cF*	a=b=c $\alpha = \beta = \gamma = 90$	*a*	cubic

*Denotes angles that are conventionally considered non-acute. The symbols encapsulated in dashed box represent Laue groups and complete box represent Laue groups and contains lattice point symmetries.

The Bravais lattice convention were taken from IUCr in 1985. This table of crystal family classification is taken from International tables of crystallography-1996.

3.2.1 Single-crystal X-ray diffraction

Single-crystal X-ray diffraction (SCXRD) is a useful analytical X-ray spectroscopic technique to detect the crystal structure of an engineered crystal studied using diffraction spots obtained from the instrumental analysis which is responsible for a crystal structure solving efficiency (whether it is a well-diffracting) crystal. The single crystal is very carefully chosen using a microscope and mounted on the goniometer and centered between the X-ray source and the detector, depending on the stability of the crystal, a cooling system might or might not be used.

The diffraction of the crystal as a result of the incident X-rays results in spots (bright or light, depending on the crystal quality) by the detector that determines the cell angles and length of the unit cell primarily and then runs are collected in reflections to decipher the entire crystal structure.

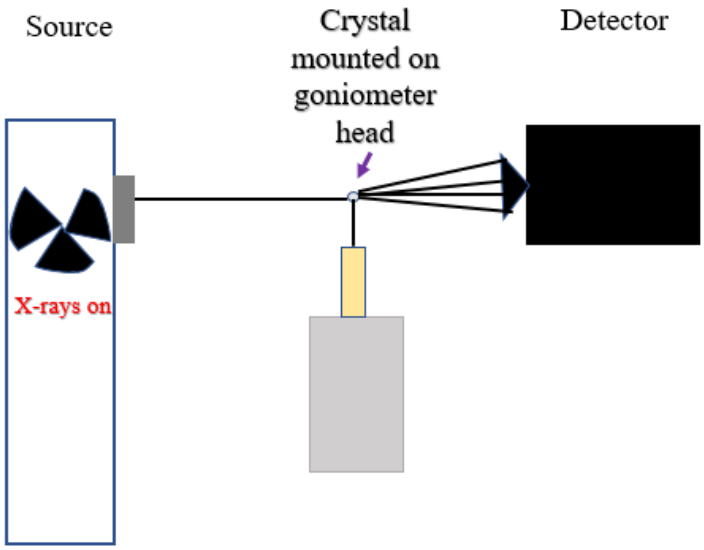

Figure 3.2.2: Simplified representation of working of a powder X-ray diffractometer where the source emits X-rays to the crystal mounted on top of goniometer head and the diffracting rays are collected by the detector as the form of spots/reflections.

Several methods used in solving crystal structures are Patterson method,[7] direct method, and advanced direct method.[8] A crystal structure refinement is very important after each step of simulation while trying to solve a crystal structure, addressing the R-factor, wR2, Goof value and other constraints owing to Q-peaks. Final structure refinement after the thermal ellipsoid plot[10,11] of the crystal structure results in a cif file which might or might not have defects in the crystal

structure solution that shows up in the process of solution and an incident X-ray absorption correction is implied to confirm the final structure to double-check the presence of any disorder or defects in the crystal structure. Software used in solving single-crystal structures have been developed over the years and don't rely on older techniques of benchtop detection which were tedious and time-consuming.

3.2.2 Powder X-ray diffraction

PXRD or powder X-ray diffraction technique is another analytical tool to identify a crystal sample to measure and determine the phase purity of the sample. This diffraction technique differs from SCXRD where it uses all the crystallite's orientation rather than a definite orientation of the single crystal due to the result of grinding the single crystal into a fine powder using a mortar-pestle to record the peak measurement or the resulting diffractogram. The parameters that are extracted from the powder X-ray technique are the unit-cell parameters and the position of the peaks or new peaks determine presence of impurity, asymmetry, new probable polymorphs, crystalline or amorphous nature and/or the relative intensity of the peak tells us about the diffraction quality of the ground powder crystal sample. The fine powdered sample is usually mount on a sample holder slit levelled well to the surface of the holder to avoid interference that may cause weird, diffracted patterns in the diffractogram. Once mounted in the sample arena, it is usually encapsulated by a chamber of incident X-ray source and a detector where using the Bragg-Brenatano[9] geometry the angle 2θ, relative to the intensity of the peaks observed is varied as an unison of angles from the crystallites with respect to the single wavelength of the incident X-rays

after being filtered through a monochromator to ensure the single wavelength and then the beam of X-rays are aligned in a specific direction due to the collimator which then hits the sample and then the diffracted X-ray is measured as the peak read by the detector which is usually measure in counts per second.

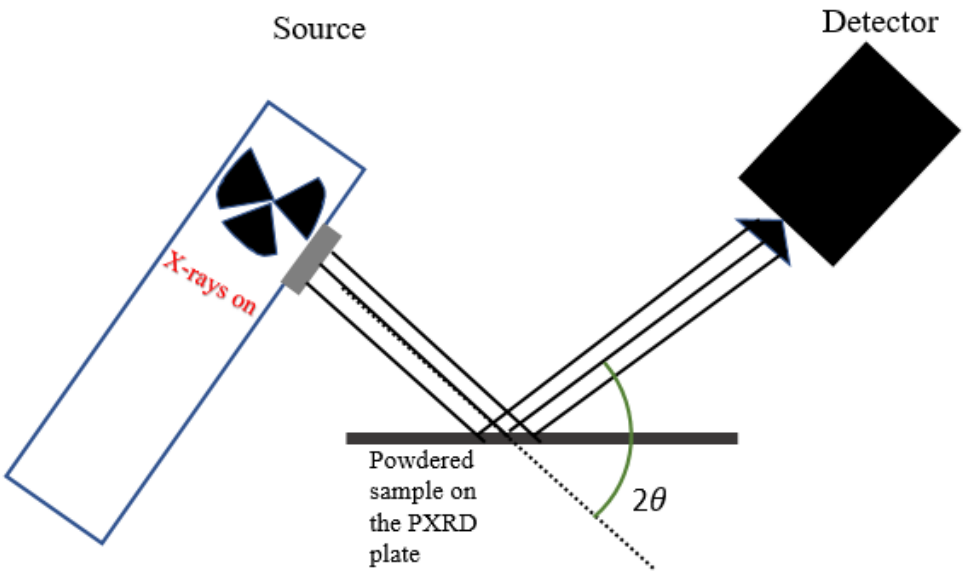

Figure 3.2.3: Simplified representation of working of a powder X-ray diffractometer where the source emits X-rays to the powdered sample placed on the PXRD slit and the diffracting rays are collected by the detector at an angle $2\boldsymbol{\theta}$ following the Bragg's law.

The diameter of the slit used in the sample is to be mentioned accurately for a precise detection of peaks that result in the diffractogram. To ensure the analytical accuracy of a crystal structure, a powder pattern is compared to the simulated powder pattern obtained after solving the single-crystal structure[12] to verify its correctness and accuracy. Minor deviations can be attributed to different orientations of the crystallites upon grinding from the single-crystal phase which restores a single orientation form while solving the single-crystal structure.

References

[1] Mulay, R. P.; Wollmershauser, J. A.; Heisel M. A.; Bei, H.; Russell, A. M.; Agnew, S. R. *Acta Mater*. **2010**, 58, 2788–2796.

[2] Cullity, B. D. *Elements of X-ray diffraction, 2nd ed*. Addison-Wesley, Reading, Mass, **1978**.

[3] Barkla, C. G. *Philos. Mag*. **1911**, 22, 396-412.

[4] Bragg, W. H. *Nature*. **1912**, 90, 219.

[5] Bragg, W. H.; Bragg, W. L. *Proc. Royal Soc. A*. **1913**, 428-438.

[6] Hahn, T. *International Tables for Crystallography, Volume A: Space Group Symmetry, 5th ed*. Springer, Drodrecht, **2005**.

[7] Patterson, A. L. Z. *Kristallogr. Cryst. Mater*. **1935**, 90, 517-542.

[8] Hauptman, H. *Science*. **1986**, 233, 178-183.

[9] Cruz-Cabeza, A. J.; Bernstein, J. *Chem. Rev*. **2014**, 114, 2170-2191.

[10] North, A. C. T; Philips, D. C. *Acta Cryst*. **1968**, A24, 351-359.

[11] Blessing, R. H. *Acta Cryst*. **1995**, A51, 33-38.

[12] Sheldrick, G. M. *TWINABS, Version 2012/1*. Georg-August-Universitat, Gottingen, Germany, **2012**.

[13] "The Nobel Prize in Physics 1915". Accessed January 31st, 2024. From: https://www.nobelprize.org/prizes/physics/1915/summary/.

[14] Aitipamula, S.; Banerjee, R. et al. *Cryst. Growth. Des*. **2012**, 12, 2147-2152.

Chapter 4. Theoretical and computational chemistry

This dissertation includes a detailed work on computation of NMR parameters to compare the relevance of experimental findings and to understand the fundamental NMR interactions studied and explored in the following Chapters.

4.1 Introduction

Quantum chemical computations with underlying theory are beneficial in understanding physical quantities and observables of molecules such as their equilibrium geometries, bonding interactions, and reaction energies, which are almost obtained accurately being a backbone of experimental findings and provides insight to understanding of structural and physical chemistry to carry forward a feasible experimental finding. Approximations are a must while computing chemical observables as it can be mathematically challenging due to equations arising from quantum chemistry that govern the molecular structure and properties which are impossible to solve analytically. There is always a compromise in choosing the correct set of approximations[1] while trying to compute the observables as a severe set of approximations might lead to less accurate calculation results and less severe approximations might give results that are more accurate. To be precise, there is no ideal set of approximations for a particular calculation method but to choose the set of approximation that is a balance between approximation and cost should be of priority.

The significant factor to be considered while computing the observables is to attain "self-consistency field" convergence[2] regardless of what method of calculation is chosen. Given below is a flow-chart which highlights the advancement of computational chemistry including methods developed to maintain a balance between accuracy and cost of the quantum chemical models/methods to obtain the computed results.

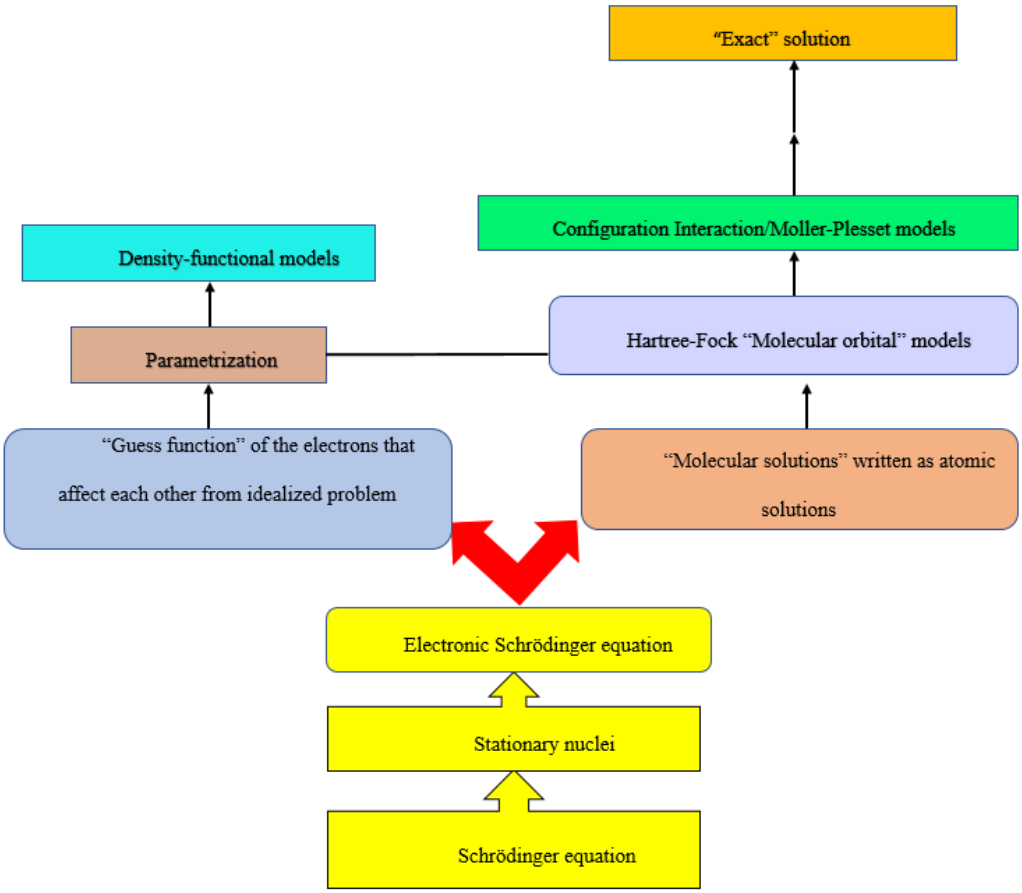

Figure 4.1.1: Flowchart of computing using different methods and levels of calculation

The Schrödinger equation ($\hat{H}\Psi = E\Psi$)[5] can be solved exactly only for one atom or molecules having one electron, thus, it becomes necessary to implement numerical methods to

calculate approximate wave functions and values such as energy, bond parameters, and dipole moments. Ab initio methods[29] such as Hartree-Fock (HF) method, post Hartree-Fock (PHF) are based on Schrödinger equation gives good agreement with experiments in calculating bond angles, lengths but are inadequate in solving many other observables. The SCF convergence is mostly far from the limit (scaling factor- N^4, where N is the system size and not number of basis functions used) thus methods where electron-correlation could be included in a realistic manner are used. Basis sets, or basis functions are used to represent the electronic wave function to turn partial differential equations of the method used into algebraic forms suitable for calculations on computer, they can either be composed of atomic orbitals yielding linear combination of atomic orbitals (LCAO) that is a usual preference in the quantum chemical field or plane waves. A judicious choice of basis-set is required to get accurate calculation results (Gaussian-type orbitals (GTO), Slater-type orbitals (STO) or numerical orbitals[28] can be used to form the basis-sets). Density Functional theory (DFT) on the other hand, expresses the energy of a molecular system as functional of the total electron density. A functional is defined as function of functions and the total electron density is a function of the nuclear coordinates. The molecular orbital which is a LCAO can be described as:

$$\Psi(\vec{r})^{MO} = \sum_{i=1}^{K} \chi_i(\vec{r}) C_i \quad \text{Eq 4.1.1}$$

Where, C_i is the mixing coefficient (variational parameter), χ_i is the atomic orbital. The number and nature of the wave functions that MO can be expanded form basis-sets. The more the variational parameters, the more the basis-sets and more accurately the wave function can be represented.

4.2 Computing NMR parameters

NMR parameters such as magnetic shielding tensors, spin-spin coupling tensors and electric field gradient tensors are useful probes for the local electronic structure and geometry of a compound.[25,26,27]

The consideration of relativistic corrections[3] while computing the NMR parameters becomes inevitable while dealing with heavy nuclei so that a reasonable agreement between experiment and theory is retained. The relativistic theory of shielding and spin-spin coupling constants are bound by relativistic many-electron atomic and molecular computations that use the four-component 'no-pair' Dirac-Coulomb-Breit (DCB) Hamiltonian[4] and some approximation of it rather than the nonrelativistic Schrödinger equation:[5]

$$\widehat{H}_{DCB} = \hat{P}^{+}\left[\sum_{i=1}^{N}(c\,\boldsymbol{\alpha}_i\hat{\boldsymbol{p}}_i + \beta_i c^2) + V_{Ni} + V_{ee} + \sum_{j>i=1}^{N}\widehat{H_{ij}^{B}} + V_{Nuc}\right]\hat{P}^{+} \quad \text{Eq 4.2.1}$$

Where, $\widehat{H}_{DCB}$ is the Dirac-Coulomb-Breit Hamiltonian, and α and β are 4×4 matrices introduced by Dirac to get the relativistic wave equation for spin ½ nuclei from 'classical' relativistic Hamiltonian functions.[6] The $\widehat{H_{ij}^{B}}$, is the Breit interaction[7] which contains the magnetic interaction and is a relativistic correction term to the electron-electron Coulomb repulsion potential term (V_{ee}) to account the non-instantaneous transmission of electron-electron interaction, which is bound by a finite speed. V_{Ni} is the electron-nucleus attraction potential term for each electron. The term that differentiates a nonrelativistic Hamiltonian from the four-component DCB Hamiltonian lies in the fact that the electron's rest mass energy is considered when there is a relativistic increase in electron's mass due to high velocity depicted by terms, $c\boldsymbol{\alpha}\hat{\boldsymbol{p}}+\beta c^2$, the kinetic energy operator for

an electron. The DCB Hamiltonian also is responsible for the spin-orbit coupling. $\hat{P}^{+}$ is the projection operator that solves some of the problems in Dirac-Coulomb operator by limiting the solutions to only positive energy spectrum of the desired electronic states given by "no-pair" approximation. The terms c and $\widehat{\boldsymbol{p}}$ are speed of light in terms of relativistic theory that is an expansion parameter of value almost equal to 137.036 in atomic units and the momentum operator.

Various attempts[8] have been made to simplify the 4×4 matrices that result in four component vector into two component vector to reduce computational effort. There is one approximation that has been found to be effective in computing NMR parameters, namely the ZORA (zeroth order regular approximation) method that serves an alternative to the Pauli Hamiltonian, the ZORA Hamiltonian,[10] which serves the two-component purpose and is given as:

$$\widehat{H}_{ZORA} = V + \frac{1}{2}\,(\hat{\boldsymbol{p}}\kappa\hat{\boldsymbol{p}}) + \frac{1}{2}\sigma_s[(\hat{\boldsymbol{p}}\kappa) \times \hat{\boldsymbol{p}}\,] \qquad \text{Eq 4.2.2}$$

Where, $\kappa = \frac{2c^2}{(2c^2 - V)}$, V is the potential energy term.

The ZORA and DK[9] method is popularly used to compute NMR parameters. The DK (Douglas-Kroll) method is another alternative to the Dirac Hamiltonian and uses a two component form. The DK method serves better in terms of gauge invariance,[11] which is a drawback of the ZORA method; however, both methods yield comparable results as per literature.

Computational methods to extract NMR parameters include ab initio methods or density functional theory (DFT). Hartree-Fock (HF) computations,[12] is still one of the common methods to compute NMR parameters of heavy atoms as found in the works of Visscher and coworkers.[13] DFT calculations are found to be the most successful in computing NMR parameters of heavy atoms.[14,15] It has been observed that relativistic NMR computations take into account the electron

density, spin density and the current density define one-electron magnetic contributions to shielding and reduced spin-spin coupling tensors obtained exactly from Kohn-Sham DFT.[16] The functionals, generalized gradient approximation (GGA),[17] local-density approximation (LDA) can be used to obtain reasonable results.[18] Spin-orbit coupling may or may not be included in obtaining relativistic methods while performing DFT NMR computations, use of scalar relativistic, ZORA Hamiltonian[23] have been mostly used and attained better outcome in computing the NMR parameters. Keeping all the computing tactics in mind, calculation models were generated using atomic coordinates from the X-ray crystal structures or created using Gaussview.[23] In this thesis, atomic coordinates were extracted from the X-ray structures and DFT calculations were carried out in Amsterdam Modelling Suite (earlier, Amsterdam Density Functional) AMS package[22] to extract the shielding tensors, J-coupling tensors and EFG tensors. The NLMO analysis[24] can decompose the orbital contribution into NMR observables that represents the core, lone-pair, and bonding orbitals. They provide a great understanding of the origins of NMR interactions and the electronic structure of molecules. NLMO shielding and spin-spin couplings were computed in AMS package[22] to retain the reasonable results of the cluster models (relativistic scalar or spin-orbit).

To include long-range effects in accurate calculations of NMR parameters, cluster models will not be always simulated but infinite crystals would be. The translational symmetry present in the unit cell that is subject to periodic boundary conditions are also incorporated certain computations which helps generate input files. Plane-wave basis-functions are used instead of atom-centered basis functions to provide the gauge-including projector augmented wave (GIPAW) approach to extract the NMR parameters.[19,20] GIPAW method considers the fact that core electrons

do not participate in the chemical bonding and stay unchanged which is very essential for heavy atoms since the core electron's oscillations with high kinetic energy requires a lot of plane-waves and is generally costly. GIPAW method is a frozen core approximation,[33] which assumes a smooth potential replaces the wave functions of core electrons and valence electrons close to the nucleus. This is termed as pseudopotential and generally, it is kept "on-the-fly" while computing NMR parameters. Two most important parameters to be optimized are the k-points and cut-off energy of the plane waves. The k-points are spaced points used in the primitive unit cell in the reciprocal unit and are to be carefully chosen so that the cut-off energy converges. The cut-off energies are nothing but the truncation of plane waves of the basis-sets. The maximum cut-off energy at which convergence of SCF is attained is chosen and all of the GIPAW calculations were carried out in CASTEP using Materials Studio.[20,21]

References

[1] Engel, T. *Quantum Chemistry & Spectroscopy*. Pearson Education, Inc., publishing as Benjamin Cummings, San Francisco, USA, **2006**.

[2] Slater, J. C. *Phys. Rev*. **1928**, 32, 339-348.

[3] Pyykkö, P. *Chem. Rev*. **1988**, 88, 563-594.

[4] Hess, B. A. '*Encyclopedia of Computational Chemistry,' Schleyer, P. v. R ed*. John Wiley & Sons, Chichester, **1998**, 2499-2508.

[5] Schrödinger, E. *Phys. Rev*. **1926**, 28, 1049-1070.

[6] Okada, S.; Shinada, M.; Matsuoka, O. *J. Chem. Phys*. **1990**, 93, 5013-5019.

[7] Moss, R. E. *Advanced Molecular Quantum Mechanics*. Chapman and Hall, London, **1973**.

[8] Autschbach, J.; Schwarz, W. H. E. *Theor. Chem. Acc*. **2000**, 104, 82-88.

[9] van Lenthe, E.; Baerends, E. J.; Snijders, J. G. *J. Chem. Phys*. **1993**, 99, 4597-4610.

[10] Kutzelnigg, W. *J. Comput. Chem*. **1999**, 20, 1199-1219.

[11] Weinberg, S. *The Quantum Theory of Fields: Volume 1, Foundations*. Cambridge University Press, Cambridge, **2005**.

[12] Crammer, C. J. *Essentials of Computational Chemistry: Theory and Models, 2nd ed*. John Wiley & Sons, Hoboken, NJ, **2004**.

[13] Visscher, L.; Enevoldsen, T. Saue, T.; Jensen, J. A.; Oddershede, J. *J. Comput. Chem*. **1999**, 20, 1262-1273.

[14] Enevoldsen, T.; Visscher, L.; Saue, T.; Jensen, J. A.; Oddershede, J. *J. Chem. Phys*. **2000**, 112, 3493-3498.

[15] Nakatsuji, H.; Takashima, H. Hada, M. *Chem. Phys. Lett*. **1995**, 233, 95-101.

[16] Kohn, W.; Sham, L. *J. Phys. Rev*. **1965**, 140, A1133-A1138 ; Hohenberg, P.; Kohn, W. *Phys. Rev. B.* **1964**, 136, B864-B871.

[17] Vosko, S. H.; Wilk, L; Nusair, M. *Can. J. Phys*. **1980**, 58, 1200-1211.

[18] Perdew, J. P.; Burke, K.; Ernzerhof, M. *Phys. Rev. Lett*. **1996**, 77, 3865-3868.

[19] Pickard, C. J.; Mauri, F. *Phys. Rev. B.* **2001**, 63, 1-13.

[20] Yates, J. R; Pickard, C. J.; Mauri, F. *Phys. Rev. B.* **200**1, 76, 1-11.

[21] Clark, S. J.; Segall, M. D.; Pickard, C. J.; Hasnip, P. J.; Probert, M. I. J.; Refson, K.; Payne, M. C. *Kristallogr-Cryst. Mater*. **2005**, 220, 567-570.

[22] ADF 2019.305 (AMS Package), SCM, Theoretical Chemistry, Vrije Universiteit, Amsterdam, The Netherlands.

[23] Frisch, M. J. et al. Gaussian. Gaussian, Inc., Wallingford CT, 2016.

[24] Autschbach, J.; Zheng, S.; Schurko, R. W. *Concepts Magn. Reson. Part A.* **2010**, 36, 84–126.

[25] Schreckenbach, G.; Ziegler, T. *Theor. Chem. Acc*. **1998**, 99, 71−82.

[26] Bonhomme, C.; Gervais, C.; Babonneau, F.; Coelho, C.; Pourpoint, F.; Azaïs, T.; Ashbrook, S. A.; Griffin, J. M.; Yates, J. R.; Mauri, F.; Pickard, C. J. *Chem. Rev.* **2012**, 112, 5733– 5779.

[27] Casabianca, L. B. *Magn. Reson. Chem.* **2020**, 58, 611−624.

[28] Lehtola, S. *Int. J Quantum Chem*. **2019**, 113, 1-31.

[29] Levine, I. N. *Quantum Chemistry*. Englewood Cliffs, New Jersey: Prentice Hall, **1991**

Part 2: SSNMR as a probe of the ChB donor and acceptor

Chapter 5. Crystal engineering, novel cocrystals and solid-state NMR of chalcogen bonds

5.1 Introduction

This Chapter of the dissertation includes engineering of novel chalcogen-bonded cocrystals and their characterization using solid-state NMR. Crystal engineering is one of the very many applications of noncovalent interactions, in this case, chalcogen bonding interactions in understanding bonding, local geometry, feasibility, and stability of a chalcogen bond with the aid of solid-state NMR. The solid-state NMR parameters including principal chemical shift tensors, isotropic chemical shift, and span to see the deviation of the magnitude of the parameters upon chalcogen bond formation to judge its strength, interaction stability and local bonding geometry. Several works regarding chalcogen bonded interactions in fields of theoretical chemistry, materials chemistry, organic chemistry have been reported to find the most suitable chalcogen atom to form stronger chalcogen bonds in terms of directionality and versatility of being a good precursor. In crystal engineering, literature studies show the order of reported noncovalent interactions reported so far are:

XB>ChB>PnB>TB>MB, where XB is halogen bonds, ChB, chalcogen bonds, PnB, pnictogen bonds, TB, tetrel bonds and MB, matere bonds. In the following Chapters, the research article featuring ways to engineer novel chalcogen-bonded cocrystals using different techniques

and their X-ray diffraction characterization succeed by final analysis using solid-state NMR is conducted.

5.2 Crystal engineering and chalcogen bonds

Crystal engineering, a distinct subject of study, involves the rational design of molecular solids from neutral or ionic functional solid-state structures with intermolecular interactions as the basic connection to build the crystals. Supramolecular synthons, that is interactions like hydrogen bonds, coordination bonds, XB, ChB, PnB, TB, MB are a part of crystal engineering strategies and find a major interest in developing crystal and structures of importance to structural and solid-state chemists. To be precise, crystal engineering is applicable to wide range of intermolecular assemblies. A crystal can be viewed as a supramolecular entity as per Lehn's argument (Lehn, 1988). Rosenfield described that the importance of intermolecular interactions is as valid a phenomenon to build crystal viewed as "a supermolecule" as to a molecule formed by covalent interactions (Rosenfield et al., 1977). The revealing aspects such as how the crystals form, their reaction mechanisms, their applications, and usefulness in various fields of chemistry was first described by (Whitesides et al., 1995) highlighting how supramolecular synthesis is different from covalent synthesis. Thermodynamic and kinetic stability play a vital role in differentiating both bonding interactions. Crystals, which were defined to be a result of balance between enthalpy and entropy, in the late 1995 it was found that they are kinetically controlled as well. The core structure owing to the crystal structures resulting from solutions are much alike to covalently formed compounds, except for a much difference in their bond energies of formation, are kinetically

controlled. Fyfe and Stoddart (Fyfe and Stoddart, 1997) give an explicit description in their work in 1997, highlighting the supramolecular synthesis of crystals in solution and the process of crystallization.

The idea of this work ahead was to follow the principal steps of crystallization techniques and to engineer reproducible cocrystals that would confirm a moderately ventured noncovalent interaction, the chalcogen bond in the solid-state. Crystals, a rather complex structural moiety than a molecule and how their unit cell and lattice orientations are affected upon the introduction of chalcogen bonds have been studied using solid-state NMR of the chalcogen atom under consideration.

Chalcogen bonds, conventionally known as the intermolecular interactions seen commonly in group 16 elements possess σ −hole sites, the electron deficient region which then interacts with a region of higher electron density resulting in a chalcogen bond is an interest observed since the introduction of XB interactions and as to how it is an analogous to hydrogen and XB interactions. Crystals highlighting such interactions are known as ChB cocrystals and are studied for its properties such as unique structure and bonding, polymorphism, catalytic utilities and much more. Typically, a ChB cocrystal is devised using crystallization techniques such as slow evaporation, mechanochemistry, vapour diffusion and cosublimation. To address a potential ChB donor and a ChB acceptor, it is essential to identify the possible σ −hole region and an electron rich donor to interact with the σ −hole region. In this Chapter, two well-known organometallic heterocycles, telluradiazole and selenodiazole are used as a potential ChB donor. For ChB acceptors, a variety of organic and inorganic compounds were tested and used with electron-rich sites/atoms. The following work describes three cocrystal systems highlighting telluradiazole and selenodiazole as

ChB donors and the ChB acceptors chosen were hydroquinone, tetraphenylphosphonium chloride and tetraethylphosphonium chloride. Single-crystal X-ray diffraction studies showed the ChB interaction between Se/Te with oxygen and chlorine atoms of the respective ChB acceptors, the bond parameters agreed with that of a ChB bond and potential interaction of the acceptor atoms with the chalcogen atom. Powder X-ray diffraction showed the phase purity of the samples and the stability of the cocrystals at room temperature. After the X-ray diffraction methods, solid-state NMR was implied to study the effects on the ChB bonds and effect on the chalcogen atoms in terms of anisotropy and other NMR interactions like indirect spin-spin coupling, dipolar coupling and quadrupolar interaction prevalent in the solid-state.

When it comes to classifying cocrystals, it might be ambiguous as to what it could be defined as, due to the reason that it has overlapping definitions with salts and polymorphs and how it could be distinguished from the other two. FDA defined cocrystals as “solids that are crystalline materials and made of two or more molecules in the same lattice.” FDA also defined salts as “any of numerous compounds that result from replacement of part or all of the acid hydrogen of an acid by a metal or a radical acting like a metal; an ionic or electrovalent crystalline solid.” Polymorphs on the other hand was defined as “Different crystalline forms of the same substance. This may include solvation or hydration products (also known as pseudopolymorphs) and amorphous forms” by the FDA. (Aitipamula et al, 2012) revealed that the classification of cocrystal as per FDA’s definition is of debate owing to the mutual exclusiveness of salts, polymorphs and cocrystals as they could be grouped together in terms of APIs. When it comes to synthesizing ChB cocrystals, which are the compounds of interest in this dissertation, it included different methods to grow the cocrystals. Slow evaporation method, which involves the mixing of the ChB donor and acceptor

in the desired molar ratio in a suitable solvent and then let the solvent evaporate slowly, was one of the most effective techniques in retrieving and reproducing the ChB cocrystals in this thesis. Vapour diffusion technique and mechanochemistry were also carried out to grow the cocrystals.

Statement of Authenticity and permissions for part 5.3: I declare that the coauthors have permitted me to include this article in my thesis and permissions from the journal *Acta. Cryst. C* was obtained to reproduce the entire research paper. I certify this work was prepared by me with the guidance, support and contributions from my supervisor, Dr. David L. Bryce and I would like to express my heartfelt gratitude to Dr. Jeffrey S. Ovens in helping me with the single-crystal X-ray structure solving techniques and submission of the novel crystal structures to the CCDC database.

5.3 ^{77}Se and ^{125}Te Solid-State NMR and X-Ray Diffraction Structural Study of Chalcogen-Bonded 3,4-Dicyano-1,2,5-Chalcogenodiazole Cocrystals

Tamali Nag[a], Jeffrey S. Ovens[a] and David L. Bryce[a]*

[a]Chemistry and Biomolecular Sciences, University of Ottawa, 10 Marie Curie Private, Ottawa, Ontario, K1N6N5, Canada

Correspondence email: dbryce@uottawa.ca

Funding information Natural Sciences and Engineering Research Council of Canada.

Synopsis Three new chalcogen-bonded cocrystals are synthesized and characterized by single-crystal X-ray diffraction, powder X-ray diffraction, and ^{77}Se/^{125}Te magic-angle spinning NMR spectroscopy.

Abstract Three novel chalcogen-bonded cocrystals featuring 3,4-dicyano-1,2,5-selenodiazole or 3,4-dicyano-1,2,5-tellurodiazole as chalcogen bond donors and hydroquinone, tetraphenylphosphonium chloride or tetraethylphosphonium chloride as chalcogen bond acceptors are prepared and characterized by single-crystal X-ray diffraction (XRD), powder X-ray diffraction, and ^{77}Se/^{125}Te magic-angle spinning solid-state NMR spectroscopy. The single-crystal XRD results show that the chalcogenodiazole molecules interact with the electron donors through two σ-holes on each of the chalcogen atoms which results in highly directional and moderately strong chalcogen bonds. Powder XRD confirms that the crystalline phases are preserved upon moderate grinding of the samples for solid-state NMR experiments. Measurement of ^{77}Se and

^{125}Te chemical shift tensors via magic-angle spinning solid-state NMR spectroscopy confirms the number of magnetically unique chalcogen sites in each asymmetric unit and reveals the impact of chalcogen bond formation on the local electronic structure. These NMR data are further assessed in the context of analogous data for a wider range of crystalline chalcogen-bonded systems.

Keywords: crystal structure; chalcogen bond; non-covalent interaction; selenium; tellurium

5.3.1 Introduction

The propensity of the elements of many groups of the periodic table to engage in non-covalent interactions via the σ-hole continues to be widely studied in the solid state, in solution, in the gas phase, and via computational chemistry. The σ-hole is an area of depleted electron density and elevated electrostatic potential which can accept electron density from a variety of electron donors (Clark et al., 2007). The σ-hole was recently visualized using Kelvin probe force microscopy (Mallada, 2021). Following the suggestion of Legon and Walker, the resulting interactions or non-covalent bonds may be termed “E bonds”, where the name of the bond reflects the electrophile involved (Legon and Walker, 2018). Thus, halogen bonds, chalcogen bonds, pnictogen bonds, and tetrel bonds, for example, are those where σ-holes on the group 17, 16, 15, and 14 elements, respectively, accept electrons (Cavallo et al., 2014). These have also long been known as secondary bonding interactions (Alcock, 1972). Recent work has expanded this concept to include e.g., triel bonds (Grabowski, 2020), aerogen bonds (Bauzá and Frontera, 2015), coinage

metal bonds (Legon and Walker, 2018), osme bonds (Daolio 2021a), and matere bonds (Daolio et al., 2021b), for example.

The chalcogen bond is defined by IUPAC a "net attractive interaction between an electrophilic region associated with a chalcogen atom in a molecular entity and a nucleophilic region in another, or the same, molecular entity" (Aakeroy et al., 2019). Chalcogen bonds and other chalcogen-chalcogen interactions are of interest for many applications including crystal engineering, catalysis, coordination chemistry, materials chemistry, and supramolecular chemistry (Bleiholder et al., 2006; Gleiter et al., 2018; Ho et al., 2020; Mahmudov et al., 2022). Chalcogen bonds are of particular interest and utility due to their predictable directionality imparted via the σ-hole as demonstrated by several recent crystal engineering examples in the literature (Kumar et al., 2018, 2020a, 2022; Xu, et al. 2020a; Dhaka, 2021a, 2021b; Huynh et al. 2017; Riel et al., 2019)

In addition to single-crystal and powder X-ray diffraction, solid-state nuclear magnetic resonance (SSNMR) spectroscopy is a well-established site-specific probe of geometry and bonding interactions (Xu et al, 2020b). As part of ongoing work in our laboratory, we have carried out ^{77}Se and ^{125}Te SSNMR experiments on a variety of chalcogen bond donors and chalcogen-bonded cocrystals as part of our efforts to establish and understand the various structural, electronic, and crystallographic influences on the selenium and tellurium chemical shift tensors (Kumar et al. 2020a, 2020b 2022; Xu et al., 2020a). In principle these tensors will report on local site symmetry, on the nature of the chalcogen bond, and on more subtle long-range crystal packing effects. In practice, more experimental NMR data are still required to build a robust framework for understanding the impact of chalcogen bonding on chemical shifts.

As part of our ongoing work on crystal engineering using chalcogen bonds, we considered further the useful 3,4-dicyano-1,2,5-selenodiazole (**1**) and 3,4-dicyano-1,2,5-tellurodiazole (**2**) molecules as chalcogen bond donors (Figure 5.3.1). These well-established donors were selected with the goal of producing new cocrystalline architectures for which only the acceptor moiety is altered with respect to known systems; in this manner the impact of different acceptor moieties on the ^{77}Se and ^{125}Te chemical shift tensors can be partly isolated and better understood. Thus, we report here the preparation and characterization of three novel cocrystals featuring **1** and **2** as chalcogenbonddonors,andhydroquinone(a),tetraethylphosphoniumchloride(b), and tetraphenylphosphonium chloride (c) as chalcogen bond acceptors (Figure 5.3.1). These acceptors were chosen in order to expand the chalcogen bonded cocrystal landscape by introducing a variety of possible electron donors (OH groups, chloride anions, and π -electrons of phenyl rings). The cocrystals and their chalcogen bonding geometries are studied by single-crystal and powder X-ray diffraction, and ^{77}Se and ^{125}Te magic-angle spinning (MAS) SSNMR spectroscopy.

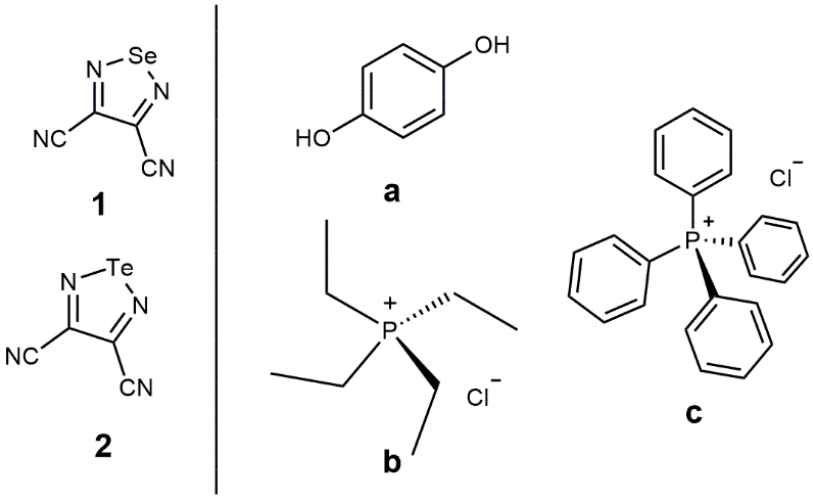

Figure 5.3.1: Molecular structures of the chalcogen bond donors 1 and 2 (left) and chalcogen bond acceptors a, b, c (right).

5.3.1 Experimental

5.3.2 Synthesis and crystallization

All starting materials were obtained from commercial suppliers. 3,4-dicyano-1,2,5-selenodiazole (**1**) was synthesized following a published procedure (Stuzhin et al., 1998). Briefly, diaminomaleonitrile and selenium dioxide were dissolved in dichloromethane and the reaction mixture was stirred for 1 h and then refluxed for 1 h. The white solid obtained was cooled to room temperature and the remaining solvent was evaporated. The residue was then vacuum filtered and dried overnight. The white solid was then placed in a cold-finger apparatus to obtain high quality and pure needle-shaped white crystals which melted at 93°C.

3,4-dicyano-1,2,5-tellurodiazole (**2**) was synthesized following a published procedure (Cozzolino et al., 2010). Briefly, diaminomaleonitrile and $TeCl_4$ in pyridine were stirred under argon for 5 min. An excess of Et_3N was added to the mixture which was then stirred for a further 10 min and left overnight in the freezer (-20°C) to give an orange-reddish filtrate which was then vacuum filtered and washed with ice-cold water, yielding yellow needle-like crystals. The compound was then dried overnight under vacuum.

In a typical procedure, cocrystal **1a** was obtained by slow evaporation of 110 mg of **1** and 33.1 mg of hydroquinone (2:1 molar ratio) from a methanol solution. Similarly, cocrystals of **2b** were obtained from a methanol solution of 110 mg of **2** and 87 mg of tetraethylphosphonium chloride (1:1 molar ratio) after reflux (20 min), cooling, and layering with diethyl ether. Cocrystals of **2c** were obtained in the same way (110 mg of **2**; 178 mg of tetraphenylphosphonium chloride; 1:2 molar ratio).

5.3.3 Single-Crystal X-ray Diffraction

Crystal data, data collection and structure refinement details are summarized in Table 5.3.1. All the crystallographic data were collected from single crystals that were harvested from the vials and were of the best quality observed under a microscope. Each crystal was then mounted on a MiTeGen MicroMount using parabar oil. A Bruker Smart Apex II and Kappa Apex diffractometer equipped with MoKα radiation (wavelength 0.7103 Å) with an APEX II CCD detector were used. The raw data collection and processing were done using the Apex3 software package from Bruker (Apex Software suite V 2010 Bruker AXS. Inc., Madison, Wisc, 2010).

5.3.4 Powder X-ray Diffraction

All samples were finely ground in a mortar and pestle to obtain fine powders of each of the cocrystals. X-ray diffractograms were then recorded on a Rigaku Ultima IV instrument with 2 θ ranging from 5° to 50° at a scan rate of 1 degree per minute in increments of 0.02° using Cu Kα radiation to confirm phase purity. All of the experimental powder X-ray diffractograms were matched with simulated patterns generated from the single-crystal X-ray structures using Mercury 2020.1.

5.3.5 Solid-State NMR Spectroscopy

^{77}Se and ^{125}Te one-pulse Bloch decay magic-angle spinning (MAS) experiments were performed with high-power proton decoupling on a Bruker Avance spectrometer operating at B_0 = 11.7 T (ν (^{1}H) = 500 MHz; ν (^{77}Se) = 95.55 MHz; ν (^{125}Te) = -158.16 MHz). A Bruker 4 mm HXY MAS probe was used for all experiments. For ^{77}Se NMR experiments carried out on **1a**, a $\pi/2$ pulse width of 5.0 μs and recycle delay of 60 s were used. For ^{125}Te NMR experiments carried

out on **2b** and **2c**, a π/2 pulse width of 3.25 μs and recycle delay of 30 to 60 s were used. MAS rates varied from 4.750 kHz to 12.000 kHz and are given in the Figure captions (*vide infra*). Further ^{77}Se and ^{125}Te MAS NMR experiments were carried out at 9.4 T; details and spectra are provided in the Supporting Information (Appendix B).

5.3.6 Results and Discussion

Cocrystals of 3,4-dicyano-1,2,5-selenodiazole and hydroquinone (**1a**), of 3,4-dicyano-1,2,5-tellurodiazole and tetraethylphosphonium chloride (**2b**), and of 3,4-dicyano-1,2,5-tellurodiazole and tetraphenylphosphonium chloride (**2c**) were prepared via slow evaporation from methanol solutions. Suitable single crystals were selected for single-crystal X-ray diffraction experiments. Shown in Table 5.3.1 are the refinement details from these experiments. Shown in Figure 5.3.2 are details from the resulting structures, depicting in particular the location of the chalcogen bonds formed during cocrystallization. The chalcogen bond distances and angles are summarized in Table 5.3.2.

Cocrystal **1a** crystallizes in the monoclinic $P2_1/c$ space group and features one molecule of **1** and half a molecule of hydroquinone in the asymmetric unit. The overall stoichiometry is two ChB donors per hydroquinone molecule. The two types of molecules are held together by both chalcogen bonds and hydrogen bonds (Figure 5.3.2). Each 3,4-dicyano-1,2,5-selenodiazole molecule forms a chalcogen bond via selenium to a hydroxyl oxygen atom on an adjacent hydroquinone molecule. The bond is characterized by a Se···O distance of 2.997 Å and a N-Se···O angle of 174.4°. The corresponding reduced distance parameter ($R_{XB} = d_{ChB}/\sum$ rvdW) is 0.88,

indicating a moderately short contact. Both OH groups of each hydroquinone molecule act as electron donors to different molecules of **1** (Figure 5.3.3). Each 3,4-dicyano-1,2,5-selenodiazole molecule further forms a hydrogen bond via one of its cyano nitrogen atoms with the hydroxyl hydrogen atom of a different hydroquinone molecule. Finally, each 3,4-dicyano-1,2,5-selenodiazole molecule is chalcogen-bonded to one of the ring nitrogen atoms on a second such molecule via the remaining σ-hole on the selenium atom. This self-complementary chalcogen bond, characterized by a Se···N distance of 2.957 Å and a N-Se···N angle of 163.0°, is reminiscent of the intramolecular chalcogen bonds seen in the crystal structures of the pure chalcogen bond donors **1** and **2** (Cozzolino, 2010; Suturina, 2011). Overall, the molecules in the crystal structure of **1a** pack together to form a zig-zag arrangement.

Cocrystal **2b** crystallizes in the triclinic *P*-1 space group and features one molecule of **2**, one tetraethylphosphonium cation in a general position, and two chloride anions on inversion centres in the asymmetric unit. The 3,4-dicyano-1,2,5-tellurodiazole molecule forms two chalcogen bonds at tellurium with the two crystallographically distinct chloride anions (Figure 5.3.2). The Te···Cl1 chalcogen bond has a length of 2.996 Å and a bond angle N-Te···Cl1 of 164.87°, while the Te···Cl2 chalcogen bond has a length of 3.084 Å and a bond angle N-Te···Cl of 171.04°. These are characterized by R_{XB} values of 0.77 and 0.80, respectively (Table 5.3.2). The tetraethylphosphonium cation does not engage in any strong intermolecular interactions; long C8-H8···N3 and C7-H7AB···N4 contacts between methyl and methylene hydrogen atoms and the two cyano nitrogen atoms on **2** are noted. 3,4-dicyano-1,2,5-tellurodiazole molecules and tetraethylphosphonium cations occupy the spaces in between sheets of chloride anions which span the *ab* planes of the crystal.

Cocrystal **2c** crystallizes in the monoclinic $P2_1/n$ space group. The asymmetric unit consists of one molecule of 3,4-dicyano-1,2,5-tellurodiazole, one tetraphenylphosphonium cation, and one chloride anion. The chloride anion forms a chalcogen bond with the tellurium atom as characterized by a Te···Cl⁻ distance of 2.673 Å and a N-Te···Cl⁻ angle of 168.0° (Figure 5.3.2). The chalcogen bond distance corresponds to the smallest R_{XB} value observed in this study, 0.69. A second chalcogen bond to tellurium is formed with the electrons of one of the phenyl rings of the cation (Figure 5.3.2). The distance from Te to the centroid of the ring is 3.959 Å (R_{XB} = 0.87) and the N-Te···centroid angle is 159.1°.This contact may be alternatively considered as an η^1 interaction with C19 of the phenyl ring (Te···C19 distance of 3.932(2) Å and N-Te···C19 angle of 170.32(5)° or an η^2 interaction with C18 and C19. Weak C-H···N hydrogen bonding interactions between the tetraphenylphosphonium cation and the tellurodiazole are noted: C6-H6···N1 (C6-N1 distance of 3.397(3) Å); C18-H18···N3 (C18-N3 distance of 3.278(2) Å); C24-H24···N2 (C24-N2 distance of 3.485 Å). The tetraphenylphosphonium cations are engaged in a translational four-fold phenyl embrace with each adjacent cation (Dance and Scudder, 1996); the phosphorus atoms, separated by 7.3 Å, are aligned along the *b* axis of the unit cell (Figure 5.3.3). The interphosphorus spacing is consistent with that seen in previous reports of various classes of four-fold phenyl embrace (Scudder and Dance, 1998).

Shown in Figures 5.3.4-5.3.6 are experimental powder X-ray diffractograms acquired for samples of **1a**, **2b**, and **2c**. Also shown are the simulated diffractograms based on the solved single-crystal X-ray structures. Despite some differences in intensities, likely attributable to preferential crystallite alignment in the sample holder, the agreement between experiment and simulation is good in all three cases. This agreement provides confidence that the crystal form has not changed

as a result of grinding and allows for a confident interpretation of the NMR data in the context of the single-crystal X-ray structures (*vide infra*).

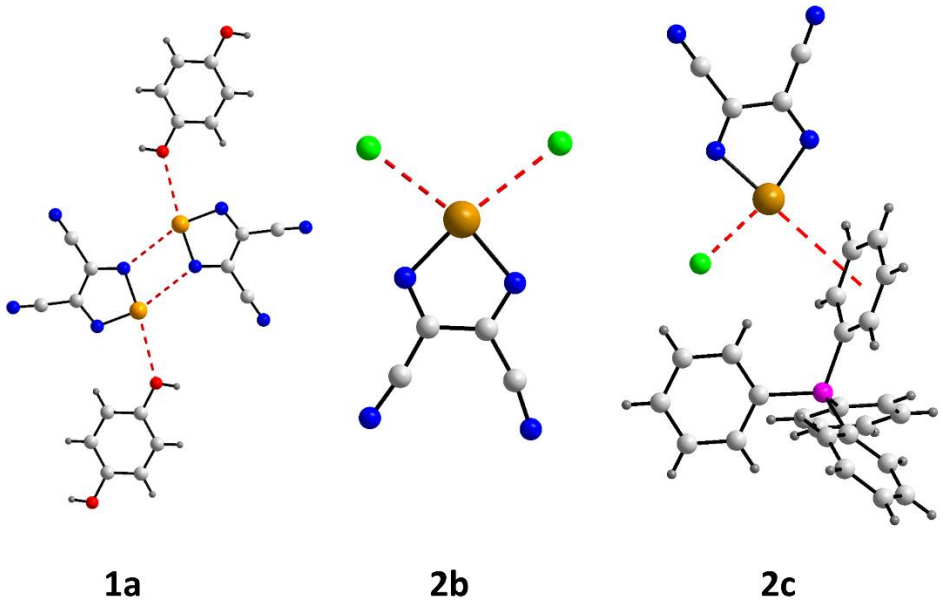

Figure 5.3.2: Local chalcogen bonding geometries from single-crystal X-ray diffraction for cocrystals 1a, 2b, and 2c. Chalcogen bonds are denoted with dashed lines.

Table 5.3.1: Refinement details from single-crystal X-ray diffraction experiments

	2c (CCDC 2174993)	**2b (CCDC 2174995)**	**1a (CCDC 2174994)**
Crystal data			
Chemical formula	$C_4N_4Te \cdot C_{24}H_{20}P \cdot Cl$	$C_4N_4Te \cdot C_8H_{20}P \cdot Cl$	$2(C_4N_4Se) \cdot C_6H_6O_2$
M_r	606.50	414.34	476.19

Crystal system, space group	Monoclinic, $P2_1/n$	Triclinic, P-1	Monoclinic, $P2_1/c$
Temperature (K)	208	213	203
a, b, c (Å)	18.2538 (5), 7.3008 (2), 20.0497 (5)	6.9500 (11), 9.5921 (15), 13.604 (2)	6.2634 (16), 7.4089 (19), 18.320 (5)
α, β, γ (°)	90, 106.867 (2), 90	102.427 (2), 101.890 (2), 91.876 (2)	90, 96.420 (5), 90
V (Å^3)	2557.02 (12)	863.8 (2)	844.8 (4)
Z	4	2	2
Radiation type	Mo $K\alpha$	Mo $K\alpha$	Mo $K\alpha$
μ (mm^{-1})	1.36	1.96	4.41
Crystal size (mm)	0.53 × 0.16 × 0.10	0.72 × 0.35 × 0.31	0.55 × 0.49 × 0.09
Data collection			
Diffractometer	Bruker *APEX*-II CCD	Bruker *APEX*-II CCD	Bruker *APEX*-II CCD
Absorption correction	Multi-scan *SADABS*	Multi-scan *SADABS*	Multi-scan *SADABS*
T_{min}, T_{max}	0.665, 0.746	0.617, 0.746	0.478, 0.747
No. of measured, independent and observed [$I > 2\sigma(I)$] reflections	58500, 7883, 6408	20481, 5948, 5740	17649, 4607, 3289
R_{int}	0.036	0.020	0.051
$(\sin \theta/\lambda)_{max}$ (Å^{-1})	0.716	0.759	0.868
Refinement			
$R[F^2 > 2\sigma(F^2)]$, $wR(F^2)$, S	0.026, 0.061, 1.04	0.036, 0.098, 1.17	0.033, 0.073, 1.00

No. of reflections	7883	5948	4607
No. of parameters	316	179	120
H-atom treatment	H-atom parameters constrained	H-atom parameters constrained	H-atom parameters constrained
$\Delta\rho_{max}$, $\Delta\rho_{min}$ (e Å^{-3})	0.73, −0.49	2.00, −1.44	0.63, −0.55

Computer programs: Bruker *APEX3*, Bruker *SAINT*, SHELXT 2014/5, *SHELXL2018*/3 (Sheldrick, 2015a,b).

Table 5.3.2: Chalcogen bond geometries[a]

cocrystal	Ch···X distance (Å)	N-Ch···X angle (°)	N_c
1a	2.997(1) (X = O)	174.41(5)	0.88
1a	2.957(1) (X = N)	162.97(5)	0.86
2b	2.9664(1) (X = Cl1)	164.87(5)	0.77
2b	3.0842(1) (X = Cl2)	171.04(5)	0.80
2c	2.6733(6) (X = Cl)	168.08(5)	0.69
2c	3.959 (X = Ph)	159.1	0.87

a. Van der Waals radii used: Te, 2.06 Å; Se. 1.90 Å; Cl^-, 1.81 Å; O, 1.52 Å; N, 1.55 Å (Bondi, 1964; Shannon, 1976).

The ^{77}Se MAS NMR spectra of cocrystal **1a** acquired in a magnetic field of 11.75 T are presented in Figure 5.3.7. The ^{125}Te MAS NMR spectra of cocrystals **2b** and **2c** acquired at 11.75 T are presented in Figures 5.3.8 and 5.3.9, respectively. Further spectra acquired in a magnetic field of 9.4 T are provided in the Supporting Information (Appendix B). Generally, spectra were acquired using a Bloch decay and high-power proton decoupling rather than via cross-polarization from protons. Bloch decay spectra offered better sensitivity because the chalcogen nuclei are

generally relatively distant from hydrogen atoms in the cocrystals (i.e., there are no hydrogen atoms on either chalcogenodiazole molecule), thereby reducing the utility of the CP process. The MAS NMR spectra all show relatively sharp and well-defined resonances, consistent with a good degree of crystallinity. Each of the spectra were acquired at a minimum of two magic-angle spinning rates in order to identify the centreband. All spectra show a single isotropic chemical shift (δ_{iso}), consistent with a single crystallographic chalcogen site in each crystal structure; this is also consistent with the single-crystal X-ray diffraction data. NMR spinning sidebands reflective of the principal components of the ^{77}Se/^{125}Te chemical shift tensor ($\delta_{11} \geq \delta_{22} \geq \delta_{33}$) were fit using an iterative Herzfeld-Berger process (Herzfeld and Berger, 1980; Eichele, 1995, 2012). The resulting data are presented in Table 5.3.3 along with the span ($\Omega = \delta_{11} - \delta_{33}$) and skew ($\kappa = 3(\delta_{22}-\delta_{iso})/\Omega$) of the ^{77}Se/^{125}Te chemical shift tensors. The ^{77}Se chemical shift tensor for pure donor **1** and the ^{125}Te chemical shift tensor for pure donor **2** have been reported recently (Kumar et al., 2020a) and these are also presented in Table 5.3.3.

Table 5.3.3: Selenium-77 and tellurium-125 chemical shift tensor data[a]

compound	nucleus	δ_{iso} / ppm	Ω / ppm	κ	δ_{11} / ppm	δ_{22} / ppm	δ_{33} / ppm
1[b,c](site 1)	^{77}Se	1592.2(0.1)	472(5)	0.05(0.01)	1824(4)	1600(2)	1352(3)
1[b,c](site 2)	^{77}Se	1548.7(0.1)	456(3)	-0.47(0.01)	1812(3)	1477(1)	1356(2)
1a	^{77}Se	1601(2)	466(10)	-0.11(0.02)	1849(4)	1582(3)	1366(3)
2[b]	^{125}Te	2332.8(0.1)	1268(3)	0.49(0.01)	2863(5)	2540(3)	1595(4)
2b	^{125}Te	2385(1)	955(10)	0.72(0.02)	2746(3)	2614(2)	1791(2)
2c	^{125}Te	2160(1)	966(10)	0.23(0.02)	2606(4)	2234(3)	1640(3)

a. Errors given are estimated from independently fitting data acquired at 9.4 and 11.75 T using an iterative Herzfeld-Berger routine. b. Data from Kumar et al. (2020a). c. Two crystallographic sites.

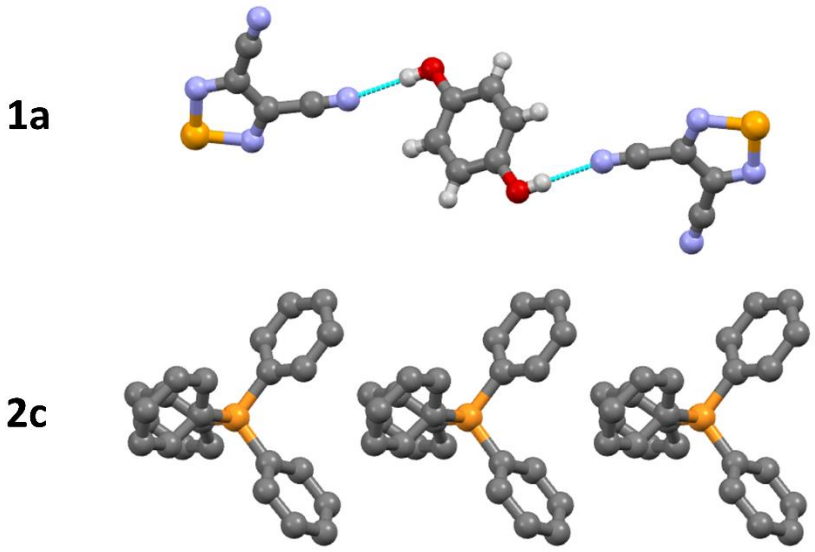

Figure 5.3.3: Top: hydrogen bonds (turquoise) between hydroquinone and 3,4-dicyano-1,2,5-selenodiazole in cocrystal 1a. Bottom: four-fold phenyl embrace motif in cocrystal 2c; hydrogen atoms are not shown.

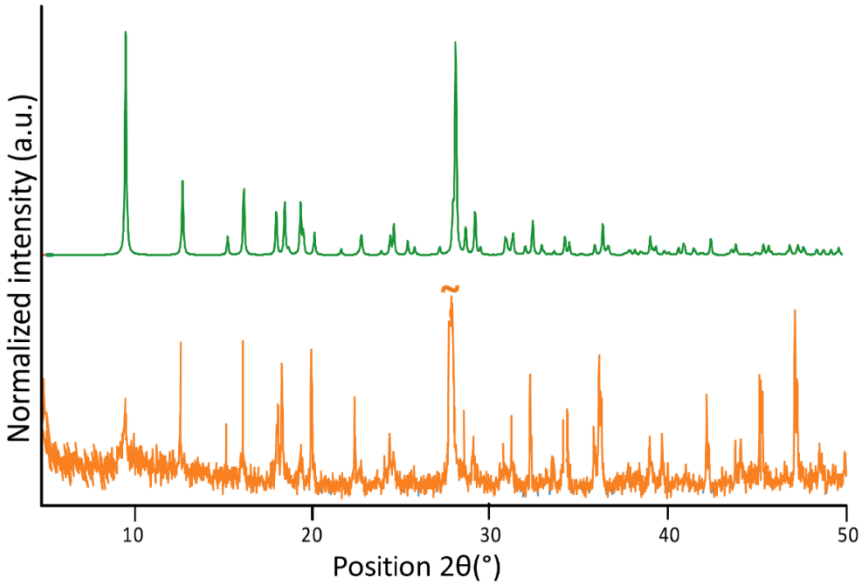

Figure 5.3.4: Powder X-ray diffractogram of 1a. Experimental: bottom, orange; simulated: top, green. The experimental peak near 2θ = 28° is cropped to enable a better view of the lower-intensity peaks.

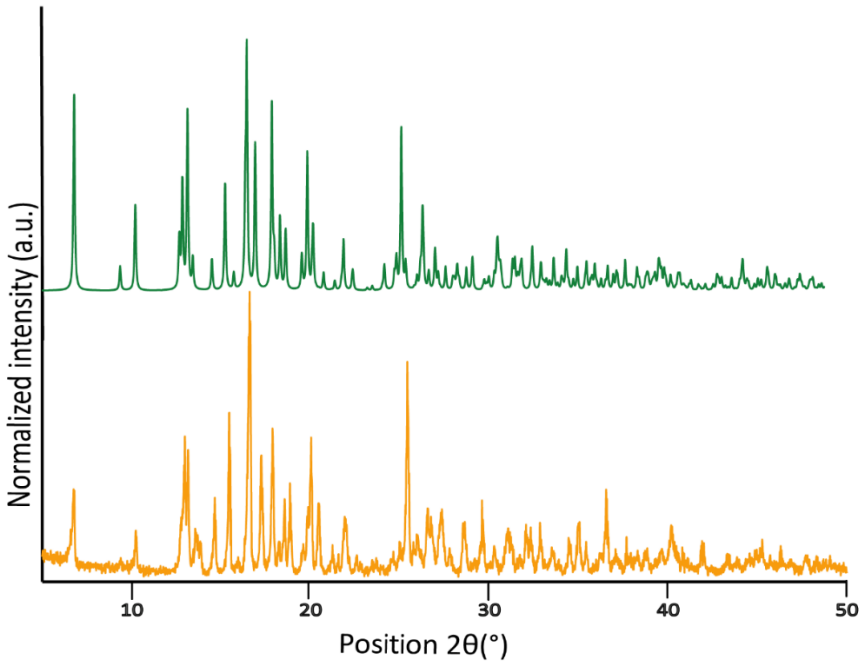

Figure 5.3.5: Powder X-ray diffractogram of 2b. Experimental: bottom, orange; simulated: top, green.

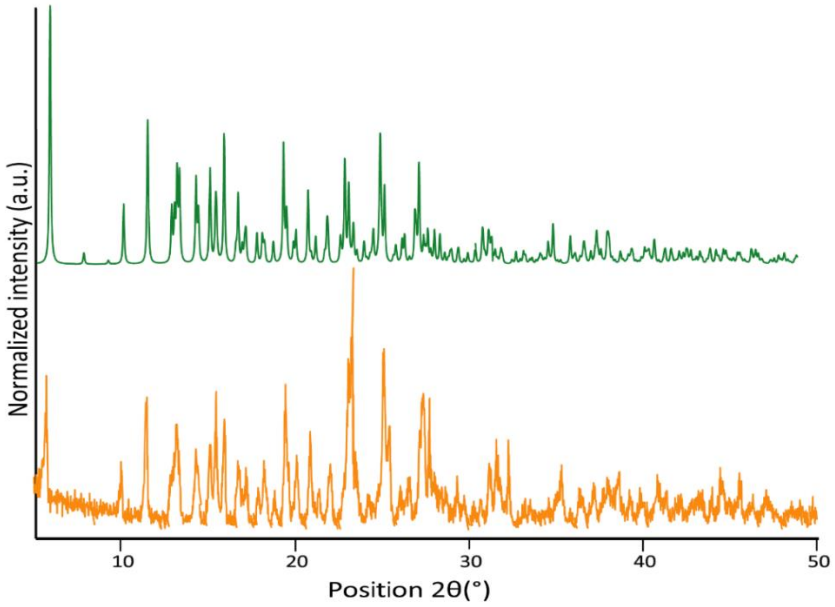

Figure 5.3.6: Powder X-ray diffractogram of 2c. Experimental: bottom, orange; simulated: top, green.

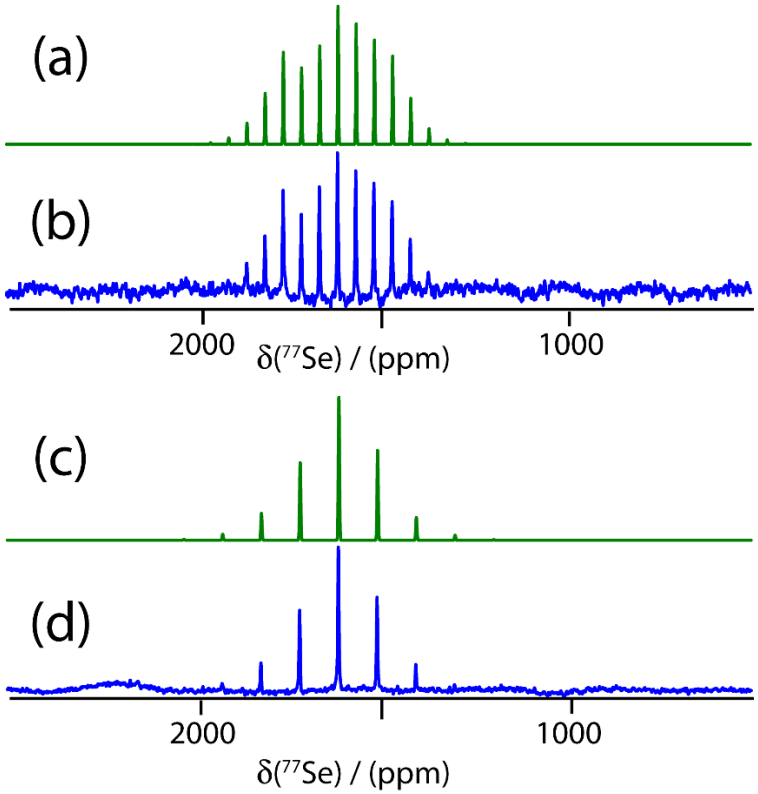

Figure 5.3.7: ^{77}Se MAS NMR spectra acquired at B_0 = 11.7 T for cocrystal 1a. Experimental spectra are shown in blue; simulated spectra are shown in green. MAS rate 4 kHz at top ((a) and (b)) and 10 kHz at bottom ((c) and (d)).

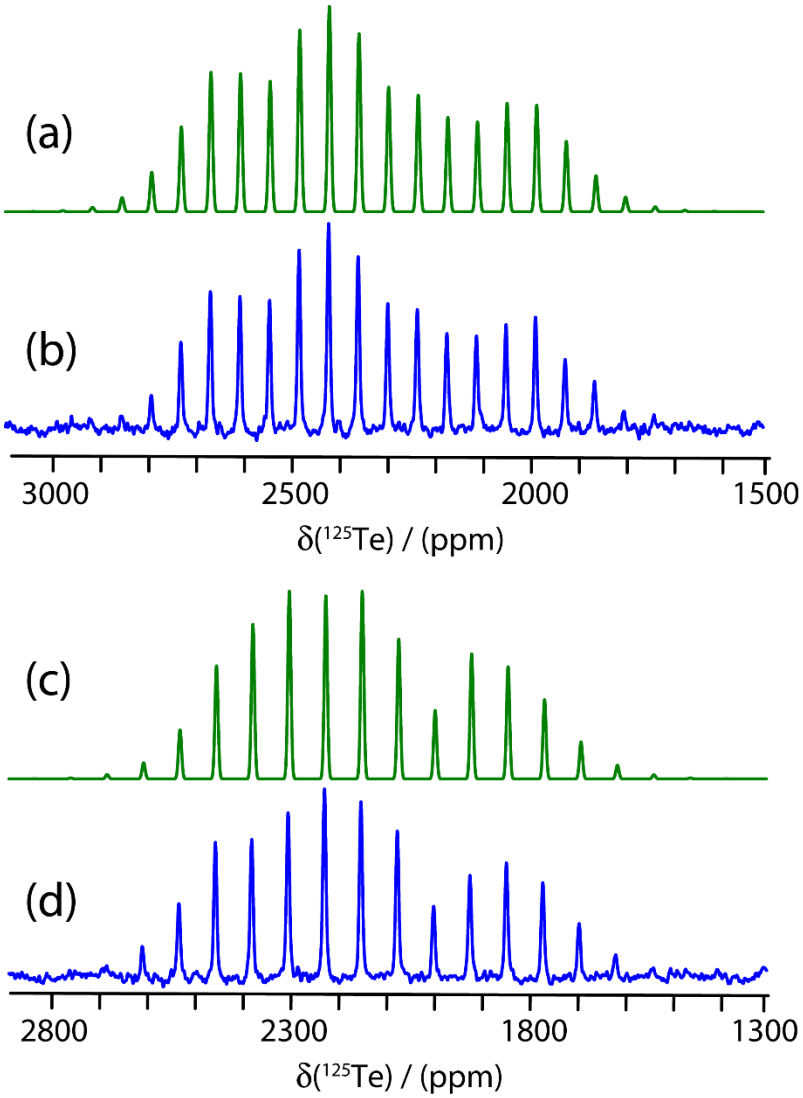

Figure 5.3.8: ^{125}Te MAS NMR spectra acquired at B_0 = 11.7 T for cocrystal 2c. Experimental spectra are shown in blue; simulated spectra are shown in green. MAS rate 9.75 kHz at top ((a) and (b)) and 12 kHz at bottom ((c) and (d)).

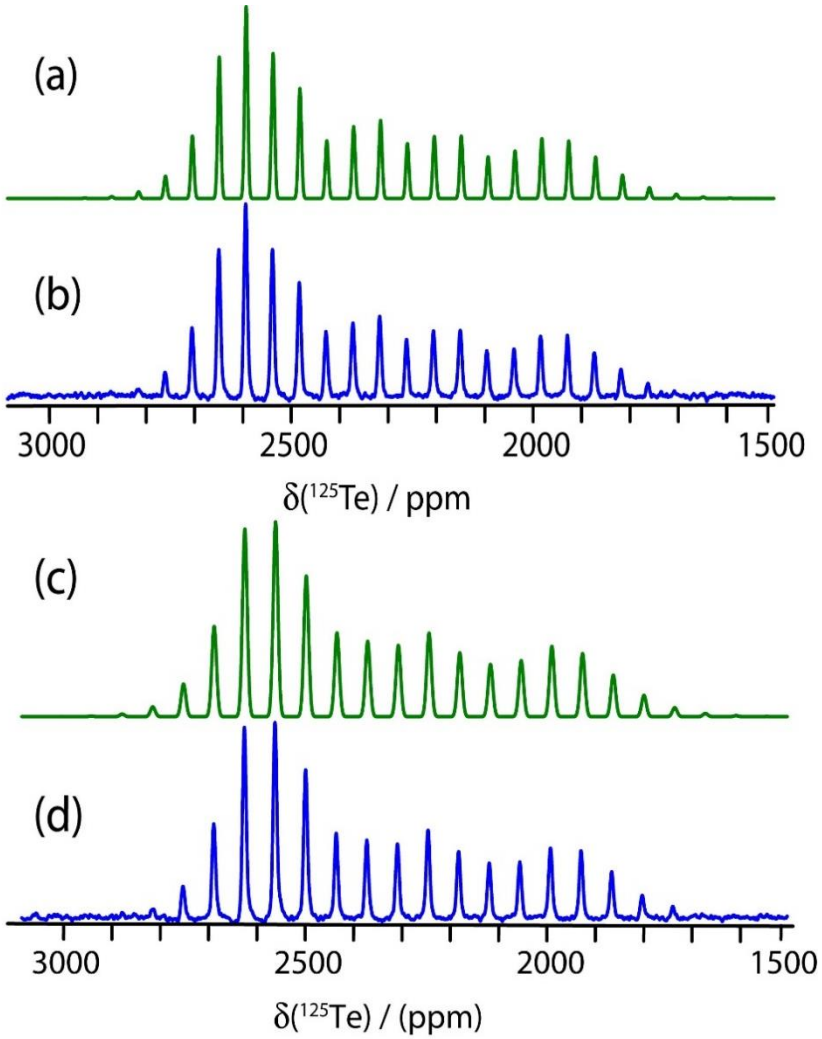

Figure 5.3.9: ^{125}Te MAS NMR spectra acquired at B_0 = 11.7 T for cocrystal 2b. Experimental spectra are shown in blue; simulated spectra are shown in green. MAS rate 8.75 kHz at top ((a) and (b)) and 10 kHz at bottom ((c) and (d)).

Pure **1** and pure **2** each form self-complementary chalcogen bonded structures in the solid state. Thus, their ^{77}Se and ^{125}Te NMR responses are not expected to represent limiting cases indicative of a lack of influence of the chalcogen bond. Nevertheless, it is instructive to compare

the chemical shift tensor magnitudes measured for the pure ChB donors and the cocrystals. In the case of **1** and **1a**, it is noted that the ^{77}Se isotropic chemical shift increases upon chalcogen bond formation. This is mainly due to an increase in the largest principal component of the chemical shift tensor δ_{11}, which increases from 1824 and 1812 ppm in **1** (two crystallographic sites) to 1849 ppm in **1a**. This is in contrast to most of the cases studied by Kumar et al. (2020a), where $\delta_{11}(^{77}\text{Se})$ was generally seen to decrease upon ChB formation to donor **1**. However, it should be noted that while cocrystal **1a** features a novel ChB with OH as the electron donor, it also maintains self-complementary ChBs between two 3,4-dicyano-1,2,5-selenodiazole molecules. Thus, the moderate change in $\delta_{iso}(^{77}\text{Se})$ as well as the span of the ^{77}Se chemical shift tensor when comparing **1** with **1a** is not surprising and is fact consistent with the retention of the self-complementary ChB motif.

In the cases of pure donor **2** and of cocrystals **2b** and **2c**, no consistent trend in the ^{125}Te isotropic chemical shift is noted upon ChB formation. This is consistent with the work of Kumar et al. (2020a). The span of the ^{125}Te chemical shift tensor, however, changes markedly from 1268 ppm for **2** to 955 and 966 ppm, respectively for **2b** and **2c**, as a result of chalcogen-bond-induced cocrystallization. These significant changes are again consistent with the body of related work on chalcogen-bonded cocrystals of 3,4-dicyano-1,2,5-tellurodiazole, where similar reductions of a few hundred ppm are noted for the span of the tellurium chemical shift tensor when other electron donor moieties are used (Kumar et al., 2020a). Future work could entail single crystal NMR studies of chalcogen-bonded cocrystals, with the goal of relating NMR interaction tensor orientations to the ChB geometry, as has recently been reported for halogen bonds (Xu et al., 2019).

5.3.7 Conclusions

Three novel cocrystals of 3,4-dicyano-1,2,5-chalcogenodiazoles have been prepared and characterized by single-crystal X-ray diffraction, powder X-ray diffraction, and solid-state ^{77}Se/^{125}Te magic-angle-spinning solid-state NMR spectroscopy. Each cocrystal features chalcogen bonds with selenium or tellurium atoms acting as electron acceptors. The chalcogen bonds, to oxygen, nitrogen, chloride anion, and aryl rings, are moderately strong and highly directional, demonstrating the robustness of the ChB motif in such systems. The solid-state NMR data are consistent with previous work examining a larger number of cocrystals of 3,4-dicyano-1,2,5-chalcogenodiazoles, and demonstrate in particular the significant sensitivity of the ^{125}Te chemical shift tensor span to chalcogen bond formation. Small changes in the ^{77}Se chemical shift tensor in a 3,4-dicyano-1,2,5-selenodiazole-hydroquinone cocrystal are consistent with the retention of self-complementary chalcogen bonds between two selenodiazole molecules in this system. Finally, this work contributes to a growing body of knowledge on chalcogen-bond-induced cocrystallization and on the relationship between selenium and tellurium chemical shift tensors and the local chalcogen bond geometry.

5.3.8 Acknowledgements

We thank the Natural Sciences and Engineering Research Council of Canada for funding.

References

Alcock, N. W. Secondary Bonding to Nonmetallic Elements. In Advances in Inorganic Chemistry and Radiochemistry; Academic Press Inc., 1972; Vol. 15, pp 1– 58.

Apex Software suite V 2010 Bruker AXS. Inc., Madison, Wisconsin USA, 2010.

Aitipamula, S. et al. (2012) *Cryst. Growth Des.* **12**, 5, 2147–2152.

Bauzá, A. & Frontera, A. (2015) *Angew. Chem. Intl. Ed.* **54**, 7340-7343.

Bleiholder, C., Werz, D. B., Köppel, H. & Gleiter, R. (2006) *J. Am. Chem. Soc.* **128**, 2666–2674.

Bondi, A. (1964) *J. Phys. Chem.* **68**, 441-451.

Cavallo, G., Metrangolo, P., Pilati, T., Resnati, T. & Terraneo, G. (2014) *Cryst. Growth Des.* **14**, 2697–2702.

Clark, T., Hennemann, M., Murray, J. S. & Politzer, P. (2007) *J. Mol. Model.* **13**, 291– 296.

Cozzolino, A. F., Yang, Q. & Vargas-Baca, I. (2010) *Cryst. Growth Des.* **10**, 4959-4964.

Dance, I. & Scudder, M. (1996) *Chem. Eur. J.* **2**, 481-486.

Daolio, A. Pizzi, A., Calabrese, M., Terraneo, G., Bordignon, S., Frontera, A. & Resnati, G. (2021a) *Angew. Chem. Intl. Ed.* **60**, 20723-20727.

Daolio, A., Pizzi, A., Terraneo, G., Frontera, A. & Resnati, G. (2021b) *ChemPhysChem* **22**, 2281-2285.

Dhaka, A., Jeannin, O., Aubert, E., Espinosa, E. & Fourmigué, M. (2021a) *Molecules* **26**, 4050.

Dhaka, A., Jeannin, O., Aubert, E., Espinosa, E. & Fourmigué, M. (2021b) *Chem. Commun.* **57**, 4560-4563.

Eichele, K. (2012) *HBA – Graphical Herzfeld-Berger Analysis*, Version 1.7.3, 1995, 2012.

Fyfe, M. C. T & Stoddart, J. F. (1997) *Acc. Chem. Res*. **30**, 10, 393-401.

Gleiter, R., Haberhauer, G., Werz, D. B., Rominger, F. & Bleiholder, C. (2018) *Chem. Rev.* **118**, 2010–2041

Herzfeld, J. & Berger, A. E. (1980) *J. Chem. Phys.* **73**, 6021-6030.

Ho, P. C., Wang, J. Z., Meloni, F. & Vargas-Baca, I. *Coord. Chem. Rev.* **422**, 213464.

Huynh, H.-T., Jeannin, O. & Fourmigué, M. (2017) *Chem. Commun.* **53**, 8467– 8469.

Grabowski, S. J. (2020) *Coord. Chem. Rev.* **407**, 213171.

Kumar, V., Leroy, C. & Bryce, D. L. (2018) *CrystEngComm* **20**, 6406-6411.

Kumar, V., Xu, Y & Bryce, D. L. (2020a) *Chem. Eur. J.* **26**, 3275-3286.

Kumar, V., Xu, Y.; Leroy, C. & Bryce, D. L. (2020b) *Phys. Chem. Chem. Phys.* **22**, 3817-3824.

Kumar, V., Triglav, M., Morin, V. M. & Bryce, D. L. (2022) *ACS Org. Inorg. Au* **2**, 252-260.

Legon, A. C. & Walker, N. R. (2018) *Phys. Chem. Chem. Phys.* **20**, 19332– 19338.

Lehn, J. M. (1988) *Angew. Chem. Int. Ed*. **27**, 89-112.

Mahmudov, K. T., Gurbanov, A. V., Aliyeva, V. A., Guedes da Silva, M. F. C., Resnati, G. & Pombeiro, A. J. L. *Coord. Chem. Rev.* **464**, 214556.

Mallada, B., Gallardo, A., Lamanec, M., De La Torre, B., Špirko, V., Hobza, P., Jelinek, P. (2021) *Science* **374**, 863– 867.

Riel, A. M. S., Huynh, H.-T., Jeannin, O., Berryman, O., Fourmigué, M. (2019) *Cryst. Growth Des.* **19**, 1418– 1425.

Rosenfield, R. E., Parthasarathy, R., Dunitz, J. D. (1977) *J. Am. Chem. Soc*. **99**, 4860.

Scudder, M. & Dance, I. (1998) *J. Chem. Soc., Dalton Trans.* 3155-3165.

Shannon, R. D. (1976) *Acta Cryst.* **A32**, 751-767.

Sheldrick, G. M. (2015a) *Acta Cryst.* **A71**.3-8.

Sheldrick, G. M (2015b) *Acta Cryst.* **C71**, 3-8.

Suturina, E. A, Semenov, N. A., Lonchakov, A. V., Bagryanskaya, I. Y., Gatilov, Y. V., Irtegova, I. G., Vasilieva, N. V., Lork, E., Mews, R., .Gritsan, N. P. & Zibarev, A. V. (2011) *J. Phys. Chem. A* **115**, 4851-4860.

Stuzhin, P. A., Bauer, E. M. & Ercolani, C. (1998) *Inorg. Chem.* **37**, 1533-1539.

Whitesides, G. M. et al., (1995) *Acc. Chem. Res*. **28**, 1, 37-44.

Xu, Y., Gabidullin, B. & Bryce, D. L. (2019) J. Phys. Chem. A **123**, 6194-6209.

Xu, Y., Kumar, V., Bradshaw, M. J. Z. & Bryce, D. L. (2020a) *Cryst. Growth Des.* **20**, 7910-7920.

Xu, Y., Szell, P. M. J., Kumar, V. & Bryce, D. L. (2020b) *Coord. Chem. Rev.* **411**, 213237.

Chapter 6. Chemical shift tensors as probes of chalcogen bonds

6.1 Introduction

As discussed in Chapter 2, chemical shielding and chemical shift scales are reverse of each other. Chemical shift of a nucleus in a NMR spectrum tells us how deshielded the nucleus is owing to its local environment due to presence of a bonding interaction, in this case chalcogen bond. In this Chapter, we will discover how the solid-state NMR study of ChB cocrystals change their nature of bonding and local geometry when a chalcogen bond is formed. The comparison is done based on the pure ChB donor studied in this work, namely, telluradiazole and its effect on ChB formation with three well-known ChB acceptors, crown-ether skeleton of OCN, SeCN and SCN salts. A study of ChB cocrystal salts and analyzing them via solid-state NMR parameters is a first witnessed in the following work.

Chemical shift scale is usually set up using a reference compound to define zero on the chemical shift scale, for example in typical solution-state NMR when performing a ^{1}H and ^{13}C NMR experiments, TMS, that is tetramethyl silane is used as a reference compound where the chemical shift is zero and then the molecules undergo the NMR experiment to output a NMR spectrum. The choice of reference compound is relative to the nucleus observed in the spectrum. The idea is to use the same compound to reference their samples before an experiment is recorded. Usually for solid-state NMR experiments recorded here, the reference compounds used for extracting the NMR results are glycine for ^{13}C, Tellurium hydroxide for ^{125}Te and ammonium chloride for ^{15}N. ^{125}Te has low receptivity as compared to well-known ^{1}H nucleus or ^{19}F spin ½

nuclei have a wider span ranging up to 3000 ppm, thus it becomes challenging to study their effects when noncovalent interactions are involved besides presence of other notable NMR interactions vividly in the solid-state. Some previous works from the group have been able to tackle this problem including this work showing a detailed amount of perspective in tracing and analyzing the NMR parameters magnitude change in terms of chemical shift.

6.2 Experimental methods and characterization

The preliminary characterization of the ChB salt cocrystals in this Chapter featuring chalcogen bonds in Te---N in telluradiazole and K-18-C-6-NCO cocrystal, Te---Se in telluradiazole and K-18-C-6-SeCN cocrystal and, Te---S in telluradiazole and K-18-C-6-SeCN was carried out using Single-crystal X-ray diffraction to verify the formation of respective chalcogen-bonded salt cocrystals, powder X-ray diffraction technique confirmed the exact same phases of crystallization, presence of no other phases. Solid-state NMR confirmed the trend reported from earlier works with respect to chemical shift tensor study and span of ^{125}Te NMR. Isotopic enrichment process was carried for ^{15}N of the isocyanate moiety to study the symmetry breakdown effect of other possible NMR interactions upon ChB bond formation in the telluradiazole and K-18-C-6-NCO cocrystal using HPDEC/MAS and CP/MAS experiments.

Statement of Authenticity and permissions for part 6.3: I declare that the coauthors have permitted me to include this article in my thesis and permissions from the journal *Facets* was obtained to reproduce the entire research paper. I would like to share equal credits with my coauthor Carina Almario, an undergrad student who worked with me on this project and helped me with the synthesis of the cocrystals, the SSNMR experiments and simulation of the experimental SSNMR spectra. I certify this work was prepared by me with the guidance, support and contributions from my supervisor, Dr. David L. Bryce.

6.3 Chemical Shift Tensors as Probes of Chalcogen Bonds. Solid-State NMR Study of Telluradiazole-XCN^- (X = O, S, Se) Salt Cocrystals

Carina Almario,[†] Tamali Nag,[†] and David L. Bryce*

ORCID:
D. L. Bryce: 0000-0001-9989-796X
T. Nag: 0000-0001-6053-8935
C. Almario: 0009-0005-2781-093X

Department of Chemistry and Biomolecular Sciences
University of Ottawa
Ottawa, Ontario, K1N6N5
Canada

[†] These authors contributed equally.

*author to whom correspondence may be addressed
dbryce@uottawa.ca
1-613-562-5800 ext 2018

Graphical abstract

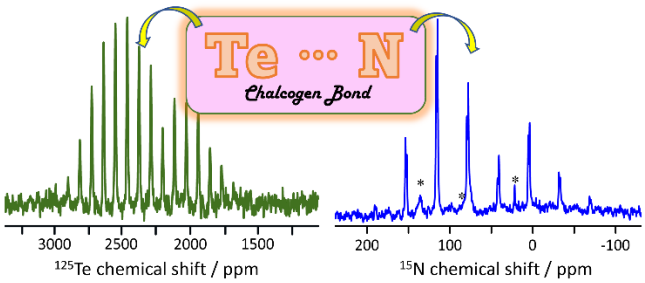

Abstract

We report experimental ^{125}Te magic-angle spinning solid-state nuclear magnetic resonance (MAS NMR) measurements of the tellurium chemical shift (CS) tensors in three [K(18-crown-6)]$^+$ 3,4-dicyano-1,2,5-telluradiazole-XCN$^-$ (X = O, S, Se) salt cocrystals featuring chalcogen bonds. These data are compared to those for pure 3,4-dicyano-1,2,5-telluradiazole (**1**). A reduction in the span of the ^{125}Te CS tensor is consistently noted in the salt cocrystals compared to pure **1**. Isotopically ^{15}N-labelled [K(18-crown-6)]$^+$[**1**-OC^{15}N]$^-$, which features a chalcogen bond between Te and the cyanate nitrogen atom, is synthesized using KOC^{15}N, and the nitrogen CS tensors are measured for both samples via ^{15}N slow MAS NMR spectroscopy. Possible dynamic disorder of the cyanate ions in KOCN is ruled out. Two crystallographically distinct nitrogen sites are resolved for the salt cocrystal. Upon formation of [K(18-crown-6)]$^+$[**1**-OC^{15}N]$^-$, the ^{15}N isotropic chemical shift and CS tensor span both decrease relative to the values for pure KOC^{15}N, and the axial symmetry of this tensor is lost. These findings are supplemented with a series of density functional theory calculations of magnetic shielding tensors using cluster models or periodic boundary conditions. Inclusion of spin-orbit relativistic effects in the calculation of tellurium shielding tensors is particularly important in achieving agreement with experiment.

Keywords. Non-covalent interaction; chalcogen bond; nuclear magnetic resonance; solid-state NMR; spectroscopy; tellurium

6.3.1 Introduction

Non-covalent bonds play important and unique roles in determining molecular structure, dynamics, and function. Such bonds may include hydrogen bonds, halogen bonds (Desiraju et al. 2013), chalcogen bonds (Aakeröy et al. 2019), tetrel bonds (Bauzá et al. 2019), pnictogen bonds (Resnati et al. 2023), and other more recently explored element-based electrostatic bonds such as regium bonds (Frontera and Bauzá 2018) or coinage metal bonds (Legon and Walker 2018), triel bonds (Grabowski 2020), spodium bonds (Bauzá et al. 2020), and matere bonds (Daolio et al. 2021), for example. In this terminology, the bond donor is named after the element participating in the bond and which accepts electrons (Cavallo et al. 2014). The bond acceptor donates electrons. The prevailing paradigm for understanding these types of non-covalent bonds often invokes the concept of a σ-hole which forms on a donor atom opposite a covalently-bonded electron-withdrawing substituent (Politzer et al. 2017). The σ-hole is an area of elevated electrostatic potential, typically coinciding with decreased electron density. Because of the way in which the σ-hole is created, the resulting non-covalent bonds tend to be highly predictable, directional, and tunable. Evidence for π character in halogen bonds has also been presented (Kellett et al. 2020). σ-hole interactions are now well established as important tools in catalysis, supramolecular chemistry, materials chemistry, and in biological systems. In the solid state, σ-hole interactions also offer a wide range of unique opportunities in crystal engineering.

Chalcogen bonds and related chalcogen-chalcogen interactions are of particular interest from a fundamental perspective and in a range of applications (Werz et al. 2002; Gleiter et al. 2003; Gleiter et al. 2018; Aakeröy et al. 2019; Scilabra et al. 2019; Haberhauer et al. 2020).

Selenium and tellurium are the most common chalcogen bond donor elements, and many examples of chalcogen-bonded systems featuring these elements have been discussed, including their applications in catalysis, materials chemistry, and synthesis (Mahmudov et al. 2017; Vogel et al. 2018; Yan et al. 2021). In order to understand the structural, electronic, and crystallographic properties of chalcogen bonds, as well as the role they may play in crystal engineering applications, it is important to develop novel analytical methods for their analysis. In addition to single-crystal X-ray diffraction, a wealth of information is available from ^{77}Se and ^{125}Te solid-state NMR studies of chalcogen-bonded solids and cocrystals (Collins et al. 1988; Stanford et al. 2014; Sanz Camacho et al. 2015; Sanz Camacho et al. 2016; Kumar et al. 2018; Sanz Camacho et al. 2018; Kumar et al. 2020a; Kumar et al. 2020b; Xu et al. 2020; Kumar et al. 2022; Nag et al. 2022).

In this work, we turn our attention to a series of three $[K(18\text{-crown-}6)]^+$ 3,4-dicyano-1,2,5-telluradiazole-XCN^- (X = O, S, Se) salt cocrystals described by Semenov et al. (2018) and which feature chalcogen bonds between tellurium and nitrogen, sulfur, and selenium, respectively (Figure 6.3.1). These systems are of particular interest because of the simplicity of the linear chalcogen bond acceptor anions and the sequestration of the potassium counterion by 18-crown-6. We hypothesized that this series of salt cocrystals could provide for a relatively direct comparison of NMR spectroscopic parameters with local chalcogen bond geometries, with a minimum of differential crystal packing effects to confound the analysis. We report here the measurement of ^{125}Te chemical shift tensors using magic-angle spinning solid-state nuclear magnetic resonance (MAS NMR) spectroscopy for the series of salt cocrystals, and discuss these data in the context of the single-crystal X-ray diffraction structures. The data are further compared to those for the pure chalcogen bond donor, 3,4-dicyano-1,2,5-telluradiazole. We additionally

describe the preparation of isotopically ^{15}N enriched $[K(18\text{-crown-6})]^+$ 3,4-dicyano-1,2,5-telluradiazole-$OC^{15}N^-$ from $KOC^{15}N$ and report the ^{15}N chemical shift tensors for both compounds. In this manner, insight into the chalcogen bond is obtained via NMR interrogation of both the donor (Te) and acceptor (N) elements in the same compound. All experimental data are further interpreted in the context of extensive density functional theory (DFT) calculations of the tellurium and nitrogen nuclear magnetic shielding tensors.

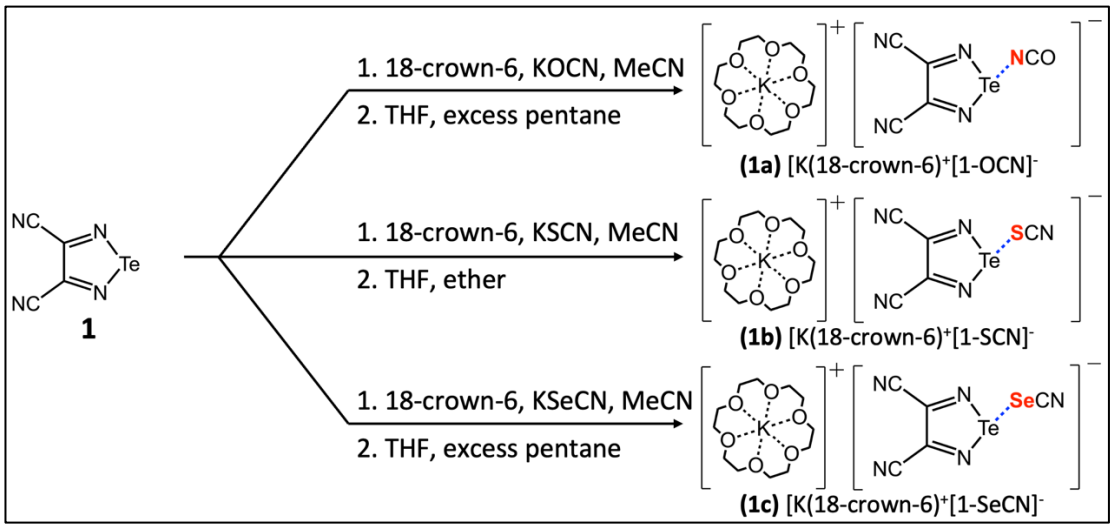

Figure 6.3.1: Schematic for the synthesis of $[K(18\text{-crown-6})]^+[1\text{-OCN}]^-$ (1a), $[K(18\text{-crown-6})]^+[1\text{-SCN}]^-$ (1b), and $[K(18\text{-crown-6})]^+[1\text{-SeCN}]^-$ (1c). Synthesis follows procedures published by and adapted from Semenov et al. (2018).

6.3.2 Experimental

(a) Synthesis and Sample Preparation

The synthesis of 3,4-dicyano-1,2,5-telluradiazole was performed using a procedure reported by Semenov et al. (2012) with some modifications (see Supplementary Material, Appendix C). The preparation of the telluradiazole-XCN^- (X = O, S, Se) salt cocrystals similarly followed procedures adapted from the literature (Figure 1; see Supplementary Material, Appendix C) (Semenov et al. 2018). $TeCl_4$, cyclic polyether 18-crown-6, KSCN, and KSeCN were obtained from Sigma-Aldrich. Diaminomaleonitrile and KOCN were obtained from Acros Organics. Isotopically enriched $KOC^{15}N$ (95%) was obtained from CortecNet. Solvents were dried with molecular sieves. Synthesis was performed using common Schlenk and vacuum-line techniques under argon. For work up, a rotary evaporator was employed to distill reaction solvents under reduced pressure. Further synthetic details are provided in the Supplementary Material (Appendix C).

(b) X-ray Diffraction

To ensure that the compounds were successfully prepared as described above, and that their morphologies matched those reported previously in the literature, single-crystal structures were determined by using a Bruker AXS Kappa Apex diffractometer equipped with MoKα (λ = 0.7103 Å) radiation with an APEX II CCD detector (University of Ottawa, Canada). Crystals were mounted onto a glass fibre and cooled to 200 K (±2 K) before data collection using a liquid nitrogen cryogen system. Raw data collection and processing were performed with the Bruker APEX III software package. Crystal structures were solved using WinGX and Olex2 software

packages. Packing diagrams were generated using Mercury 4.1.0 and POV-Ray, and the former was used to measure bond angles and bond distances.

Powder X-ray diffractograms were acquired using a Rigaku Ultima IV powder diffractometer (University of Ottawa, Canada) with a copper source and one diffracted beam monochromator. Relevant parameters include a 2θ scan angle of 5 to 50º, a scanning speed of 1º/min, a division slit of 1/3º, a scattering slit of 1/3º, a division height of 10 mm, and a rectangular slit of 0.6 mm. Experimental diffractograms were compared to simulated patterns generated from single-crystal structure cifs using Mercury software (CCDC 2021).

(c) Solid-State Nuclear Magnetic Resonance Spectroscopy

^{125}Te and ^{15}N SSNMR spectra were acquired using a 400 MHz Bruker Avance III NMR spectrometer operating at 9.4 T with a 4 mm Bruker HXY probe (University of Ottawa, Canada). Samples were finely ground using a mortar and pestle and packed into 4 mm o.d. zirconia rotors. Spectra were acquired using high-power decoupling (62.5 kHz) with magic angle spinning (HPDEC-MAS) or cross-polarization MAS (CP-MAS). ^{125}Te chemical shifts were measured with respect to solid telluric acid, $Te(OH)_6$ (δ_{iso} = 685.5 and 692.2 ppm relative to Me_2Te at 0 ppm) (Collins et al. 1987). ^{15}N chemical shifts were referenced to isotopically enriched $^{15}NH_4Cl$ (δ_{iso} = 39.3 ppm relative to NH_3(l) at 0 ppm) (Bertani et al. 2014). Data for each sample were collected at different MAS rates ranging from 1.500 to 11.000 kHz to determine the isotropic peak(s) and to measure chemical shift anisotropy via a Herzfeld Berger analysis (Herzfeld and Berger 1980) using the HBA software package (Eichele 1995). Typical recycle delays for the ^{125}Te direct-observe experiments were 60 s. Further experimental details are provided in the Supplementary Material (Appendix C).

(d) Density Functional Theory Calculations

DFT calculations of magnetic shielding tensors were carried out using two methods: a cluster-model approach within the Amsterdam Density Functional (ADF) software and an approach using periodic boundary conditions as implemented in the CASTEP software package. Both sets of calculations used the published single-crystal structures of compounds **1**, **1a**, **1b**, and **1c** (Semenov 2018) as described below.

Cluster models of compounds **1**, **1a**, **1b**, and **1c** were built for DFT calculations carried out using Amsterdam Density Functional software, part of the Amsterdam Modeling Suite (2019.305) (te Velde, 2001; Baerends et al., 2019). In each case, a model was generated to ensure the coordination environment of the tellurium atom of interest was properly described (e.g., including close contacts) (see Supplementary Material, Appendix C). No geometry optimization was subsequently performed. The zeroth-order regular approximation (ZORA) method was used to include (i) scalar relativistic terms and, in a second set of calculations, (ii) scalar and spin-orbit (so) relativistic terms in the magnetic shielding tensor calculations (Schreckenbach and Ziegler 1995, 1996, 1997; Wolff and Ziegler 1998; Wolff et al. 1999; Autschbach and Zurek 2003; Autschbach 2013). The PBE0 functional (Adamo and Barone 1999) was used with the TZ2P basis set.

Experimentally established crystallographic information files (CIF) were used as input for CASTEP (version 20.11; Clark et al. 2005) calculations of nuclear magnetic shielding tensors using the gauge-including projector-augmented wave (GIPAW) DFT method (Pickard and Mauri 2001; Profeta et al. 2003, Yates et al. 2007). CCDC codes are as follows (Semenov 2018): BIHQOB (**1a**; ccdc 1837178), BIHQUH (**1b**; ccdc 1837179), BIHRAO (**1c**; ccdc 1837180).

Calculations on KOCN were performed using a CIF based on the published single-crystal X-ray structure (Hendricks and Pauling 1925); however, this structure features a 50:50 (presumed) static disorder of the oxygen and nitrogen atoms. To model this disorder, the structure was manually modified in Materials Studio 5.0 to generate a supercell structure with *P*1 symmetry (lattice parameters $a = b = 6.070$ Å, c = 7.030 Å) wherein half of the disordered sites were randomly assigned as oxygen atoms and half as nitrogen atoms while ensuring each of the resultant ions were cyanates. Materials Studio 5.0 was used to create CASTEP .param and .cell files for all structures. The PBE (Perdew et al., 1996) and RPBE (Hammer et al., 1999) functionals were employed in separate sets of calculations using on-the-fly pseudopotentials. Cut-off energies were typically incremented to several hundred eV to ensure convergence of the computed magnetic shielding tensors (*vide infra*). Both the default Koelling-Harmon (Koelling and Harmon 1977) and ZORA-scalar relativistic treatments were used, in separate sets of calculations. The k-points used to sample the Brillouin zone were determined using the 'fine' automated setting of Materials Studio. Convergence behaviour with respect to k-point setting is shown in the Supplementary Material (Appendix C).

Finally, two additional series of calculations were performed on small model systems using Gaussian 09 software (B3LYP/DGDZVP) and ADF software (ZORA-so, SAOP/QZ4P). The models were constructed from the available CIFs and specific distances and angles were varied to assess the ^{125}Te and ^{15}N magnetic shielding tensor response.

EFGShield version 4.7 (Adiga et al. 2007) and MagresView version 1.6.2 (Sturniolo et al. 2016) were used to parse and visualize tensor output from the various sets of DFT calculations.

Magnetic shielding tensors were converted to chemical shift tensors according to $\delta = (\sigma_{ref}-\sigma)/(1-\sigma_{ref})$. The experimental absolute ^{125}Te shielding scale was used where $\sigma_{ref}(Me_2Te) = 4333$ ppm (Jameson and Jameson 1987). The experimental absolute ^{15}N shielding scale was used where $\sigma_{ref}(NH_3(l)) = 244.6$ ppm (Jameson et al. 1981).

6.3.3 Results and Discussion

(a) NMR Spectroscopy

Compound **1**, as well as cocrystals **1a**, **1b**, and **1c**, were prepared according to adapted literature procedures. Single crystals of **1a**, **1b**, and **1c** were grown and their crystal structures verified by single-crystal X-ray diffraction. In all three cases, the same structures were obtained as those reported in the literature. The morphology and phase purity of powders of these cocrystals were similarly assessed via powder X-ray diffraction (Figure 6.3.2 and Supplementary Material, Appendis C). These findings allow for a confident interpretation of solid-state NMR data in the context of the diffraction-based structures (*vide infra*).

With the goal of investigating the impact on the cyanate nitrogen chemical shift tensor of chalcogen bond formation to tellurium in cocrystal **1a**, a second sample was prepared using isotopically ^{15}N-enriched KOCN (95%). This isotopically enriched sample presented a powder X-ray diffractogram identical to that for the natural abundance sample and identical to that simulated based on the single crystal X-ray structure (Figure 6.3.2). These data show that the crystal structure of both the natural abundance sample and the isotopically enriched sample prepared herein are consistent with that reported via single-crystal X-ray diffraction.

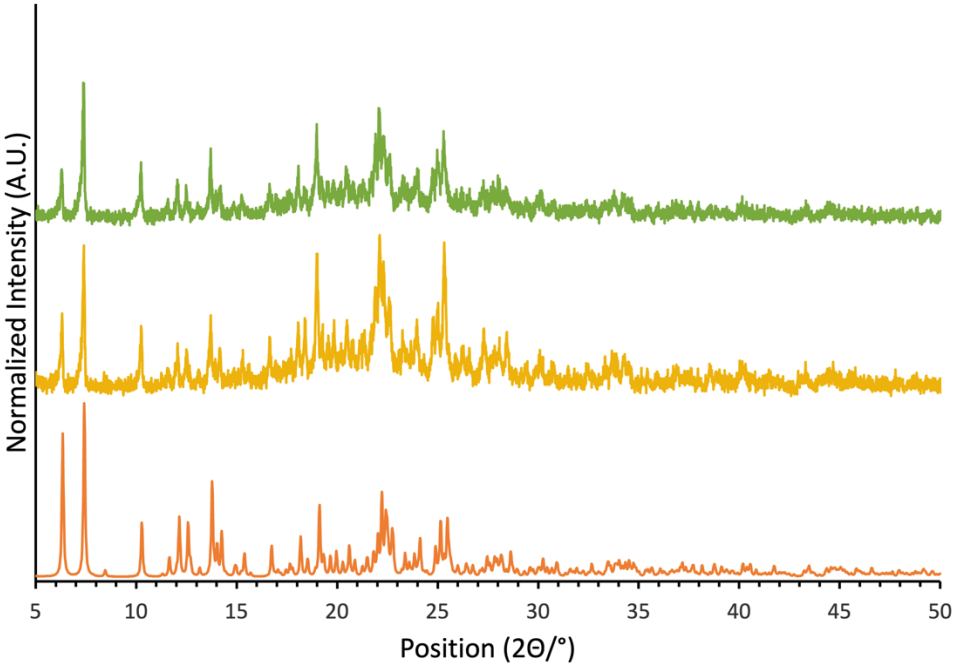

Figure 6.3.2: Experimental PXRD diffractograms of $[K(18\text{-crown-6})]^{+}[1\text{-OCN}]^{-}$ (1a) in yellow (unlabelled KOCN) and green (^{15}N-labelled KOCN). The simulated diffractogram based on the single-crystal X-ray structure (CCDC code BIHQOB) is shown at the bottom (orange). The vertical scale has been approximately normalized by eye, not with respect to any particular peak.

The ^{125}Te magic-angle spinning NMR spectra of solid powdered **1a**, **1b**, and **1c** are presented in Figures 6.3.3, 6.3.4, and 6.3.5. Spectra were acquired with high-power proton decoupling. Cross-polarization from protons did not yield good-quality NMR spectra, likely owing to the fact that the tellurium atoms in each sample are relatively distant from the only hydrogens in the system. Furthermore, these hydrogens are found on the 18-crown-6 rings, which are known to be mobile (Buchanan et al. 1987; Ratcliffe et al. 1992), thereby further weakening dipolar interactions between ^{1}H and ^{125}Te necessary for cross-polarization. The ^{125}Te MAS NMR spectra were acquired in a moderate magnetic field of 9.4 T, which was found to offer a good balance

between sensitivity and spectral broadening due to chemical shift anisotropy. Spectra were generally acquired with at least two different MAS rates (9.000 and 11.000 kHz) in order to distinguish the isotropic peaks from the spinning sidebands. These sideband manifolds were fit using the Herzfeld-Berger method (Herzfeld and Berger 1980) to determine the three principal components of the chemical shift tensors ($\delta_{11} \geq \delta_{22} \geq \delta_{33}$) as well as the span ($\Omega = \delta_{11}-\delta_{33}$) and skew ($\kappa = 3(\delta_{22}-\delta_{iso})/\Omega$) of these tensors. The data are presented in Table 5.3.2, along with previously reported data for pure ChB donor **1**.

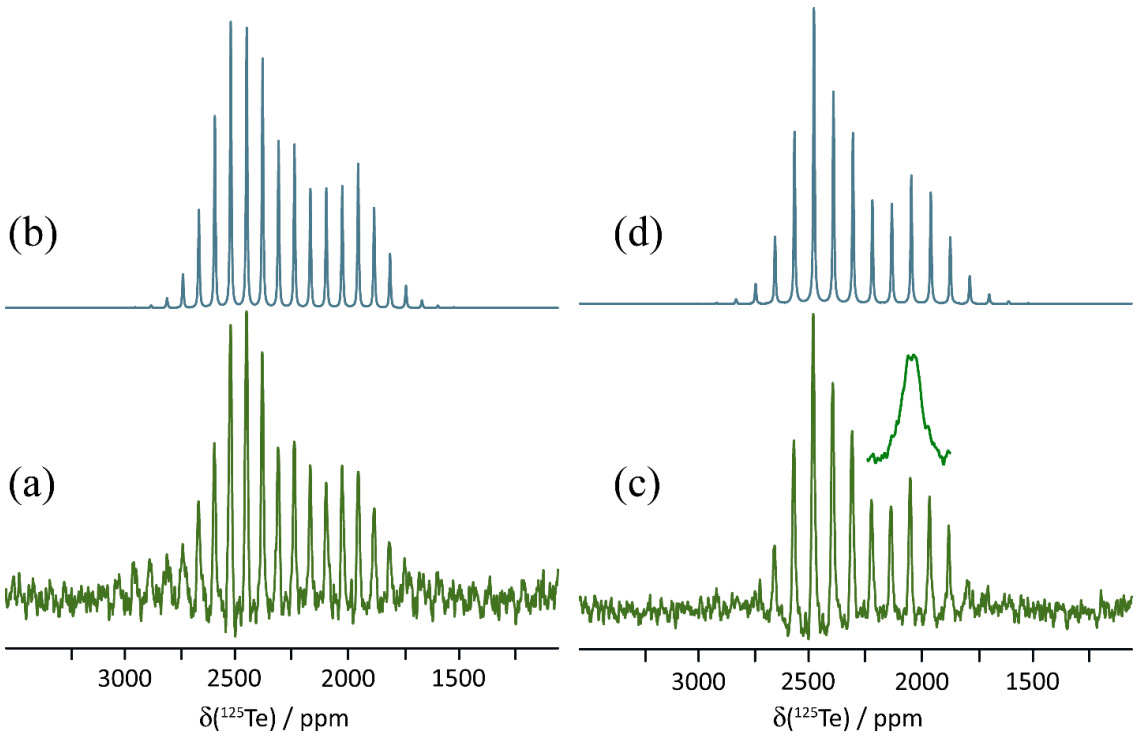

Figure 6.3.3: Tellurium-125 magic-angle spinning NMR spectra of cocrystal 1a. B_0 = 9.4 T. MAS rate = 9.000 kHz (a, b) or 11.000 kHz (c, d). Experimental spectra (a, c) were acquired using a Bloch decay with high-power proton decoupling. Spectra simulated based on Herzfeld-Berger analyses are shown above (b, d). The inset in (c) shows an enlargement of the centreband region, with possible evidence for two crystallographically distinct tellurium sites.

Pure **1** crystallizes in the $P2_12_12_1$ space group and features a single crystallographically distinct tellurium atom. Each tellurium atom has two σ-holes available for chalcogen bonding with two additional molecules of 3,4-dicyano-1,2,5-telluradiazole, with electron donation coming from the ring nitrogens. The two resulting Te···N chalcogen bonds have distances of 2.659 and 2.767 Å, and N-Te···N angles of 152.1 and 149.1°, respectively. These interactions result in planar sheets of molecules within the crystal. The strength of these chalcogen bonds may be gauged via the reduced distance parameter (Table 6.3.1), $R_{ChB} = d_{ChB}/\Sigma_{vdW}$ (where d_{ChB} is the distance between Te and N, and Σ_{vdW} is the sum of the van der Waals radii of Te and N). The R_{ChB} values for **1** are 0.74 and 0.77. The ^{125}Te chemical shift tensor data for **1** (Table 6.3.2) have been reported previously; briefly, the isotropic chemical shift is 2332.8 ppm and the span is 1268 ppm (Kumar et al. 2020b). The observation of one chemical shift is consistent with the presence of a single crystallographically distinct tellurium atom in the unit cell of **1**.

Salt cocrystal **1a** crystallizes in the $P2_1/c$ space group and features two crystallographically distinct tellurium atoms, each of which are engaged in chalcogen bonding via a single σ-hole to the nitrogen atom of the cyanate ion. These nitrogen atoms are also each in proximity to a potassium cation, each of which are complexed by an 18-crown-6 molecule. The two tellurium sites, and the geometries of the two Te···N chalcogen bonds, are very similar. For example, the two Te···N distances are 2.546 and 2.533 Å and the two N-Te···N angles are 166.2 and 163.8°. The ^{125}Te MAS NMR experiments show inconclusive evidence for these two similar sites, with a possibly unresolved doublet with peak maxima at approximately 2315.7 and 2311.1 ppm (Figure 6.3.3). The spinning sideband pattern was analyzed to obtain chemical shift tensor parameters

using one isotropic chemical shift at 2313.1 ppm (Figure 6.3.3). The resulting span of the tensor is 740 ppm, a decrease of 528 ppm relative to pure **1**.

Salt cocrystal **1b** crystallizes in the *P*1 space group and has one crystallographically distinct tellurium atom which engages in chalcogen bonding with the sulfur atom of the thiocyanate anion at a distance of 3.038 Å. The N-Te···S chalcogen bond angle is 166.8°. ^{125}Te MAS NMR shows a characteristic spinning sideband manifold about the single isotropic chemical shift, consistent with the X-ray crystal structure (Figure 6.3.4). The isotropic chemical shift is 2389.2 ppm and the span of the tensor is 1168 ppm, much larger than that for **1a**, but still smaller than for the pure chalcogen bond donor **1**.

Finally, salt cocrystal **1c** crystallizes in the *P*1 space group and has one crystallographically distinct tellurium atom which engages in chalcogen bonding with the selenium atom of the selenocyanate anion at a distance of 3.126 Å. The N-Te···Se chalcogen bond angle is 167.2°. Again, the ^{125}Te MAS NMR spectrum is consistent with the X-ray diffraction structure, showing one isotropic chemical shift at 2376.3 ppm (Figure 6.3.5). The span of the chemical shift tensor, 1136 ppm, is again smaller than that seen for the pure donor **1**.

Table 6.3.1: Structural information for pure ChB donor **1** and its chalcogen-bonded salt cocrystals

	$r_{Te\cdots X}$ / Å	R_{ChB}[a]	$\theta_{Te\cdots XC}$ / °	CCDC ref
1	2.659 (X = N)	0.74	152.1	AREGEK
	2.767 (X = N)	0.77	149.4	

1a-mol1[b]	2.546 (X = N)	0.71	166.2	BIHQOB
1a-mol2[b]	2.533 (X = N)	0.70	163.8	BIHQOB
1b	3.038 (X = S)	0.79	166.8	BIHQUH
1c	3.126 (X = Se)	0.79	167.2	BIHRAO

a. Van der Waals radii used: 2.06 Å for Te; 1.55 Å for N; 1.80 Å for S; 1.90 Å for Se (Bondi 1964). b. ‘mol1’ and ‘mol2’ refer to the two crystallographically distinct molecules in the unit cell.

The principal components of the ^{125}Te chemical shift tensors measured presently, as well as the isotropic chemical shifts and CS tensor spans, are consistent with data acquired for other similar tellurium-based systems featuring chalcogen bonds (Kumar et al. 2020b; Nag et al. 2022). When forming cocrystals of 3,4-dicyano-1,2,5-telluradiazole, it is a general conclusion that the isotropic ^{125}Te chemical shift can either increase or decrease modestly, and that the span of the tellurium chemical shift tensor almost always decreases, often by hundreds of ppm.

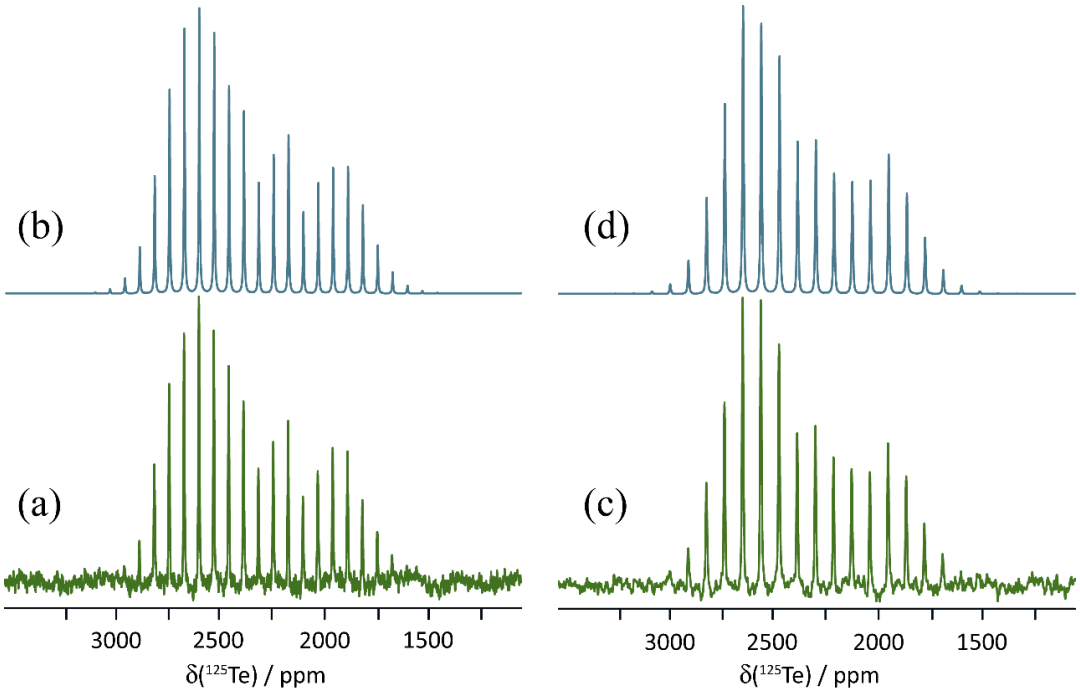

Figure 6.3.4: Tellurium-125 magic-angle spinning NMR spectra of cocrystal 1b. B_0 = 9.4 T. MAS rate = 9.000 kHz (a, b) or 11.000 kHz (c, d). Experimental spectra (a, c) were acquired using a Bloch decay with high-power proton decoupling. Spectra simulated based on Herzfeld-Berger analyses are shown above (b, d).

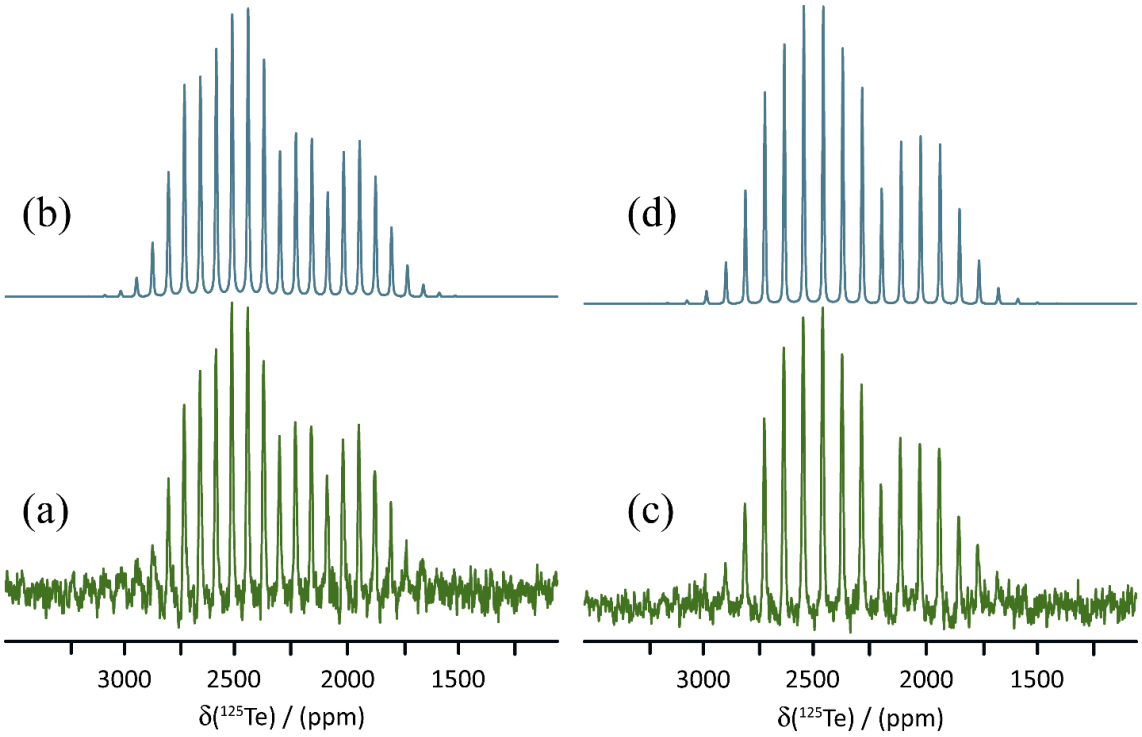

Figure 6.3.5: Tellurium-125 magic-angle spinning NMR spectra of cocrystal 1c. B_0 = 9.4 T. MAS rate = 9.000 kHz (a, b) or 11.000 kHz (c, d). Experimental spectra (a, c) were acquired using a Bloch decay with high-power proton decoupling. Spectra simulated based on Herzfeld-Berger analyses are shown above (b, d).

The ^{15}N MAS NMR spectra of isotopically ^{15}N-enriched KOC^{15}N and ^{15}N-**1a** are shown in Figure 6.3.6. The X-ray diffraction structure of KOCN includes oxygen and nitrogen occupying the same sites with a 50:50 occupancy, thus suggesting the possibility of static or dynamic disorder in the structure. This compound packs in the *I*4/*mcm* space group and the nitrogen/oxygen sites have local C_{2v} symmetry. This symmetry means that the ^{15}N chemical shift tensor may have up to three unique principal components. Fitting of the ^{15}N MAS NMR spinning sideband manifold results in a chemical shift tensor with axial symmetry (δ_{iso} = 90.7 ppm and Ω = 231 ppm). Although the fitting process can be subject to errors (Hodgkinson and Emsley 1997), a perfectly axially symmetric tensor would be consistent with the two components which lie perpendicular to the cyanate axis having very similar magnitudes. DFT calculations of the nitrogen shielding tensor (*vide infra*) confirm that there is no dynamic disorder of the cyanate ions at room temperature, as the magnitude of Ω(^{15}N) is not averaged compared to the values obtained by DFT at 0 K.

The ^{15}N MAS NMR spectrum of ^{15}N-**1a** presents two distinct chemical shifts and spinning sideband patterns, consistent with the presence of two crystallographically distinct cyanate ions in the X-ray diffraction structure of this salt cocrystal (Figure 6.3.6). The isotropic chemical shifts are 79.5 and 77.8 ppm, and the spans of these tensors are 222 and 191 ppm, respectively. It is seen that both the isotropic shifts and the spans are reduced compared to those in pure KOCN. This is mainly attributed to changes in δ_{33}, the principal component which lies along the cyanate ion's axis. Its value increases from -64 ppm in KOCN to -55 and -38 ppm in each of the two sites in **1a**. Furthermore, the axial symmetry of the ^{15}N chemical shift tensor in KOCN is lost upon formation

of a chalcogen bond to tellurium in **1a**. This can be quantified by the decrease in the skew of the tensor from 1.00 to 0.63, or alternatively by the decrease in the value of the intermediate component δ_{22} from 168 ppm to 126 ppm (site 1) or 118 ppm (site 2). This loss of axial symmetry is also indicative of a decrease in symmetry at nitrogen in the cyanate ion.

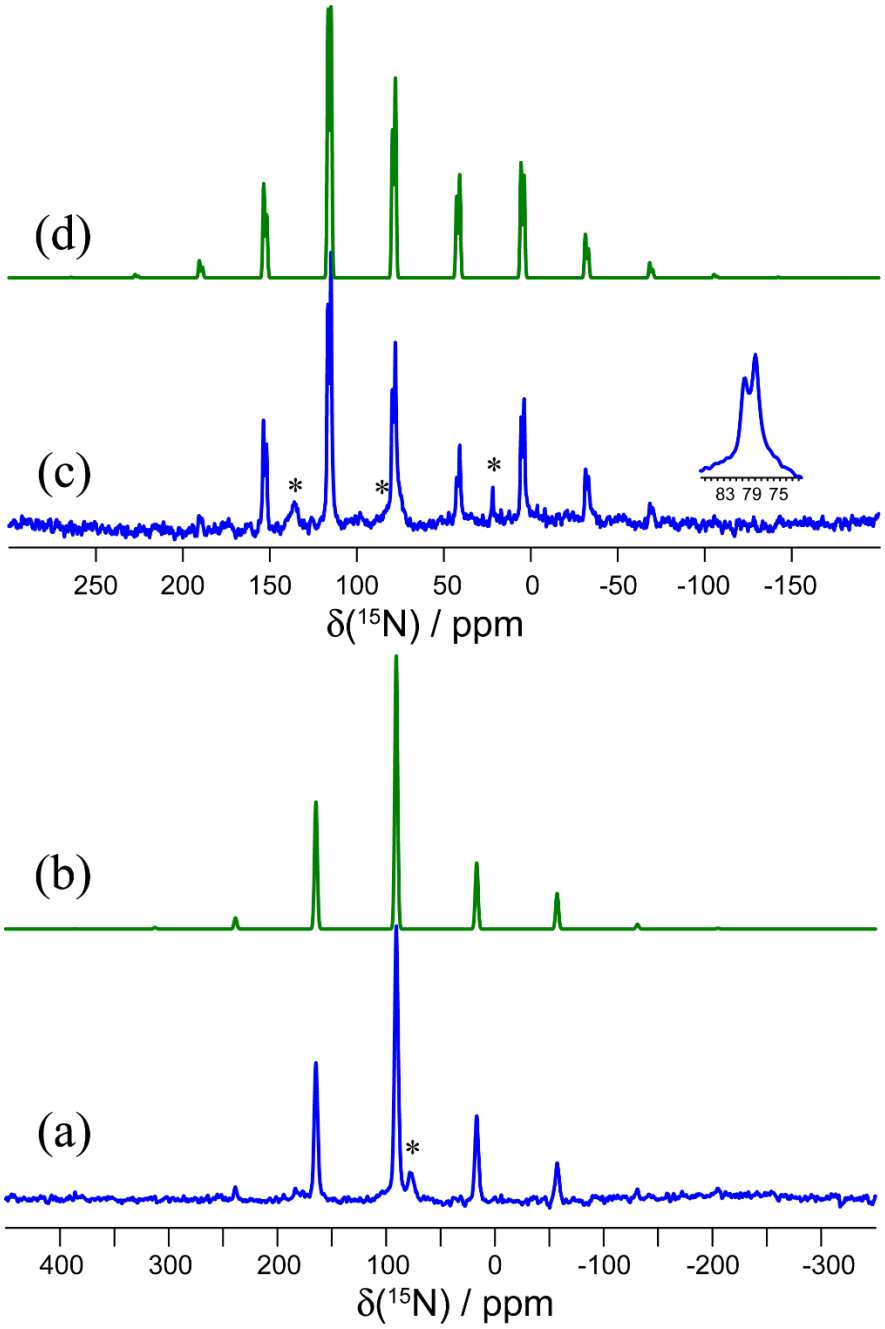

Figure 6.3.6: Nitrogen-15 magic-angle spinning NMR spectra of (a) ^{15}N-enriched KOCN (MAS rate of 3.000 kHz) and (c) ^{15}N-enriched cocrystal 1a (MAS rate of 1.500 kHz). B_0 = 9.4 T. The enlarged inset in (c) shows the resolution of the two centrebands for the two crystallographically

distinct nitrogen sites. Simulated spectra based on Herzfeld-Berger analyses are shown in (b) and (d). Impurity peaks are marked with asterisks.

Table 6.3.2: Experimentally measured ^{125}Te and ^{15}N chemical shift tensors for the ChB donor (1), starting material (a), and cocrystals 1a-c.

sample	nucleus	δ_{iso} (ppm)	Ω	κ	δ_{11} (ppm)	δ_{22} (ppm)	δ_{33} (ppm)
1[a]	^{125}Te	2332.8(0.1)	1268 (3)	0.49	2863(5)	2540 (3)	1595 (4)
KOCN	^{15}N	90.7 (0.2)	231(1)	1.00	168 (1)	168 (1)	-64 (1)
1a	^{15}N (site 1)	79.5 (0.2)	222 (5)	0.63	167 (5)	126 (3)	-55 (4)
1a	^{15}N (site 2)	77.8 (0.2)	191 (7)	0.63	153 (6)	118 (3)	-38 (5)
1a	^{125}Te	2313.1 (1)[b]	740 (6)	0.49	2623 (10)	2434 (6)	1883 (7)
1b	^{125}Te	2389.2 (1)	1168 (5)	0.48	2880 (2)	2576 (1)	1712 (3)
1c	^{125}Te	2376.3 (0.7)	1136 (14)	0.34	2880 (2)	2504 (9)	1744 (13)

a. From Kumar et al., 2020b. b. There is an unresolved splitting due to two crystallographically distinct sites with peak maxima of approximately 2315.7 and 2311.1 ppm.

(b) DFT Calculations of Magnetic Shielding Tensors

Density functional theory calculations of the tellurium magnetic shielding tensors in **1**, **1a**, **1b**, and **1c** were carried out using a variety of approaches. The results of these calculations are summarized in Table 6.3.3. Four sets of data are presented. The first two, carried out using a ZORA relativistic treatment as implemented in ADF, use a cluster model, the PBE0 functional, and the TZ2P basis set. In one set of calculations, only a scalar relativistic treatment is used, while in the second one a spin-orbit relativistic treatment is used. The other two sets of calculations, carried out using the GIPAW approach as implemented in CASTEP, used the RPBE functional. In one set of calculations, the default Koelling-Harmon scalar relativistic method is used, while in the

second one the scalar relativistic ZORA method is employed. These various sets of calculations help to determine the relative importance of including the crystal lattice in the model used (as is done using periodic boundary conditions in the GIPAW approach) compared to the model used to treat relativistic effects. A cursory inspection of the data in Table 6.3.3 suggests that the ZORA-spin orbit method, using a cluster model, provides results in best agreement with the experimental data.

Selected data from Table 6.3.3 are plotted in Figures 6.3.7 and 6.3.8. In Figure 6.3.7, the experimental ^{125}Te chemical shift tensor spans (Ω), in navy blue, are compared to the DFT-computed values. Comparing the spans is one way to assess the computed values, as it removes the impact of imperfections in the computed isotropic magnetic shielding constant. The experimental values of the spans range from a low of 740 ppm for **1a** to a high of 1268 ppm for pure chalcogen bond donor **1**. The ZORA-spin orbit calculations (ADF) provide the best agreement with these experimental data; in the case of molecule 2 of salt cocrystal **1a**, the computed value of 730.4 ppm is less than 2% below the experimental value. The computed value for **1b** is in worst agreement with experiment, where an overestimation of 24% is seen (1453 ppm vs 1168 ppm). The ZORA-scalar calculations (ADF) provide the next-best agreement with experiment, but the spans are consistently underestimated by approximately 10 to 45 %. GIPAW calculations using the Koelling-Harman scalar relativistic treatment consistently underestimate the experimental values by up to nearly 50%. Finally, the GIPAW calculations using the ZORA scalar relativistic treatment fare worst in comparison to experiment with most values underestimated by approximately 50%.

Table 6.3.3: DFT-computed ^{125}Te magnetic shielding tensors

	1	**1a-**	**1a-**	**1b**	**1c**
Cluster model, PBE0/TZ2P, ZORA-so (ADF)					
σ_{11}	688.4	910.8	852.6	311.0	296.9
σ_{22}	939.2	1125.6	1161.9	911.8	936.1
σ_{33}	2029.	1641.2	1638.3	1763.	1697.
σ_{is}	1219.	1225.9	1217.6	995.4	976.9
Ω	1341.	730.4	785.7	1452.	1400.
κ	0.63	0.41	0.21	0.17	0.09
Cluster model, PBE0/TZ2P, ZORA-scalar (ADF)					
σ_{11}	338.6	365.2	375.4	-38.0	-43.0
σ_{22}	606.3	722.3	784.0	536.1	545.4
σ_{33}	1231.	852.5	795.4	978.8	974.0
σ_{is}	725.6	646.7	651.6	492.3	492.1
Ω	893.4	487.3	420.0	1016.	1016.
κ	0.40	-0.47	-0.95	-0.13	-0.16
Periodic boundary conditions, GIPAW, RPBE, 700 eV, Koelling-Harmon-scalar					
σ_{11}	248.8	349.8[a]	376.3[a]	119.4	136.5
σ_{22}	383.1	727.2[a]	828.4[a]	506.1	658.3
σ_{33}	977.0	749.1[a]	872.9[a]	793.7	874.8
σ_{is}	548.3	608.7[a]	692.5[a]	473.0	556.5
Ω	692.2	399.2[a]	496.6[a]	674.3	738.2
κ	0.72	-0.89[a]	-0.82[a]	-0.15	-0.41
Periodic boundary conditions, GIPAW, RPBE, 700 eV, ZORA-scalar (CASTEP)					
σ_{11}	737.7	799.2[a]	822.2[a]	582.7	598.7
σ_{22}	826.5	1145.6	1239.7	941.5	1083.
σ_{33}	1378.	1166.6	1282.8	1208.	1283.
σ_{is}	981.0	1037.1	1114.9	910.9	988.6
Ω	641.0	367.4[a]	460.6[a]	625.9	685.2
κ	0.72	-0.89[a]	-0.81[a]	-0.15	-0.41

a. 500 eV cut-off. See Supplementary Material (Appendix C) for convergence tests.

A further assessment of the DFT-computed tellurium magnetic shielding tensors is presented in Figure 6.3.8, where the individual principal components are plotted against the experimental chemical shift tensor values for the four computational methods used. Again, the ZORA-spin orbit approach provides the best agreement; the slope of the line of best fit (-1.1304) is the closest to unity among the four methods, the Pearson correlation coefficient of 0.9531 is the highest among the for methods, and the intercept of 3777.6 ppm is the closest to the experimental absolute shielding constant for dimethyltelluride, 4333 ppm. The remaining methods do not fare as well, with slopes as low as -0.4983 for the ZORA-scalar (CASTEP) calculations and R^2 values as low as 0.7768 for the Koelling-Harmon (CASTEP) calculations. The computed intercept for the latter set of calculations is also very low, 1869.7 ppm.

From all of these calculations, it may be concluded that the ZORA-spin orbit approach, using cluster models, provides the best results for the systems studied herein. The substantial role of spin-orbit relativistic effects seems to be the most important consideration. Upward spin-orbit shifts of several hundred ppm in each the principal components of the magnetic shielding tensor are seen when comparing the ZORA-scalar results to the ZORA-spin orbit results. These spin-orbit effects are much more important in the systems studied here than any potential effects on the magnetic shielding tensors from the surrounding molecules in the crystal lattice. This finding is consistent with previous literature reports on unrelated tellurium-containing systems (Alkan and Dybowski 2018).

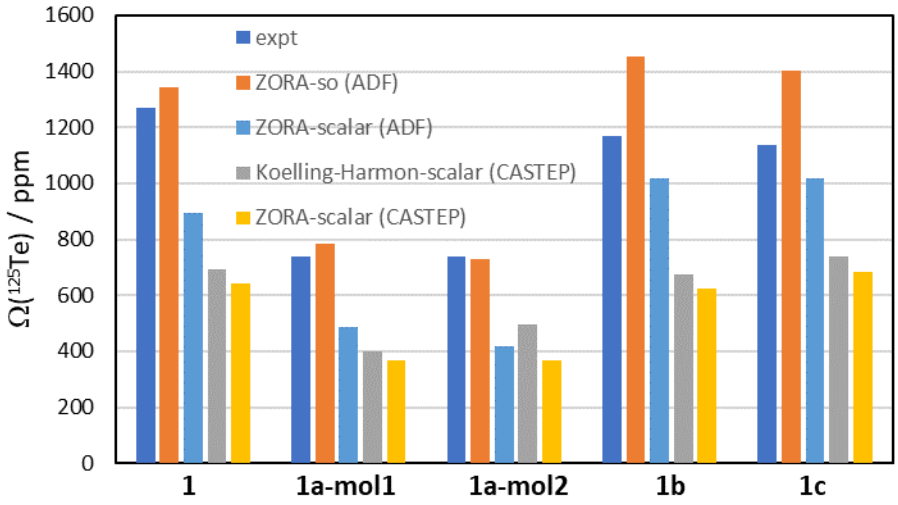

Figure 6.3.7: Comparison of experimental (navy blue) and computed tellurium magnetic shielding tensor spans. Orange: ZORA-so (ADF); blue: ZORA-scalar (ADF); grey: Koelling-Harmon-scalar (CASTEP); yellow: ZORA-scalar (CASTEP).

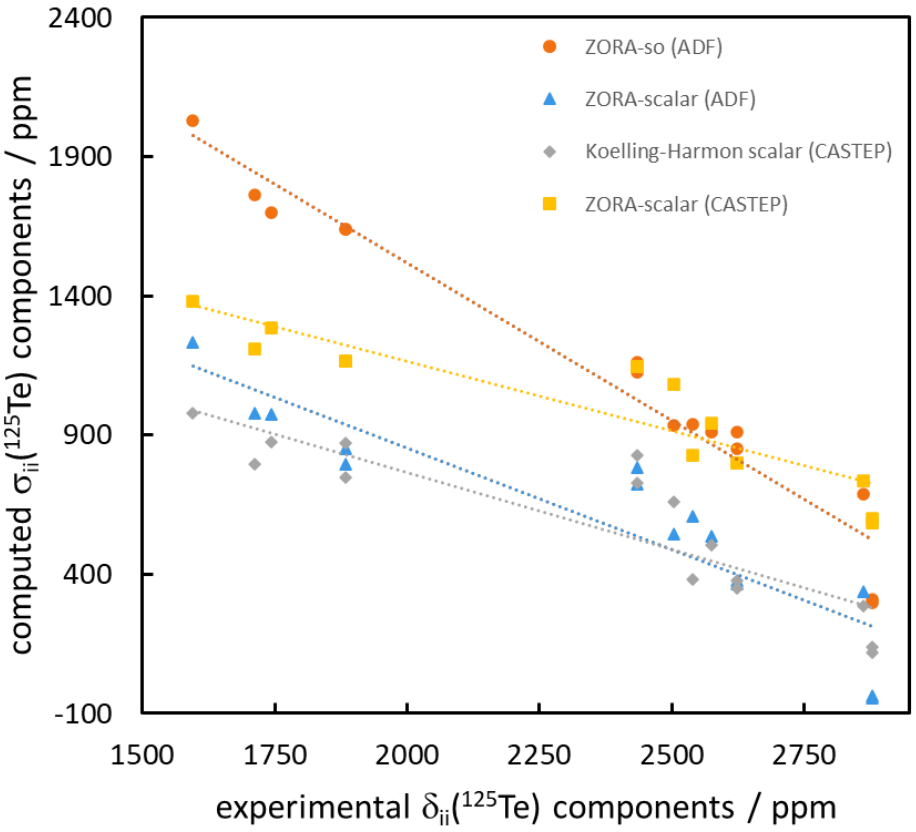

Figure 6.3.8: DFT-computed tellurium magnetic shielding tensor principal components plotted against experimental ^{125}Te chemical shift tensor principal components. Orange circles: ZORA-so (ADF) [$\sigma_{ii} = -1.1304\delta_{ii} + 3777.6$ ppm; $R^2 = 0.9531$]; blue triangles: ZORA-scalar (ADF) [$\sigma_{ii} = -0.7255\delta_{ii} + 2302.9$ ppm; $R^2 = 0.8259$]; grey diamonds: Koelling-Harmon-scalar (CASTEP) [$\sigma_{ii} = -0.5518\delta_{ii} + 1869.7$ ppm; $R^2 = 0.7768$]; yellow squares: ZORA-scalar (CASTEP) [$\sigma_{ii} = -0.4983\delta_{ii} + 2159.4$ ppm; $R^2 = 0.8036$].

DFT-computed ^{15}N magnetic shielding tensors for KOCN and for the salt cocrystals **1a**, **1b**, and **1c** are shown in Table 6.3.4. The same four methods used above for ^{125}Te magnetic shielding tensors were also used to calculate the ^{15}N magnetic shielding tensors, except in the case of KOCN where building a cluster model was not realistic. The nuclear magnetic

shielding values have also been converted to chemical shifts using the experimental absolute shielding scale for nitrogen. As nitrogen is a lighter element, the impact of including spin-orbit relativistic effects is inconsequential for the systems studied here (i.e., changes in the components are less than 0.5 ppm). The computed ^{15}N isotropic chemical shift for KOCN, 80.7 ppm (GIPAW, RPBE, 500 eV, Koelling-Harmon) is 10 ppm lower than the experimental value of 90.7 ppm. The span of the ^{15}N chemical shift tensor for KOCN is calculated at the same level of theory to be 221.4 ppm, again about 10 ppm lower than the experimental value of 231(1) ppm. These discrepancies arise entirely due to underestimations of the δ_{11} and δ_{22} principal components, i.e., those which lie perpendicular to the cyanate principal axis. The δ_{33} component is calculated more easily as, in the limit of an isolated linear system, the paramagnetic contribution to the shielding constant is zero. It is seen that the experimental and computed values of δ_{33}(^{15}N) in KOCN are in agreement (-64(1) ppm and -63.9 ppm, respectively). The DFT calculations of ^{15}N chemical shift tensors for both crystallographic sites in salt cocrystal **1a**, which features a chalcogen bond between the cyanate nitrogen atom and the tellurium atom, do not generally reproduce the experimentally observed decrease in span. When the same computational method is used for KOCN and for **1a** (GIPAW, RPBE, 500eV, Koelling-Harmon), an increase in the span from 221.4 ppm to 248.2 ppm is seen for site 1, and a small increase from 221.4 ppm to 222.6 ppm is seen for site 2. This is dominated by an increase in δ_{11}, which is not seen experimentally.

Table 6.3.4: DFT-computed ^{15}N magnetic shielding and chemical shift tensors

	σ_{11} / ppm	σ_{22} / ppm	σ_{33} / ppm	δ_{11} / ppm	δ_{22} / ppm	δ_{33} / ppm	δ_{iso} / ppm	Ω / ppm	κ
KOCN[a]	87.1	96.3	308.5	157.6	148.4	-63.9	80.7	221.4	0.92
KOCN[b]	87.4	96.6	308.6	157.2	148.0	-64.0	80.4	221.2	0.92
1a-mol1[a]	52.4	75.5	300.6	192.2	169.1	-56.0	101.7	248.2	0.81
1a-mol2 *a*	64.3	81.4	286.9	180.4	163.2	-42.3	100.4	222.6	0.85
1a-mol1 *b*	52.6	75.8	300.8	192.0	168.8	-56.2	101.6	248.2	0.81
1a-mol2 *b*	64.7	81.8	287.1	179.9	162.8	-42.5	100.1	222.4	0.85
1a-mol1[c]	64.2	98.2	313.7	157.1	131.8	-54.7	78.1	249.6	0.73
1a-mol2 *c*	87.6	112.8	299.3	180.5	146.4	-69.2	85.9	211.7	0.76
1a-mol1 *d*	69.5	98.3	337.8	151.3	122.0	-65.3	69.3	268.3	0.79
1a-mol2 *d*	93.4	122.6	309.9	175.1	146.3	-93.3	76.1	175.3	0.73

a. GIPAW, RPBE, 500eV, Koelling-Harmon. b. GIPAW, RPBE, 500eV, ZORA-scalar. c. ADF, PBE0/TZ2P, ZORA-scalar. d. ADF, PBE0/TZ2P, ZORA-spin-orbit.

In addition to the impact of chalcogen bonding on the magnitudes of the tellurium and nitrogen magnetic shielding tensors, the impact on the orientations of these tensors in the molecular frame were considered. This absolute orientational information is not available from NMR studies of powdered samples; rather, approaches such as single-crystal NMR must be used. Recent experimental single-crystal NMR work from our group demonstrated how changes in chemical shift tensor orientations could be correlated with halogen bond geometry in a series of phosphine oxide-iodoperfluorobenzene cocrystals (Xu et al. 2019). Presently, the results of DFT computations of the tellurium and nitrogen tensor orientations are assessed. As shown in Figure 6.3.9, in both pure chalcogen bond donor **1**, and in each of the cocrystals **1a**, **1b**, and **1c**, the largest (and pseudounique) component of the ^{125}Te magnetic shielding tensor lies approximately perpendicular to the telluradiazole plane. In pure **1**, the structure of which features self-complementary Te···N chalcogen bonds, the direction of the least shielded σ_{11} component bisects the N-Te-N angle of the telluradiazole ring. The orientation of σ_{11} is modified away from this bisector as a result of chalcogen bonds to N, S, or Se. This change in orientation is also clearly reflective of the change in local symmetry about the telluradiazole ring. Conversely, the change in the orientation of the nitrogen chemical shift tensor in **1a** when compared to pure KOCN is negligible (Figure 6.3.10); a deviation of the σ_{33} component of only 3° from the cyanate axis is noted in **1a**.

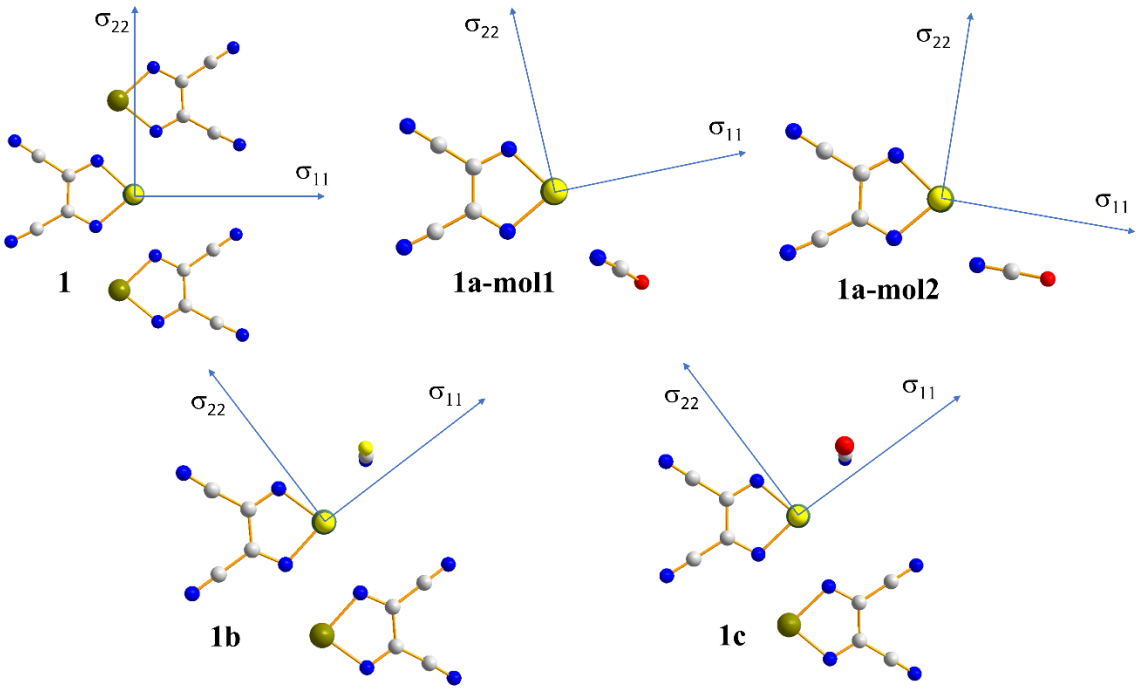

Figure 6.3.9: ZORA-so (PBE0/TZ2P) DFT-computed ^{125}Te magnetic shielding tensor orientations. In each case, σ_{33} is perpendicular to the plane of the telluradiazole ring. Note that for 1a the entire cluster used for the calculation is not shown for clarity. The complete model is shown in the Supplementary Material (Appendix C).

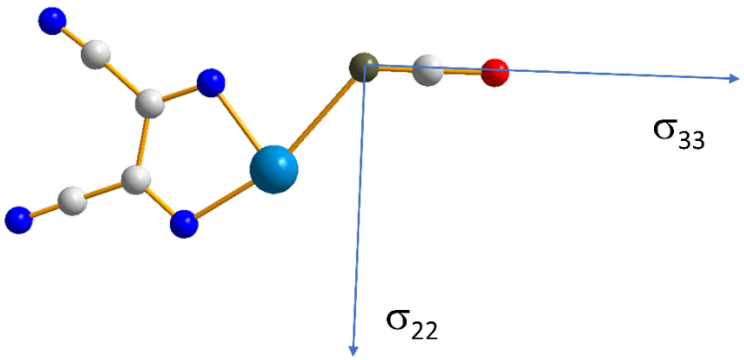

Figure 6.3.10: ZORA-so (PBE0/TZ2P) DFT-computed ^{15}N magnetic shielding tensor orientation in 1a. σ_{11} is perpendicular to the plane of the page. The σ_{33} component deviates from the NCO

axis by approximately 3°. Note that the entire cluster used for the calculation is not shown for clarity. The complete model is shown in the Supplementary Material (Appendix C).

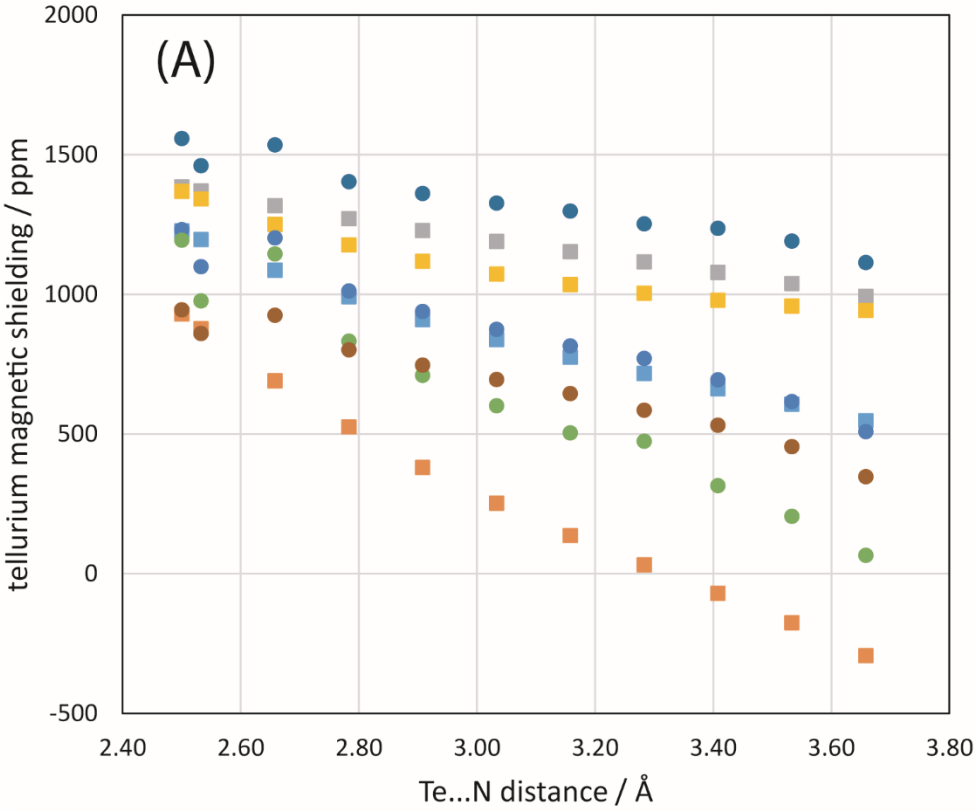
(A)
tellurium magnetic shielding / ppm
2000
1500
1000
500
0
-500
2.40
2.60
2.80
3.00
3.20
3.40
3.60
3.80
Te...N distance / Å

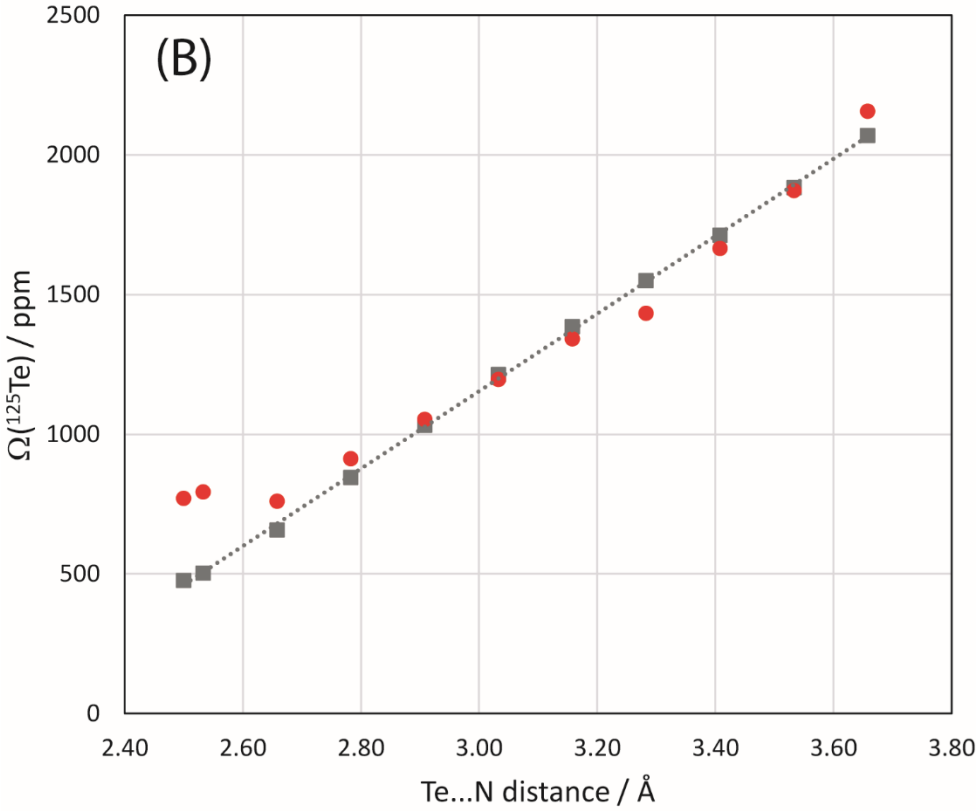
(B)
Ω(125Te) / ppm
2500
2000
1500
1000
500
0
2.40
2.60
2.80
3.00
3.20
3.40
3.60
3.80
Te...N distance / Å

Figure 6.3.11: (A) DFT-computed tellurium magnetic shielding tensor components and isotropic magnetic shielding as a function of tellurium-nitrogen distance for a model comprising telluradiazole 1 and the NCO^- anion built from the crystal structure for 1a. The Te···NC angle was fixed at the experimental value of 163.8°. Squares: B3LYP/DGDZVP (σ_{11}: orange; σ_{22}: yellow; σ_{33}: grey; σ_{iso}: blue); circles: ZORA-so, SAOP/QZ4P (σ_{11}: green; σ_{22}: brown; σ_{33}: navy blue; σ_{iso}:light blue). (B) DFT-computed tellurium magnetic shielding tensor spans for the same model. Red circles: ZORA-so, SAOP.QZ4P; grey squares: B3LYP/DGDZVP.

Finally, a simple model of **1** and the NCO^- anion was constructed and the Te···N distance systematically modified to assess its impact on the ^{125}Te and ^{15}N magnetic shielding tensors of the chalcogen bond donor and acceptor, respectively. B3LYP/DGDZVP and ZORA-so (SAOP/QZ4P) calculations were both performed. The general trend noted for ^{125}Te (Figure 6.3.11) is that the span of the tellurium shielding tensor decreases as the chalcogen bond shortens and strengthens. This finding is consistent with the experimental data and with the other sets of calculations discussed above. In the case of ^{15}N in the cyanate anion, an increase in the span is instead noted (Figure 6.3.12) as the chalcogen bond shortens. This is generally consistent with the DFT results in Table 6.3.4, but in contrast with the experimental observation that the span of the ^{15}N chemical shift tensor decreases when engaged in a chalcogen bond in **1a**. At the shortest relevant distances shown in Figure 6.3.12, however, the span of the nitrogen magnetic shielding tensors becomes almost invariant to further reduction in the Te···N distance, suggesting that in this regime other structural factors may contribute to the observed experimental decrease in span.

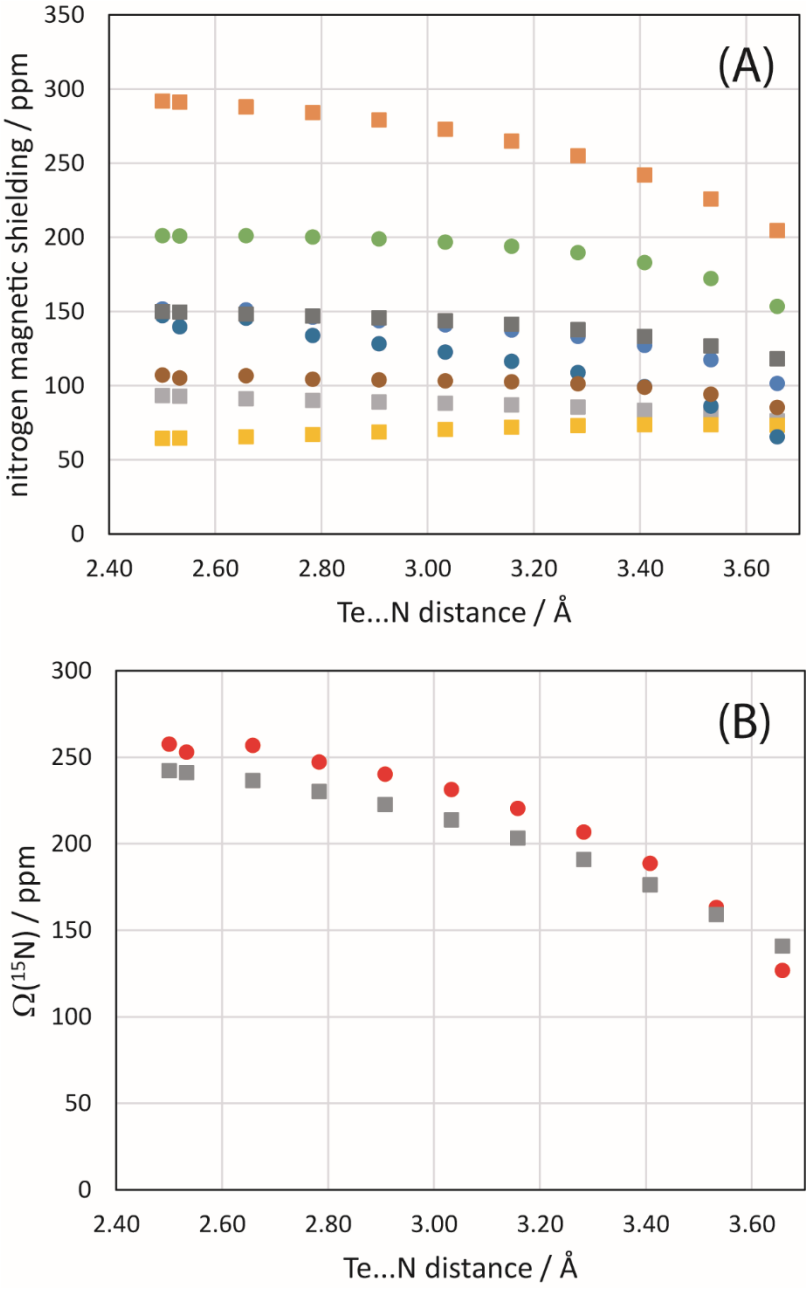

Figure 6.3.12: (A) DFT-computed nitrogen magnetic shielding tensor components and isotropic magnetic shielding as a function of tellurium-nitrogen distance for a model comprising telluradiazole 1 and the NCO^- anion built from the crystal structure for 1a. The Te···NC angle was fixed at the experimental value of 163.8°. Squares: B3LYP/DGDZVP (σ_{11}: yellow; σ_{22}: light grey; σ_{33}: orange; σ_{iso}: dark grey); circles: ZORA-so, SAOP/QZ4P (σ_{11}: brown; σ_{22}: dark blue; σ_{33}:

green; σ_{iso}: light blue). (B) B) DFT-computed nitrogen magnetic shielding tensor spans for the same model. Red circles: ZORA-so, SAOP.QZ4P; grey squares: B3LYP/DGDZVP

6.3.4 Conclusions

Tellurium-125 chemical shift tensors have been measured and used as probes of chalcogen bonding in a series of three analogous salt cocrystals. These appear to be the first such measurements for chalcogen-bonded salt cocrystals. The ^{125}Te isotropic chemical shift is seen to increase or decrease upon formation of the salt cocrystals, while the span of the chemical shift tensor consistently decreases as a result of the formation of new chalcogen bonds. These findings are consistent with prior work on neutral cocrystal systems. No simple correlations with chalcogen bond distance or angle are observed, suggesting that even in a series of analogous (but not isomorphic) systems, long-range crystal packing effects contribute non-trivially to the ^{125}Te chemical shift tensors.The ^{15}N chemical shift tensors were measured for pure potassium cyanate and for its chalcogen-bonded salt cocrystal. These data ruled out dynamic disorder of the cyanate ions at room temperature in pure KOCN. The ^{15}N isotropic chemical shift and CS tensor span both decreased upon formation of a chalcogen bond to tellurium.

Extensive DFT calculations of the ^{125}Te and ^{15}N magnetic shielding tensors provided some degree of agreement with experiment, but also highlighted some of the difficulties in describing systems where both spin-orbit relativistic effects and long-range crystal packing effects are important. Computed ^{125}Te tensor orientations show a moderate response to the formation of chalcogen bonds in the salt cocrystals studied here. The inclusion of spin-orbit

relativistic effects was found to be crucial to achieve improved agreement with the experimental ^{125}Te chemical shift tensors.

In conclusion, this work offers new experimental and computational insight into chalcogen bonds in solids via ^{125}Te and ^{15}N chemical shift tensors. In particular, in the case of [K(18-crown-6)]$^{+}$ 3,4-dicyano-1,2,5-telluradiazole-OC^{15}N^{-}, the simultaneous NMR response of both the donor and acceptor atoms in the same chalcogen bond has been assessed through measurement of their respective chemical shift tensors.

Supplementary Material

Synthetic details; further details on solid-state NMR experiments; additional X-ray diffractograms; further details on DFT calculations in Appendix C.

Competing Interests Statement

The authors declare there are no competing interests related to this manuscript.

Data Availability

Data are available upon reasonable request from the authors.

6.3.5 Acknowledgements

D. L. B. thanks the Natural Sciences and Engineering Research Council of Canada for funding. We are grateful to Shubha Gunaga, Dr. Jeffrey Ovens, and Sarah Osterholm for single-

crystal X-ray diffraction measurements, and to Dr. Patrick Szell and Vincent Morin for NMR technical support. We thank the members of the Bryce Lab for assistance in proofreading the manuscript.

References

Aakeröy CB, Bryce DL, Desiraju GR, Frontera A, Legon AC, Nicotra F, Rissanen K, Scheiner S, Terraneo G, Metrangolo P, and Resnati G. 2019. Definition of the chalcogen bond. Pure and Applied Chemistry, 91, 1889-1892. https://doi.org/10.1515/pac-2018-0713

Adamo C and Barone V. 1999. Toward reliable density functional methods without adjustable parameters: The PBE0 model. Journal of Chemical Physics, 110, 6158-6170. https://doi.org/10.1063/1.478522

Adiga S, Aebi D, and Bryce DL. 2007. EFGShield — A program for parsing and summarizing the results of electric field gradient and nuclear magnetic shielding tensor calculations. Canadian Journal of Chemistry, 85, 496-505. https://dx.doi.org/10.1139/v07-069

Alkan F and Dybowski C. 2018. Spin-orbit effects on the ^{125}Te magnetic-shielding tensor: A cluster-based ZORA/DFT investigation. Solid State Nuclear Magnetic Resonance, 95, 6-11. https://doi.org/10.1016/j.ssnmr.2018.08.005

Autschbach J. 2013. The role of the exchange-correlation response kernel and scaling corrections in relativistic density functional nuclear magnetic shielding calculations with the zeroth-order regular approximation. Molecular Physics, 111, 2544-2554. https://doi.org/10.1080/00268976.2013.796415

Autschbach J and Zurek E. 2003. Relativistic density-functional computations of the chemical shift of ^{129}Xe in Xe@C60. Journal of Physical Chemistry A, 107, 4967-4972. https://doi.org/10.1021/jp0346559

Baerends EJ, Ziegler T, Atkins AJ, Autschbach J, Baseggio O, Bashford D, Bérces A, Bickelhaupt FM, Bo C, Boerrigter PM, Cappelli C, Cavallo L, Daul C, Chong DP, Chulhai DV, Deng L, Dickson RM, Dieterich JM, Egidi F, Ellis DE, van Faassen M, Fan L, Fischer TH, Förster A, Fonseca Guerra C, Franchini M, Ghysels A, Giammona A, van Gisbergen SJA, Goez A, Götz AW, Groeneveld JA, Gritsenko OV, Grüning M, Gusarov S, Harris FE, van den Hoek P, Hu Z, Jacob CR, Jacobsen H, Jensen L, Joubert L, Kaminski JW, van Kessel G, König C, Kootstra F, Kovalenko A, Krykunov MV, Lafiosca P, van Lenthe E, McCormack DA, Medves M, Michalak A, Mitoraj M, Morton SM, Neugebauer J, Nicu VP, Noodleman L, Osinga VP, Patchkovskii S, Pavanello M, Peeples CA, Philipsen PHT, Post D, Pye CC, Ramanantoanina H, Ramos P, Ravenek W, Reimann M, Rodríguez JI, Ros P, Rüger R, Schipper PRT, Schlüns D, van Schoot H, Schreckenbach G, Seldenthuis JS, Seth M, Snijders JG, Solà M, Stener M, Swart M, Swerhone D, Tognetti V, te Velde G, Vernooijs P, Versluis L, Visscher L, Visser O, Wang F, Wesolowski TA, van Wezenbeek EM, Wiesenekker G, Wolff SK, Woo TK, and Yakovlev AL. ADF 2019.305, SCM, Theoretical Chemistry, Vrije Universiteit, Amsterdam, The Netherlands. http://www.scm.com

Bauzá A, Seth SK, and Frontera A. 2019. Tetrel bonding interactions at work: Impact on tin and lead coordination compounds. Coordination Chemistry Reviews, 384, 107-125. https://doi.org/10.1016/j.ccr.2019.01.003

Bauzá A, Alkorta I, Elguero J, Mooibroek TJ, and Frontera A. 2020. Spodium bonds: noncovalent interactions involving group 12 elements. Angewandte Chemie International Edition, 59 , 17482-17487. https://doi.org/10.1002/anie.202007814

Bertani P, Raya J, and Bechinger B. 2014. ^{15}N chemical shift referencing in solid state NMR. Solid State Nuclear Magnetic Resonance, 61-62, 15-18. https://doi.org/10.1016/j.ssnmr.2014.03.003

Bondi A. 1964. van der Waals volumes and radii. Journal of Physical Chemistry, 68, 441–451. https://doi.org/10.1021/j100785a001

Buchanan GW, Kirby RA, Ripmeester JA, and Ratcliffe CI. 1987. Solid phase stereochemical dynamics of 18-crown-6 ether and its KNCS complex as studied by low temperature carbon-13 nuclear magnetic resonance. Tetrahedron Letters, 28, 4783-4786. https://doi.org/10.1016/S0040-4039(00)96624-3

Cavallo G, Metrangolo P, Pilati T, Resnati G, and Terraneo G. 2014. Naming interactions from the electrophilic site. Crystal Growth and Design, 14, 2697–2702. https://doi.org/10.1021/cg5001717

Clark SJ, Segall MD, Pickard CJ, Hasnip PJ, Probert MJ, Refson K, and Payne MC. 2005. First principles methods using CASTEP. Zeitschrift fuer Kristallographie, 220(5-6). 567-570. https://doi.org/10.1524/zkri.220.5.567.65075

Collins MJ, Ripmeester JA, and Sawyer JF. 1987. CP/MAS tellurium-125 NMR in solids: an example of ^{125}Te-^{35,37}Cl *J* coupling. Journal of the American Chemical Society, 109, 4113–4115. https://doi.org/10.1021/ja00247a047

Collins MJ, Ripmeester JA, and Sawyer JF. 1988. Tellurium-125 solid-state NMR spectra and secondary bonding arrangements for some salts of the trimethyltelluronium and triphenyltelluronium cations. Journal of the American Chemical Society, 110, 8583-8590. https://doi.org/10.1021/ja00234a002

Daolio A, Pizzi A, Terraneo G, Frontera A, and Resnati G. 2021. Anion···anion interactions involving σ-holes of perrhenate, pertechnetate and permanganate anions. ChemPhysChem, 22. 2281-2285. https://doi.org/10.1002/cphc.202100681

Desiraju GR, Ho PS, Kloo L, Legon AC, Marquardt R, Metrangolo P, Politzer P, Resnati G, and Rissanen K. 2013. Definition of the halogen bond (IUPAC Recommendations 2013). Pure and Applied Chemistry, 85, 1711-1713. http://dx.doi.org/10.1351/PAC-REC-12-05-10

Eichele, K. 1995. HBA – Graphical Herzfeld-Berger Analysis software. Version 1.7.3.

Frontera A and Bauzá A. 2018. Regium–π bonds: an unexplored link between noble metal nanoparticles and aromatic surfaces. Chemistry – A European Journal. 24, 7228–7234. https://doi.org/10.1002/chem.201800820

Gleiter R, Werz DB, and Rausch BJ. 2003. A world beyond hydrogen bonds?—chalcogen–chalcogen interactions yielding tubular structures. Chemistry – A European Journal, 9, 2676-2683. https://doi.org/10.1002/chem.200204684

Gleiter R, Haberhauer G, Werz DB, Rominger F, and Bleiholder C. 2018. From noncovalent chalcogen–chalcogen interactions to supramolecular aggregates: experiments and calculations. Chemical Reviews, 118, 2010-2041. https://doi.org/10.1021/acs.chemrev.7b00449

Grabowski SJ. 2020. Triel bond and coordination of triel centres – comparison with hydrogen bond interaction. Coordination Chemistry Reviews, 407, 213171. https://doi.org/10.1016/j.ccr.2019.213171

Haberhauer G and Gleiter R. 2020. The nature of strong chalcogen bonds involving chalcogen-containing heterocycles. Angewandte Chemie International Edition, 59, 21236-21243. https://doi.org/10.1002/anie.202010309

Hammer B, Hansen LB, and Nørskov JK. 1999. Improved adsorption energetics within density-functional theory using revised Perdew-Burke-Ernzerhof functionals. Physical Review B, 59, 7413-7421. https://doi.org/10.1103/PhysRevB.59.7413

Hendricks SB and Pauling L. 1925. The crystal structures of sodium and potassium trinitrides and potassium cyanate and the nature of the trinitride group. Journal of the American Chemical Society, 47, 2904–2920. https://doi.org/10.1021/ja01689a008

Herzfeld J and Berger AE. 1980. Sideband intensities in NMR spectra of samples spinning at the magic angle. Journal of Chemical Physics, 73, 6021-6030. https://doi.org/10.1063/1.440136

Hodgkinson P and Emsley L. 1997. The reliability of the determination of tensor parameters by solid-state nuclear magnetic resonance. Journal of Chemical Physics, 107, 4808-4816. https://doi.org/10.1063/1.474844

Jameson CJ, Jameson AK, Oppusunggu D, Wille S, Burrell PM, and Mason J. 1981. ^{15}N nuclear magnetic shielding scale from gas phase studies. Journal of Chemical Physics, 74, 81–88. https://doi.org/10.1063/1.440797

Jameson CJ and Jameson AK. 1987. Concurrent ^{19}F and ^{77}Se or ^{19}F and ^{125}Te NMR T_1 measurements for determination of ^{77}Se and ^{125}Te absolute shielding scales. Chemical Physics Letters, 135, 254-259. https://doi.org/10.1016/0009-2614(87)85151-5

Kellett CW, Kennepohl P, and Berlinguette CP. 2020. π covalency in the halogen bond. Nature Communications, 11, 3310. https://doi.org/10.1038/s41467-020-17122-7

Koelling DD and Harmon BN. 1977. A technique for relativistic spin-polarised calculations. Journal of Physics C: Solid State Physics, 10, 3107-3114. https://doi.org/10.1088/0022-3719/10/16/019

Kumar V, Triglav M, Morin VM, and Bryce DL. 2022. On the predictability of chalcogen-bond-driven crystal engineering. an X-ray diffraction and selenium-77 solid-state NMR investigation of benzylic selenocyanate cocrystals. ACS Organic and Inorganic Au, 2, 252-260. https://doi.org/10.1021/acsorginorgau.1c00051

Kumar V, Xu Y, Leroy C, and Bryce DL. 2020a. Direct investigation of chalcogen bonds by multinuclear solid-state magnetic resonance and vibrational spectroscopy. Physical Chemistry Chemical Physics, 22, 3817-3824. https://doi.org/10.1039/C9CP06267J

Kumar V, Xu Y, and Bryce DL. 2020b. Double chalcogen bonds: crystal engineering stratagems via diffraction and multinuclear solid-state magnetic resonance spectroscopy. Chemistry – A European Journal, 26, 3275-3286. https://doi.org/10.1002/chem.201904795

Kumar V, Leroy C, and Bryce DL. 2018. Halide ion recognition via chalcogen bonding in the solid state and in solution. directionality and linearity. CrystEngComm, 20, 6406-6411. http://dx.doi.org/10.1039/C8CE01365A

Legon AC and Walker NR. 2018. What's in a name? ‘Coinage-metal’ non-covalent bonds and their definition. Physical Chemistry Chemical Physics, 20, 19332-19338. https://doi.org/10.1039/C8CP03432J

Mahmudov KT, Kopylovich MN, Guedes da Silva MFC, and Pombeiro AJL. 2017. Chalcogen bonding in synthesis, catalysis and design of materials. Dalton Transactions, 46, 10121-10138. https://doi.org/10.1039/C7DT01685A

Mercury 2021.1.0 (Build 319587). Copyright © CCDC, 2001-2021.

Nag T, Ovens JS, and Bryce DL. 2022. ^{77}Se and ^{125}Te Solid-state NMR and X-ray diffraction structural study of chalcogen-bonded 3,4-dicyano-1,2,5-chalcogenodiazole cocrystals. Acta Crystallographica, C78, 517-523. https://doi.org/10.1107/S2053229622008518

Perdew JP, Burke K, and Ernzerhof M. 1996. Generalized gradient approximation made simple. Physical Review Letters, 77, 3865-3868. https://doi.org/10.1103/PhysRevLett.77.3865

Pickard CJ and Mauri F. 2001. All-electron magnetic response with pseudopotentials: NMR chemical shifts. Physical Review B, **63**, 245101. https://doi.org/10.1103/PhysRevB.63.245101

Politzer P, Murray JS, Clark T, and Resnati G. 2017. The σ-hole revisited. Physical Chemistry Chemical Physics. 2017, 19, 32166–32178. https://doi.org/10.1039/C7CP06793C

Profeta M, Mauri F, and Pickard CJ. 2003. Accurate first principles prediction of ^{17}O NMR parameters in SiO_2: assignment of the zeolite ferrierite spectrum. Journal of the American Chemical Society, **125**, 541-548. https://doi.org/10.1021/ja027124r

Ratcliffe CI, Ripmeester JA, Buchanan GW, and Denike JK. 1992. A molecular merry-go-round: motion of the large macrocyclic molecule 18-crown-6 in its solid complexes studied by ^{2}H NMR. Journal of the American Chemical Society, 114, 3294-3299. https://doi.org/10.1021/ja00035a021

Resnati et al. 2023. https://iupac.org/recommendation/definition-of-the-pnictogen-bond/ Copyright © 2023 IUPAC. Accessed May 2023.

Sanz Camacho P, McKay D, Dawson DM, Kirst C, Yates JR, Green TFG, Cordes DB, Slawin AMZ, Woollins JD, and Ashbrook SE. 2016. Investigating unusual homonuclear intermolecular

"through-space" J couplings in organochalcogen systems. Inorganic Chemistry, 55, 10881–10887. https://doi.org/10.1021/acs.inorgchem.6b01121

Sanz Camacho P, Athukorala Arachchige KS, Slawin AMZ, Green TFG, Yates JR, Dawson DM, Woollins JD, and Ashbrook SE. 2015. Unusual intermolecular "through-space" J couplings in P–Se heterocycles. Journal of the American Chemical Society, 137, 6172–6175. https://doi.org/10.1021/jacs.5b03353

Sanz Camacho P, Stanford MW, McKay D, Dawson DM, Athukorala Arachchige KS, Cordes DB, Slawin AMZ, Woollins JD, and Ashbrook SE. 2018. Polymorphism, weak interactions and phase transitions in chalcogen–phosphorus heterocycles. Chemistry – A European Journal, 24 11067-11081. https://doi.org/10.1002/chem.201800978

Schreckenbach G and Ziegler T. 1996. The calculation of NMR shielding tensors based on density functional theory and the frozen-core approximation. International Journal of Quantum Chemistry, 60, 753-766. https://doi.org/10.1002/(SICI)1097-461X(1996)60:3%3C753::AID-QUA4%3E3.0.CO;2-W

Schreckenbach G and Ziegler T. 1997. Calculation of NMR shielding tensors based on density functional theory and a scalar relativistic Pauli-type Hamiltonian. The application to transition metal complexes. International Journal of Quantum Chemistry, 61, 899-918. https://doi.org/10.1002/(SICI)1097-461X(1997)61:6%3C899::AID-QUA3%3E3.0.CO;2-R

Schreckenbach G and Ziegler T. 1995. Calculation of NMR shielding tensors using gauge-including atomic orbitals and modern density functional theory. Journal of Physical Chemistry, 99, 606-611. https://doi.org/10.1021/j100002a024

Scilabra P, Terraneo G, and Resnati G. 2019. The chalcogen bond in crystalline solids: a world parallel to halogen bond. Accounts of Chemical Research, 52, 1313-1324. https://doi.org/10.1021/acs.accounts.9b00037

Semenov NA, Pushkarevsky NA, Beckmann J, Finke P, Lork E, Mews R, Bagryanskaya IY, Gatilov YV, Konchenko SN, Vasiliev VG, and Zibarev AV. 2012. Tellurium–nitrogen π-heterocyclic chemistry – synthesis, structure, and reactivity toward halides and pyridine of 3,4-dicyano-1,2,5-telluradiazole. European Journal of Inorganic Chemistry, 2012, 3693-3703. https://doi.org/10.1002/ejic.201200376

Semenov NA, Gorbunov DE, Shakhova MV, Salnikov GE, Bagryanskaya IY, Korolev VV, Beckmann J, Gritsan NP, and Zibarev AV. 2018. Donor–acceptor complexes between 1,2,5-chalcogenadiazoles (Te, Se, S) and the pseudohalides CN− and XCN− (X=O, S, Se, Te). Chemistry – A European Journal, 24, 12983-12991. https://doi.org/10.1002/chem.201802257

Stanford MW, Knight FR, Athukorala Arachchige KS, Sanz Camacho P, Ashbrook SE, Bühl M, Slawin AMZ, and Woollins JD. 2014. Probing interactions through space using spin–spin coupling. Dalton Transactions 43, 6548-6560. https://doi.org/10.1039/C4DT00408F

Sturniolo S, Green TFG, Hanson RM, Zilka M, Refson K, Hodgkinson P, Brown SP, and Yates JR. 2016. Visualization and processing of computed solid-state NMR parameters: MagresView and MagresPython. Solid State Nuclear Magnetic Resonance, 78, 64-70. https://doi.org/10.1016/j.ssnmr.2016.05.004

te Velde G, Bickelhaupt FM, Baerends EJ, Fonseca Guerra C, van Gisbergen SJA, Snijders JG, and Ziegler T. 2001. *Chemistry with ADF*. Journal of Computational Chemistry 22, 931-967. https://doi.org/10.1002/jcc.1056

Vogel L, Wonner P, and Huber SM. 2018. Chalcogen bonding: an overview. Angewandte Chemie International Edition, 58, 1880-1891.https://doi.org/10.1002/anie.201809432

Werz DB, Gleiter R, and Rominger F. 2002. Nanotube formation favored by chalcogen−chalcogen interactions. Journal of the American Chemical Society, 124, 10638-10639. https://doi.org/10.1021/ja027146d

Wolff SK, Ziegler T, van Lenthe E, and Baerends EJ. 1999. Density functional calculations of nuclear magnetic shieldings using the zeroth-order regular approximation (ZORA) for relativistic effects: ZORA nuclear magnetic resonance. Journal of Chemical Physics, 110, 7689-7698. https://doi.org/10.1063/1.478680

Wolff SK and Ziegler T. 1998. Calculation of DFT-GIAO NMR shifts with the inclusion of spin-orbit coupling. Journal of Chemical Physics, 109, 895-905. https://doi.org/10.1063/1.476630

Xu Y, Gabidullin B, and Bryce DL. 2019. Single-crystal NMR characterization of halogen bonds. Journal of Physical Chemistry A, 123, 6194-6209. https://doi.org/10.1021/acs.jpca.9b03587

Xu Y, Kumar V, Bradshaw MJZ, and Bryce DL. 2020. Chalcogen-bonded cocrystals of substituted pyridine n-oxides and chalcogenodiazoles: an X-ray diffraction and solid-state NMR investigation. Crystal Growth and Design, 20, 7910-7920. https://doi.org/10.1021/acs.cgd.0c01173

Yan W, Zheng M, Xu C, and Chen FE. 2021. Harnessing noncovalent interaction of chalcogen bond in organocatalysis: From the catalyst point of view. Green Synthesis and Catalysis, 2, 329-336. https://doi.org/10.1016/j.gresc.2021.08.002

Yates JR, Pickard CJ, and Mauri F. 2007. Calculation of NMR chemical shifts for extended systems using ultrasoft pseudopotentials. Physical Review B, **76**, 024401. https://doi.org/10.1103/PhysRevB.76.024401

Part 3: Quadrupolar nuclei and chalcogen bonded systems

Statement of Authenticity and permissions for Chapter 7: I declare that the coauthors have permitted me to include this article in my thesis and this manuscript is submitted for publication. I would like to thank Dr. Victor Terskikh for his unsurmountable help and mentoring at the high field NMR facility, NRC, Canada with the high field spectra acquisitions. I certify this work was prepared by me with the guidance, support and contributions from my supervisor, Dr. David L. Bryce.

Chapter 7. Experimental Evidence for Non-Fermi-Contact *J* Coupling Across Chalcogen Bonds in Ionic Salt Cocrystal Polymorphs

Tamali Nag,[a] Victor V. Terskikh,[b] and David L. Bryce*[a]

[a] T. Nag and Prof. Dr. D. L. Bryce
Department of Chemistry and Biomolecular Sciences
University of Ottawa
Ottawa, Ontario, Canada K1H5H5
E-mail: dbryce@uottawa.ca
[b] Dr. V. V. Terskikh
Metrology
National Research Council Canada
Ottawa, Ontario, Canada K1A 0R6

Abstract

A pair of novel polymorphic ionic cocrystals of 3,4-dicyanotelluradiazole and tetraphenylphosphonium bromide are synthesized and are characterized by single-crystal XRD. Strong and directional non-covalent chalcogen bonds (ChB) between Te and Br are analyzed via solid-state NMR to reveal large and anisotropic **J**(^{125}Te,$^{79/81}$Br) coupling tensors, providing unequivocal evidence for non-Fermi contact contributions across ChBs. Along with large $^{79/81}$Br quadrupolar couplings for the Br^- anions, these data are established as new tools to characterize chalcogen bonds and to differentiate between ChB polymorphs.

7.1 Introduction

Non-covalent interactions are ubiquitous in the chemical and biochemical sciences, playing critical structural and dynamic roles in fields as diverse as crystal engineering, (bio)catalysis, materials chemistry, and structural biology. Beyond the most common and well-known hydrogen

bonds, van der Waals' interactions, π–π and cation-π interactions, for example, several other σ-hole type bonds have taken on increased prominence in recent years.[1] These include now well-established halogen bonds,[2] chalcogen bonds,[3] and pnictogen bonds[4] as well as lesser-studied classes including tetrel bonds, triel bonds, matere bonds, regium bonds, and erythronium bonds, among others.[5] In each of these cases, the bond is named after the nature of the element which accepts electrons, in analogy with hydrogen bonds.[6] A breakthrough in characterizing and understanding hydrogen bonds occurred in the late 1990s, when Grzesiek and coworkers developed NMR methods to measure indirect nuclear spin-spin (*J*) couplings across hydrogen bonds in biomolecules.[7] These couplings afforded insight into the nature of the hydrogen bond as well as the relationship between *J* and the local hydrogen bond geometry. *J* couplings across σ-hole type bonds have been far less studied,[8] in part due to experimental difficulties arising from the nuclear spin properties of the isotopes involved (e.g., low sensitivity, large quadrupole moments). Because *J* coupling is a result of the transmission of spin information from one nucleus to another via the intervening electrons, the measurement of complete **J** tensors across σ-hole bonds should provide an exquisitely sensitive novel probe of these interactions.

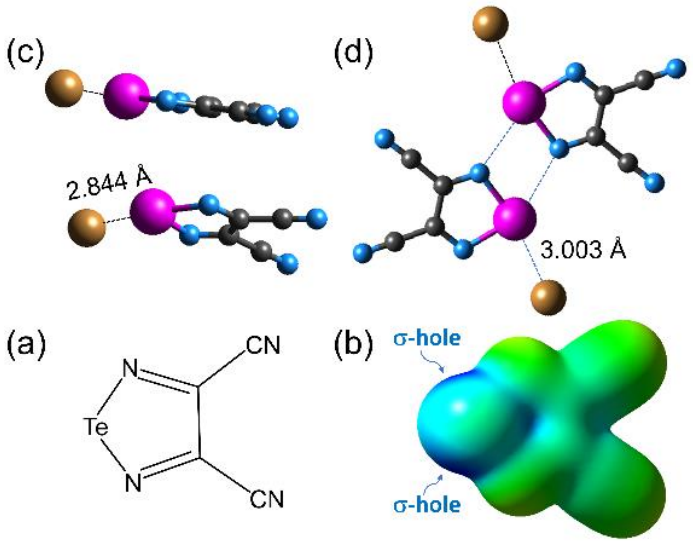

Figure 7.1: (a) Molecular structure of ChB donor 3,4-dicyanotelluradiazole. (b) Molecular electrostatic potential surface of the ChB donor, where deep blue indicates elevated electrostatic potential. (c,d) Details from the SCXRD structures of 1 and 2, respectively. Te: magenta; Br: brown; N: blue; C: black. ChB are indicated with dashed lines.

7.2 Results and Discussion

We report here the preparation of two novel ionic cocrystal polymorphs comprised of 3,4-dicyanotelluradiazole and tetraphenylphosphonium bromide and which feature Te···Br chalcogen bonds (Fig. 7.1). These systems are characterized by single-crystal X-ray diffraction and multinuclear (^{125}Te, $^{79/81}$Br) solid-state magnetic resonance spectroscopy to reveal substantial anisotropic **J**(^{125}Te, $^{79/81}$Br) couplings across chalcogen bonds as well as diagnostic $^{79/81}$Br quadrupolar coupling constants, both of which differentiate between the polymorphs and provide clear experimental evidence for non-Fermi contact coupling across the chalcogen bond.

3,4-dicyanotelluradiazole was prepared as described by Cozzolino et al.[9] and cocrystallized with tetraphenylphosphonium bromide in ethanol under slightly different conditions (see SI, Appendix D) to yield two ionic cocrystal polymorphs **1** and **2** (Fig. 7.1). Single crystals of each were grown from diethyl ether and their structures were solved by single-crystal X-ray diffraction (Table 7.1).

Table 7.1: Crystallographic information and chalcogen bond geometrical details for polymorphic ionic cocrystals 1 and 2.[a]

	1	**2**
Formula	$C_{28}H_{20}BrN_4PTe$	$C_{28}H_{20}BrN_4PTe$
Space group	*Pna*2$_1$	*P*2$_1$/*n*
Cell dimensions	*a* = 7.3911(2) Å *b* = 21.5505(6) Å *c* = 16.2621(5) Å	*a* = 16.1554(6) Å *b* = 7.2241(3) Å *c* = 22.6459(9) Å
Cell angles	α = 90.0° β = 90.0° γ = 90.0°	α = 90.0° β = 101.241(2)° γ = 90.0°
Te···Br distance	2.844 Å	3.003 Å
N-Te···Br angle	167.8°	166.3°

[a] See SI (Appendix D) for further crystallographic details. CCDC deposition numbers 2314483 and 2314484.

Both polymorphs feature short and directional Te···Br chalcogen bonds. In the case of **1**, the Te···Br distance is 2.844 Å and the N-Te···Br ChB angle is 167.8°. For **2**, the Te···Br distance is 3.003 Å and the N-Te···Br ChB angle is 166.3°. In **1**, chalcogen-bonded moieties are stacked, with a Te-Te distance of 3.732 Å (Fig. 7.1(c)). Only one of the two σ-holes on Te is occupied in

1. In **2**, both σ-holes are occupied; one by a bromide anion and the second by a nitrogen atom from an adjacent 3,4-dicyanotelluradiazole molecule, resulting in a complementary coplanar arrangement (Fig. 7.1(d)). Each structure features a single crystallographically distinct Te-Br pair.

To characterize the Te···Br chalcogen bonds in **1** and **2**, ^{125}Te magic-angle spinning (MAS) NMR spectra were recorded in applied magnetic fields of 9.4 or 11.75, and 21.1 T (Fig. 7.2). The multiplets seen in these spectra are determined by several parameters including the isotropic ($J(^{125}\text{Te}, ^{79/81}\text{Br})_{iso}$) and anisotropic ($\Delta J(^{125}\text{Te}, ^{79/81}\text{Br})$) indirect nuclear spin-spin coupling, the direct ^{125}Te-$^{79/81}$Br dipolar coupling, the $^{79/81}$Br nuclear quadrupolar coupling constant (C_Q) and quadrupolar asymmetry parameter (η_Q), as well as the relative orientation of the dipolar and quadrupolar coupling tensors. The analysis used here assumes an axially symmetric **J** tensor coincident with the dipolar coupling tensor. In analyzing the ^{125}Te NMR spectra, care must be taken to simultaneously include couplings to both bromine isotopes, taking into account their different natural abundances (^{79}Br: 59.69%; ^{81}Br: 49.31%), quadrupole moments ($Q(^{81}\text{Br})/Q(^{79}\text{Br})$ = 0.8354,[10] and magnetogyric ratios ($\gamma(^{81}\text{Br})/\gamma(^{79}\text{Br})$ = 1.0779). Simulations were done using WSOLIDS1.[11]

To minimize the number of unknown adjustable parameters used when fitting the ^{125}Te MAS NMR spectra, ^{79}Br and ^{81}Br WURST-QCPMG[12] NMR spectra were acquired in a magnetic field of 21.1 T to independently measure $C_Q(^{79/81}\text{Br})$ and η_Q for each sample (Fig. 7.3; Table 7.2). These central-transition spectra are broad (over 12 MHz in the case of the ^{79}Br NMR spectrum of **1**) and were acquired in several pieces (see SI, Appendix D). Proper simulation required an exact diagonalization of the Zeeman-quadrupolar Hamiltonian as implemented in QUEST software due

to the large quadrupolar interactions.[13] The resulting $C_Q(^{79/81}Br)$ values are among the largest measured directly by NMR spectroscopy,[14] and map out a new frequency range characteristic of chalcogen bonds (Fig. 7.3(i)). $C_Q(^{81}Br)$ for 'free' bromide anions are generally below 30 MHz, although $CaBr_2$ has a value of 62.8(4) MHz.[15] In systems where Br^- is a halogen bond acceptor, values generally range from 20 to 60 MHz, although 12.3(2) MHz was recorded for 2-iodoanilinium bromide.[16] $C_Q(^{81}Br)$ values for covalently-bonded bromine atoms have been measured by NQR spectroscopy and are on the order of 500 MHz.[17]

The magnitude and relative ordering of the experimental C_Q values for **1** and **2** are well reproduced by GIPAW DFT[18] calculations (see SI, Appendix D).

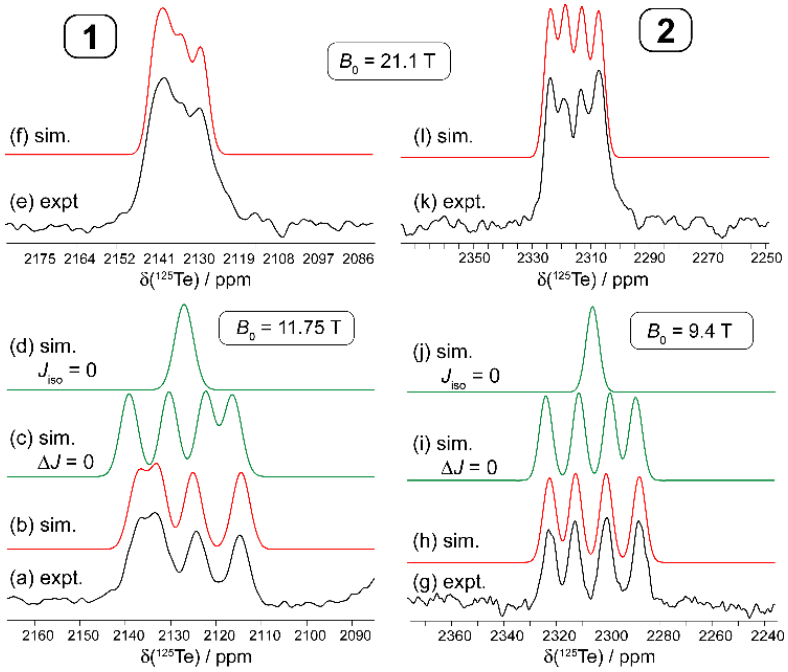

Figure 7.2: Reconstructed infinite speed centreband ^{125}Te MAS NMR spectra of ionic cocrystal polymorphs 1 (left) and 2 (right) acquired at B_0 = 21.1 T (top) and 11.75 or 9.4 T (bottom). (a), (e): Experimental spectra for 1; (b), (f): simulated spectra for 1. (c), (d): simulated spectra with ΔJ

or J_{iso} set to zero. (g), (k): Experimental spectra for 2; (h), (l): simulated spectra for 2. (i), (j): simulated spectra with ΔJ or J_{iso} set to zero.

With this information in hand, the ^{125}Te MAS NMR spectra were simulated (Fig. 7.2). For a spin-1/2 nucleus (^{125}Te) *J*-coupled to a spin-3/2 nucleus ($^{79/81}$Br), four peaks are expected; however, the spacing between them is determined by all of the above-mentioned parameters.[19]

As shown in Fig 7.2, good agreement with experiment is only achieved when large anisotropic *J* couplings are included in the simulation ($\Delta J(^{125}\text{Te},^{79}\text{Br})$ = 870 ± 300 Hz for 1 and 500 ± 400 Hz for 2 (Table 7.2). The isotropic $J(^{125}\text{Te},^{79}\text{Br})_{iso}$ couplings are also sizable, -1200 ± 50 Hz for **1** and -1400 ± 50 Hz for **2**. Excluding anisotropic or isotropic *J* coupling from the simulation results in poor agreement with experiment as shown in Fig. 7.2(c), (d), (i), (j). Furthermore, the experimentally observed field dependence of the multiplet shape is reproduced via simulations using the same parameters (Fig. 7.2). Because reliable ΔJ values are relatively rare in the literature, and because the values obtained here are large, additional steps were taken to ensure the accuracy of the spectral fits (see SI, Appendix D).

Further credence for the substantial isotropic and anisotropic *J* coupling data may be obtained by comparing the reduced coupling constants ($K = 4\pi^2 J/\gamma_N\gamma_{N'}h$) to those known for similar spin pairs (*i.e.*, period 4 and 5 elements). For example, experimentally K_{iso} = (763 ± 5) and ΔK = (-785 ± 11) x 10^{20} N A^{-2} m^{-3} for I_2; computed data for BrI are K_{iso} = 610.0 and ΔK = -693.4 x 10^{20} N A^{-2} m^{-3}; experimentally K_{iso} = ± (294 ± 1) and ΔK = -(423 ± 79) x 10^{20} N A^{-2} m^{-3} for Te-Te coupling in $(Me_4N)_2Te_2$.[20] These data compare well with the present data for **1**, for which K_{iso} = +(125 ± 5) and ΔK = -(91 ± 31) x 10^{20} N A^{-2} m^{-3}; that is, the couplings seen for the covalently-

bonded systems are all larger than is what is seen for the non-covalent chalcogen bond, which provides some indication that the values measured presently are not unreasonably large.

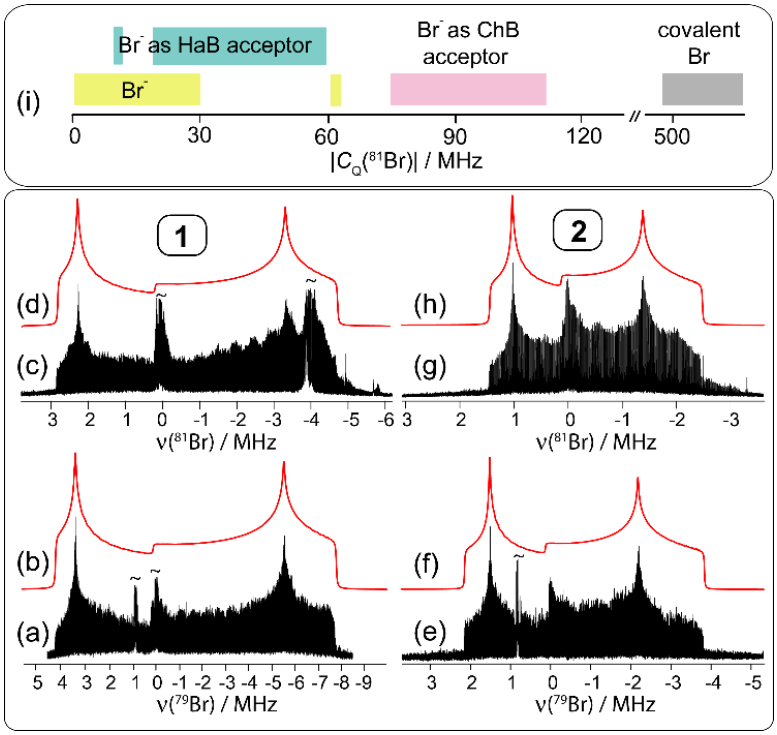

Figure 7.3: ^{79}Br (bottom) and ^{81}Br (middle) WURST-QCPMG NMR spectra of stationary powdered samples of ionic cocrystal polymorphs 1 (left) and 2 (right) acquired at B_0 = 21.1 T. (a), (c): Experimental spectra for 1; (b) (d): simulated spectra for 1. (e), (g): Experimental spectra for 2; (f) (h): simulated spectra for 2. Artifacts truncated by tildes are due to residual tetraphenylphosphonium bromide (~0 kHz)[21] and copper from the NMR coil. (i) Ranges of C_Q(^{81}Br) values for various Br environments; there are exceptions to these ranges.[14]

Table 7.2: Experimental tellurium-125 and bromine-79 NMR coupling parameters for ionic cocrystal polymorphs 1 and 2.

	1	**2**

$J(^{125}\text{Te},^{79}\text{Br})_{iso}$ / Hz	-1200 ± 50	-1400 ± 50
$\Delta J(^{125}\text{Te},^{79}\text{Br})$ / Hz	+870 ± 300	+500 ± 400
$R_{DD}(^{125}\text{Te},^{79}\text{Br})$[a] / Hz	-417	-355
$C_Q(^{79}\text{Br})$[d] / MHz	+132 ± 1	+91.7 ± 0.5
η_Q	0.17 ± 0.01	0.27 ± 0.01

[a] Dipolar coupling, $R_{DD} = (m_0/4\pi)(\hbar/2\pi)\gamma_N\gamma_{N'}\langle r_{NN'}^{-3}\rangle$. Fixed at value obtained from single-crystal X-ray structure. [b] The positive sign of $C_Q(^{79/81}\text{Br})$ as well as the coincidence between the largest component of the quadrupolar tensor and the dipolar tensor was confirmed via GIPAW DFT calculations (see SI, Appendix D).

The observation of substantial *J* coupling across the chalcogen bonds in **1** and **2**, as with other measurements of *J* couplings across non-covalent bonds, cannot directly confirm or refute whether the interaction is attractive in nature. The substantial values of $\mathbf{J}(^{125}\text{Te},^{79/81}\text{Br})$ do confirm that there is significant orbital overlap between tellurium and bromine, consistent with the presence of a non-covalent interaction. Furthermore, the significant anisotropy of the coupling tensor importantly provides direct experimental evidence for non-Fermi contact contributions to this tensor. According to the non-relativistic Ramsey formalism, the **J** tensor may be decomposed into contributions from the Fermi-contact mechanism, a diamagnetic spin-orbital mechanism, a paramagnetic spin-orbital mechanism, and a spin-dipolar mechanism.[22] Analogues of these mechanisms have been described incorporating spin-orbit relativistic effects.[23] The FC mechanism is dominant for many coupling constants, particularly those involving ^{1}H and some other light elements. However, as the FC mechanism is purely isotropic, it is insufficient to explain the highly anisotropic **J** couplings observed presently. Thus, other, anisotropic mechanisms must be operative in *J* couplings across Te···Br chalcogen bonds.

DFT calculations of the tellurium-bromine *J* couplings were carried out (see SI, Appendix D). These are challenging because ideally one must include periodic boundary conditions to properly model the bromide anion environment in particular, but one must also include spin-orbit relativistic effects to properly calculate couplings involving a heavy element such as Te. GIPAW DFT calculations (which use periodic boundary conditions)[24] including scalar relativistic effects provide very good results for $J(^{125}Te,^{79}Br)_{iso}$, -1303 and -1385 Hz, and for ΔJ (865 and -642 Hz) for **1** and **2**, respectively. ZORA-DFT calculations including spin-orbit relativistic effects[25] carried out on a simple model of the telluradiazole interacting with Br^- also provide very good values for $J(^{125}Te,^{79}Br)_{iso}$ of -1239 and -1028 Hz and ΔJ values of +1282 and +951 Hz, for **1** and **2**, respectively. These are within, or just outside the experimental errors, which is impressive given that the bromide anion's environment is not well-described in the small cluster model employed. All calculations predict a highly asymmetric **J** tensor, while the spectral simulations used assume an axially symmetric **J** tensor coincident with the dipolar tensor. The computed anisotropy in **J** arises largely from the Fermi-contact spin-dipolar cross term as well as the paramagnetic spin-orbital term.

7.3 Conclusions

In conclusion, large anisotropic **J** and quadrupolar couplings have been measured for Te and Br nuclei involved in non-covalent chalcogen bonds. The reduced isotropic coupling constants are up to 85% smaller than corresponding values for comparable 4^{th} and 5^{th} period elements when they are engaged in covalent bonds. The sizable anisotropy of *J* coupling across the tellurium-bromine ChB provides clear experimental evidence for non-Fermi contact contributions to this

coupling, implying a constructive mixing between orbitals centred on the two nuclei. In addition, the magnitudes of the bromine quadrupolar couplings measured for bromide anions acting as ChB acceptors have been shown to be characteristic of the ChB when compared to other available data. Finally, all NMR parameters discussed clearly differentiate between two polymorphic ionic cocrystals, further demonstrating the exquisite sensitivity of the measured coupling constants to small differences in the ChB environment. Overall, this communication sheds new light on the nature of the chalcogen bond and elucidates the potential of studying σ-hole interactions via NMR analyses of challenging nuclei.

Supporting Information

Additional experimental details, spectra, and data. The authors have cited additional references within the Supporting Information (Appendix D).[26]

7.4 Acknowledgements

The authors are grateful to Dr. J. S. Ovens and to Dr. P. M. J. Szell for technical assistance. D. L. B thanks NSERC for funding. Access to the 21.1 T spectrometer is provided thanks to support from the National Research Council Canada, the University of Ottawa, and the Canada Foundation for Innovation.

Keywords: chalcogen bond • indirect nuclear spin-spin coupling • polymorphism • solid-state NMR • crystal engineering

References

[1] L. Brammer, A. Peuronen, T. M. Roseveare, *Acta Cryst. C* **2023**, *79*, 204.

[2] G. Cavallo, P. Metrangolo, R. Milani, T. Pilati, A. Priimagi, G. Resnati, G. Terraneo, *Chem. Rev.* **2016**, *116*, 2478.

[3] (a) R. Gleiter, G. Haberhauer, D. B. Werz, F. Rominger, C. Bleiholder, *Chem. Rev.* **2018**, *118*, 2010. (b) C. B. Aakeroy, D. L. Bryce, G. R. Desiraju, A. Frontera, A. C. Legon, F. Nicotra, K. Rissanen, S. Scheiner, G. Terraneo, P. Metrangolo, G. Resnati, *Pure Appl. Chem.* **2019**, *91*, 1889.

[4] G. Resnati, D. L. Bryce, G. R. Desiraju, A. Frontera, I. Krossing, A. C. Legon, P. Metrangolo, F. Nicotra, K. Rissanen, S. Scheiner, G. Terraneo, *Pure Appl. Chem.* in press, 2024. https://doi.org/10.1515/pac-2020-1002

[5] See e.g., (a) A. Daolio, A. Pizzi, G. Terraneo, A. Frontera, G. Resnati, *ChemPhysChem* **2021**, *22*, 2281.(b) Y. Xu, M. Calabrese, A. Pizzi, T. Nag, I. Hung, Z. Gan, G. Resnati, D. L. Bryce, *Chem. Commun.* **2023**, *59*, 12609. (c) M. Calabrese, R. M. Gomila, A. Pizzi, A. Frontera, G. Resnati, *Chem. Eur. J.* **2023**, *29*, e202302176.

[6] G. Cavallo, P. Metrangolo, T. Pilati, G. Resnati, G. Terraneo, *Cryst. Growth Des.* **2014**, *14*, 2697.

[7] (a) A. J. Dingley, S. Grzesiek, *J. Am. Chem. Soc.* **1998**, *120*, 8293. (b) F. Cordier, S. Grzesiek, *J. Am. Chem. Soc.* **1999**, *121*, 1601.

[8] (a) M. J. Collins, J. A. Ripmeester, J. F. Sawyer, *J. Am. Chem. Soc.* **1987**, *119*, 4113. (b) M. J. Collins, J. A. Ripmeester, J. F. Sawyer, *J. Am. Chem. Soc.* **1988**, *110*, 8583. (c) J. Viger-

Gravel, J. Meyer, I. Korobkov, D. L. Bryce, *CrystEngComm* **2014**, *16*, 7285. (d) P. Sanz Comacho, K. S. A. Arachchige, A. M. Z. Slawin, T. F. G. Green, J. R. Yates, D. M. Dawson, J. D. Woollins, S. E. Ashbrook, *J. Am. Chem. Soc.* **2015**, *137*, 6172. (e) P. Sanz Camacho, D. McKay, D. M. Dawson, C. Kirst, J. R. Yates, T. F. G. Green, D. B. Cordes, A. M. Z. Slawin, J. D. Woollins, S. E. Ashbrook, *Inorg. Chem.* **2016**, *55*, 10881.

[9] A. F. Cozzolino, Q. Yang, I. Vargas-Baca, *Cryst. Growth Des.* **2010**, *10*, 4959.

[10] P. Pyykkö, *Mol. Phys.* **2018**, *116*, 1328.

[11] K. Eichele, WSOLIDS1 NMR Simulation Package version 1.20.22, 2014.

[12] L. A. O'Dell, R. W. Schurko, *Chem. Phys. Lett.* **2008**, *464*, 97.

[13] (a) F. A. Perras, D. L. Bryce, *Angew. Chem. Int. Ed.* **2012**, *51*, 4227. (b) F. A. Perras, C. M. Widdifield, D. L. Bryce, *Solid State Nucl. Magn. Reson.* **2012**, *45-46*, 36.

[14] (a) P. M. J. Szell, D. L. Bryce, *Annu. Rep. Nucl. Magn. Reson. Spectrosc.* **2020**, *100*, 97. (b) R. P. Chapman, C. M. Widdifield, D. L. Bryce, *Prog. Nucl. Magn. Reson. Spectrosc.* **2009**, *55*, 215.(c) S. N. S. Lamahewage, B. A. Atterberry, R. W. Dorn, E. Gi, M. R. Kimball, J. Blümel, J. Vela, A. J. Rossini, *Phys. Chem. Chem. Phys.* **2024**, https://doi.org/10.1039/D3CP05055F.

[15] C. M. Widdifield, D. L. Bryce, *J. Phys. Chem. A* **2010**, *114*, 2102.

[16] (a) R. J. Attrell, C. M. Widdifield, I. Korobkov, D. L. Bryce, *Cryst. Growth Des.* **2012**, *12*, 1641. (b) J. Viger-Gravel, S. Leclerc, I. Korobkov, D. L. Bryce, *J. Am. Chem. Soc.* **2014**, *136*, 6929.

[17] (a) E. A. C. Lucken, *Nuclear Quadrupole Coupling Constants*, Academic Press, London, 1969. (b) P. Cerreia Vioglio, P. M. J. Szell, M. R. Chierotti, R. Gobetto, D. L. Bryce, *Chem. Sci.* **2018**, *9*, 4555.

[18] (a) M. D. Segall, P. J. D. Lindan, M. J. Probert, C. J. Pickard, P. J. Hasnip, S. J. Clark, M. C. Payne, *J. Phys. Condens. Matter* **2002**, *14*, 2717. (b) M. Profeta, F. Mauri, C. J. Pickard, *J. Am. Chem. Soc.* **2003**, *125*, 541.

[19] (a) A. C. Olivieri, *J. Magn. Reson.* **1989**, *81*, 201.(b) S. H. Alarcón, A. C. Olivieri, R. K. Harris, *Solid State Nucl. Magn. Reson.* **1993**, *2*, 325. (c) K. Eichele, R. E. Wasylishen, J. S. Grossert, A. C. Olivieri, *J. Phys. Chem.* **1995**, *99*, 10110.

[20] (a) J. Vaara, J. Jokisaari, R. E. Wasylishen, D. L. Bryce, *Prog. Nucl. Magn. Reson. Spectrosc.* **2002**, *41*, 233. (b) R. J. Batchelor, F.W.B. Einstein, I. D. Gay, C. H. W. Jones, R. D. Sharma, *Inorg. Chem.* **1993**, *32*, 4378. (c) D. L. Bryce, R. E. Wasylishen, J. Autschbach, T. Ziegler, *J. Am. Chem. Soc.* **2002**, *124*, 4894.

[21] K. M. N. Burgess, I. Korobkov, D. L. Bryce, *Chem. Eur J.* **2012**, *18*, 5748.

[22] N. F. Ramsey, *Phys. Rev.* **1953**, *91*, 303.

[23] P. Pyykkö, *Chem. Phys.* **1977**, *22*, 289.

[24] S. A. Joyce, J. R. Yates, C. J. Pickard, F. Mauri, *J. Chem. Phys.* **2007**, *127*, 204107.

[25] (a) G. te Velde, F.M. Bickelhaupt, E.J. Baerends, C. Fonseca Guerra, S.J.A. van Gisbergen, J.G. Snijders, T. Ziegler, *J. Comp. Chem.* **2001**, *22*, 931. (b) ADF 2019, SCM, Theoretical Chemistry, Vrije Universiteit, Amsterdam, The Netherlands, http://www.scm.com. (c) J. Autschbach, T. Ziegler, *J. Chem. Phys.* **2000**, *113*, 9410.

[26] (a) G. M. Sheldrick, *Acta Crystallogr. Sect. A* **2008**, *64*, 112. (b) L. J. Farrugia, *J. Appl. Crystallogr.* **2012**, *45*, 849. (c) C. B. Hübschle, G. M. Sheldrick, B. Dittrich, *J. Appl. Crystallogr.* **2011**, *44*, 1281.

Chapter 8: Iodide anion as an indirect probe of the chalcogen bond: A solid-state NMR and NQR study

8.1 Introduction

Halogen bonds, XB, the noncovalent interaction that consists of a halogen bond donor and a halogen bond acceptor have been widely explored and are still an interesting subject of supramolecular chemistry. Iodine, of group 17, is widely known for its propensity to form halogen bonds[1] due to its size and highly polarizable nature. Examples where iodine acts as a halogen bond donor are extensively studied. In this Chapter, iodine is found to act as a chalcogen-bond acceptor owing to the presence of a chalcogen bond donor here with σ-holes.[7] The chalcogen bond donor used here is telluradiazole with Te sites containing the σ-holes and tetraphenylphosphonium iodide as the chalcogen bond acceptor, where the rich electron density in the iodide interacts with the electron deficient region of the Te atom to create a ChB. This work includes tackling of a very challenging quadrupolar nucleus, ^{127}I (I = 5/2) in a ChB-bonded system with the novel engineered cocrystal of telluradiazole and tetraphenylphosphonium iodide. The second-order quadrupolar interaction of ^{127}I gives a broad NMR spectrum[2,20] which is most easily studied in high applied magnetic fields. Solid-state NMR and NQR studies of ^{127}I in this cocrystal show that we can trace back the structural properties and local geometry of the chalcogen formed between Te and I upon cocrystallization. It also explains the change in NMR parameters of the starting material, **d**, when it forms a ChB with ChB donor, telluradiazole and how the quadrupolar iodine nucleus influences

the ChB interaction (of Te···I). Computational chemistry was used in addition to SSNMR, NQR, and X-ray diffraction experiments to determine the values of quadrupolar C_Q and η.

8.2 Experimental Methods

i) Synthesis: The ChB donor, telluradiazole (**1**) was synthesized and purified following the procedure discussed in the previous Chapter given by Semenov et al.[3] Tetraphenylphosphonium iodide (**d**), the ChB acceptor, was purchased from Sigma-Aldrich (≥98% purity). The cocrystallization of ChB donor, **1**, and acceptor **d** was carried out by refluxing their 1:1 mixture in about 6 mL of methanol and then refluxed for 20 minutes, cooled down to room temperature and then layered with diethyl ether (about 3 mL) and left for 2 days to slowly evaporate to get bright red cocrystals. The melting point recorded was 180°C for the novel cocrystal formed, namely, **1.d** (Figure 8.2.1).

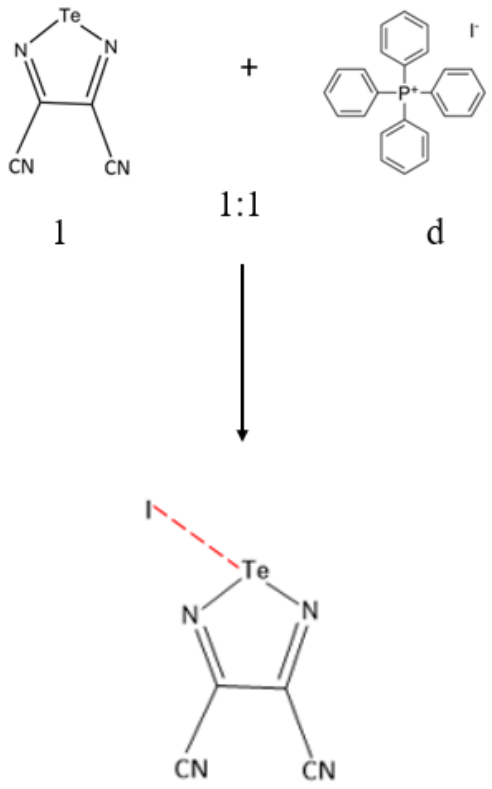

Figure 8.2.1: Synthesis of cocrystal **1.d** depicting ChB between Te and I.

ii) Single-Crystal X-ray Diffraction: Single crystal X-ray diffraction of the cocrystal **1.d** was performed on a BRUKER kappa instrument. The single crystal was carefully chosen with the help of parabar oil and mounted on the goniometer head of the diffractometer allowing the detector to centralize the angle of the mounted goniometer to obtain reflections. Data were collected using the direct method with optimum reflections showing good diffraction from the BRUKER kappa single crystal diffractometer at room temperature. The diffractometer was equipped with a sealed Mo tube source of 0.71073 Å wavelength detected by an APEX II CCD detector. The raw data for all the reflections were processed using the BRUKER APEX II software package, keeping the

semi-empirical absorption corrections of the reflections obtained. The crystal structure was solved and refined with the help of SHELXL[4] software and the systematic absences and the unit cell in the diffraction data were consistent with that of a $P2_1/n$ space group.

iii) Powder X-ray Diffraction: The powder pattern of cocrystal **1.d** was measured using a Bruker D8 Endeavour instrument containing a 1 kW Cu Kα radiation source from a sealed tube and a LynxEye XE-T high-speed detector operating at a wavelength of λ= 1.54056 Å at 298 K. The 2Θ value ranged from 5° to 60° and a 1.83 degree per minute scan rate was used. The PXRD diffractograms were acquired to check the phase purity of the sample and for any possible chance of polymorph formation. The experimental PXRD peaks were carefully compared with those from the simulated powder pattern from the single-crystal diffraction result of the cocrystal (Figure 8.3.2).

iv) Solid-State NMR: Solid-state NMR experiments on cocrystal **1.d** and starting material **d** were performed at three different magnetic fields, B_0 = 9.4 T, B_0= 11.7 T, and B_0= 21.1 T to acquire the ^{125}Te,^{127}I, and ^{31}P spectra.

^{125}Te HPDEC/MAS experiments were performed on a Bruker AVANCE III HD 500 spectrometer to obtain the spectrum at two different MAS speeds (12 kHz and 7 kHz) to get the isotropic chemical shift. The acquisition parameters to run the experiment were optimized after being referenced to solid telluric acid with chemical shifts 685.5 ppm and 692.2 ppm.[13] The Tellurium 90° pulse used was 1.6 μs, the recycle delay used was 60 s, the number of scans was

4000, and the isotopic shift for ^{125}Te was recorded at 2345.7 ppm with an acquisition time of 50 ms.

^{31}P CP/MAS experiments carried out on starting material **d** (CCDC refcode: SATSUB) and cocrystal **1.d** were acquired on Bruker AVANCE II 400 and AVANCE III HD 500 spectrometers at different MAS speeds (9 and 1.5 kHz) and the acquisition parameters were optimized using ammonium dihydrogen phosphate as the reference compound at 0.81 ppm. The proton 90° pulse used was 3.55 μs at power level of 4 dB. The contact pulse used was 4.5 ms, the decoupler pulse length was 6.5 μs and the swfttppm decoupling sequence was applied during the acquisition time. The recycle delay chosen was 10 s and about 1800 scans were acquired. The isotropic ^{31}P chemical shift extracted was 21.5 ppm.

^{127}I solid-echo NMR experiments were performed on Bruker AVANCE III HD 500 and Bruker AVANCE II 900 spectrometers to obtain the ^{127}I quadrupolar coupling constant and asymmetry parameter for starting material **d** and cocrystal **1.d**. The acquisition parameters were optimized using solid potassium iodide as the reference compound at 192.8 ppm. The ^{127}I NMR spectrum at 11.7 T field was not recorded successfully for cocrystal **1.d** due to large second-order quadrupolar effects. An ultra-high field of 21.1 T was used to record the very wide ^{127}I NMR spectra. For the starting material **d**, however, at 11.7 T the spectrum was collected using the VOCS method (variable offset cumulative spectrum). At 11.7 T magnetic field, the acquisition parameters for **1.d** were, 32k number of scans (NS) obtained using 4 mm HXY triple channel MAS. The offset was set to 200 kHz and 13 pieces were collected, the recycle delay was 0.25 s with a spectral window of 3 MHz. The ^{127}I 90° pulse was 1.5 µs at 121 W power level.

QCPMG and solid-echo experiments were carried out at B_0 = 21.1 T for starting material **d** and cocrystal **1.d**. The acquisition parameters were optimized using solid KI at 192.8 ppm to obtain the ^{127}I spectra. A recycle delay of 0.5 s, a ^{127}I 90 ° pulse of 1 µs, offset of 100 kHz, 6 pieces, echo delay of 50 µs and a spectral window of 1 MHz were implemented to acquire the spectra for the starting material, **d**. For the cocrystal, **1.d**, ^{127}I spectra was collected by VOCS method (variable offset cumulative spectrum) and the acquisition parameters noted were NS: 64k, obtained using a 4 mm homemade probe bba_3-4mm. The offset was set to 0.5 MHz, 32 pieces were collected, relaxation delay (D1) used was 0.1 s, echo delay (D6) of 19 µs, sweep width (SWH) of 3 MHz, and, the ^{127}I 90° pulse used was 1 µs at -21.8 dB power level.

v) ^{127}I NQR: Solid-state ^{127}I NQR spectroscopy for cocrystal **1.d** was performed by placing the sample in a 5 mm glass insert in a static 4 mm Bruker single channel probe. The set-up sample used was H_5IO_6 which in the literature reported one of its NQR transitions as 44.976 MHz.[15] The ^{127}I 90° pulse and other acquisition parameters for the solid-echo experiment were optimized using this set-up sample before moving on to cocrystal **1.d**. The entire set up was placed in zero magnetic field, the probes connected to the preamplifier, to generate the frequencies required for ^{127}I. Finally, the ^{127}I solid-echo experiment was executed to obtain two transition frequencies for **1.d**. The frequencies of the first and second transitions of ^{127}I were obtained at 48.976 and 75.776 MHz.

vi) Computational Chemistry: DFT calculations on the starting material **d**, and the novel cocrystal featuring the unique ChB interaction (**1.d**) have been performed to extract the calculated ^{125}Te shielding components, and, iodine C_Q and η values in both compounds. The calculated

isotropic chemical shift and principal components of ^{125}Te in the cocrystal were also compared to the reported experimental values of the starting material, **1**, from the literature.[15] DFT calculations were performed using the Amsterdam Modelling Suite (AMS package)[17] using cluster models of the cocrystal **1.d** and **d** to extract ^{125}Te shielding components. GIPAW-DFT calculations were also performed using CASTEP[16] considering the crystallographic information file, keeping all the cell-parameters fixed and without any other geometric optimizations to extract the ^{127}I EFG tensors, quadrupolar coupling constant values and asymmetry parameters for **d** and **1.d**, respectively. Relativistic corrections (spin-orbit) were applied by using the Zeroth Order Regular Approximation (ZORA), a Statistically Averaged Orbital Potential (SAOP) basis set, and a GGA-RPBE functional to obtain the calculated NMR parameters. The C_Q and asymmetry parameters were calculated using CASTEP where the cluster models underwent the built-in relativistic correction in CASTEP (Koelling-Harmon), a GGA-RPBE functional used and the cut-off energy used was 600 eV without any optimization of the cluster models and keeping the unit cell constraints fixed.

8.3 Results and Discussion

Noncovalent interactions, in this case, the ChB interaction between Te and I in the novel cocrystal **1.d** are studied. The structural and geometric deviation of the isolated starting material, **d** (CCDC REFCODE: SATSUB), upon forming a ChB with telluradiazole (**1.d**) containing the σ-hole region in Te where the I of **d** interacts, is reflected in the asymmetry parameter and quadrupolar coupling constant values of iodine. ChB in the cocrystal **1.d** and not the starting

material, **d**, is reflected in the quadrupolar coupling constant and asymmetry parameter values of ^{127}I.

Single-crystal X-ray diffraction studies confirmed the crystallization of cocrystal **1.d** into space group P_21/n.

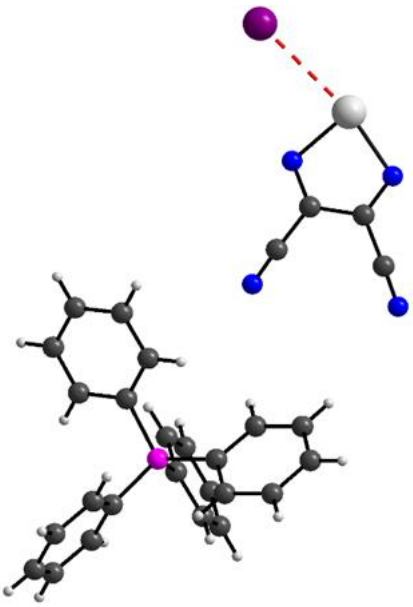

Figure 8.3.1: Single-crystal structure of cocrystal **1.d** (white-Te, purple-I red dashed line represents the ChB interaction between Te and I).

Tetraphenylphosphonium iodide, **d**, crystallizes in the space group, $I\bar{4}$, which is also known as the body-centered tetragonal crystal, and is a class of symmetric orthorhombic crystal system. . The single-crystal X-ray data also confirmed the Te---I ChB distance to be 3.291 Å and the N-Te-I bond angle to be 169.14° for **1.d**. A detailed information on the single-crystal X-ray diffraction parameters can be found in Table 8.3.1.

Table 8.3.1: Single-crystal X-ray diffraction values of **1.d** and **d**.

Sample	**Cocrystal 1.d**	**Starting material d (CCDC REFCODE = SATSUB)***
Formula	$C_{28}H_{20}PIN_4Te$	$C_{24}H_{20}PI$
Space group	$P2_1/n$	$I\bar{4}$
Cell dimensions	a = 7.3692(2) Å b = 22.3670(5) Å c = 16.3060(4) Å	a = b= 11.9785 (14) Å c = 6.9809 (9) Å
Cell volume	2678.51 $Å^3$	1001.65 $Å^3$
Te---I bond distance	3.291 Å	-
N-Te-I bond angle	169.14°	-

The powder X-ray pattern for the experimental and simulated cocrystal **1.d** (Figure 8.3.2) based on the solved single-crystal X-ray structure were in good agreement and did not involve any phase changes keeping the structural integrity intact on being ground into fine powder. This observation gives assurance to further interpret NMR data of cocrystal **1.d** and **d**.

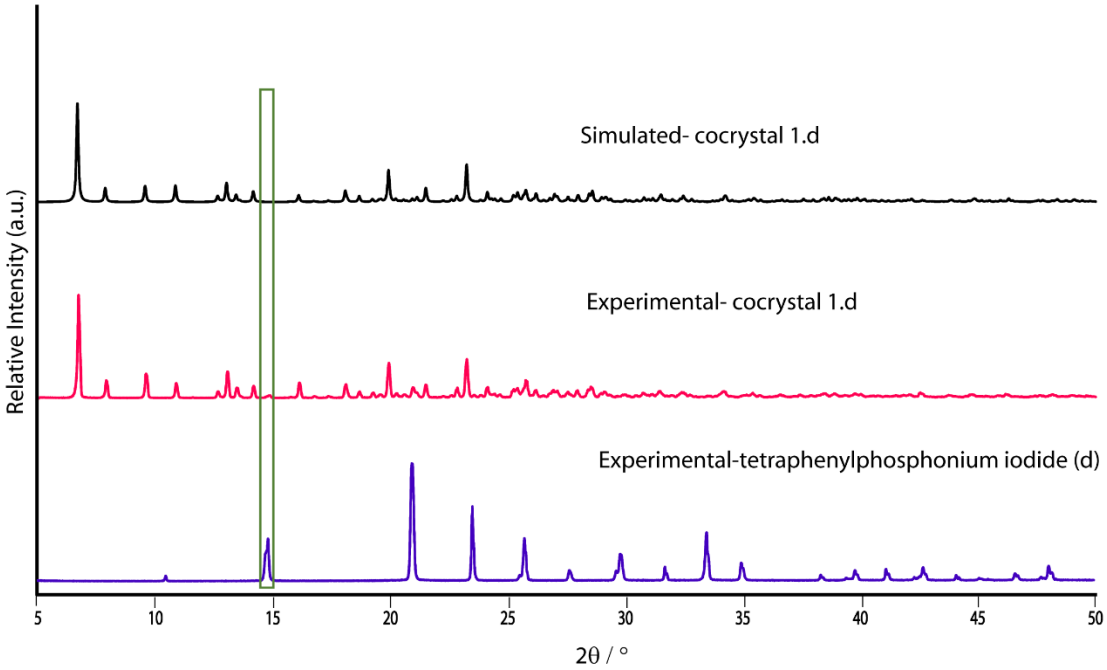

Figure 8.3.2: Powder X-ray diffractogram of cocrystal **1.d**, simulated-black, experimental- pink and starting material **d),** experimental- violet. The green highlighted peak at 14.8°shows trace of the starting material **d)** tetraphenylphosphonium iodide in the experimental powder pattern of **1.d**

A thorough study of the nature of the cocrystal **1.d** was confirmed when the solid-state NMR experiments were executed to give us the asymmetry parameter in the cocrystal caused by the presence of ChB interaction. The highly quadrupolar iodine nucleus experienced a vast increase in the quadrupolar coupling constant value on ChB formation (**d** to **1.d**) (Table 8.3.2). The experimental data obtained with the aid of solid-state NMR are given in Table 8.3.2. The value of the isotropic chemical shift and span for ^{125}Te of cocrystal **1.d** was recorded at 2256.7 ppm and 960.78 ppm whereas for the starting material **1**, the literature value of ^{125}Te chemical shift and span was observed as 2332.8 ppm and 1268 ppm[14] respectively (Figure 8.3.3).

Phosphorus-31 SSNMR experiments (Figure 8.3.4) at various spinning speeds of ChB acceptor, **d** and cocrystal **1.d** confirmed the deviation of ^{31}P isotropic chemical shift from 21.07 ppm in **d** to 21.5 ppm in **1.d**. Iodine NMR acted as a probe of the ChB interaction for cocrystal **1.d** and starting material **d**.

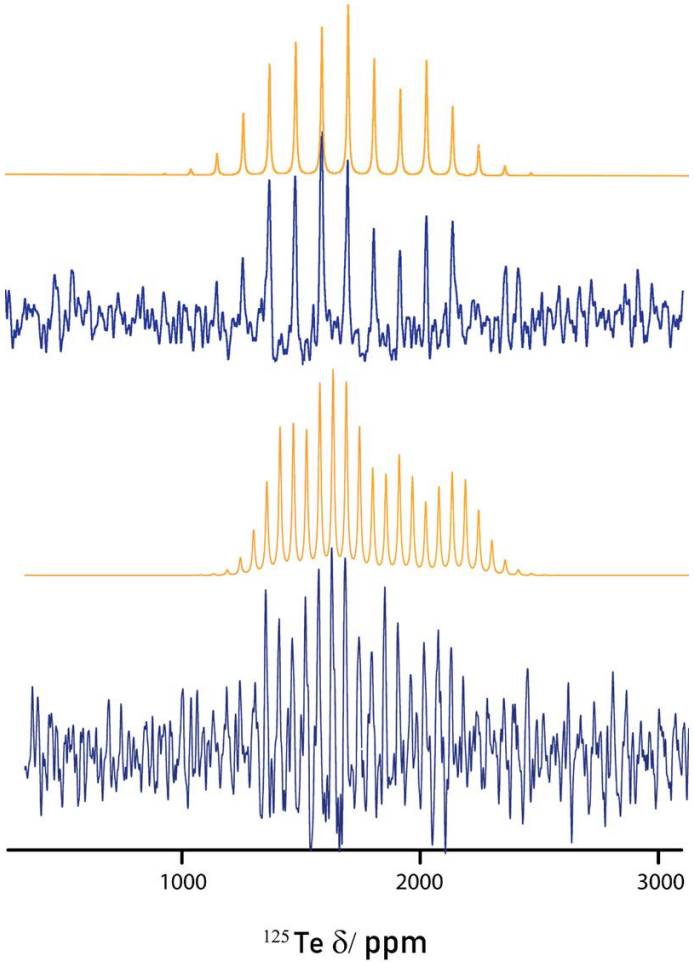

Figure 8.3.3: ^{125}Te HPDEC/MAS NMR spectra acquired at 11.75 T magnetic field at 7 kHz (below) and 12 kHz (above) MAS rates. Blue-experimental and yellow-simulated using in WSolids.[12]

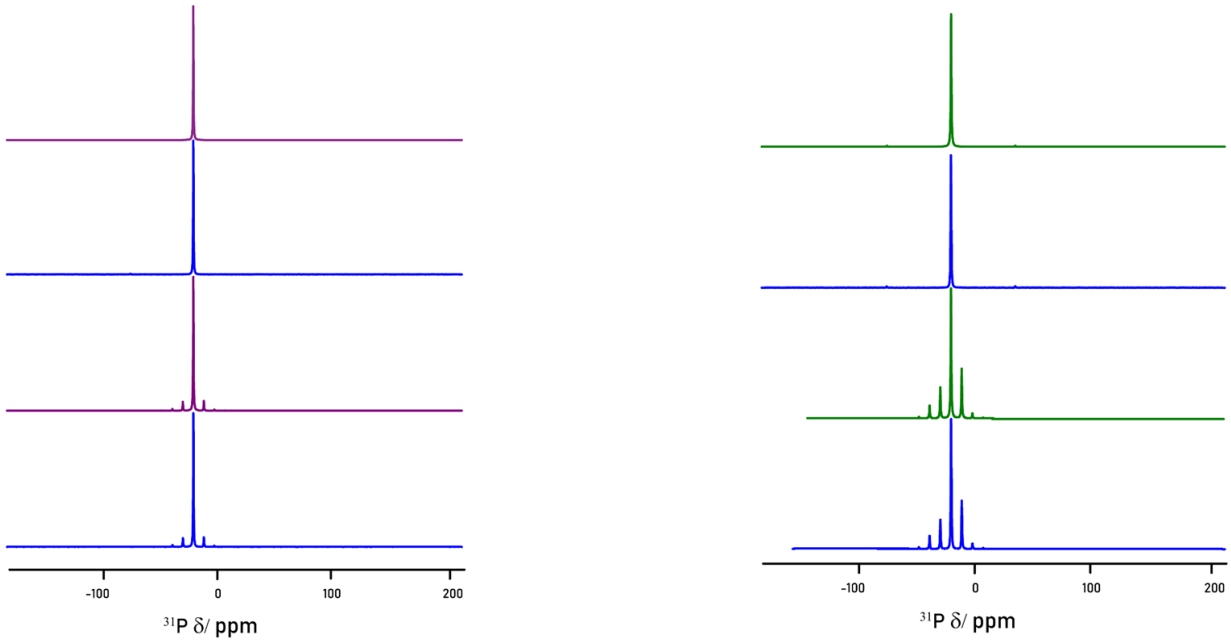

Figure 8.3.4: ^{31}P CP/MAS NMR spectra of pure tetraphenylphosphonium iodide (**d**) (left) and cocrystal **1.d** (right) at 1.5 kHz and 9 kHz (blue-experimental) MAS rates acquired at 9.4 T magnetic field (purple, green-simulated using DMFit).[11]

It was rather difficult to acquire the ^{127}I SSNMR spectra at a field of 11.7 T due to a highly quadrupolar nucleus as iodine I=5/2, thus a ultrahigh magnetic field was required to tackle the broad quadrupolar patterns.[18,20] NQR spectroscopy was also taken up to figure out and agree with the C_Q and asymmetry parameter obtained for cocrystal **1.d** which are listed in Table 8.3.1. A study on metal alkali halides featuring ^{127}I SSNMR by Widdifield in 2010 shows a higher-order quadrupolar induced effects on the SSNMR line shapes.[19] The iodine SSNMR spectra (Figure 8.3.5) show that the C_Q value for ^{127}I increases from 50 MHz to 253 MHz on the ChB interaction formation from **d** to **1.d**. The impurity at 0 ppm is due to the remnants from starting material, **d**. bond in the cocrystal **1.d** (Figure 8.3.6) justifies the higher quadrupolar coupling constant in the

iodine NMR consistent with previous findings[18,19] related to quadrupolar nucleus. The iodine spectra recorded for the cocrystal **1.d** was found to be 17 MHz wide which is extremely challenging and only feasible to acquire at very high magnetic fields.

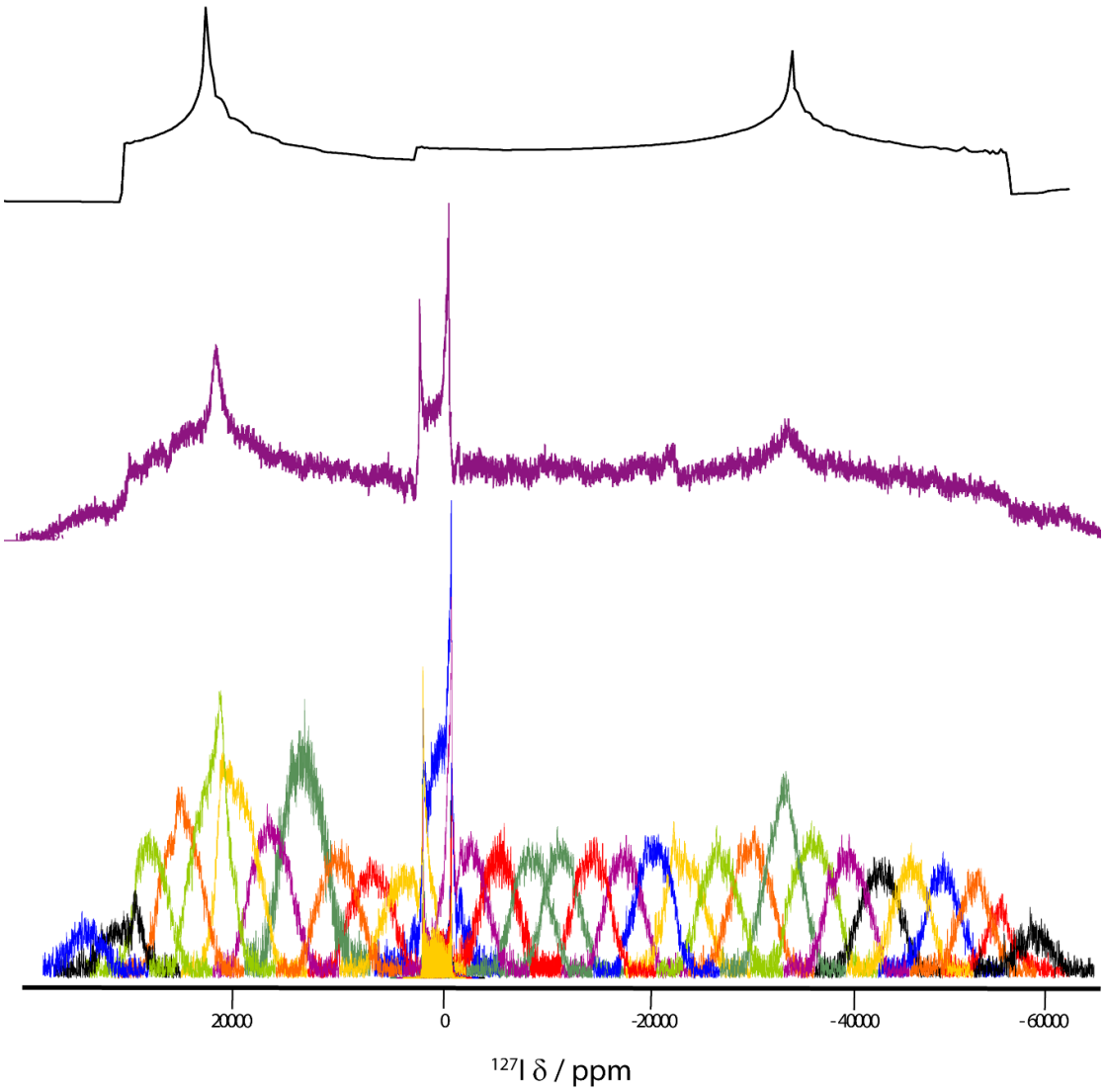

Figure 8.3.5: ^{127}I solid-echo spectra of cocrystal **1.d** at 21.1 T magnetic field. Magenta- all the offsets added up acquired with VOCS method, black-simulated using QUEST.[10] 17 MHz wide spectra. Impurity peak at 0 ppm resulting from remnants of starting material, **d**

Table 8.3.2: Experimental ^{127}I NMR parameters for cocrystal **1.d** and pure ChB acceptor **d** obtained using QUEST simulation software.[10]

Sample	^{127}I $\lvert C_Q \rvert$ / MHz	^{127}I η	^{127}I ν_1/ MHz	^{127}I ν_2/ MHz
d	50 ± 1	0.02	-	-
1.d	253 ± 2	0.23	48.976 ± 0.200	75.776 ± 0.200

Table 8.3.3: GIPAW-DFT computed NMR parameters for cocrystal **1.d** and pure ChB acceptor **d**.

Sample	^{127}I $\lvert C_Q \rvert$ / MHz	^{127}I η	^{125}Te σ_{11} /ppm	^{125}Te σ_{22} / ppm	^{125}Te σ_{33} / ppm	^{125}Te δ_{iso} / ppm	^{125}Te span Ω / ppm	^{125}Te skew κ
1.d	325.11	0.4	472.78	474.68	287.47	3921.30	549.00	-0.405
d	68.83	0.02	-	-	-	-	-	-

The computed electric field gradient tensor of ^{127}I with the values calculated from CASTEP and extracted with EFGShield software,[6] show that the EFG tensors on I of the ChB acceptor, **d** are mutually perpendicular (Figure 8.3.6 and Table 8.3.3). The EFG tensors and the breakdown of symmetry from $I\bar{4}$ to $P_2 1/n$ at the iodide anion in tetraphenylphosphonium iodide to Te···I ChB in the cocrystal **1.d** (Figure 8.3.7) justifies the higher quadrupolar coupling constant in the iodine

NMR consistent with previous findings[18,19] related to quadrupolar nucleus. The DFT computed ^{125}Te span and magnetic shifts for **1.d** were obtained by varying the Te---I bond-distance and keeping the N-Te-I bond angle fixed in each case. The ChB strength increased as the Te---I bond distance shortened, which was marked by a decrease in ^{125}Te span and the magnetic shift principal components. ZORA-spuin-orbit relativistic effects were implied throughought the calculations to address the relativiatic effects of heavy atoms that are Te and I. These findings are in good agreement with previous reported values from our group[14,22] and this work where the ^{125}Te experimental data of **1.d** shows the same trend in the span and chemical shift with respect to pure starting material **1**.[14]

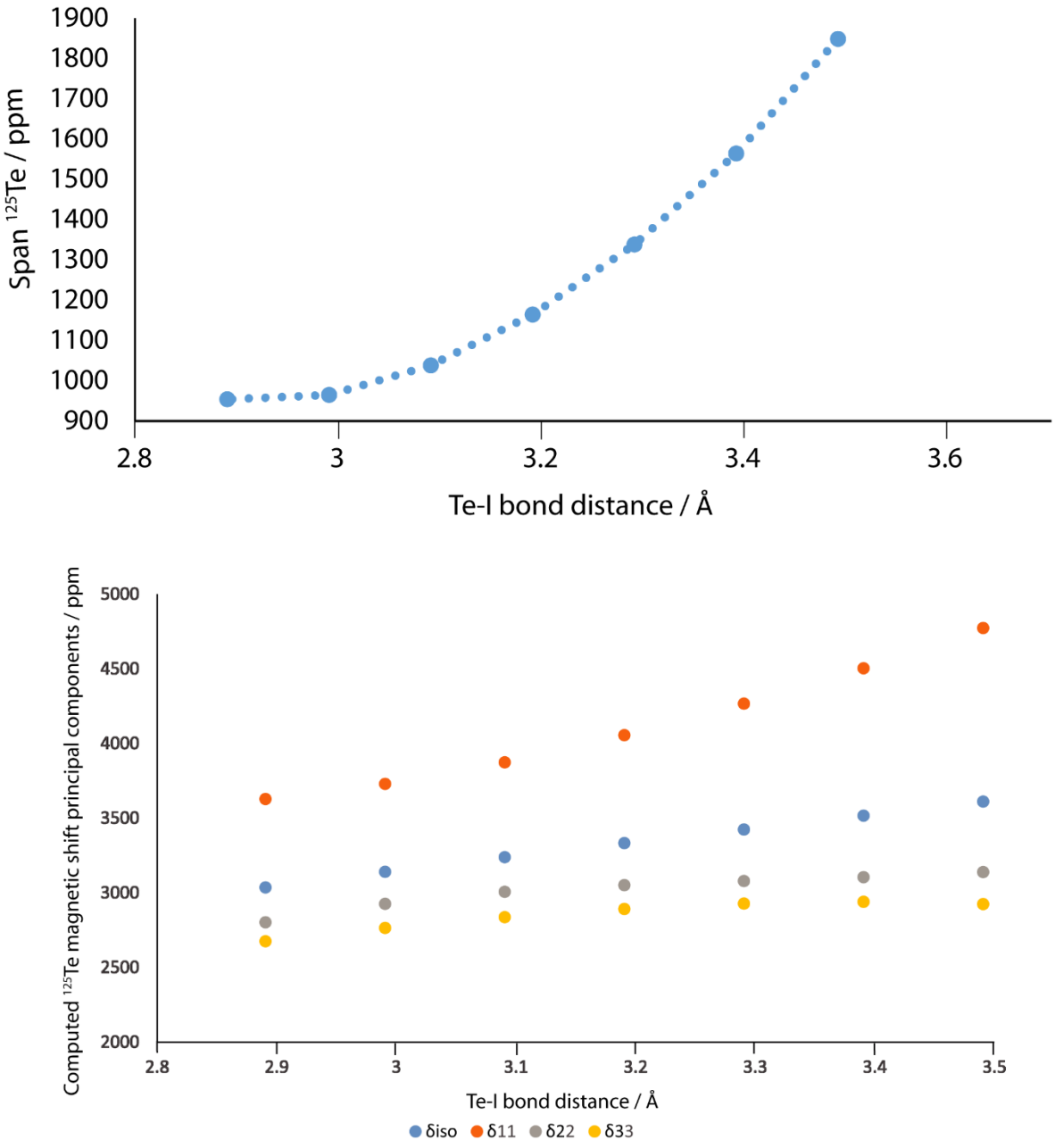

Figure 8.3.6: DFT Computed span of ^{125}Te versus varied Te---I bond distance at fixed bond angle of 169.14° between N-Te···I of cocrystal **1.d** cluster model (top). DFT Computed magnetic shift principal components versus varied bond distances of Te···I in cocrystal **1.d** cluster model

(bottom). ZORA, spin-orbit, SAOP functional and QZ4P basis-set was used. The calculations were carried out in ADF 2019.[9]

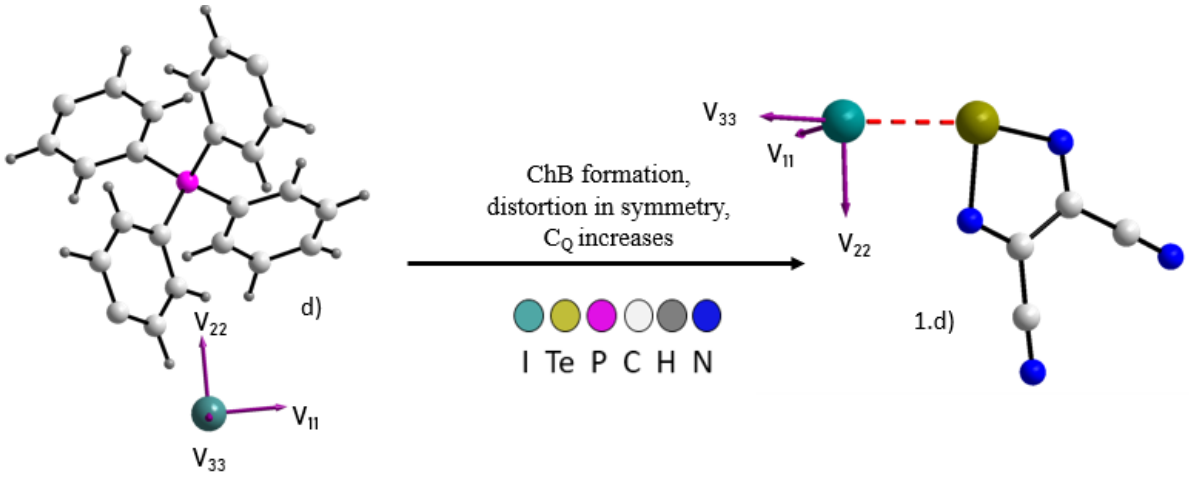

Figure 8.3.7: EFG tensors on losing its axial symmetry on ChB formation from pure ChB acceptor **d** to cocrystal **1.d**, the tensors components were obtained using GIPAW-DFT calculations and extracted using EFGShield software.

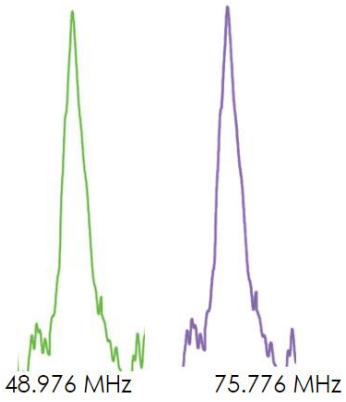

Figure 8.3.8: NQR frequencies obtained at zero magnetic field for ^{127}I for cocrystal **1.d**.

The NQR resonance spectroscopy supports the ChB interaction between a quadrupolar iodine and a spin ½ Te in terms of the two observed transitions at 48.976 MHz and 75.776 MHz for ^{127}I for which the asymmetry parameter obtained was 0.23 (in **1.d**) from 0.02 (in **d**).

The computational results obtained for iodine in the cocrystal **1.d** agree with the increase in quadrupolar coupling constant and asymmetry parameter value just as the experimental value produced as seen in Table 8.3.2.

8.4 Conclusions

A novel cocrystal featuring Te···I chalcogen bonds was synthesized and studied using solid-state NMR and NQR to decipher the large quadrupolar interactions from iodine atom as the ChB acceptor nucleus in **d**, and its contribution to the chemical and structural properties of the ChB, Te···I in the cocrystal **1.d**. 17 MHz wide iodine-127 NMR spectra of the cocrystal showed the effects of ChB involved between the Te -spin-1/2 and quadrupolar iodine-spin-5/2 nucleus. The deviation of symmetry from body-centered tetragonal in tetraphenyl phosphonium iodide where the iodide ion is isolated and excess in electrons to a monoclinic cocrystal of Te···I ChB displays the importance of quadrupolar coupling of iodine to tellurium. The computational results agree with the trend seen in the experimental results where the C_Q and η increased upon the ChB formation and symmetry breakdown (electric field gradient tensors of the cluster models also prove the same) and the ^{125}Te span and chemical shift tensor components decreased on ChB formation. To support the iodine quadrupolar parameters, the NQR frequencies of iodine show two transitions that were resolved owing to the challenging iodine SSNMR experiments and

tracing down the C_Q value of the cocrystal. Previous Chapters show how CS tensors, *J*-coupling tensors was used a probe of the ChB. This work is a testament to quadrupolar coupling interaction being another important SSNMR probe of the ChB.

References

[1] Terraneo, G.; Resnati, G.; Metrangolo, P. *Iodine and Chemistry applications, Ch-8: Iodine and Halogen Bonding*, 159-194, Kaiho, T. John Wiley & Sons, USA, **2015**.

[2] Widdifield, C. M.; Bryce, D. L. *J. Phys. Chem. A.* **2010**, 114, 40, 10810–10823.

[3] Semenov, N. A.; Pushkarevsky, N. A; Beckmann, J. Finke.; P. Lork, E.; Mews, R.; Bagryanskaya, I. Y.; Gatilov, Y. V.; Konchenko, S. N.; Vasiliev, V. G.; Zibarev, A. V.; Chem. *Eur. J. Inorg. Chem*. **2012,** 3693–3703.

[4] Sheldrick, G. M. *TWINABS, Version 2012/1*. Georg-August-Universitat, Gottingen, Germany, **2012**.

[5] Liao, M. Y.; Harbison, G. S. *J. Chem. Phys*, **1994**, 100, 3, 1895-1901.

[6] Adiga, S.; Aebi, D.; Bryce, D. L. *Can. J. Chem***. 2007**, 85, 496-505.

[7] Politzer, P.; Murray, J. S.; Clark, T.; Resnati, G. *Chem. Phys. Phys. Chem*. **2017**, 19, 32166-32178.

[8] Szell, P. M. J.; Grebert, L.; Bryce, D. L. *Angew. Chem. Intl. Ed*. **2019**, 58, 13479-13485.

[9] ADF 2019, SCM, Theoretical Chemistry, Vrije Universiteit, Amsterdam, The Netherlands, http://www.scm.com.

[10] Perras, F. A.; Widdifield, C. M.; Bryce, D. L. *Solid. State. Nucl. Magn. Reson*. **2012**, 45-46, 36-44.

[11] Massiot, D.; Fayon, F.; Capron, M.; King, I.; Le Calve, S.; Alonso, B.; Durand, J. O.; Bujoli, B.; Gan, Z.; Hoatson, G. *Magn. Reson. Chem*. **2002**, 40, 70-76.

[12] Eichele, K. WSOLIDS1 NMR Simulation Package version 1.20.22, 2014.

[13] Jameson, C. J.; Jameson, A. K. *Chem. Phys. Lett*. **1987**, 135, 254-259.

[14] Kumar, V.; Xu, Y.; Bryce, D. L. *Chem. Eur. J*. **2020**, 26, 3275-3286.

[15] Ramaprabhu, S.; Rama Rao, K. V. S.; Weiss, A. *J. Mol. Struct*. **1983**, 111, 295-300.

[16] Yates, J. R.; Pickard, C. J.; Mauri, F. *Phys. Rev. B*. **200**1, 76, 024401.

[17] ADF 2019, SCM, Theoretical Chemistry, Vrije Universiteit, Amsterdam, The Netherlands, http://www.scm.com.

[18] Attrell, R. J.; Widdifield, C. M.; Korobkov, I.; Bryce, D. L. *Cryst. Growth. Des*. **2012**, 12, 1643-1651.

[19] Widdifield, C. M.; Bryce, D. L. *J. Phys. Chem. A*. **2010**, 114, 10810-10823.

[20] Bryce, D. L.; Sward, G. D. *Magn. Reson. Chem*. **2006**, 44, 409-450.

[21] Almario, C.; Nag, T.; Bryce, D. L. *Facets*, **2023**, 8, 1-14.

Part 4: Conclusions

This section of the dissertation includes a concrete set of explanations of the findings and observations of the works in part 2 and 3. Solid-state NMR experiments have been used widely to probe the formation, structure, and analysis of noncovalent interactions. This technique has been paired with X-ray crystallographic studies to comply with and find clarity in determining the structural aspects and the behavioral trend in the electronic structure and local molecular geometry by extracting the NMR observables with previously reported and synthesized ChB compounds. Each of the cocrystals synthesized followed different techniques of crystallization such as slow evaporation, solvent diffusion, mechanochemistry; however, slow evaporation yielded in better quality and reproducible cocrystals which were inferred to have ChB interaction present in them. All the experimental analyses were supported by computational results in calculating the NMR parameters specific to each work.

Part 2 of this dissertation dealt with several polycrystalline solid-state NMR experiments done on crystal-engineered cocrystals featuring ChB. Synthesis of novel cocrystals that featured ChB which would be appropriate as a precursor to basis of many organo-heterocycles useful in fields of catalysis, pharmaceuticals, and materials chemistry were experimented on. A literature survey of potential ChB donor and acceptors were researched and the ways to reproduce them were verified. Five-membered heterocyclic rings containing Se and Te were extensively studied throughout. The propensity of ChB formation of donors, 3,4-dicyano-1,2,5-telluradiazole and 3,4-dicyano-1,2,5-selenodiazole feature two σ-holes in their Ch atom sites, making the ChB donor highly directional. The ChB acceptors chosen were hydroquinone, with the O of the carbonyl group as the electron withdrawing moiety that interacted with 3,4-dicyano, 1,2,5-selenodiazole to

result in ChB interaction, similarly, 3,4-dicyano-1,2,5-telluradiazole interacted with tetraethylphosphonium chloride and tetraphenylphosphonium chloride, where the Cl^- ion acted as the electron-rich moiety to result in a ChB. A thorough study of the novel ChB cocrystal in Chapter 5 was done after preliminary X-ray studies that ensured the crystalline properties and geometry of the crystal via SCXRD and then on further grinding of the crystal for PXRD, showed the phase purity and existence of a singular phase and no transformation whatsoever. Once the X-ray studies confirmed the structural aspects of the cocrystals, SSNMR experiments were carried out to see how the ChB formation causes change in NMR observables from that of the isolated ChB donor/acceptor and the trend in those observables.

Chapter 6 dealt with salt cocrystals featuring ChB interaction between tellurium of 3,4-dicyano-1,2,5-telluradiazole and N, S and Se of KOCN, KSCN and KSeCN and 18-crown-6 salt. Chemical shift and magnetic shielding tensor principal components were used to probe the ChB interactions in Chapter 5 where $^{77}Se/^{125}Te$ CP/MAS and HPDEC/MAS SSNMR experiments were carried out at multiple spinning speeds to extract the isotropic peaks and to testify the validity of the isotropic chemical shift. It was found that in the cocrystal featuring Te···Cl in cocrystal of tetraethylphosphonium chloride with telluradiazole, the ^{125}Te isotropic chemical shift increased and the span decreased. The Te---Cl in tetraphenylphosphonium chloride the isotropic chemical shift was found to decrease with respect to telluradiazole, but the span decreased displaying the sensitivity of ^{125}Te to ChB formation in terms of chemical shift tensors and span. The ^{77}Se chemical shift tensor and span matched the trend of decreasing span values and increase in isotropic chemical shift values, relevant to our group's previous trends on ChB interaction studies. This hydroquinone-selenodiazole cocrystal's ChB are a testament to the retention of self-

complementary chalcogen bonds between two selenodiazole molecules in this system (two crystallographically distinct Se sites in the ChB donor, selenodiazole).

In Chapter 6, chemical shift tensors were used as probe for the ChB in various salt cocrystals featuring Te···N/S/Se interactions and was observed via ^{125}Te SSNMR experiments. The trend of the NMR observables and strength of which ChB were pronounced as an effect of ChB interaction, both electronically and via structural analysis were revealed with the aid of SSNMR.

^{15}N chemical shift tensor components and span were measured via SSNMR experiments in telluradiazole-KOCN-18-C-6 cocrystal, where the KOCN was isotopically enriched with ^{15}N. The nitrogen-15 isotropic chemical shift tensor of the cocrystal decreased on ChB formation from pure KOCN, and the axial symmetry of KOCN was disrupted upon ChB formation in the cocrystal, and the span decreased as well. This was a proof of how SSNMR could also be used to probe the ChB acceptor. The results obtained from experiments were in good compliance with the DFT calculations performed on the cluster models. The calculations proved that relativistic spin-orbit calculations were best matched for these ChB interactions, due to presence of heavy atom, Te in them.

Part 3 focused on the findings of novel cocrystals featuring ChB interactions between telluradiazole and tetraphenylphosphonium bromide and tetraphenylphosphonium iodide and their structural elucidation and the effect of quadrupolar interaction with spin-1/2 nucleus, Te.

Chapter 7 showed the findings of novel polymorphic cocrystals synthesized using slow evaporation and reproducible polymorphs of telluradiazole and tetraphenylphosphonium bromide. The SCXRD results confirmed the formation of two polymorphs and the PXRD confirmed no phase change while the crystals were grounded into fine powder, interestingly so, the SSNMR

resulted in multiplets while the ^{125}Te SSNMR was performed as though the SCXRD depicted only one crystallographic Te site in each of the polymorph. The idea was to decode the centre-band of the spectra obtained for each of the polymorph to see what amount of quadrupolar interaction from the quadrupolar bromine when Te···Br ChB interaction formed, affected the splitting pattern of the spin-1/2 tellurium. The *J*-coupling between Te···Br for both the polymorphs were in the range of 1200 to 1500 Hz and the anisotropy factor ranged from 2000-4000 Hz for both the polymorphs, highlighting the importance of quadrupolar coupling from the Bromine which played a crucial role in this huge anisotropic magnitude. The quadrupolar coupling constant and asymmetry parameter of bromine was extracted from high-magnetic field regime and was implied to simulate the broad Te line shapes which very well matched the experimental centre-band in each Te-125 spectrum of the polymorphs. Bromine, being a spin-3/2 quadrupolar nucleus showed a distinct contribution to the J-coupling via is asymmetric electron cloud and the EFG tensors from the starting material of tetraphenylphosphonium bromide broke down as to when ChB interaction was prominent in the polymorphs, making the quadrupolar coupling constant rise and so did the asymmetry parameter. The dipolar coupling of $^{79/81}$Br was also taken into consideration while simulating the tellurium spectra to attribute to the broad multiplet centre band observed.

GIPAW-DFT ZORA relativistic correction (periodic boundary conditions) calculations were performed on both $^{79/81}$Br and ^{125}Te. The computed quadrupolar coupling constant values and asymmetry parameters of $^{79/81}$Br and ^{125}Te chemical shift tensor parameters were in agreement with the trend observed in the simulated experimental SSNMR experimental results. To conclude, large anisotropic *J* and quadrupolar couplings have been measured for Te and Br nuclei involved in non-covalent chalcogen bonds. The reduced isotropic coupling constants are approximately 70

to 85% smaller than corresponding values for comparable 4^{th} and 5^{th} period elements when they are engaged in covalent bonds. The sizable anisotropy of *J* coupling across the tellurium-bromine ChB provides clear experimental evidence for non-Fermi contact contributions to this coupling, implying a constructive mixing between orbitals centered on the two nuclei. In addition, the magnitudes of the bromine quadrupolar couplings measured for bromide anions acting as ChB acceptors have been shown to be characteristic of the ChB when compared to other available data. Finally, all NMR parameters discussed clearly differentiate between two polymorphic ionic cocrystals, further demonstrating the exquisite sensitivity of the measured coupling constants to small differences in the ChB environment. Overall, this work sheds new light on the nature of the chalcogen bond and elucidates the potential of studying σ-hole interactions via NMR analyses of challenging nuclei.

Chapter 8 showed the ChB interaction between yet another quadrupolar nucleus iodine (I=5/2) and Te (I=1/2), this study was supported by NQR spectroscopy of iodine in zero magnetic field. The two transitions obtained from iodine NQR were also confirmed by the high-field solid-state NMR spectroscopy of iodine which is usually challenging due to even broader line shape and higher spectral width. The asymmetry parameter of a tetragonally symmetric iodine nucleus in tetraphenylphosphonium iodide, which retained the axial symmetry of iodine nucleus in the ideal state was broken upon ChB interaction with Te nucleus in the cocrystal. The quadrupolar interaction was rather predominant than the *J* and residual dipolar coupling which averaged out the Te spectra in a single line shape and the isotropic peak was found to decrease than that of the starting material, telluradiazole and the span decreased on ChB formation. The quadrupolar

coupling constants and the asymmetry parameter obtained from both experimental and calculation agree with the findings of the experiment.

Future works

The growing importance of σ-hole interactions pertaining to noncovalent interactions promises variety of supramolecular synthons also belonging to group 14, 15, and 18, namely the tetrel,[1] pnictogen[2] and aerogen[3] bonds other than group 16 and 17 of the periodic table. The attractive interactions arising from the electrophilic sites with the electron-rich moieties specific to the class of σ-hole interactions of the above groups of the periodic table can be tuned to enhance the rising applications in the supramolecular chemistry, molecular recognition, organocatalysis, material science and pharmaceuticals.[11-14] Previously, NMR response of the tetrel bond, chalcogen bond, halogen bond, pnictogen bond and matere[4] bonds have been explored in polycrystalline samples with the help of SSNMR in our group.[5,6,7,8] In part 2 and 3 of this dissertation we explore how various NMR observables can act as the probe of the ChB in the solid-state. SSNMR not only helped probe just the ChB donor, but also, the ChB acceptor and the ChB bond itself using CS tensors, *J* tensors and EFG tensors. Unique and novel ChB cocrystals were synthesized which revealed various electronic and geometric connectivities of the ChB. In Chapter 7, the *J*-coupling between Te and Br revealed that the presence of a highly quadrupolar nuclei determines the strength of ChB interactions (more specifically how strongly the ChB donor is coupled to the quadrupolar nucleus) to yield a multiplet line shape in the ^{125}Te SSNMR spectra. The scope of

exploring noncovalent interactions, particularly, σ-hole interactions, with the aid of SSNMR is emerging and the property, local electronic environments and bonding characteristics can be well-defined. Resonant Acoustic Mixing,[9] an effective method in mechanochemical cocrystallization can also be included in designing various classes of cocrystals, salt cocrystals, multicomponent and ionic cocrystal polymorphs beside the conventional crystallization techniques. Variable temperature SSNMR experiments[10] could be applied to understand the ChB dynamics and could serve as a mechanistic pathway for probing the ChB interactions.

References

[1] Bauza, A.; Mooibroek, T. J.; Frontera, A. *Angew. Chem. Int. Ed.* **2013**, 52, 12317-12321.

[2] Resnati, G.; Bryce, D. L.; Desiraju, G. r.; Frontera, A.; Krossing, I.; Legon, A. C.; Metrangolo, P.; Nicotra, F.; Rissanen, K.; Scheiner, S.; Terraneo, G. *Pure. Appl. Chem*. **2024**, 1-11.

[3] Esrafili, M. D.; Mohammadian-Sabet, F.; Solimannejad, M. *Chem. Phys. Lett*. **2016**, 659, 196-202.

[4] Gomila, R. M.; Frontera, A. *Molecules*, **2022**, 27, 3-7.

[5] Southern, S. A.; Nag, T.; Kumar, V.; Triglav, M.; Levin, K.; Bryce, D. L. *J. Phys. Chem. C*. **2022**, 126, 1, 851-865.

[6] Xu, Y.; Szell, P. M.J; Kumar, V.; Bryce, D. L. *Coord. Chem. Rev*. 2020, 411, 213237, 1-22.

[7] Kumar, V.; Xu, Y.; Bryce, D. L. *Phys. Chem. Chem. Phys*. **2020**, 22, 3817-3824.

[8] Xu, Y.; Calabrese, M.; Pizzi, A.; Nag, T.; Hung, I.; Gan, Z.; Resnati, G.; Bryce, D. L. *Chem. Commun*. **2023**, 59, 12609-12612.

[9] Nari, A.; Ovens, J. S.; Bryce, D. L. *RSC Mechanochem*. **2024**, 1-13.

[10] Kong, X.; O'Dell, L. A.; Terskikh, V. V.; Ye, E.; Wang, R.; Wu, G. *J. Am. Chem. Soc*. **2012**, 134, 35, 14609-14617.

[11] Zeng, R.; Gong, Z.; Yan, Q. *J. Org. Chem*. **2020**. 85, 8397-8404.

[12] Lim, J. Y. C.; Beer, P. D. *Chem*. **2018**, 4, 731-783.

[13] Benz, S.; Lopez-Andarias, J.; Mareda, J.; Sakai, N.; Matile, S. *Angew. Chem. Int. Ed*. **2017**, 56, 812-815.

[14] Ho, P. C.; Wang, J. Z.; Meloni, F.; Vargas-Barca, I. *Coord. Chem. Rev*. **2020**, 422, 213464 (1-11).

Appendix A:

Computed NMR parameters- with reference to Chapter 4

This section shows that cluster models were chosen highlighting the ChB interactions as the main interest of the thesis to scrutinize the NMR parameters and the influence on them due to ChB interactions and formation, their electronic environment, stability, geometry, and other factors. To ensure the integrity of the novel or learned chalcogen-bonded cocrystals, the cluster models were created keeping the bond parameters intact, which were obtained from the cif files and then introduced to computations in both periodic boundary conditions and without it to understand the difference in the computed results leading to accuracy in trends and correctness with the experimental result. Few of the cluster models were moulded into varying one of the bond parameters at a time to see the notable change of NMR parameter's response to the magnitude of ChB in the engineered cocrystals.

Amsterdam Modelling Suite, CASTEP package and Gaussian 09 programs were employed in studying the cluster models and extract NMR parameters of importance owing to the prominent solid-state NMR interactions responsible in the solid-state spectra obtained henceforth focusing mainly on the Chalcogen atoms and its ChB interaction with the atom in question for various cocrystal systems. Relativistic corrections, which are a mandate in the heavier congeners in group 16 and other heavier nuclei that interacts with the chalcogen atom in the ChB interactions have been considered to compare the computation where relativistic corrections were not used.

Cluster models and extraction of NMR parameters

Figure 1 and Figure 2 are two ChB novel cocrystals which were experimentally studied and experimented on using SSNMR experiments and the nuclear magnetic shielding parameters were extracted using DFT calculations on the Amsterdam Modelling suite with relativistic corrections. The cluster models (b) in the Figures were built using the cif files (a). The calculations comprised of Statistically Averaged Orbital Potential (SAOP) basis set and a GGA-PBE functional to obtain the nuclear magnetic shielding parameters and the principal components. The principal shielding parameters were converted to chemical shift to match the correctness of the observables and identify the trend of ChB bond strength and directionality when one of the bond parameters were varied at a time (bond distance or bond angle). The span and isotropic shift being highly crucial parameters were observed to decrease upon ChB formation (detailed explanations in the Chapters 5 and 6).

Table of computed NMR parameters for cluster models in Figure A1-yellow and A2-green.

r (Å)	Θ (°)	$^{77}Se/^{125}Te$ σ_{iso}/ppm	^{77}Se δ_{iso} /ppm	$^{77}Se/^{125}Te$ σ_{11}/ppm	$^{77}Se/^{125}Te$ σ_{22}/ ppm	$^{77}Se/^{125}Te$ σ_{33}/ ppm	$^{77}Se/^{125}Te$ δ_{11} /ppm	^{77}Se /$^{125}Te\delta_{22}$ /ppm	$^{77}Se/^{125}Te$ δ_{33} /ppm	Span /ppm	Skew//ppm
2.67322	168.0783	1297.772	3035.228	1510.314	948.458	1434.545	3526.644	2953.525	2625.515	901.129	-0.272
2.79822	168.0783	1189.674	3143.326	1347.198	913.252	1308.57	3560.520	3150.620	2718.837	841.683	0.026
2.92322	168.0783	1095.470	3237.530	1200.939	883.138	1202.333	3651.123	3268.717	2792.749	858.373	0.109
3.04822	168.0783	1012.577	3320.423	1068.377	857.533	1111.821	3802.657	3306.794	2851.818	950.839	-0.043
3.17322	168.0783	937.462	3395.538	945.067	834.973	1032.347	3980.984	3305.136	2900.493	1080.491	-0.251
2.67322	150	1762.039	2570.961	1856.824	1489.131	1940.161	3054.740	2408.359	2249.783	804.958	-0.606
2.67322	155	1657.085	2675.915	1772.503	1334.942	1863.809	3157.516	2497.932	2372.297	785.219	-0.68
2.67322	160	1533.993	2799.007	1681.108	1182.927	1737.945	3285.203	2591.675	2520.142	765.061	-0.813
2.67322	165	1392.516	2940.484	1578.794	1035.329	1563.425	3429.735	2795.459	2596.258	833.477	-0.522
2.67322	175	1072.224	3260.776	1344.542	772.11	1100.02	3787.715	3312.751	2681.861	1105.854	0.141
2.67322	180	909.058	3423.942	1219.869	670.366	836.938	4044.862	3506.967	2719.997	1324.865	0.188

r (Å)	Θ (°)	$^{77}Se/^{125}Te$ σ_{iso}/ppm	^{77}Se δ_{iso} /ppm	$^{77}Se/^{125}Te$ σ_{11}/ppm	$^{77}Se/^{125}Te$ σ_{22}/ ppm	$^{77}Se/^{125}Te$ σ_{33}/ ppm	$^{77}Se/^{125}Te$ δ_{11} /ppm	^{77}Se /$^{125}Te\delta_{22}$ /ppm	$^{77}Se/^{125}Te$ δ_{33} /ppm	Span /ppm	Skew//ppm
2.76363	179.769	227.721	1841.279	248.216	177.775	257.172	1988.948	1887.503	1647.385	341.563	0.406
2.88863	179.769	224.858	1844.142	235.206	185.801	253.566	1980.363	1901.932	1650.129	330.234	0.525
3.01363	179.769	224.322	1844.678	226.176	193.872	252.917	1974.846	1909.355	1649.832	325.014	0.597
3.13863	179.769	225.116	1843.884	219.762	201.607	253.978	1972.600	1911.219	1647.833	324.767	0.622
3.26363	179.769	226.637	1842.363	215.059	208.862	255.989	1972.920	1909.281	1644.888	328.031	0.612
2.76363	150	385.731	1683.269	305.473	644.885	206.836	2266.492	1565.785	1217.529	1048.963	-0.336
2.76363	155	378.173	1690.827	297.415	563.62	273.484	2155.957	1619.797	1296.726	859.23	-0.248
2.76363	160	364.051	1704.949	289.308	485.033	317.811	2067.420	1651.664	1395.763	671.657	-0.238
2.76363	165	341.856	1727.144	278.314	409.533	337.72	2001.243	1666.521	1513.666	487.577	-0.373
2.76363	170	310.904	1758.096	262.523	337.509	332.68	1957.555	1671.238	1645.493	312.062	-0.835
2.76363	175	271.416	1797.584	241.055	269.494	303.7	1936.230	1798.511	1658.010	278.220	0.01

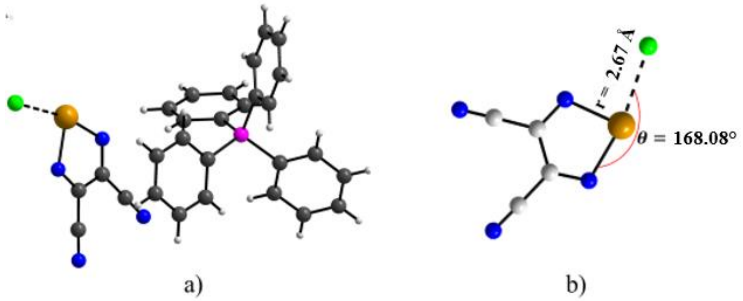

Figure A1. Single-crystal structures of a) tetraphenylphosphonium chloride and telluradiazole, b) cluster model chosen, where bond angle or bond distance are varied when one of them is kept fixed for each of the computations.

Figure A2. Single-crystal structures of a) dimethyl sulfoxide and selenodiazole b) cluster model chosen, where bond angle or bond distance are varied when one of them is kept fixed for each of the computations.

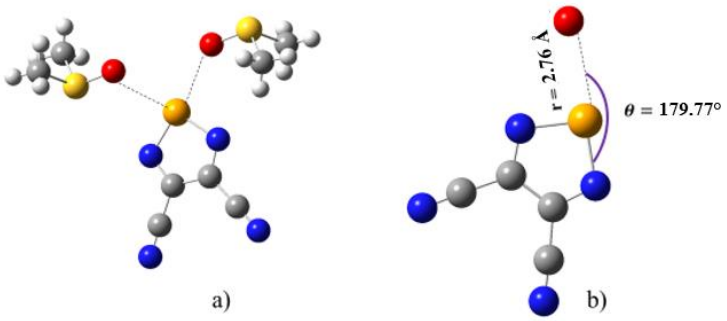

Appendix B:

Supporting information of Chapter 5

S1. Additional solid-state NMR spectra

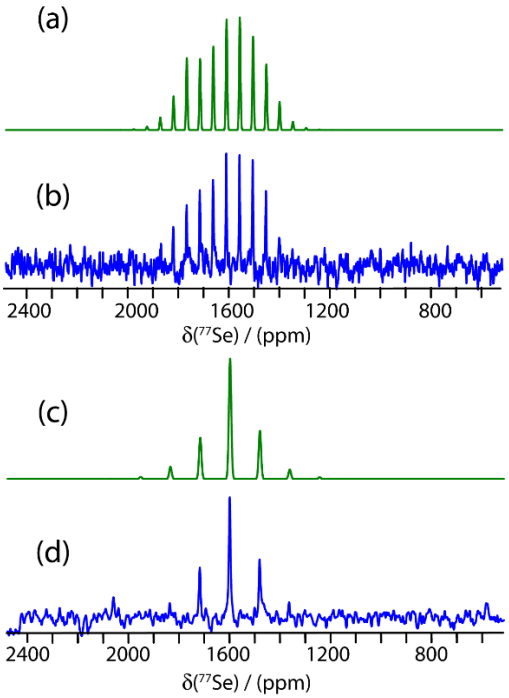

Figure S1 ^{77}Se CP/MAS NMR experiments acquired with proton decoupling at B_0 = 9.4 T for cocrystal **1a**. Experimental spectra are shown in blue and simulated spectra are shown in green. Top: MAS rate = 4 kHz; bottom: MAS rate = 9 kHz.

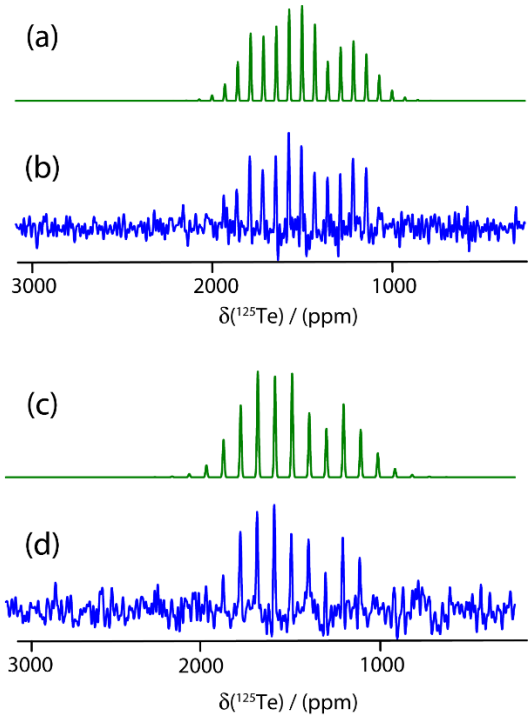

Figure S2 ^{125}Te Bloch decay MAS NMR experiments acquired with proton decoupling at B_0 = 9.4 T for cocrystal **2c**. Experimental spectra are shown in blue and simulated spectra are shown in green. Top: MAS rate = 9 kHz; bottom: MAS rate = 12 kHz.

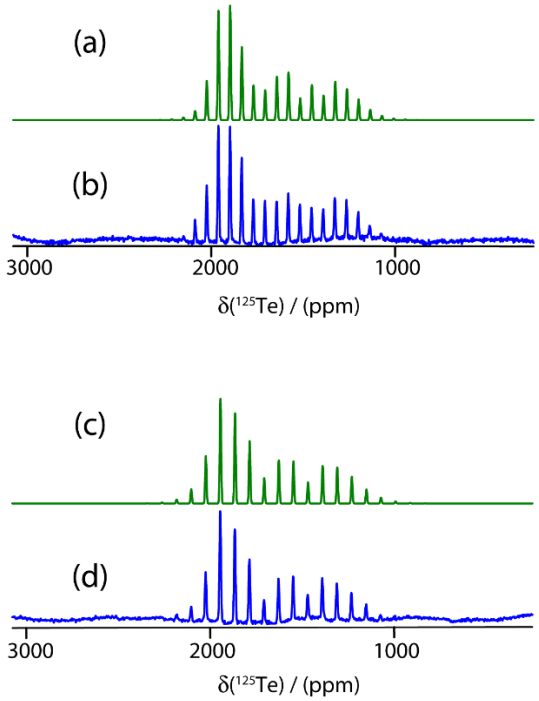

Figure S3 ^{125}Te Bloch decay MAS NMR experiments acquired with proton decoupling at B_0 = 9.4 T for cocrystal **2b**. Experimental spectra are shown in blue and simulated spectra are shown in green. Top: MAS rate = 8 kHz; bottom: MAS rate = 10 kHz.

Appendix C:

Supporting Information of Chapter 6

Chemical Shift Tensors as Probes of Chalcogen Bonds. Solid-State NMR Study of Telluradiazole-XCN^- (X = O, S, Se) Salt Cocrystals

Carina Almario,[†] Tamali Nag,[†] and David L. Bryce*

ORCID:

D. L. Bryce: 0000-0001-9989-796X

Department of Chemistry and Biomolecular Sciences

University of Ottawa

Ottawa, Ontario, K1N6N5

Canada

[†] These authors contributed equally.

*author to whom correspondence may be addressed

dbryce@uottawa.ca

1-613-562-5800 ext 2018

1. Synthesis and Sample Preparation

(a) Synthesis of 3,4-dicyano-1,2,5-telluradiazole ChB donor (1):

Synthesis of **1** was performed using a procedure by Semenov et al. (2012) with some modifications. At ambient temperature and under argon using a Schlenk line, a stirred solution of $TeCl_4$ (0.457 g, 1.70 mmol) in pyridine (15 mL) was added dropwise to a solution of diaminomaleonitrile (0.187, 1.73 mmol) in pyridine (15 mL). After the reaction was stirred for 10 minutes, Et_3N (2.5 mL, 18 mmol) was added to deprotonate the diaminomaleonitrile to produce a brown solution. This solution was stirred for an additional 20 minutes. The flask was stored in the freezer (-15 ± 2 ºC) to induce precipitation. The next day, the product was treated with iced water to remove any traces of Et_3NH and pyridine, collected by filtration, and dried under vacuum overnight to obtain a bright yellow solid powder product (1.072g, 55.5%) with a melting point of 248 ± 2 °C. The overall synthesis of **1** is illustrated Figure S1.

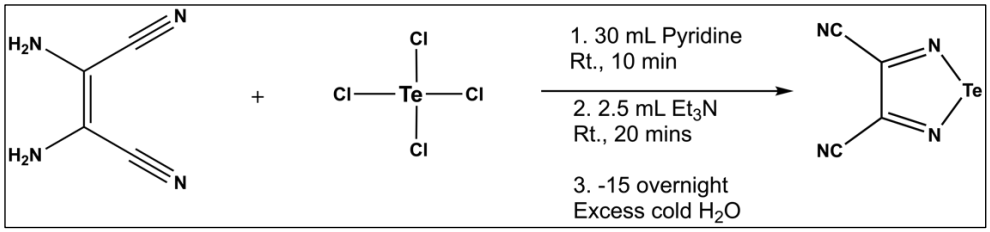

Figure S1. Schematic for the synthesis of 3,4-dicyano-1,2,5-telluradiazole (1) with starting materials diaminomaleonitrile and $TeCl_4$.

(b) Synthesis of [K(18-crown-6)] [1-XCN] (X= O, S, Se):

At ambient temperature, an equimolar mixture of KXCN (X = O, S, Se), 18-crown-6, and **1** in 20 mL of MeCN was stirred for 1 hour. The specific molar amounts of KOCN, KSCN, and KSeCN were 0.5, 0.6, and 0.5 mmol, respectively. The obtained solution was distilled to produce a residual oil which was then dissolved in 20 mL of THF and an excess of pentane was added to precipitate the product. The flask was then stored in the freezer overnight (-15 ± 2 ºC) before being mixed with additional cold pentane or ether. If no visible precipitate formed, the flask was stirred for about 10 minutes in an ice bath. Finally, the precipitate was filtered off and dried in vacuum overnight. The synthesis can be represented as shown in Figure S2.

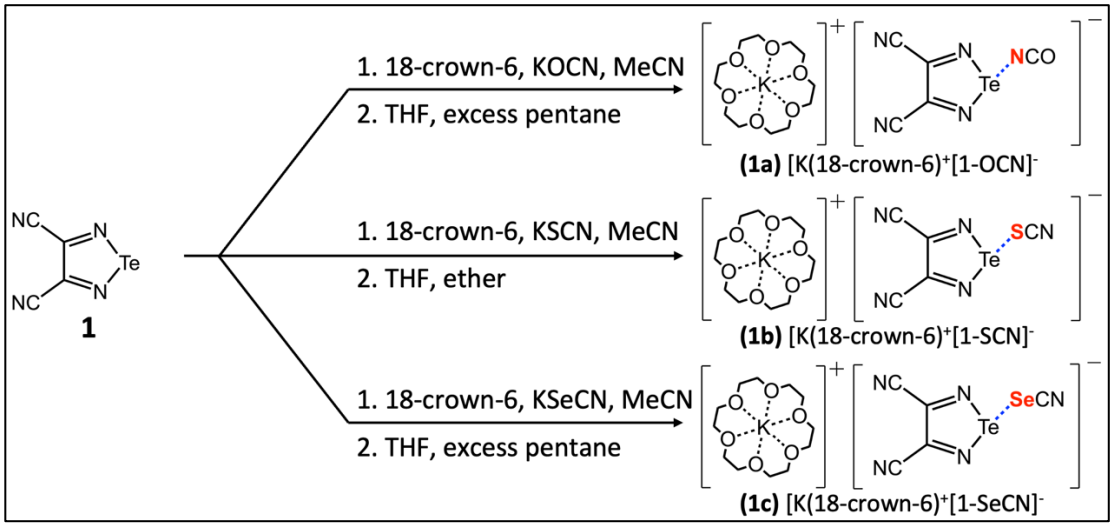

Figure S2. Schematic for the synthesis of [K(18-crown-6)]$^+$[**1**-OCN]$^-$ (**1a**), [K(18-crown-6)]$^+$ [**1**-SCN]$^-$ (**1b**), and [K(18-crown-6)]$^+$ [**1**-SeCN]$^-$ (**1c**).

(c) Recrystallization

To produce crystals suitable for SCXRD, solvent diffusion and vapour diffusion were used. 10 mg of each product was mixed into a solution of 1 mL of THF then either layered directly on top or placed in a separate vial of 2 mL of pentane. Since THF has a higher boiling point (66°C) than pentane (36.1°C), pentane is more volatile and will slowly diffuse over the gas phase into the other solvent, resulting in oversaturation, nucleation, and crystallization. Two sets of vials for products were prepared at room temperature and fridge temperature and allowed to diffuse over the course of a few weeks to a month until visible crystals were observed in the inner vial.

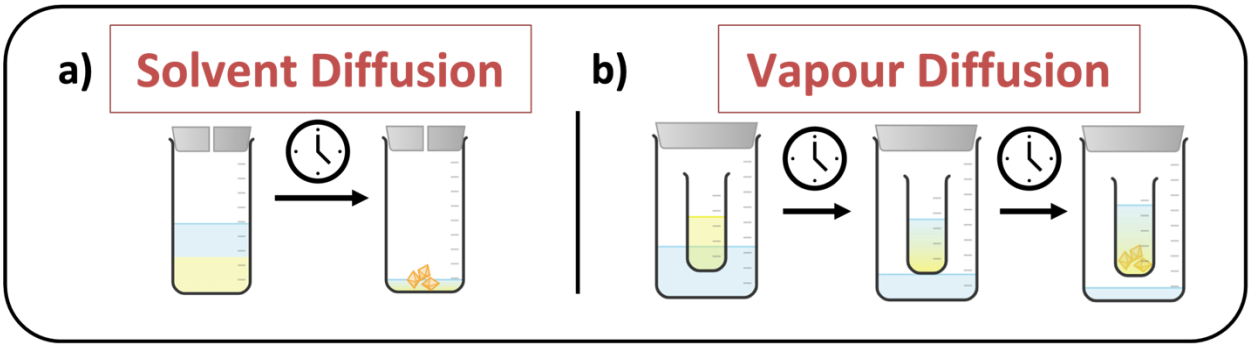

Figure S3. Recrystallization techniques performed where the product was dissolved in a solvent (THF) then an antisolvent (pentane) was either a) directly layered atop the solvent or b) placed in a separate vial and allowed to diffuse and recrystallize the product over time.

(d) Solution NMR spectroscopy

All solution NMR analyses were carried out using a Bruker AVANCE 300 MHz spectrometer (University of Ottawa, Canada) at room temperature. Solutions were prepared by mixing 0.2 mg of product in either 800 µL of $CDCl_3$ (**1a**) or DMSO (**1b**, **1c**). ^{1}H and ^{13}C solution

NMR analyses were used as a preliminary study to confirm the formation of the desired and pure product by comparing the experimental chemical shifts with reported literature.

2. Solid-State NMR: Experimental Details

Table S1. Experimental SSNMR parameters

Sample	***Nucleus***	***Pulse program***	***90° pulse width (μs)***	***Recycle delay (s)***	***Number scans***
1	^{125}Te	CP-MAS	3.10	240	1042
a*	^{15}N	ZG	3.50	60	1024
1a*	^{15}N	HPDEC-MAS	3.50	100	2048
1a	^{125}Te	HPDEC-MAS	3.75	60	1450
1b	^{125}Te	HPDEC-MAS	3.10	60	4392
1c	^{125}Te	HPDEC-MAS	3.75	60	2780

3. DFT Calculations: Further Details

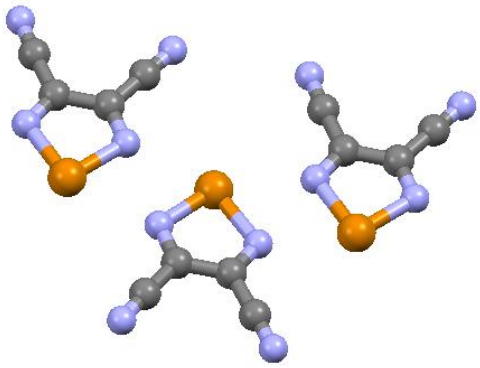

Figure S4. Cluster model used for **1**. Results are reported for the central tellurium atom, which forms two chalcogen bonds with nitrogen atoms on adjacent molecules.

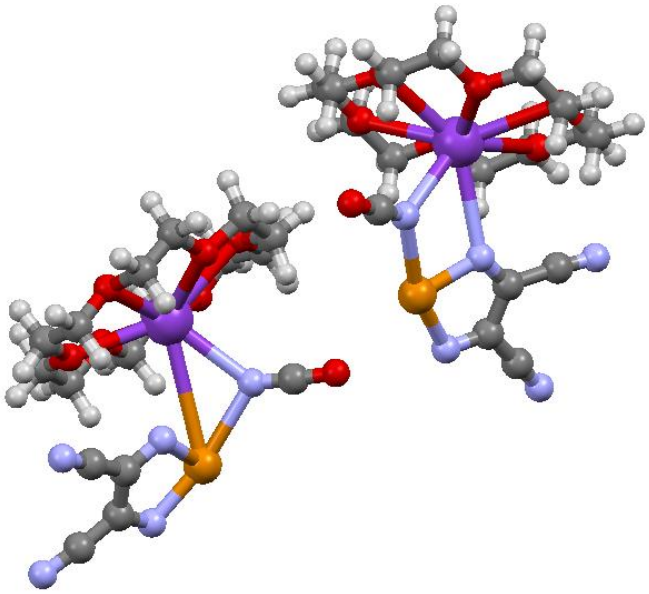

Figure S5. Cluster model used for compound **1a**. Separate calculations were carried out for molecule 1 and molecule 2.

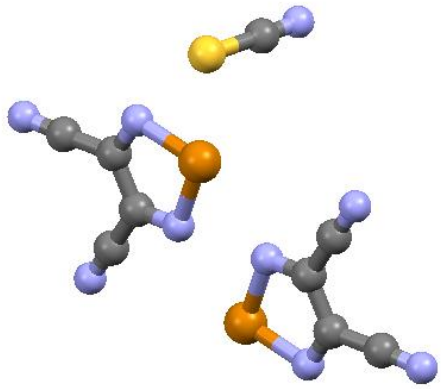

Figure S6. Cluster model used for compound **1b**. Data are reported for the tellurium atom which has a chalcogen bond to sulfur.

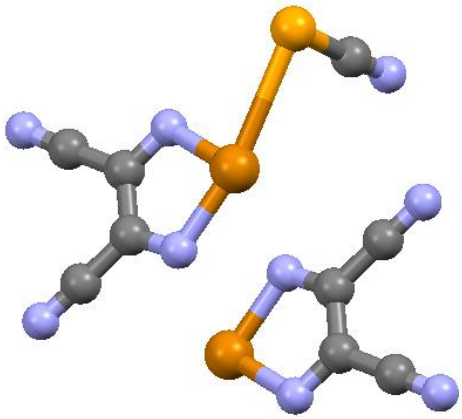

Figure S7. Cluster model used for compound **1c**. Data are reported for the tellurium atom which has a chalcogen bond to selenium.

Convergence of CASTEP Calculations of Magnetic Shielding Tensors

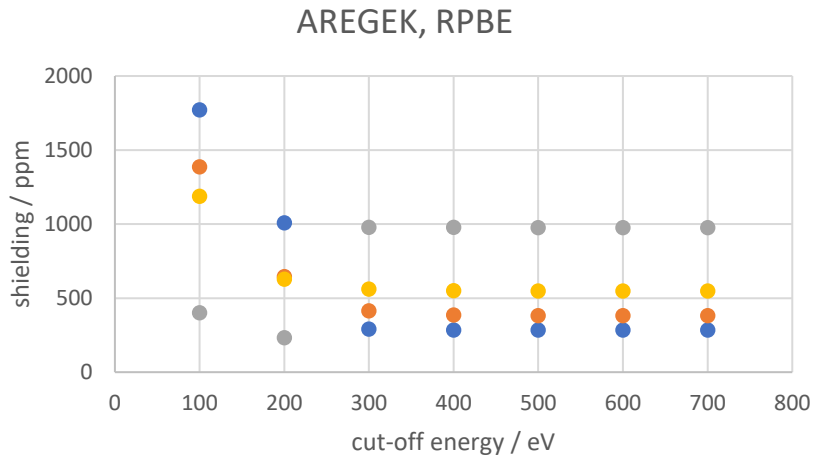

Figure S8. Convergence of calculated tellurium magnetic shielding tensor principal components and isotropic magnetic shielding constant (yellow dots) with respect to planewave cut-off energy for compound **1** (CCDC code AREGEK), using the RPBE functional. The 'fine' setting was used for k-points.

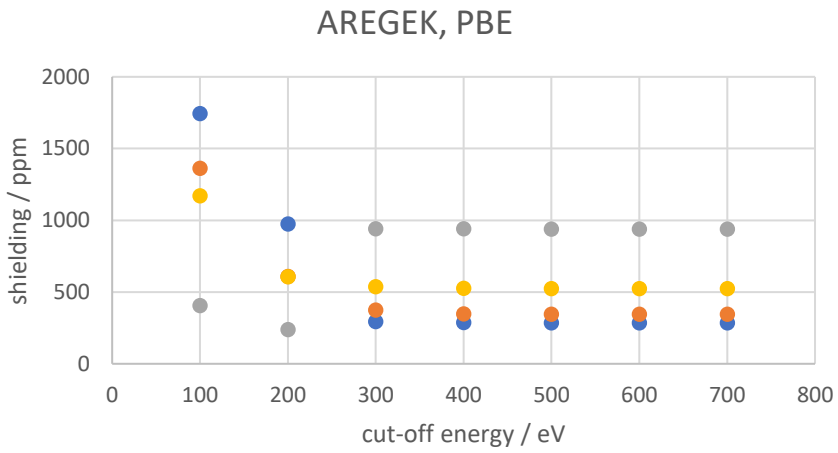

Figure S9. Convergence of calculated tellurium magnetic shielding tensor principal components and isotropic magnetic shielding constant (yellow dots) with respect to planewave cut-off energy

for compound **1** (CCDC code AREGEK), using the PBE functional. The ‘fine’ setting was used for k-points.

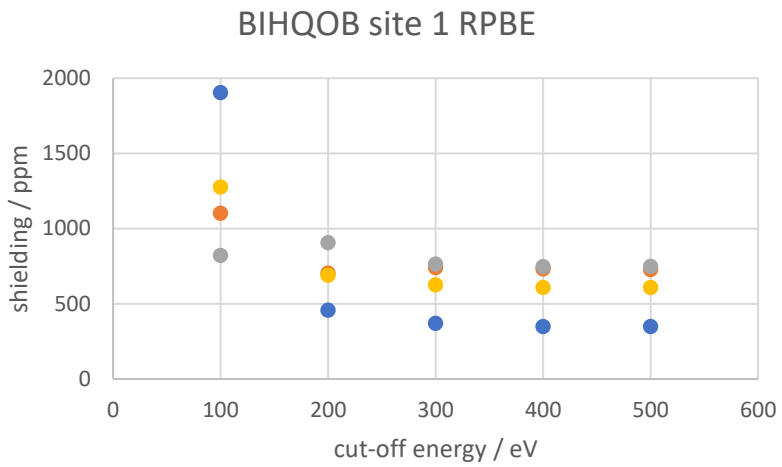

Figure S10. Convergence of calculated tellurium magnetic shielding tensor principal components and isotropic magnetic shielding constant (yellow dots) with respect to planewave cut-off energy for compound **1a, site 1** (CCDC code BIHQOB), using the RPBE functional. The ‘fine’ setting was used for k-points.

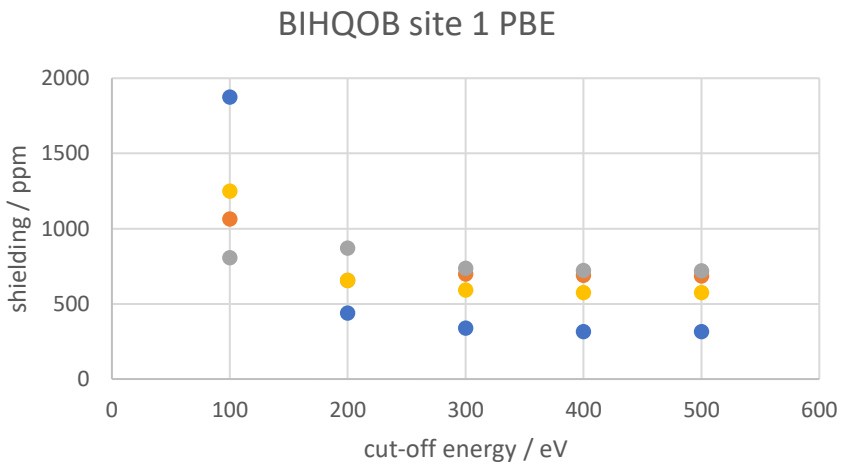

Figure S11. Convergence of calculated tellurium magnetic shielding tensor principal components and isotropic magnetic shielding constant (yellow dots) with respect to planewave cut-off energy for compound **1a, site 1** (CCDC code BIHQOB), using the PBE functional. The ‘fine’ setting was used for k-points.

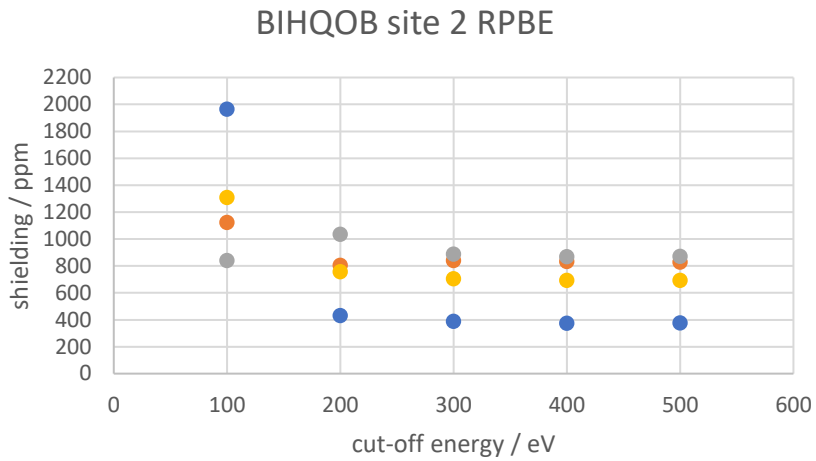

Figure S12. Convergence of calculated tellurium magnetic shielding tensor principal components and isotropic magnetic shielding constant (yellow dots) with respect to planewave cut-off energy for compound **1a, site 2** (CCDC code BIHQOB), using the RPBE functional. The 'fine' setting was used for k-points.

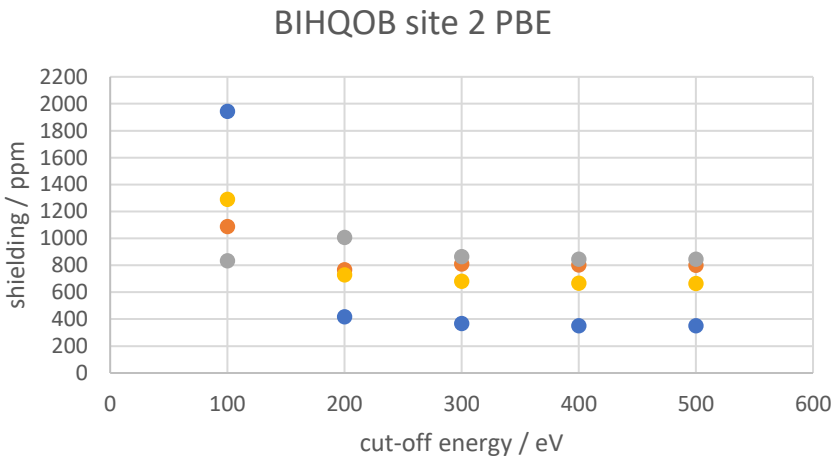

Figure S13. Convergence of calculated tellurium magnetic shielding tensor principal components and isotropic magnetic shielding constant (yellow dots) with respect to planewave cut-off energy

for compound **1a, site 2** (CCDC code BIHQOB), using the PBE functional. The ‘fine’ setting was used for k-points.

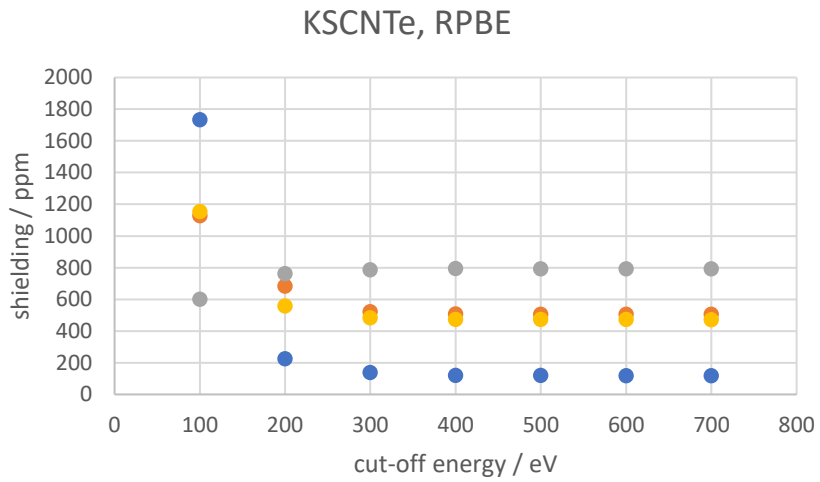

Figure S14. Convergence of calculated tellurium magnetic shielding tensor principal components and isotropic magnetic shielding constant (yellow dots) with respect to planewave cut-off energy for compound **1b**, using the RPBE functional. The 'fine' setting was used for k-points.

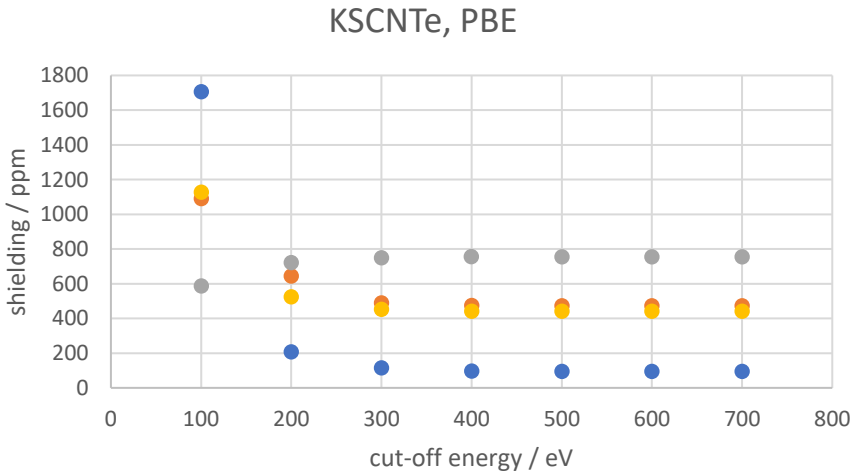

Figure S15. Convergence of calculated tellurium magnetic shielding tensor principal components and isotropic magnetic shielding constant (yellow dots) with respect to planewave cut-off energy for compound **1b**, using the PBE functional. The 'fine' setting was used for k-points.

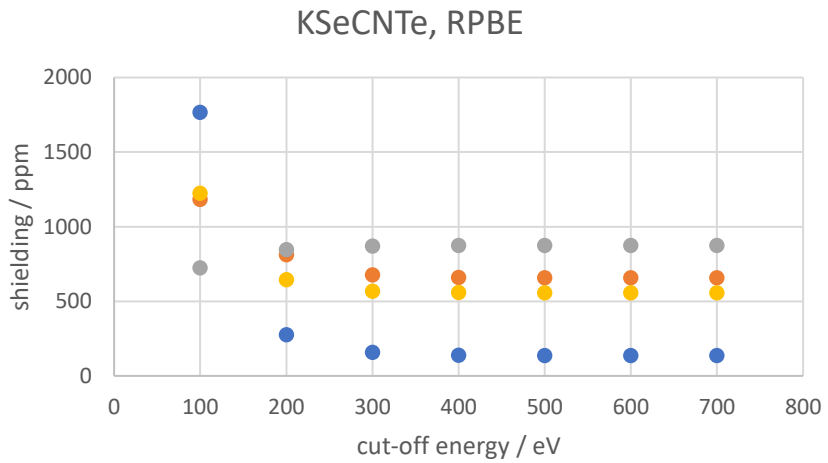

Figure S16. Convergence of calculated tellurium magnetic shielding tensor principal components and isotropic magnetic shielding constant (yellow dots) with respect to planewave cut-off energy for compound **1c**, using the RPBE functional. The 'fine' setting was used for k-points.

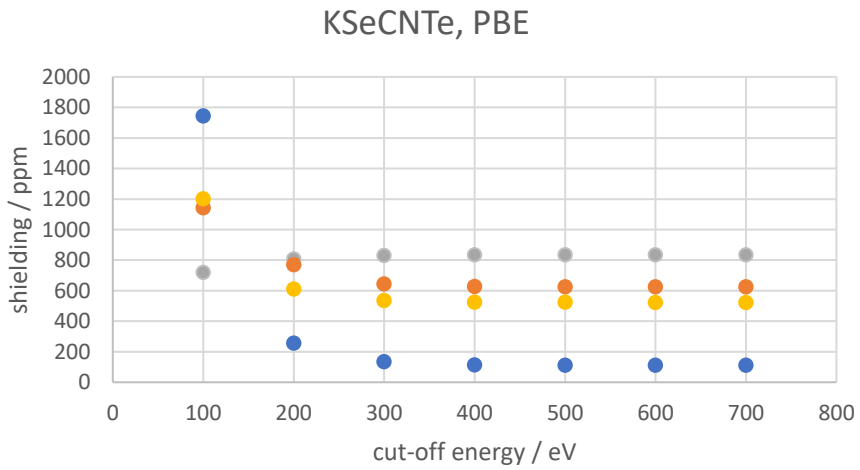

Figure S17. Convergence of calculated tellurium magnetic shielding tensor principal components and isotropic magnetic shielding constant (yellow dots) with respect to planewave cut-off energy for compound **1c**, using the PBE functional. The 'fine' setting was used for k-points.

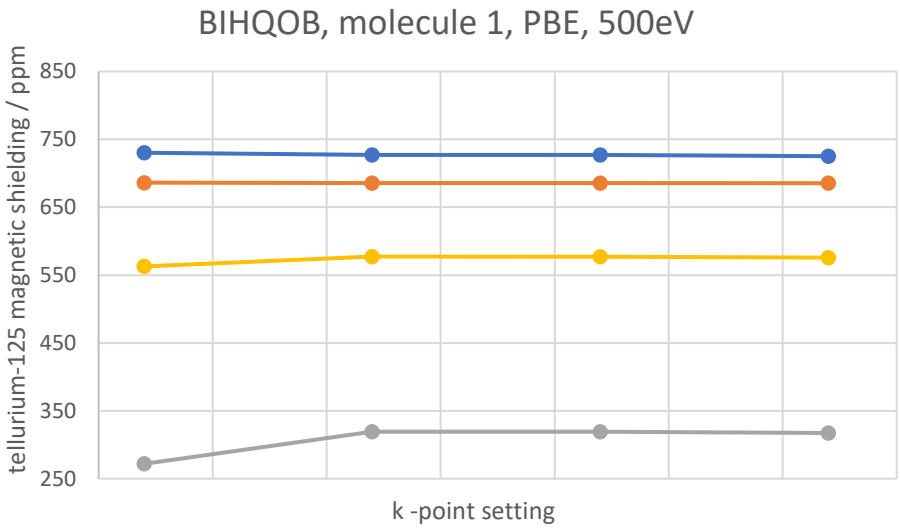

Figure S18. Convergence of calculated tellurium magnetic shielding tensor principal components and isotropic magnetic shielding constant (yellow dots) with respect to k-point setting for compound **1a, site 1** (CCDC code BIHQOB), using the PBE functional and a 500 eV cut-off energy. The settings used, from left to right, are gamma, coarse, medium, and fine.

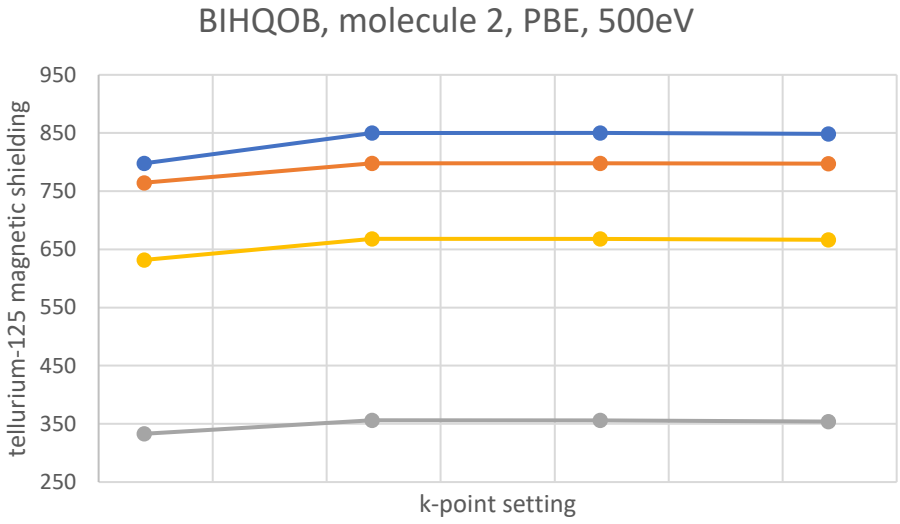

Figure S19. Convergence of calculated tellurium magnetic shielding tensor principal components and isotropic magnetic shielding constant (yellow dots) with respect to k-point setting for

compound **1a, site 2** (CCDC code BIHQOB), using the PBE functional and a 500 eV cut-off energy. The settings used, from left to right, are gamma, coarse, medium, and fine.

Appendix D:

Supporting Information of Chapter 7

1. Synthesis of **1** and **2**

The synthesis of 3,4-dicyanotelluradiazole was carried out using the procedure given by Cozzolino et al.[i] and the compound was further purified using cold-finger sublimation. Unit cell measurement via X-ray diffraction confirmed the space group of AREGEK (CCDC refcode). Tetraphenylphosphonium bromide (refcode DEMYEZ01) was purchased from Sigma Aldrich (98%). Polymorphs **1** (1:1) and **2** (1:2) (150.0 mg of ChB donor and 271.6 mg of ChB acceptor, tetraphenylphosphonium bromide for **1**; 103.3 mg of ChB donor and 373.0 mg of ChB acceptor, tetraphenylphosphonium bromide for **2**) were produced by refluxing the chalcogen bond acceptor and chalcogen bond donor in 4-5 mL of ethanol for 15 minutes, cooling to room temperature, and layering with 1-2 mL of diethyl ether. Slow evaporation of solvent was allowed under room temperature conditions. The melting point recorded for cocrystal **1** is 160°C whereas **2** yielded 165°C.

2. Single-crystal X-ray diffraction

Single crystals of **1** and **2** were chosen carefully and mounted on a goniometer head using MiTeGenMicromounts™ precision tools on glass fibres. The data were collected using a Bruker Kappa Apex II diffractometer with MoKα radiation of wavelength 0.7103 Å as the X-ray source and an APEX II CCD detector. The data were collected at room temperature and the raw data obtained from the Bruker Apex III software was further solved and refined using SHELXL and

SHELXle packages.[ii] Hydrogen atom positions were defined based on geometric considerations and the non-hydrogen positions were determined anisotropically. CCDC deposition numbers 2314483 and 2314484.

3. Powder X-ray diffraction

Powder X-ray diffractograms show the phase purity of **1** and **2** (Figures S1 and S2) obtained using a Bruker D8 Endeavour instrument containing a 1 kW Cu Kα radiation source from a sealed tube and a LynxEye XE-T high-speed detector operating at a wavelength of λ = 1.54056 Å at 298 K. Data were acquired with a 1.83 degree per minute scan rate.

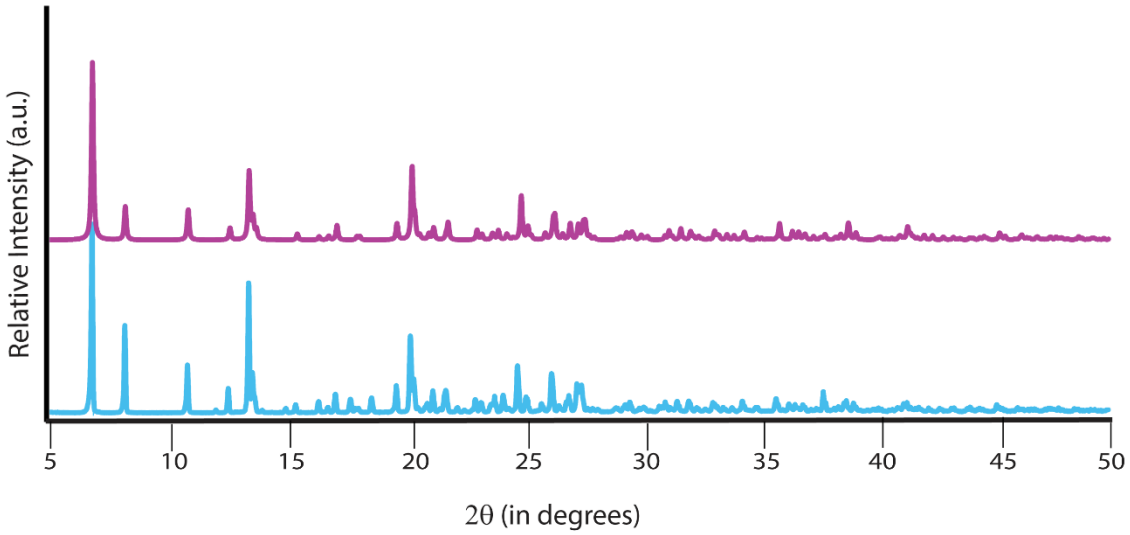

Figure S1. PXRD pattern of **1**. (Sky blue: experimental; purple-simulated).

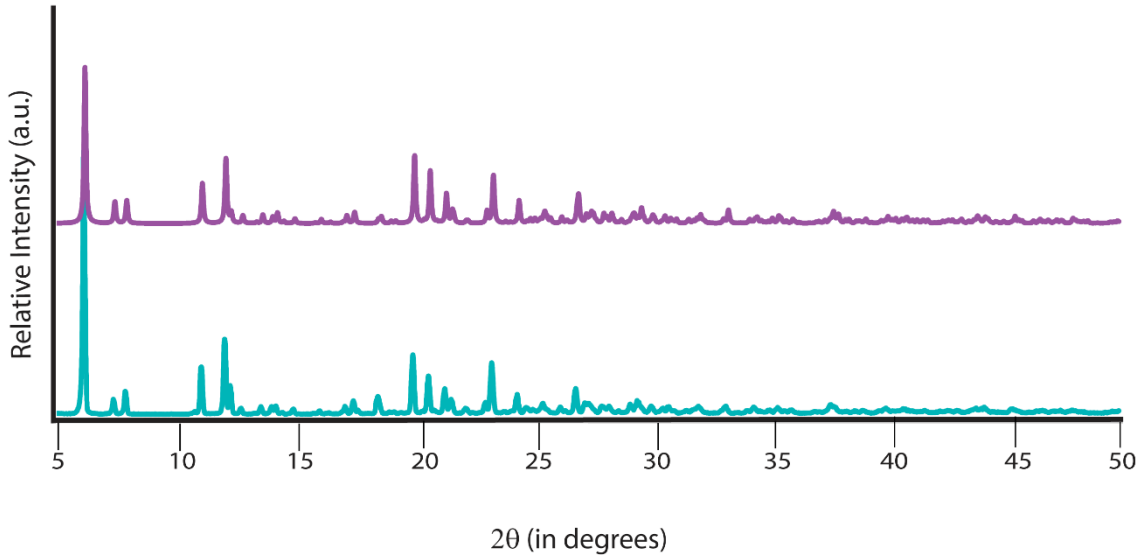

Figure S2. PXRD pattern of **2** (cyan: experimental; purple: simulated).

4. Multinuclear solid-state magnetic resonance experiments

Polymorphs **1** and **2** were finely ground and packed in 4 mm zirconia rotors. A HPDEC/MAS pulse sequence was used to obtain ^{125}Te NMR spectra at different spinning speeds ranging from 9 to 12 kHz at room temperature using a Bruker Avance III 400 NMR spectrometer (B_0 = 9.4 T) and a Bruker Avance III HD 500 spectrometer (B_0 = 11.75 T), both equipped with a triple-resonance 4 mm MAS probe.

Further ^{125}Te solid-state NMR experiments were performed on a Bruker Avance II 900 (B_0 = 21.1 T) spectrometer using a 2.5 mm HX MAS probe where the samples were packed in 2.5 mm zirconia rotors and spun at 30 kHz.

Chemical shifts were referenced to solid telluric acid ($Te(OH)_6$) (δ = 685.5 ppm and 692.2 ppm).[iii] Specific acquisition parameters for the tellurium NMR spectra are given in Table S1.

$^{79/81}$Br solid-state NMR measurements were executed on a Bruker Avance II 900 (B_0= 21.1 T) spectrometer. WURST-QCPMG and simple echo sequences were employed. The finely ground polymorphs (**1** and **2**) and the starting material (ChB acceptor) were individually tightly sealed with Teflon tape and then parafilm in a transparent Teflon tube and inserted in the coil of a home-built 5 mm single channel probe to acquire the resulting bromine spectra. The acquisition parameters are listed in Table S2.

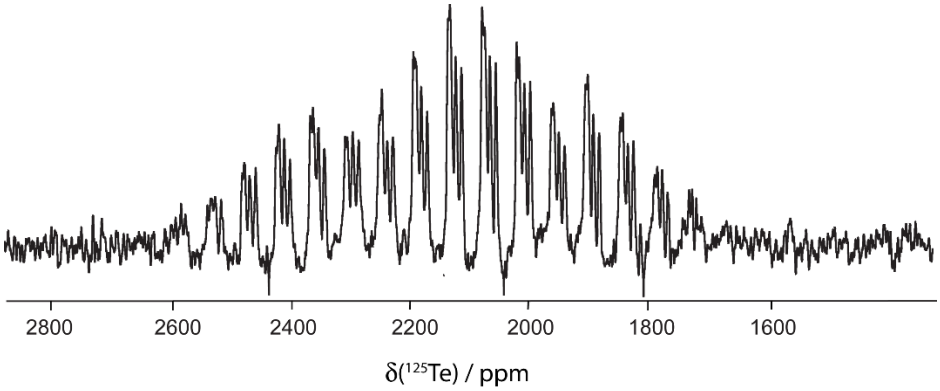

Figure S3. ^{125}Te HPDEC/MAS NMR spectrum of **1** (9 kHz MAS) acquired at 11.75 T. The isotropic chemical shift at this field and MAS rate, 2127 ppm, was found to be temperature-dependent (2136 ppm with 30 kHz MAS at 21.1 T).

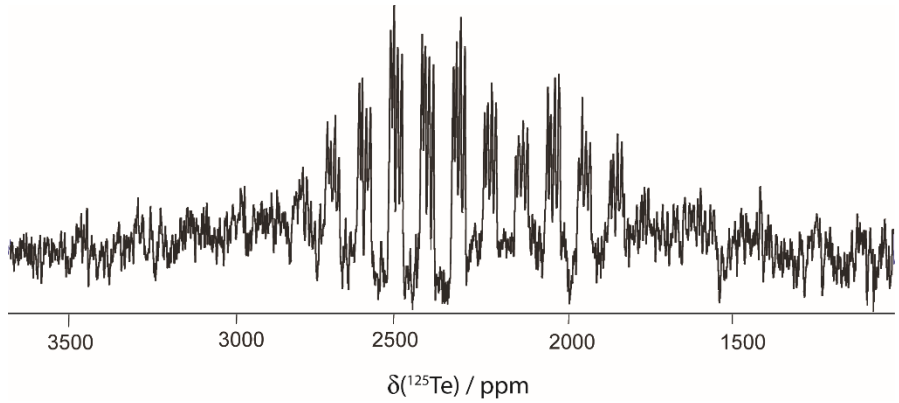

Figure S4. ^{125}Te HPDEC/MAS NMR spectrum of **2** (12 kHz MAS) acquired at 9.4 T. The isotropic chemical shift at this field and MAS rate, 2306 ppm, was found to be temperature-dependent (2311 ppm with 30 kHz MAS at 21.1 T).

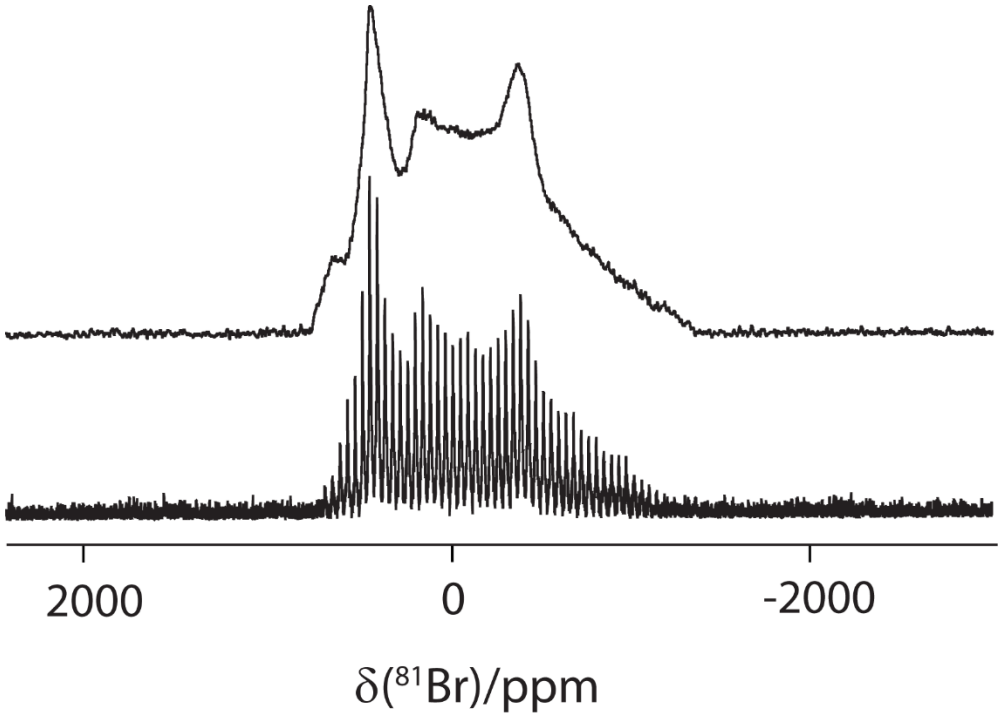

Figure S5. ^{81}Br NMR spectra of a stationary tetraphenylphosphonium bromide powder. Top: echo experiment; bottom: WURST-QCPMG experiment. The bromide ions are disordered

over two sites and the difficulties in unambiguously analyzing the static $^{79/81}$Br NMR spectrum has been discussed previously.[iv]

Table S1. Acquisition parameters for ^{125}Te NMR data

Compound	Number of scans	Recycle delay (s)	π/2 pulse length (μs)	MAS frequency (kHz)
1	19k	10	2.0 (π/4)	30 (B_0 = 21.1 T)
1	2945	30	3.25	9 (B_0 = 11.75 T)
1	2773	30	3.25	11.75 (B_0 = 11.75 T)
1	8k	10	1.60	9 (B_0 = 9.4T)
1	8k	10	1.60	12 (B_0 = 9.4T)
2	8k	10	1.60	9 (B_0 = 9.4 T)
2	24k	10	2.00 (π/4)	30 (B_0 = 21.1 T)

Table S2. Acquisition parameters for $^{79/81}$Br NMR data

Compound	Number of scans	Recycle delay (s)	Pulse sequence	Echo delay or WURST pulse (μs)	Spike separation/ kHz	Number of echoes	Spectral width per O1 step / MHz	Offset frequency (kHz) // number of O1 steps
TPPBr[a] (^{79}Br)	8k	0.25	WURST-QCPMG	10	10	32	5	-
TPPBr (^{81}Br)	4k	0.25	WURST-QCPMG	10	10	64	5	-
TPPBr (^{79}Br)	16k	0.25	echo	30	-	-	2	150 // 3
TPPBr (^{81}Br)	8k	0.25	echo	30	-	-	2	200 // 3
1 (^{79}Br)	16k	0.10	WURST-QCPMG	10	10	48	5	500 // 34
1 (^{81}Br)	12k	0.10	WURST-QCPMG	10	10	32	5	500 // 17
2 (^{79}Br)	16k	0.10	WURST-QCPMG	10	10	48	5	500 // 14
2 (^{81}Br)	8k	0.10	WURST-QCPMG	10	10	48	5	500 // 9

a. TPPBr = tetraphenylphosphonium bromide

5. Additional spectral simulations

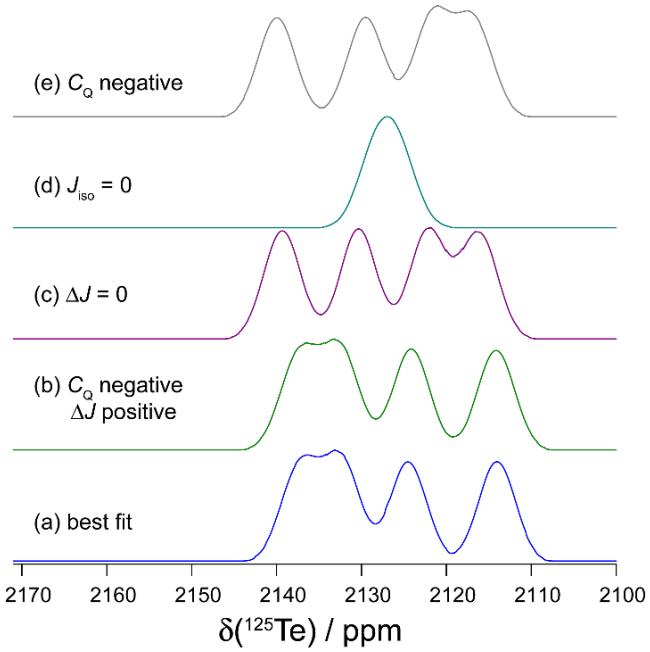

Figure S6. Spectral simulations of the infinite speed ^{125}Te MAS NMR spectrum of **1** at 11.75 T. (a) Best fit spectrum as shown in the main text, using all parameters given in Table 2 of the main text. (b) Same as (a), but with the sign of C_Q changed to negative and ΔJ changed to -3500 Hz. (c) Same as (a), but with $\Delta J = 0$. (d) Same as (a), but with $J_{iso} = 0$. (e) Same as (a), but with the sign of C_Q changed to negative. Simulations were carried out using WSOLIDS1[v] using the "MAS Spin-1/2 coupled to a quadrupolar nucleus (Diag.)" module and correcting for a known problem with the sign of C_Q when the magnetogyric ratio of the observed nucleus is negative.

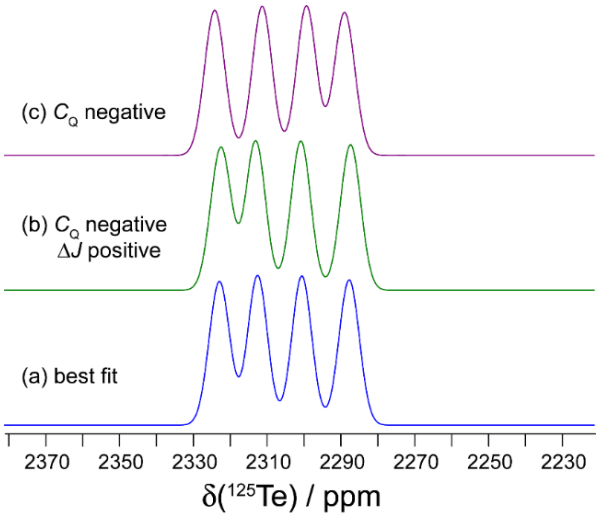

Figure S7. Spectral simulations of the infinite speed ^{125}Te MAS NMR spectrum of **2** at 9.4 T. (a) Best fit spectrum as shown in the main text, using all parameters given in Table 2 of the main text. (b) Same as (a), but with the sign of C_Q changed to negative and ΔJ changed to -2000 Hz. (c) Same as (a), but with the sign of C_Q changed to negative. Simulations were carried out using WSOLIDS1[v] using the "MAS Spin-1/2 coupled to a quadrupolar nucleus (Diag.)" module and correcting for a known problem with the sign of C_Q when the magnetogyric ratio of the observed nucleus is negative.

6. Density functional theory computations

(i) GIPAW DFT - CASTEP

One set of calculations was carried out using CASTEP software[vi] with the crystallographic information files of **1** and **2** used as input structures. Indirect nuclear spin-spin coupling and quadrupolar coupling tensors were calculated using the GIPAW DFT method including ZORA scalar relativistic corrections with cut-off energies ranging from 600 to 900 eV to test the self-consistent field convergence (see Table S3; Figure S8). All of the classical Ramsey mechanisms were included in the calculations: Fermi-contact, spin-dipolar diamagnetic spin-orbital, and paramagnetic spin-orbital. The RPBE functional and a k-point grid of 1×3×1 with spacing of 0.05 $Å^{-1}$ were used. Although this method used periodic boundary conditions to describe the complete crystallographic structure, spin-orbit relativistic corrections were not possible.

Table S3. Indirect nuclear spin-spin coupling and quadrupolar coupling tensor magnitudes calculated using the GIPAW DFT method (ZORA scalar; 900 eV cutoff).[a]

	1	**2**
$C_Q(^{79}Br)$ / MHz	+167.1	+120.9
η	0.20	0.31
$J(^{125}Te,^{81}Br)_{iso}$ / Hz	-1405	-1493
$\Delta J(^{125}Te,^{81}Br)$ / Hz	932	-692
J_{33}-J_{11} / Hz	1201	-718
$J(^{125}Te,^{81}Br)_{11}$ / Hz	-1985	-1236
$J(^{125}Te,^{81}Br)_{22}$ / Hz	-1446	-1289
$J(^{125}Te,^{81}Br)_{33}$ / Hz	-784	-1954

a. $|J_{33} - J_{iso}| \geq |J_{11} - J_{iso}| \geq |J_{22} - J_{iso}|$; $\Delta J = J_{33} - (J_{11} + J_{22})/2$

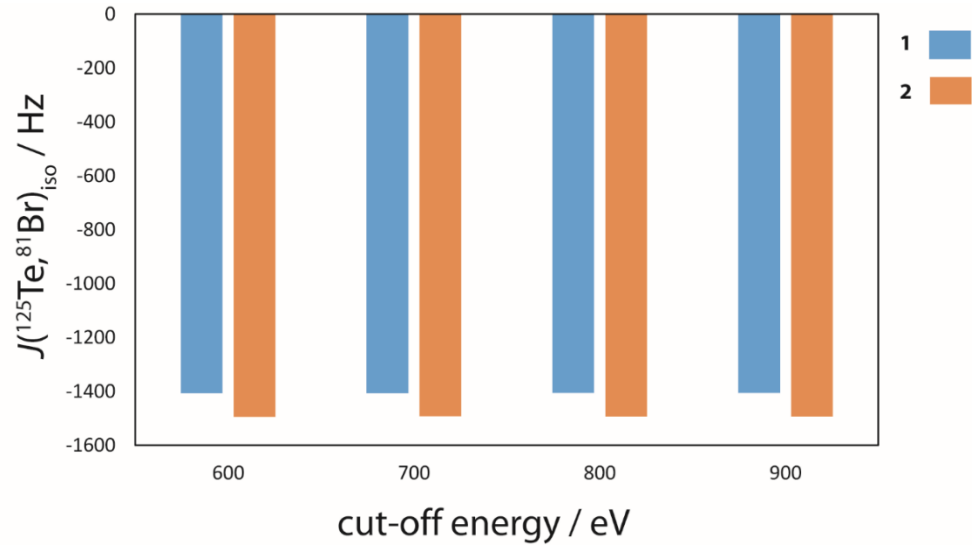

Figure S8. Convergence behaviour of $J(^{125}\text{Te},^{81}\text{Br})_{iso}$ as a function of GIPAW cut-off energy for ionic cocrystal polymorphs **1** and **2**.

(ii) ZORA DFT - AMS

A second set of DFT calculations of the indirect nuclear spin-spin coupling tensors was carried out using Amsterdam Modelling Suite.[vii] This allowed for the treatment of scalar and spin-orbit relativistic corrections using the zeroth order regular approximation (ZORA). All ZORA relativistic analogues of the classic Ramsey mechanisms, and their cross terms, were included in the calculations: Fermi-contact, spin-dipolar diamagnetic spin-orbital, and paramagnetic spin-orbital. A cluster model comprised of a telluradiazole moiety interacting with one bromide ion was used for compounds **1** and **2**, with the coordinates taken from their crystallographic information files. The hybrid PBE0 functional was used with the ZORA TZ2P-J basis set. While this method allows for spin-orbit relativistic corrections, it does not use periodic boundary conditions and therefore the environment of the bromide anion in particular is not expected to be well-modelled.

Table S4. ZORA-DFT computed indirect nuclear spin-spin coupling tensor magnitudes (PBE0/TZ2P-J).[a]

	ZORA scalar		ZORA spin-orbit	
	1	**2**	**1**	**2**
$J(^{125}Te,^{81}Br)_{iso}$ / Hz	-1280	-1092	-1335	-1108
$\Delta J(^{125}Te,^{81}Br)$ / Hz	1394	1112	1382	1025
J_{33}-J_{11} / Hz	1782	1450	1740	1338
$J(^{125}Te,^{81}Br)_{11}$ / Hz	-2133	-1801	-2154	-1763
$J(^{125}Te,^{81}Br)_{22}$ / Hz	-1356	-1124	-1437	-1137
$J(^{125}Te,^{81}Br)_{33}$ / Hz	-351	-351	-414	-425

a. $|J_{33} - J_{iso}| \geq |J_{11} - J_{iso}| \geq |J_{22} - J_{iso}|$; $\Delta J = J_{33} - (J_{11} + J_{22})/2$

References

[i] A. F. Cozzolino, Q. Yang, I. Vargas-Baca, *Cryst. Growth Des.* **2010**, *10*, 4959.

[ii] (a) G. M. Sheldrick, *Acta Crystallogr. Sect. A* **2008**, *64*, 112. (b) L. J. Farrugia, *J. Appl. Crystallogr*. **2012**, *45*, 849. (c) C. B. Hübschle, G. M. Sheldrick, B. Dittrich, *J. Appl. Crystallogr.* **2011**, *44*, 1281.

[iii] M. J. Collins, J. A. Ripmeester, J. F. Sawyer, *J. Am. Chem. Soc.* **1987**, *119*, 4113.

[iv] K. M. N. Burgess, I. Korobkov, D. L. Bryce, *Chem. Eur J.* **2012**, *18*, 5748.

[v] K. Eichele, WSOLIDS1 NMR Simulation Package version 1.20.22, 2014.

[vi] M. D. Segall, P. J. D. Lindan, M. J. Probert, C. J. Pickard, P. J. Hasnip, S. J. Clark, M. C. Payne, *J. Phys. Condens. Matter* **2002**, *14*, 2717.

[vii] (a) G. te Velde, F.M. Bickelhaupt, E.J. Baerends, C. Fonseca Guerra, S.J.A. van Gisbergen, J.G. Snijders, T. Ziegler, *J. Comp. Chem*. **2001**, *22*, 931. (b) ADF 2019, SCM, Theoretical Chemistry, Vrije Universiteit, Amsterdam, The Netherlands, http://www.scm.com. (c) J. Autschbach, T. Ziegler, *J. Chem. Phys.* **2000**, *113*, 9410.

Appendix E:

List of contributions of Tamali Nag

Publications

Nag, T.; Terskikh, V. V.; Bryce, D. L. Experimental Evidence for Non-Fermi-Contact *J* Coupling Across Chalcogen Bonds in Ionic Salt Cocrystal Polymorphs, *Angew. Chem. Int. Ed*. **2024**, e202402441 **.**

Xu, Y.; Calabrese, M.; Pizzi, A.; **Nag, T.**; Hung, I.; Gan, Z.; Resnati, G.; Bryce, D. L. Non-Covalent Matere Bonds in Perrhenates Probed via Ultrahigh-Field Rhenium-185/187 NMR and Zero-Field NQR Spectroscopy. *Chem. Commun*. **2023**, 59, 12609-12612.

Almario, C.[1]; **Nag, T.[1]**; Bryce, D. L. Chemical Shift Tensors as Probes of Chalcogen Bonds. Solid-State NMR study of Telluradiazole-XCN^- (X= O, S, Se) Salt Cocrystals. *Facets*, **2023**, 8, 1-14.

[1]. These authors contributed equally.

Nag, T.; Ovens, J. S.; Bryce, D. L. ^{77}Se and ^{125}Te Solid-State NMR and X-ray Diffraction Structural Study Of Chalcogen-Bonded 3,4-Dicyano-1,2,5-Chalcogenodiazole Cocrystals. *Acta. Cryst. C.* **2022**, 78, 517-523. (Cover article)

Southern, S. A.; **Nag, T.**; Bryce, D. L. NMR Response of the Tetrel Bond Donor. *J. Phys. Chem. C*. **2022**, 126, 851-865. (Cover article)

Hajjar, C.; **Nag, T.**; Al Sayed, H.; Ovens, J. S.; Bryce, D. L. Stoichiomorphic Halogen Bonded cocrystals. A Case Study of 1,4-Diiodotetrafluorobenzene and 3-Nitropyridine. *Can. J. Chem*. **2022**, 100, 245-251.

Conference Presentations and Participation

1. **Nag, T.** and Bryce, D. L. Halide ion as Indirect Probe to Chalcogen Bond. A Solid-State NMR and NQR Study. Poster presentation at International conference on Analytical Sciences and Spectroscopy, July 2023, Ottawa, Ontario, Canada.
2. **Nag, T.**[1]; Almario, C.[1]; Bryce, D. L. Chemical Shift Tensors as Probes of Chalcogen Bonds. Solid-State NMR study of Telluradiazole-XCN^- (X= O, S, Se) Salt Cocrystals. Oral presentation at Ottawa-Carleton Chemistry Institute Research Day, May 2023, Ottawa, Ontario, Canada.
3. **Nag, T.**; Ovens, J. S.; Bryce, D. L. ^{77}Se and ^{125}Te Solid-State NMR and X-ray Diffraction Structural Study Of Chalcogen-Bonded 3,4-Dicyano-1,2,5-Chalcogenodiazole Cocrystals. Poster presentation at Rocky Mountain Conference on Magnetic Resonance, July 2022, Copper Mountain, Colorado, USA.
4. **Nag, T.**; Ovens, J. S.; Bryce, D. L. ^{77}Se and ^{125}Te Solid-State NMR and X-ray Diffraction Structural Study Of Chalcogen-Bonded 3,4-Dicyano-1,2,5-Chalcogenodiazole Cocrystals.

Oral presentation at International Conference on Analytical Sciences and Spectroscopy, August 2022, Kingston, Ontario, Canada.

5. **Nag, T.**; Ovens, J. S.; Bryce, D. L. ^{77}Se and ^{125}Te Solid-State NMR and X-ray Diffraction Structural Study Of Chalcogen-Bonded 3,4-Dicyano-1,2,5-Chalcogenodiazole Cocrystals. Poster presentation at Canadian Chemistry Conference and Exhibition (best poster prize sponsored by ISMAR), June 2022, Calgary, Alberta, Canada.
6. Participant, Experimental NMR Conference, March 2021 (online).
7. **Nag, T.**; Kumar, V.; Xu, Y.; Ovens, J. S.; Bryce, D. L. SSNMR and X-ray diffraction Study of Chalcogen-Bonded Cocrystals. Poster presentation at Canadian Chemistry Conference and Exhibition, August 2021, online.
8. Online Participant at 4th International Symposium on Halogen Bonding, November 2020, Stellenbosch, South Africa.
9. Online participant, MIT Zoominar, July 2020.
10. Participant at MOOT NMR Symposium 2019, University of Ottawa, Ottawa, Canada.
11. Participant at CACSB Conference, February 2019, PRIST University, Tamil Nadu, India.
12. **Nag, T.** and Balakrishnarajan, M. M. Noncovalent interactions in Chalcogen-Bonded Topological Insulators: A theoretical Case Study. Oral presentation at Current Trends in Chemistry Symposium (best oral presentation), December 2018, Pondicherry University, Puducherry, India.
13. **Nag, T.**; Chandra, S. Demonstration of Unfolding of Proteins. Workshop held by DBT-STAR, January 2016, Lady Brabourne College, Kolkata, India.

14. Participant, Dipta Memorial Symposium of Astrophysics and Cosmology, October 2015, Bose Institute, Kolkata, India.